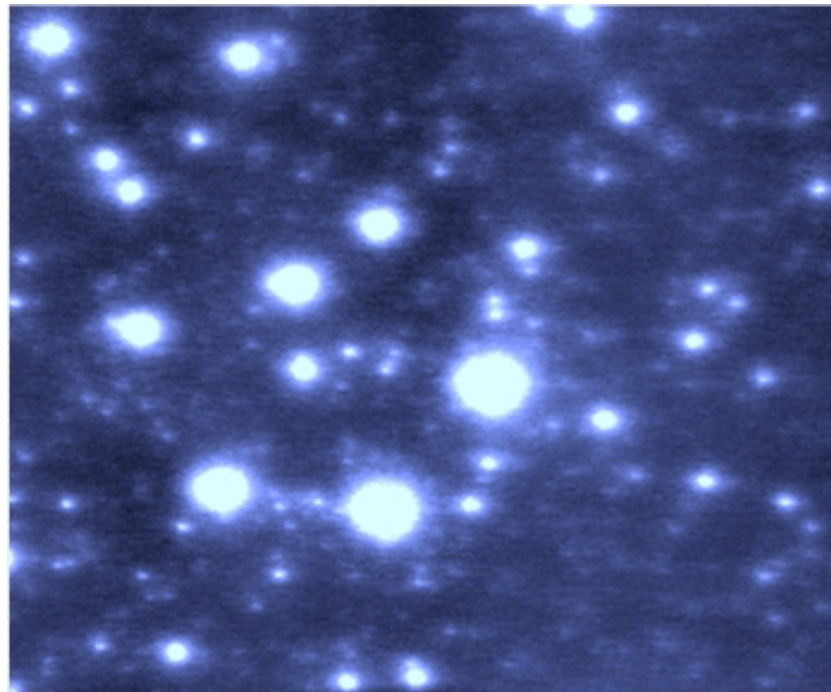


LUCKY IMAGING: DIFFRACTION-LIMITED ASTRONOMY FROM THE GROUND IN THE VISIBLE

Nicholas Michael Law

Institute of Astronomy & Selwyn College

Cambridge University



Dissertation submitted for the degree of Doctor of Philosophy

Summary

LUCKY IMAGING: DIFFRACTION-LIMITED ASTRONOMY FROM THE GROUND IN THE VISIBLE

Nicholas Michael Law

This thesis describes the development and use for science of the Cambridge Lucky Imaging system LuckyCam, designed for astronomical imaging through Earth's turbulent atmosphere. I demonstrate that in good conditions LuckyCam gives diffraction-limited images in I-band, matching the resolution of the Hubble Space Telescope from the ground. In poorer conditions, the system improves the imaging resolution by factors of 3-4. The system is shown to reliably achieve very-high-resolution output images which are useful for a wide variety of astronomical programmes. The L3CCD (EMCCD) detector allows noise-free photon counting at CCD quantum efficiencies; calibration methods developed for astronomy with this detector are presented. My design and implementation of both fast LuckyCam data acquisition software and an automated Lucky Imaging pipeline is discussed in detail. I also present several methods for the measurement of the parameters of close binary systems using LuckyCam data, as well as calibration methods for speckle imaging using L3CCD detectors.

In the second part of this thesis, I detail the LuckyCam Very Low Mass (VLM) binary survey, a search for close companions to nearby late-M-dwarf stars. 110 targets are imaged at 0.1 arcsec resolution in only 16 hours on-sky, a very fast rate compared to other high resolution imaging systems. 21 new VLM binaries are found, a ~25% increase in the known number. Several more exotic systems were discovered during the surveys, such as a possible substellar companion, and a wide triple system. The orbital radius distribution of the binaries is found to have an apparently sharp change at around the M5.0-M5.5 spectral type, with the earlier-type stars having a large population of binaries wider than 10AU.

Declaration

I hereby declare that this dissertation entitled *Lucky Imaging: Diffraction-Limited Astronomy from the Ground in the Visible* is not substantially the same as any that I have submitted for a degree or diploma or other qualification at any other University.

I further state that no part of my thesis has already been or is being concurrently submitted for any such degree, diploma or other qualification.

This dissertation is the result of my own work and includes nothing which is the outcome of work done in collaboration except where specifically indicated in the text. Those parts of this thesis which have been published are as follows:

1. Chapter 4 is based on the paper LUCKY IMAGING: HIGH ANGULAR RESOLUTION IMAGING IN THE VISIBLE FROM THE GROUND Nicholas Law, Craig Mackay, John Baldwin, *Astronomy & Astrophysics* 446, 739-745 (2006).
2. Chapters 6 & 7 include results from 10 NEW VERY LOW MASS CLOSE BINARIES RESOLVED IN THE VISIBLE Nicholas Law, Simon Hodgkin, Craig Mackay, John Baldwin *Astron.Nachr.* 326 1024-1025 (2005).
3. Chapter 6 is based on DISCOVERY OF FIVE VERY LOW MASS CLOSE BINARIES, RESOLVED IN THE VISIBLE WITH LUCKY IMAGING Nicholas Law, Simon Hodgkin, Craig Mackay *Monthly Notices of the Royal Astronomical Society*, 398 2006.
4. The results in chapter 7 are soon to be submitted for publication.

This dissertation contains fewer than 60,000 words.

Nicholas M. Law

Cambridge, UK

23 May 2006

Acknowledgements

Many, many thanks to my supervisor, Craig Mackay, for proposing such a great project and offering amiable and incisive guidance. Thanks also to him for the construction and taming of LuckyCam, very congenial observing trips, and generally making it a fantastic three years.

Many thanks also to Simon Hodgkin, for making the whole VLM binaries thing make sense. And the project benefited greatly from a slew of insightful comments at Lucky group meetings from John Baldwin and Peter Warner. Thanks also to John for wit and insight on the 2004 LuckyCam run, and for coming up with the original Cambridge Lucky Imaging concept.

The staff at the Nordic Optical Telescope could hardly have been more accommodating, and helped to make the observing runs extremely smooth and very productive. Particular praise goes to Graham Cox, Peter Brandt, Peter Sorensen, and Johannes Andersen. For many an entertaining coffee, tea, and trip to the Castle, thanks to the students, postdocs and office-mates at the IOA, far too numerous to list here, but including Jamie, Laurie, Jeremy, Jessie, David, Rob, Ross, James, Natasha, Simon, Viv, and everyone else. I am also very grateful to all the IOA staff (Margaret, Sian and Paul particularly), who really make the IOA a great place to work.

Depending on the reader's preference, thanks might go to David Fried, for the "Lucky" nomenclature. After the November 2005 observing run, where the detection of Mars often proved challenging, no thanks are allocated to Tropical Storm Delta.

Huge thanks to Adrienne for being wonderful throughout my PhD. Finally, and definitely not least, enormous thanks to my parents for (among many other things!) giving me the astronomy bug, and supporting me though this project.

I acknowledge with gratitude the support of a PPARC fellowship. This thesis is based on observations made with the Nordic Optical Telescope, operated on the island of La Palma jointly by Denmark, Finland, Iceland, Norway, and Sweden, in the Spanish Observatorio del Roque de los Muchachos of the Instituto de Astrofisica de Canarias. This research has made use of NASA's Astrophysics Data System Bibliographic Services, as well as the SIMBAD database and VizieR catalogue access tools operated at CDS, Strasbourg, France. A few of the results were based on observations made with the NASA/ESA Hubble Space Telescope, obtained from the data archive at the Space Telescope Institute.

Contents

1	Introduction	15
1.1	The Effects of Atmospheric Turbulence	15
1.1.1	Long and short exposure point spread functions	16
1.1.2	Turbulence characterisation	17
1.2	Correction Methods	19
1.2.1	Lucky Imaging	21
1.2.2	Adaptive Optics	21
1.2.3	Tip/tilt correction systems	22
1.2.4	Speckle Interferometry	23
1.2.5	Interferometry	24
1.2.6	The capabilities of presently available systems	24
1.3	The Lucky Imaging Technique	24
1.3.1	Previous systems	25
1.3.2	Camera requirements for a diffraction-limited Lucky Imaging system . .	27
1.3.3	The Cambridge Lucky Imaging system	29
1.4	The Structure of this Thesis	29
1.5	Summary	30
2	The LuckyCam Data Acquisition System	31
2.1	Introduction	31
2.2	LuckyCam Optics	31
2.2.1	LuckyCam in 2005	34
2.3	L3CCDs	36
2.3.1	Multiplication noise	38
2.3.2	Photon counting	39
2.3.3	Bias, flats & cosmic rays	41
2.3.4	Gain calibration	43
2.4	Data acquisition - PixCel LC	46
2.4.1	Interface upgrades	47
2.4.2	The PIXEL LC backend	49
2.4.3	Realtime Lucky Imaging	50

2.4.4	Realtime compression	51
2.4.5	LuckyCam control	53
2.5	Summary	55
3	The Lucky Imaging Data Reduction Pipeline	57
3.1	The Lucky Imaging Process	57
3.1.1	Frame selection	58
3.1.2	Image alignment	58
3.2	Pipeline Implementation	60
3.3	LSCRIPT	62
3.4	CLEANUP & BIASGEN	62
3.5	LUCKY	65
3.5.1	Setup	65
3.5.2	Initial processing	68
3.5.3	Frame quality and shift-lock determination	68
3.5.4	Final high-resolution image reconstruction	69
3.5.5	Further processing	70
3.6	Summary	75
4	Lucky Imaging Performance	77
4.1	The PSFs produced by Lucky Imaging	78
4.2	Lucky Imaging Performance	81
4.2.1	On-axis resolution improvement	81
4.2.2	Isoplanatic patch	84
4.2.3	Wide-field Lucky Imaging in the blue	85
4.2.4	Narrow-Band imaging	87
4.2.5	Spectroscopy	87
4.2.6	Nebulosity	89
4.2.7	High time resolution imaging with LuckyCam	89
4.2.8	A comparison with HST	91
4.3	Signal-to-noise Ratio (SNR) Considerations	92
4.4	Lucky Imaging Requirements	94
4.4.1	Guide star flux	94
4.4.2	Sky coverage	95
4.4.3	Frame rates	95
4.5	Summary	96
5	Measuring Close Binary Parameters with LuckyCam	97
5.1	Introduction	97
5.2	Close Binary Photometry	97
5.2.1	The faint guide star PSF	98

5.2.2	Tripling	98
5.2.3	PSF fitting	100
5.3	Speckle Interferometry with L3CCDs	103
5.3.1	The speckle imaging method	103
5.3.2	L3CCD specifics	104
5.3.3	Measuring binary parameters from speckle data	107
5.4	Summary	110
6	The LuckyCam Survey for VLM Binaries	
	I. M5.5-M8 dwarfs within 40pc	111
6.1	Introduction – VLM Binaries	111
6.1.1	Why high-resolution imaging?	112
6.1.2	Why LuckyCam?	113
6.2	The Sample	116
6.2.1	Proper motion biases	116
6.2.2	Target List	116
6.3	Observations	117
6.3.1	Binary detection and photometry	119
6.3.2	Sensitivity	122
6.4	Results & Analysis	122
6.4.1	Confirmation of the binaries	122
6.4.2	Distances, ages and masses	124
6.4.3	Sensitivity to white dwarf companions	124
6.4.4	Notes on the new systems	124
6.4.5	A companion to Ross 530	128
6.5	Discussion	128
6.5.1	The binary frequency of M5.5-M8.0 stars in this survey	128
6.5.2	Contrast Ratios	129
6.5.3	The distribution of orbital radii	129
6.6	Summary	129
7	The LuckyCam Survey for VLM Binaries	
	II. M4.5-M6.0 Targets	133
7.1	The Sample	133
7.1.1	X-ray selection	134
7.1.2	Target distributions	138
7.2	Observations	139
7.2.1	Binary detection and photometry	139
7.2.2	Sensitivity	140
7.3	Results & Analysis	140

7.3.1	Confirmation of the binaries	140
7.3.2	The nature of the target stars	143
7.3.3	Distances	144
7.3.4	Notes on some individual systems	146
7.4	Discussion	149
7.4.1	The binary frequency of stars in this survey	149
7.4.2	Biases in the X-ray sample	151
7.4.3	Is X-ray activity an indicator of binarity?	152
7.4.4	Contrast ratios	153
7.4.5	The distribution of orbital radii	154
7.5	Conclusions from the LuckyCam Surveys	156
7.5.1	Extensions to the LuckyCam VLM Binary Surveys	158
7.6	Summary	159
8	Conclusions	161
8.1	Lucky Imaging Performance	161
8.2	Future Prospects for Lucky Imaging	162
Bibliography		164

List of Figures

1.1 An example of the effects of seeing	16
1.2 Short exposure point spread functions	18
1.3 PSF shape changes induced by changing turbulence strength	20
1.4 Diagram of a typical LGS AO system	22
1.5 The capabilities of currently-available ground based imaging systems	25
1.6 Strehl ratio probabilities	26
2.1 The November 2005 version of LuckyCam (1)	32
2.2 The November 2005 version of LuckyCam (2)	33
2.3 A sketch of the optical layout of the 2005 version of LuckyCam.	35
2.4 L3CCD layout	37
2.5 L3CCD output signal probabilities	37
2.6 LuckyCam linearity verification	39
2.7 Typical LuckyCam output signal histogram	40
2.8 Photon counting	40
2.9 L3CCD gain measurement	43
2.10 The average horizontal shape of single-photon events	45
2.11 Calibration of LuckyCam photometry against SDSS standards	45
2.12 PixCel LC: LuckyCam data acquisition	48
2.13 PixCel LC data processing path	49
2.14 Realtime compression	53
2.15 The LuckyCam control interface.	54
2.16 Schematic of the LuckyCam control system	55
3.1 Comparison between the brightest speckle position and the centroid position . .	59
3.2 The distance between the PSF centroid and the brightest speckle, as a function of frame quality	60
3.3 The LuckyCam data reduction pipeline	61
3.4 Automated selection of guide stars	63
3.5 Cleanup processing	64
3.6 Lucky imaging processing flowchart	66

3.7 An example LUCKY settings file	67
3.8 The Drizzle process	70
3.9 Image reconstruction methods	71
3.10 Autoguider simulations	72
3.11 Rapid variations in cloud transmission	74
3.12 Detripling	76
4.1 Lucky Imaging of the core of M15	78
4.2 Average radial Lucky Imaging profiles	79
4.3 Resolution as a function of seeing and percentage selection	80
4.4 FWHM & FWHEF improvements	82
4.5 Airy rings	83
4.6 Isoplanatic patch example	84
4.7 Fast seeing variations	85
4.8 Lucky Imaging in B-band	86
4.9 Spectroscopy	88
4.10 Lucky Imaging of the Crab Nebula	88
4.11 High-time-resolution imaging of the Crab Pulsar	91
4.12 A comparison of HST and LuckyCam I-band imaging	92
4.13 Lucky Imaging SNR model	93
4.14 Guide star flux requirements	94
4.15 Frame rate requirements	96
5.1 Automated PSF fitting	99
5.2 PSF fitting accuracy	102
5.3 Speckle imaging example	103
5.4 L3CCD speckle imaging calibration process	105
5.5 Fitting binary parameters to power spectra	109
6.1 Known VLM binaries	113
6.2 Sample colour-magnitude diagram	114
6.3 The distribution of the target sample in K magnitude and V-K colour	118
6.4 Calibration of the LuckyCam photometry against SDSS standards	120
6.5 Contrast ratio sensitivity	121
6.6 Simulated faint companion PSFs	121
6.7 Lucky imaging of the five new binaries	123
6.8 Mass models for LSPM J1735+2634	125
6.9 The companion to Ross 530	128
6.10 Mass ratios	130
6.11 Orbital radii	131

7.1	The two samples in K, V-K and distance	135
7.2	The observed samples, plotted in a V/V-K colour-magnitude diagram. The background distribution shows all stars in the LSPM-North catalogue.	138
7.3	The newly discovered binaries	141
7.4	The stars in the sample which have a spectral type listed in the SIMBAD database	145
7.5	LuckyCam and HST imaging of the triple system GJ1245AC	148
7.6	The orbit of GJ 1245AC	150
7.7	The fraction of stellar luminosity which appears as X-Ray emission in the X-ray sample targets.	152
7.8	The i-band contrast ratios of the detected binaries vs. separation in arcsecs . . .	153
7.9	The i-band contrast ratios of the detected binaries vs. separation in AU	154
7.10	The histogram distribution of orbital radii of the detected binaries in the sample.	155
7.11	Orbital radius in the detected binaries as a function of colour	156
7.12	Cumulative orbital radius distributions	157

List of Tables

6.1	The observed sample	115
6.2	Observations of the new binary systems	126
6.3	New binary systems' component properties.	127
7.1	The observed non-X-ray-emitting sample	136
7.2	The observed X-ray emitting sample	137
7.3	Previously known binaries re-detected by LuckyCam	138
7.4	The observed properties of the detected binaries	142
7.5	DSS confirmation of some of the new binaries	143
7.6	The apparent V-K colour of unresolved binary systems	145
7.7	The derived properties of the binary systems	147

1

Introduction

The resolution of all large ground-based telescopes is severely limited by the effects of atmospheric turbulence. At even the best sites, the resolution of a 2.5m telescope is degraded by at least a factor of five in the visible.

This thesis presents the development and use of the Lucky Imaging technique, an elegant method of obtaining diffraction-limited images using large telescopes. As well as discussing the implementation of a fully automated Lucky Imaging pipeline, and investigating the performance of the technique in detail, I use the Lucky Imaging system to perform two surveys for very low mass stellar and substellar companions to M-dwarfs.

In this introduction, I first describe the blurring effects of atmospheric turbulence (seeing), then discuss several methods that have been or are used to reduce the resolution loss, before concluding with a detailed look at Lucky Imaging.

1.1 The Effects of Atmospheric Turbulence

The effects of turbulence on astronomical imaging with a telescope were first described shortly after the invention of the instrument (Galileo, 1610). Short exposure images rapidly change in both shape and position; long exposure images are very blurred (figure 1.1).

A huge variety of astronomical imaging programs rely on greater angular resolution than can

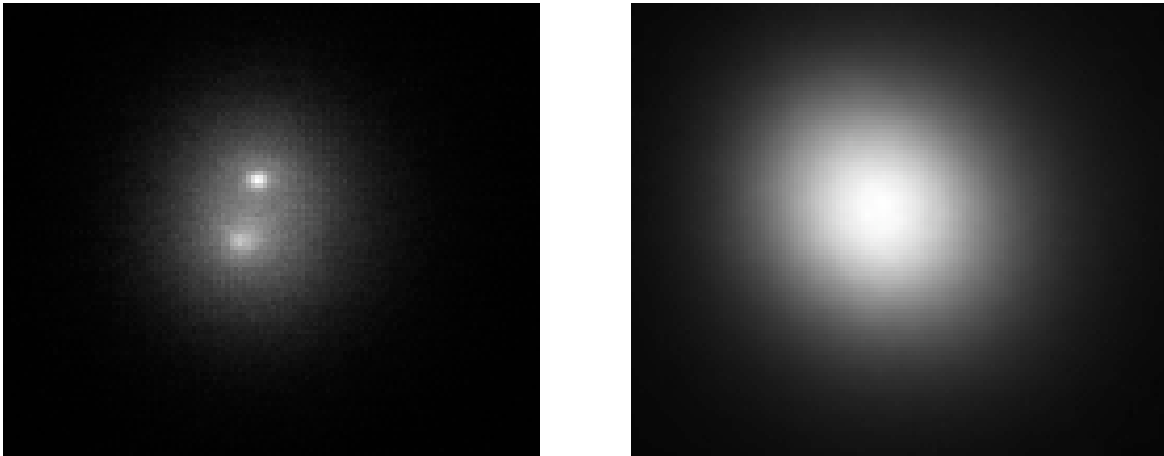


Figure 1.1: The 0.31 arcsec binary LP 359-186 (the companion was discovered as part of the VLM binary survey described in chapter 7). The left panel shows a Lucky Imaging near-diffraction-limited image; the right shows the same target as viewed by a standard CCD camera. The binary is unresolved in the seeing-limited case, where the PSF FWHM is approximately 0.8 arcsec. In this case, telescope wind-shake introduces a slight elongation into the seeing-limited PSF. Almost all VLM binaries cannot be resolved from the ground without turbulence-compensation systems.

be achieved from the ground with seeing-limited instruments. As an illustration of this, Livio et al. (2003) details a spectacular decade of science performed with the 2.5m Hubble Space Telescope. Space telescopes are, however, extremely costly compared to ground-based systems, and the achievement of similar resolution from the ground is a very active area of research. I detail the major turbulence-compensation methods in section 1.2; Lucky Imaging is the only method which is capable of achieving Hubble Space Telescope resolution in the visible (demonstrated in chapters 4, 6 and 7).

1.1.1 Long and short exposure point spread functions

On large telescopes, there are two important regimes of imaging – long and short (less than $\sim 1/4$ second) exposures. Because the structure of the turbulence above the telescope is continually changing, the short-exposure point spread function (PSF) is very variable. Short exposure images take the form of speckle patterns (figure 1.2), consisting of multiple distorted and overlaid copies of the diffraction-limited PSF. Short exposure PSFs thus retain information at the diffraction limit in their speckle patterns, although it is usually very highly distorted.

Long exposure images are simply the sum of a large number of short exposure images. Because the short-exposure PSF is highly variable, both in structure and centroid position, the summed long-exposure PSF is highly blurred compared to the diffraction limits, by factors of 5-15 \times on a 2.5m telescope at a good site.

To increase the signal-to-noise, almost all astronomical imaging is performed with long expo-

sures, unless conditions (such as high sky brightness in the infrared) prevent it. Most conventional infrared and visible astronomical imaging on large ground-based telescopes does not retain information at the diffraction limit of the telescope, unless turbulence correction measures are employed.

1.1.2 Turbulence characterisation

Turbulence induced phase errors are typically on the order of a few wavelengths. The total atmospheric turbulence strength is usually characterised by the quantity r_0 – the size of diffraction-limited aperture which has the same resolution as an infinite seeing-limited aperture. The RMS phase error across a circle of diameter r_0 is approximately 1 radian, conventionally measured at 550nm wavelength (Fried, 1967). Because it is expressed in terms of phase error, the parameter (and equivalently the image-degrading effect of the turbulence) is strongly dependant on wavelength, being proportional to $\lambda^{6/5}$. Figure 1.3 shows examples of the image distortions induced in short exposure images by different values of r_0 .

Atmospheric turbulence is usually modelled using a Kolmogorov power spectrum, developed by Tatarski (1961) on the basis of studies by Kolmogorov (1941). In the Kolmogorov model, the mean-square difference in phase between two points on a wavefront separated by a distance \mathbf{r} is:

$$D_\phi(\mathbf{r}) \equiv \langle |\phi(\mathbf{r}') - \phi(\mathbf{r}' + \mathbf{r})|^2 \rangle = 6.88 \left(\frac{|\mathbf{r}|}{r_0} \right)^{5/3} \quad (1.1)$$

This model is supported by a variety of experimental measurements (for example, Colavita et al. (1987); Buscher et al. (1995); Nightingale & Buscher (1991)), and is widely used. However, other studies have found significant deviations from Kolmogorov statistics – for example, di Folco et al. (2003) found the turbulence at the Very Large Telescope Interferometer to have a spectral slope consistently 10-20% lower than Kolmogorov. The illustrative simulations presented in this introduction assume a Kolmogorov power spectrum, generated using code kindly supplied by David Buscher.

Seeing

A well-figured telescope with an aperture much smaller than r_0 will provide images which are limited only by the diffraction limit of its aperture; equivalently (Fried, 1966), the seeing disk size ϵ at an effective wavelength λ is:

$$\epsilon = 0.98 \frac{\lambda}{r_0} \quad (1.2)$$

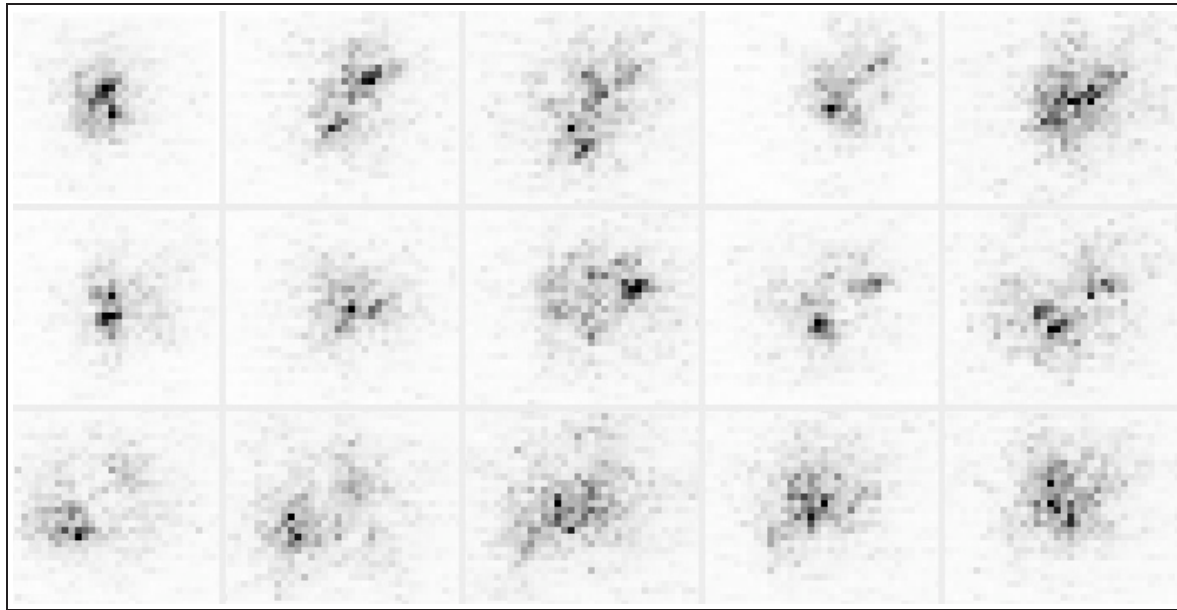


Figure 1.2: An example set of I-band LuckyCam short exposure images of the $I=+11.1$ mag star Ross 530. The frames are sequential 33ms exposures, with time increasing left-to-right and up-to-down. The frames have a resolution of 0.04 arcsecs per pixel, which slightly undersamples the 0.08 arcsec FWHM I-band diffraction-limit of the 2.5m Nordic Optical Telescope used for these observations. The first frame has the 17th highest Strehl ratio in this 3600 frame, 2 minute run, and is the closest-to-diffraction-limited shown in this figure. Note the very fast light concentration and PSF shape changes, and the general decline in quality over the 600ms period shown here.

ϵ is the turbulence-limited long exposure resolution on a telescope much larger than r_0 . The astronomical seeing is usually measured (during general observations) from the FWHM of the turbulence-limited long exposure PSF.

Unfortunately, r_0 rarely exceeds 50cm at the best astronomical sites (for example, Aristidi et al. (2005)), and is more usually 10-20cm (for example, Vernin & Munoz-Tunon (1994)). The seeing (also by convention measured at 550nm) is only very rarely better than 0.5 arcsec at even the best sites, a factor of ten wider than the diffraction-limited resolution of a 2.5m telescope.

Variability

There are two main components in the coherence timescales of atmospheric turbulence. Firstly, the short-exposure (speckle) coherence time gives the timescale over which high-resolution-imaging systems must be able to correct incoming turbulence errors. The speckle coherence time τ_0 has been measured by a variety of authors (for example, Dainty et al. (1981); Vernin & Munoz-Tunon (1994); Roddier et al. (1990); Buscher (1994); Scaddan & Walker (1978)). Generally these studies give values on the order of a few milliseconds or 10s of milliseconds, although there is some disagreement over the detailed definition of the coherence time that

should be used (Buscher, 1993).

Secondly, the seeing itself changes on timescales anywhere between seconds to hours and up (chapter 4, and Racine (1996); Vernin & Muñoz-Tuñón (1998)). Tokovinin et al. (2003) find that the seeing decorrelates at different timescales (between minutes and hours) at different altitudes.

Isoplanatic Angle

The light from two astronomical objects separated by a small angle will travel on slightly different paths through the turbulence in the Earth's atmosphere. If the objects are separated by a large angle, corrections based on the shape of one object's wavefront will not be applicable to the other's wavefront, because their turbulence induced errors will be different. If turbulence corrections are made on the basis of a single guide star, the isoplanatic angle gives the angular distance from that star at which the corrections are still valid for other objects. There are a number of different quantities referred to as the isoplanatic angle, in particular the speckle imaging and adaptive optics isoplanatic angles, which are subtly different. In this thesis I define the isoplanatic angle as the radius at which the Strehl ratio of LuckyCam-corrected images drops to $1/e$ of its on-axis value. The isoplanatic angles noted below may not be exactly comparable (even with each other), but give an idea of the expected values.

Roddier et al. (1982) reviews a number of isoplanatic angle measurements, again usually measured at 550nm. Typical values for speckle imaging range from 4-10 arcsec, although the adaptive optics isoplanatic patch is expected to be $\sim 30\%$ smaller. Vernin & Munoz-Tunon (1994) find that at the La Palma Observatory, where all LuckyCam runs 2000-2005 were made, the speckle imaging isoplanatic angle at 550nm is around two arcsecs. This very small angle does not agree with measurements made with LuckyCam, where angles between 15-30 arcsecs are observed in I-band; the discrepancy is discussed in chapter 4.

1.2 Correction Methods

I briefly list below the main techniques that have been developed to combat the problem of atmospheric turbulence, along with some illustrative examples of instruments that employ them.

The quality of images produced by these correction methods is usually measured in one of two ways: the FWHM (full width at half maximum) of the PSFs, or their Strehl Ratio. FWHM is usually used to describe performance which does not approach the diffraction limit, where the seeing increases the image width. The Strehl Ratio, defined as the ratio of the PSF peak flux to the peak flux for a PSF acquired with a perfect telescope with no turbulence, is used to describe

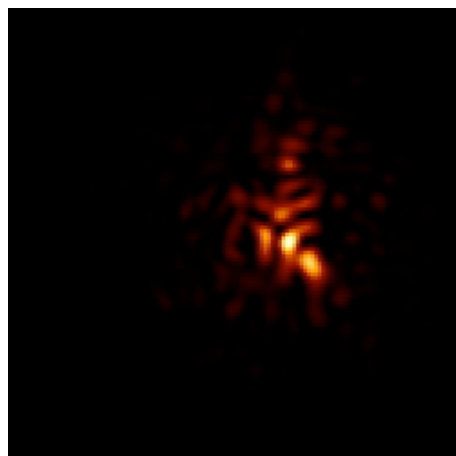
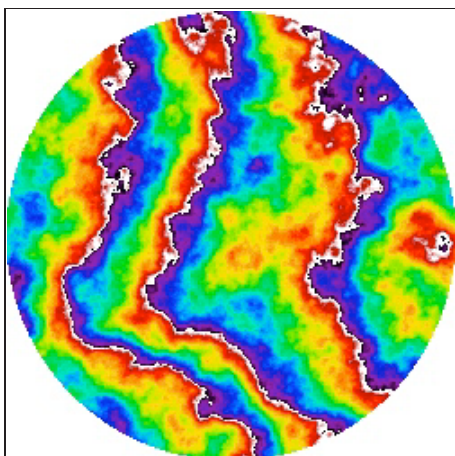
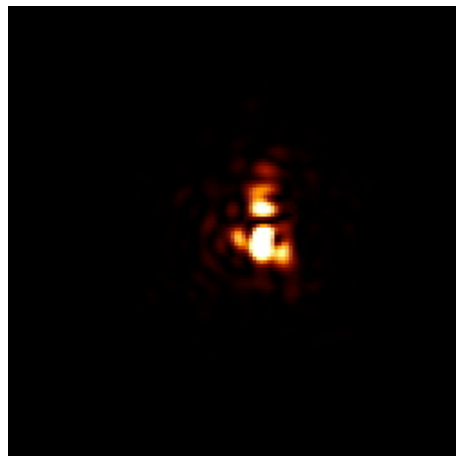
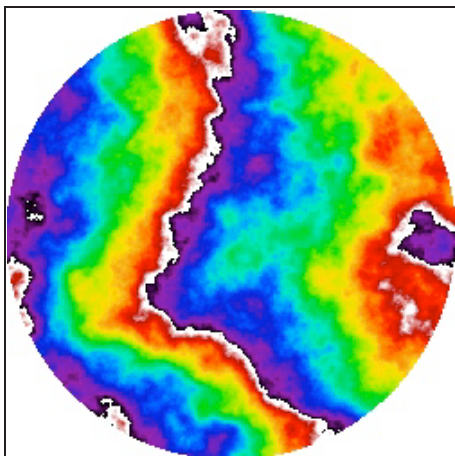
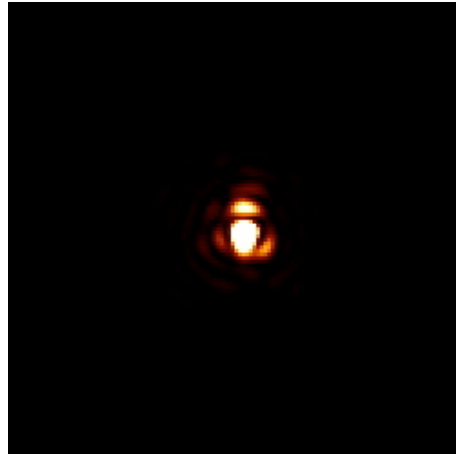
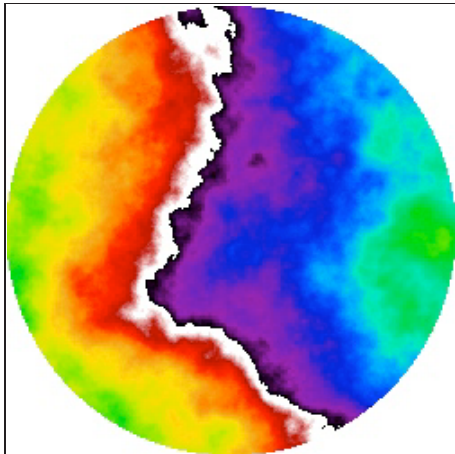


Figure 1.3: The large changes in PSF shape induced by a change in turbulence strength, with the wavefront shape unchanged. The three pairs of images show the effect of turbulence with 2, 5 & 10 r_0s across the telescope diameter. The number of speckles, the centroid position and the position of the brightest speckle all change. The phase screen colour map wraps at 2π radians of phase error, and the PSFs are all displayed on the same colour scale. The phase screen is the same in each case, with only the turbulence strength changed.

the light concentration of systems which give a core with diffraction-limited resolution.

In this thesis I use the terms diffraction-limited or near-diffraction-limited to describe PSFs which have a FWHM equal to that expected for the telescope with no atmospheric turbulence ($1.22\lambda/D$, for effective wavelength λ and telescope diameter D).

1.2.1 Lucky Imaging

The subject of this thesis, Lucky Imaging offers a particularly elegant and uncomplicated solution to the blurring effects of atmospheric turbulence. Among the rapid turbulent fluctuations of the atmosphere, moments of relatively quiet air appear, lasting a few tens of milliseconds. Imaging at high frame rates (frame times \approx the atmospheric coherence time) allows us to follow rapid seeing variations and select those times with very much better images – effectively integrating only during periods of truly superb seeing.

The frames recorded by LuckyCam are sorted according to quality; only the best frames are aligned and co-added to produce a final image. On a 2.5m telescope, the system routinely achieves the diffraction-limit at I-band (Strehl Ratio 0.2, FWHM 0.08 arcsec). The details of the Lucky Imaging process, such as the frame selection level, can all be optimised during post-processing of the data.

Lucky Imaging is treated in much more detail in section 1.3.

1.2.2 Adaptive Optics

Adaptive Optics (AO) describes technologies that actively correct in realtime the detailed wavefront perturbations introduced by the atmosphere. They do so by the addition of a deformable mirror (DM) into the optical path; figure 1.4 shows a schematic of a typical AO system. A wavefront sensor tracks the shape of the incoming wavefront using a nearby guide star. The DM is commanded to deform such that light reflecting from the mirror acquires path length errors designed to cancel out those induced by the atmospheric turbulence.

AO systems are in routine use on many large telescopes: for example, Keck (Wizinowich et al., 2000), VLT (Brandner et al., 2002), MMT (Wildi et al., 2003), and Subaru (Takami et al., 2003). These systems are currently limited to near infra-red operation only, usually $\sim 1.2\text{-}2.2\mu\text{m}$, but achieve near diffraction-limited resolutions (Strehl Ratio > 0.2 , usually at the longer wavelengths).

The AO systems are limited in useful wavelength by the accuracy to which the wavefront can be measured and corrected. In particular, a more precise correction requires more light from the guide star with which to measure the wavefront, as well as higher resolution deformable mirrors. Typical natural guide star AO systems only achieve full correction in the near-infrared

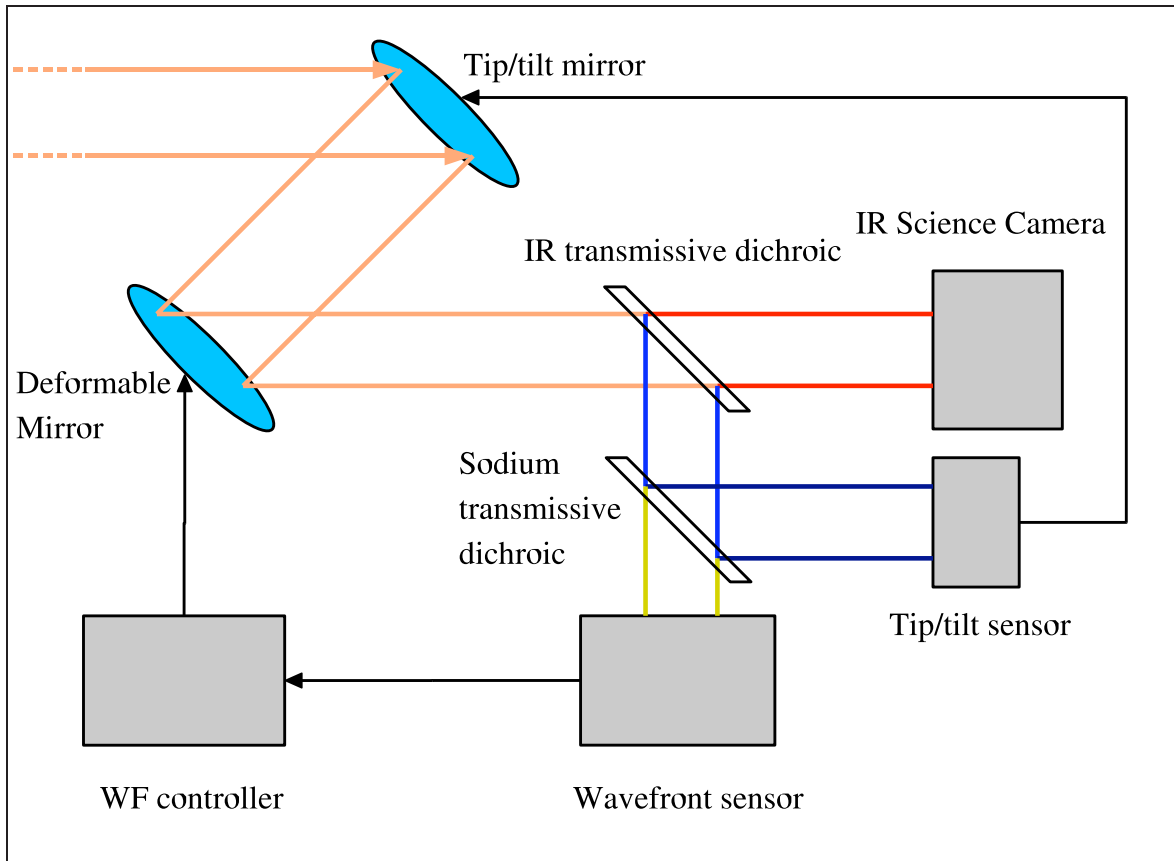


Figure 1.4: A diagram of a typical Sodium laser guide star adaptive optics system, excluding the laser launch systems. Light enters from the telescope at the top left, and is corrected for tip/tilt before further correction by the deformable mirror. IR wavelengths ($> 1\mu\text{m}$) are sent to the science camera. Light from the sodium layer excited by the laser is used for the detailed wavefront sensing, while tip/tilt is measured from the visible light from a nearby natural guide star. Adapted from Wizinowich et al. (2006).

with guide stars brighter than about ~ 12 mags (for example, van Dam et al. (2006)).

This limitation can be overcome with the use of laser guide star (LGS) systems, where an artificial star is created either by downwards Rayleigh scattering or by excitation of the high-altitude sodium layer. These systems are (as of 2006) starting to become operational for near-infrared science use (for example Brown et al. (2005)).

1.2.3 Tip/tilt correction systems

Tip/tilt correction systems correct for image motion, usually using a movable mirror and an image position monitor. The stabilised image is then integrated on a standard visible or infrared detector. Alternatively, the development of orthogonal transfer CCDs (Tonry et al., 1997) allows the image motion corrections to be performed directly on the CCD chip, by moving the stored charge both vertically and horizontally. When packed together into very large

(GigaPixel) arrays, these devices can act as very wide-field imagers with “rubber” focal planes – that is, image motion corrections which vary across the field of view (Tonry et al., 2002).

In the near-infrared on smaller (1-4m) telescopes, the bulk of the phase error can often be corrected by removing image motion – at $2.2\mu\text{m}$ on a 3.6m telescope, tip/tilt correction improves 0.6 arcsec seeing images to 0.3 arcsec FWHM (Roddier et al., 1991). Jim et al. (2000) describes a tip/tilt corrected secondary mirror on the University of Hawaii 2.2m telescope that also achieves K-band images with 0.3 arcsec FWHM.

The TRIFFID camera (eg. O’Sullivan et al. (1998) and references therein) employs offline data-processing of photon counted data for resolution enhancement. The system includes a pupil mask matched to the prevailing seeing (to maximise the tip/tilt component), and shift-and-add processing of the data is performed after the observations. FWHM improvements of a factor of two have been obtained (Butler et al., 1996).

In the visible, tip/tilt makes up a smaller component of the wavefront error. Systems which correct tip/tilt as well as performing some long-timescale image selection (for example, Nieto et al. (1988); Crampton et al. (1992)) obtain typical FWHM resolution improvements on the order of 10-30%.

1.2.4 Speckle Interferometry

First suggested by Labeyrie (1970), speckle interferometry relies on the fact that the final image $I(x, y)$ is the atmospheric PSF $P(x, y)$ convolved with the target object’s brightness distribution $O(x, y)$:

$$I(x, y) = P(x, y) * O(x, y) \quad (1.3)$$

Since the short-exposure speckle pattern contains information at the diffraction limit of the telescope (each speckle is the size of a diffraction-limited PSF), processing of short exposure images can recover information on the object brightness distribution on those small scales. Speckle imaging is in use in a number of science programmes, particularly in imaging binary stars, where the speckle patterns are particularly simple (for example, Mason et al. (2006); Horch et al. (2002)).

Speckle imaging requires reasonable signal-to-noise short exposure images, a capability which has been limited on standard CCD detectors – for example, a recently developed system, the RIT-Yale Tip-tilt Speckle Imager, is expected to be able to resolve binary stars down to ~ 11.3 mags (Meyer et al., 2006).

The very sensitive and fast imaging capabilities of LuckyCam make it an ideal speckle detector as well as Lucky Imager, as the problems of acquiring sufficient signal-to-noise in the PSF

are roughly same in the two techniques. In chapter 7 I apply speckle imaging techniques to very close binaries discovered with Lucky Imaging, in order to improve the accuracy and precision of the derived binary parameters. The LuckyCam L3CCD photon event shape requires unique calibration procedures for speckle imaging; the techniques that I developed for this are presented in chapter 5.

1.2.5 Interferometry

Interferometers recombine the incoming wavefronts from different telescopes (or separated parts of the same telescope), producing a set of fringes from which the target object's high-angular-resolution brightness distribution can be calculated. Interferometry is used routinely by radio astronomers for image reconstruction, because of the otherwise prohibitive telescope sizes required to achieve useful resolution at radio wavelengths.

Using a single telescope with its aperture masked to form several smaller ones, diffraction-limited imaging in the visible has been successfully demonstrated on 5m-class telescopes (Baldwin et al., 1986; Haniff et al., 1987; Gorham et al., 1989). However, these systems require very small apertures to attain sufficient visibility on the fringes, although recent developments using the Lucky Imaging concept can eliminate that problem (Mackay, 2005).

Imaging has also been demonstrated with instruments which combine light from different telescopes (described in Michelson (1920)) – for example, the Cambridge Optical Aperture Synthesis Telescope (COAST, Baldwin et al. (1994)). COAST consists of four 50cm telescopes, which combine visible light over a number of baselines. Science observations using the interferometric combination of light from multiple large telescopes have also recently been performed in the near and mid infrared on the Keck and VLTI interferometers (for example, Mennesson et al. (2005); Chesneau et al. (2005)).

1.2.6 The capabilities of presently available systems

Collating the capabilities of the systems described above, a gap is evident (figure 1.5) – with the exception of Lucky Imaging, no currently available ground-based system is capable of general astronomical imaging with resolution better than 0.3 arcsec in the visible. Lucky Imaging fills that gap simply and elegantly.

1.3 The Lucky Imaging Technique

A Lucky Imaging system takes very short exposures, on the order of the atmospheric coherence time. The rapidly changing turbulence leads to a very variable PSF; the variability of the PSF

	Red 700-1000nm	Near-Infrared 1200-2200nm
0.3 arcsec resolution	Tip/tilt	Tip/tilt
0.1 arcsec resolution, Strehl Ratio > 0.2	Lucky Imaging (speckle) (interferometry)	AO (speckle) (interferometry)
0.1 arcsec resolution using faint guide stars	Lucky Imaging	LGS AO

Figure 1.5: A collation of the capabilities of currently-available ground based imaging systems. The area shaded in red is the gap in general imaging capabilities that LuckyCam fills – 0.1 arcsec resolution imaging in the visible. The ability to use faint guide stars is important to allow coverage of a reasonable fraction of the sky with the imaging technique in question. Speckle imaging and interferometry are listed in brackets because they are usually used for specialised purposes, where a model of the target object is already known or suspected (eg. searches for binary stars).

leads to some frames acquired by the Lucky Imaging system being better quality than the rest. Only the best frames are selected, aligned and co-added to give a final image with much improved angular resolution.

1.3.1 Previous systems

A number of instruments have been specifically designed to take advantage of rapidly varying seeing statistics. Most of these instruments use integration times in the range of seconds (to reduce readout noise), and thus could not perform true Lucky Imaging, or reach anywhere near diffraction-limited performance. They provide, however, useful improvements in the apparent seeing. There are two main classes of this type of instrument: cameras with optics or electronics designed to recenter and select images during integration, and direct short exposure imagers where the final image reconstruction is undertaken offline.

HRCam (McClure et al., 1989) is an example of the first class of instrument. Used on the Canada-France-Hawaii telescope (CFHT), it incorporated a fast tip/tilt mirror to follow centroid image motion and a shutter to reject periods of poorer seeing. It typically achieved 10-20% improvements in FWHM resolution (Crampton et al., 1992).

An instructive example of the second, offline data-processing class of instruments is described in Nieto et al. (1987). Using the European Space Agency Photon-Counting Detector (di Serego Alighieri & Perryman, 1986) with effective integration times of 1.5-20 seconds, they selected and recentered images to form final science images with FWHM resolutions improved by ~30

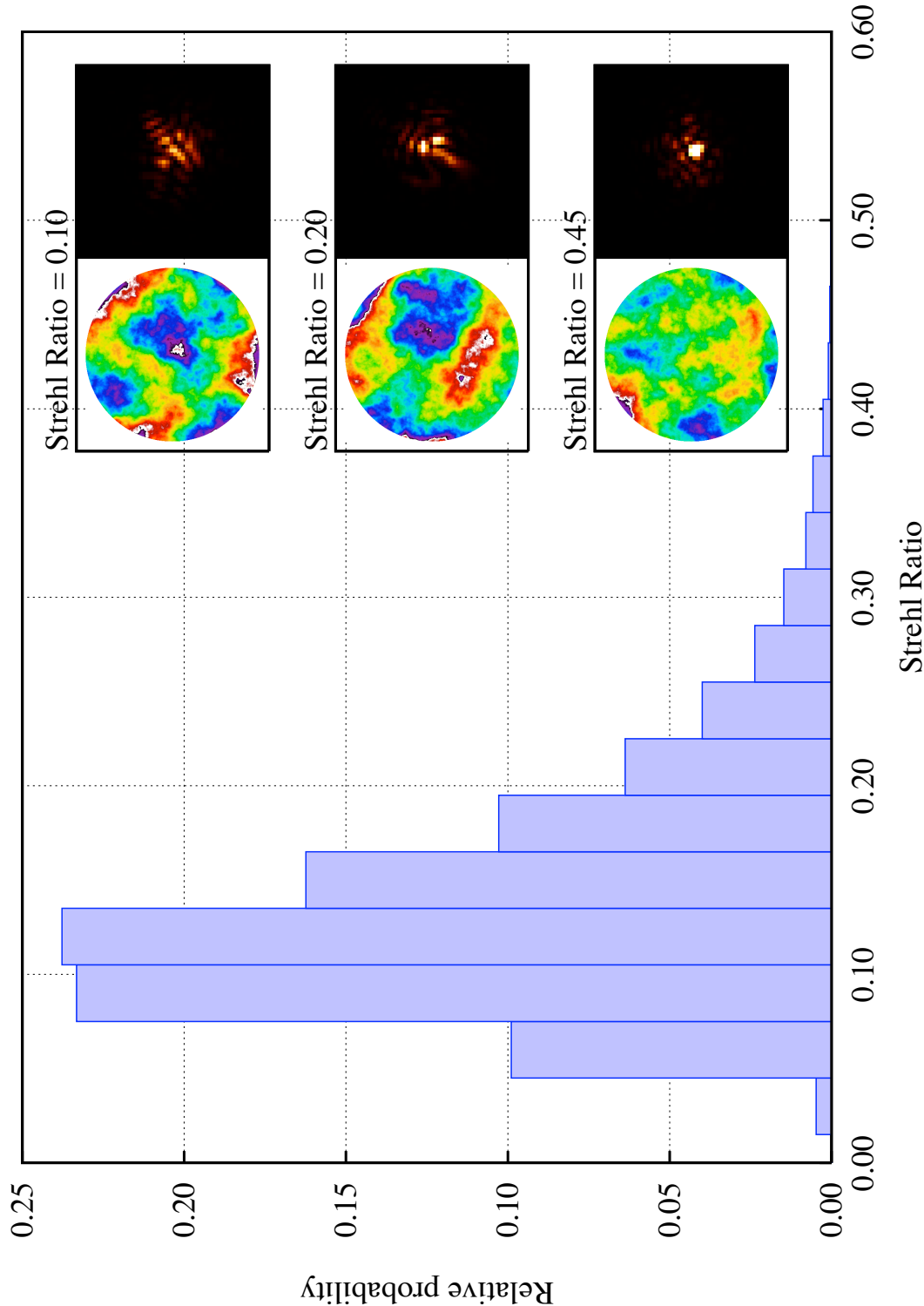


Figure 1.6: The relative probability of obtaining frames with given Strehl Ratios. The histogram shows the short exposure Strehl Ratio probability density function calculated from 20,000 simulations of Kolmogorov phase screens. The probability density function is normalised to an arbitrary total value, and is calculated for an optically perfect telescope with δ_{10} of atmospheric turbulence across its diameter. The panels on the right show example wavefronts for particular Strehl ratios (left panels) and the corresponding monochromatic short exposure PSFs (right panels). Note there is significant low-level speckled noise remaining even in the exposure with a Strehl ratio of 0.45. Real PSFs are degraded by the effects of a longer exposure time, finite bandwidth, mirror aberrations and light scattering.

per cent (Nieto et al., 1988). Nieto & Thouvenot (1991) describes some more details of the reconstruction process. Crucially, because their integrations times are so long, their images did not have a speckled character. The system thus does not retain diffraction-limited imaging, but rather takes advantage of long-timescale changes in the seeing itself. They also align images on the basis of the image centroid (actually the correlation between the long exposure integrated image and the short exposure frames), which removes the tip/tilt component of the turbulence but does not allow diffraction-limited image reconstruction even if the imaging frame rate is high. The benefits of alignment on the brightest speckle rather than the image centroid are discussed in detail in for example Christou (1991).

More recently, fast CCD imagers have enabled near diffraction-limited Lucky Imaging on both relatively small telescopes (0.36m, Davis & North (2001)) and medium-sized telescopes (60 inch, (Dantowitz et al., 2000)). The availability of cheap webcams has also allowed amateur astronomers to perform automated frame selection and alignment imaging*. However, the high noise introduced by running these CCD-based systems fast enough to sample the atmospheric coherence time requires very bright (generally planetary) targets.

1.3.2 Camera requirements for a diffraction-limited Lucky Imaging system

Lucky Imaging is a fairly forgiving process – under almost all conditions frame selection and alignment gives a very significant resolution increase. However, the requirements for diffraction-limited imaging on 2.5m telescopes, the aim of the LuckyCam programme, are much more stringent.

Telescope Size

All high-resolution imaging systems are limited in the size of telescope for which they can adequately correct the turbulence-induced wavefront errors – there is simply more turbulence to correct as the area of the telescope increases.

As the telescope area increases, the probability of getting a diffraction-limited short-exposure image decreases rapidly. Fried (1978) coined the term “lucky exposures” to describe such frames (defined as the phase errors across the telescope aperture having an RMS error of <1 rad.). He found that the probability P of getting a diffraction-limited image varies as

$$P \approx 5.6 \exp \left[-0.1557 (D/r_0)^2 \right] \quad (1.4)$$

where D is the telescope diameter. The expression assumes a telescope that has several turbu-

*For example, RegiStax, free software for amateur Lucky Imaging, is available at <http://registax.astronomy.net>.

lence cells across its diameter ($D/r_0 > \sim 4$), and that the only variations in the turbulence follow Kolmogorov statistics. Under these assumptions, given a value of r_0 of say 35cm (reasonable for observations in I-band [700nm-800nm] in good conditions), the probability of getting a good image is quite high on relatively small telescopes (30% on a 1.5m telescope) and very low on larger telescopes (essentially zero for a 10m telescope). An example of the probability of obtaining a range of different image qualities in a particular seeing is shown in figure 1.6.

Lucky Imaging benefits from using large telescope apertures in two ways. Firstly, more light is collected by the telescope, allowing fainter guide stars and thus imaging over a larger area of the sky (see chapter 4), as well as imaging of fainter science targets. Secondly, larger telescope apertures have smaller diffraction limits, increasing the final resolution of the system. It is thus beneficial to use as large a telescope as can be managed while still having a reasonable probability of obtaining diffraction-limited frames.

If we adopt a minimum of a 1% frame selection, for a $r_0 = 35\text{cm}$ the maximum usable telescope aperture for near diffraction-limited imaging is 2.25m. Of course, a different selection level and/or atmospheric conditions will affect this minimum size. In practise, because it is complicated to change the aperture of the telescope being used, we use a 2.5m telescope and adjust the selection criteria to give a useful trade off between the loss in signal from using fewer frames and the resolution of the final image.

Frame rate

The Lucky Imaging system should operate quickly enough to “freeze” the atmosphere (sample within the coherence time) so that, when a diffraction-limited period occurs, it can be recorded without the addition of the non-diffraction-limited time periods surrounding it. As described in section 1.1.2, the coherence time is usually a few to a few tens of milliseconds, depending on atmospheric conditions and the type of measurement.

On-sky measurements of the Lucky Imaging turbulent timescale using the LuckyCam system are presented in Tubbs (2004) and chapter 4. On the basis of that data a minimum of 30 frames per second are required for most observed conditions at the Nordic Optical Telescope, where all LuckyCam data has been acquired. However, the frame rate must be increased still further in times of poor seeing to obtain the best quality (chapter 4).

Sensitivity

The chief limit on previous Lucky Imaging-style systems has been the low sensitivity of the detectors used, requiring very bright guide stars in the field of view from which to estimate the image quality and position. The faintest usable guide star has a direct effect on the potential target-availability of the system, whether we require the science target to be bright enough to

serve as its own guide star or simply that a bright enough guide star is randomly in the field of view. The impact of guide star brightness on the sky coverage of the system is discussed in chapter 4.

1.3.3 The Cambridge Lucky Imaging system

The Cambridge Lucky Imaging system, LuckyCam, meets and often exceeds the above requirements. It is based on an L3CCD system which gives photon-counting imaging at CCD quantum efficiencies, and therefore allows guiding on very faint guide stars. The L3CCD is run at a 5-7 MHz pixel rate, giving frame rates of between 12 and 100 frames per second, and thus fully sampling the atmospheric coherence time in almost all encountered conditions. Finally, in all data presented in this thesis the system was used on the 2.56m Nordic Optical Telescope (NOT), an aperture size that (as demonstrated in chapters 6 and 7) allowed routine diffraction-limited imaging in the visible.

A version of LuckyCam was first described in Baldwin et al. (2001). For those tests, a standard CCD camera was used to obtain diffraction-limited images of stars brighter than $I=+6$ mags on the NOT in the visible. This represented a significant advance, in that very few other resolution improvement systems operate in the visible, and the presented system was extremely simple and cheap. However, the $I=+6$ mags guide star brightness limit imposed by the high readout noise of the standard CCD used limited the system to technology demonstration.

Tubbs et al. (2002) and Tubbs et al. (2003) demonstrate the first Lucky Imaging observations with an L3CCD-based camera, with guide stars as faint as $I=+16$ mags. The Lucky Imaging isoplanatic patch in these observations is demonstrated to have a FWHM of 50 arcsecs, much larger than would be expected for I-band observations. Tubbs (2004) covers all LuckyCam developments up to 2003 in great detail.

I have published several papers describing my Lucky Imaging work. Law et al. (2006b) investigates in detail the on-sky performance of Lucky Imaging systems in a variety of conditions, and forms the base for chapter 4. Law et al. (2005) gives initial results from my LuckyCam survey for Very Low Mass (VLM) binaries. Law et al. (2006a), on which chapter 6 is based, presents the first part of the LuckyCam VLM binary survey. Finally, a further much larger sample of VLM binaries is to be published, based on the results detailed in chapter 7.

1.4 The Structure of this Thesis

This thesis is divided into two parts: the Lucky Imaging system, and astronomy that I have performed with LuckyCam.

Chapter 2 details the LuckyCam hardware and discusses the use of L3CCDs for astronomical

imaging. I then describe the data acquisition and camera control software I have written for LuckyCam, including a realtime Lucky Imaging preview system for use during observing. My implementation of the LuckyCam data reduction pipeline is described in chapter 3. Chapter 4 is a detailed investigation into the performance of Lucky Imaging in a wide range of atmospheric conditions.

In chapter 5 I detail several data reduction and calibration methods unique to Lucky Imaging and/or L3CCD data that I have developed for the measurement of close binary parameters. In chapters 6 and 7 I present the LuckyCam survey for very low mass binaries, with two separate samples of late-M-dwarf targets.

Finally, I summarise my conclusions in chapter 8.

1.5 Summary

- Atmospheric turbulence severely reduces the resolution of ground-based telescopes.
- Several correction methods have been employed to reduce the effects of the turbulence, but there is a gap in the system capabilities – imaging at 0.1 arcsec resolution in the visible is not possible from the ground, except for:
 - Lucky Imaging is a simple technique that attains near-diffraction-limited images in the visible on 2.5m telescopes.
 - In Lucky Imaging, the target is observed at a high enough frame rate to freeze the changing atmospheric turbulence. The PSF quality changes from frame to frame; the Lucky Imaging system selects the best frames, then aligns and co-adds them to produce a high-resolution image.
 - An ideal visible-light Lucky Imaging camera would have very high sensitivity (for use on faint guide stars), a frame rate in excess of 30 frames per second, and be used on a 2.5m telescope.
 - LuckyCam, the Cambridge Lucky Imaging system, meets those requirements.

2

The LuckyCam Data Acquisition System

2.1 Introduction

In this chapter I describe the LuckyCam data acquisition systems, from the optics and electronics to the realtime analysis and data storage software.

In the area of data acquisition, I have been responsible for all software used in the LuckyCam system once the camera electronics have passed pixel data to the data acquisition PC. The software includes a video display, realtime Lucky Imaging and other analysis, the data storage systems (which store 14MB/sec continuously for entire observation nights) and realtime data compression. I have also written the optics control system for the 2006 version of LuckyCam. The LuckyCam optical hardware was designed and built by Craig Mackay (and John Baldwin in 2000-2004); the LuckyCam control electronics were designed and built by Craig Mackay. The DSP camera control system was written by Ali Basden. The custom L3CCD clocking and readout electronics are described in detail in Mackay et al. (2004).

2.2 LuckyCam Optics

Since the initial experiments in July 2000, there have been several version of LuckyCam, the Cambridge Lucky Imaging system. All versions from 2000-2005 were designed for the Cassegrain focus of the 2.5m Nordic Optical Telescope (NOT) at La Palma, Canary Islands.

The 2006 version is designed for the Nasmyth focus of the 3.6m New Technology Telescope (NTT) at the La Silla observatory, Chile. Extensive details of the 2000-2003 LuckyCam versions are given in Tubbs (2004).

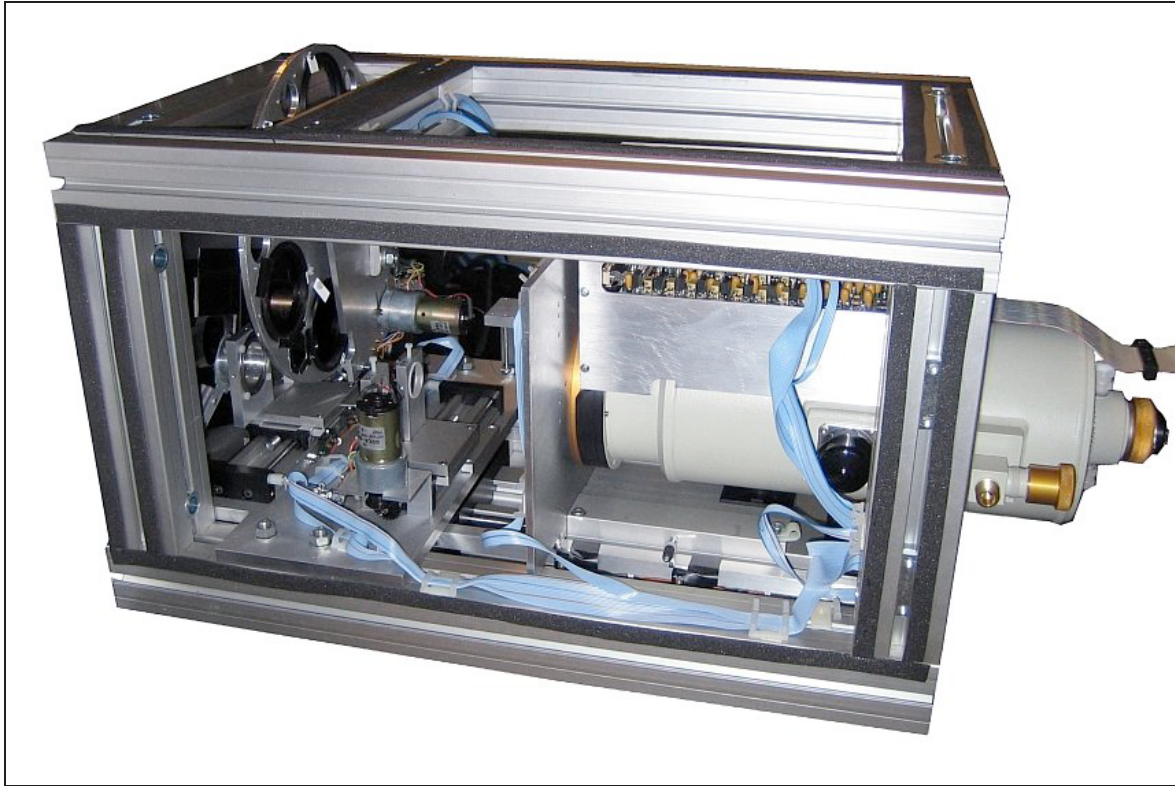


Figure 2.1: The November 2005 version of LuckyCam.

Although the details differ, the versions of LuckyCam have essentially the same optical layout – in almost all LuckyCam observations light from the telescope simply passes through a lens (to adjust the image scale) and a filter, before arriving at the CCD. No active optical elements are included, leading to a very elegant and cheap system. The evolution of the LuckyCam system was as follows:

2000. A standard front-illuminated frame-transfer CCD39, run by an AstroCam 4100 controller was used for initial testing of Lucky Imaging with bright stars. The f/11 beam from the telescope was converted to f/33 using a single achromat giving a pixel scale of 40 mas (milliarcseconds) per pixel.

2001-2. A 624×288 pixel E2V CCD65 L3CCD was used for faint guide star Lucky Imaging. The light path within the (~ 1 meter long) instrument was folded into a 'Z' shape. One of the fold mirrors was formed from two mirrors butted together at a slight mutual angle. This allowed two stars separated by up to 30 arcsec to be imaged within a few arcsec on the L3CCD, for tests of the isoplanatic angle size at larger radii than would otherwise be possible.

2003. The CCD65 was replaced by a 536×528 pixel E2V front-illuminated frame transfer

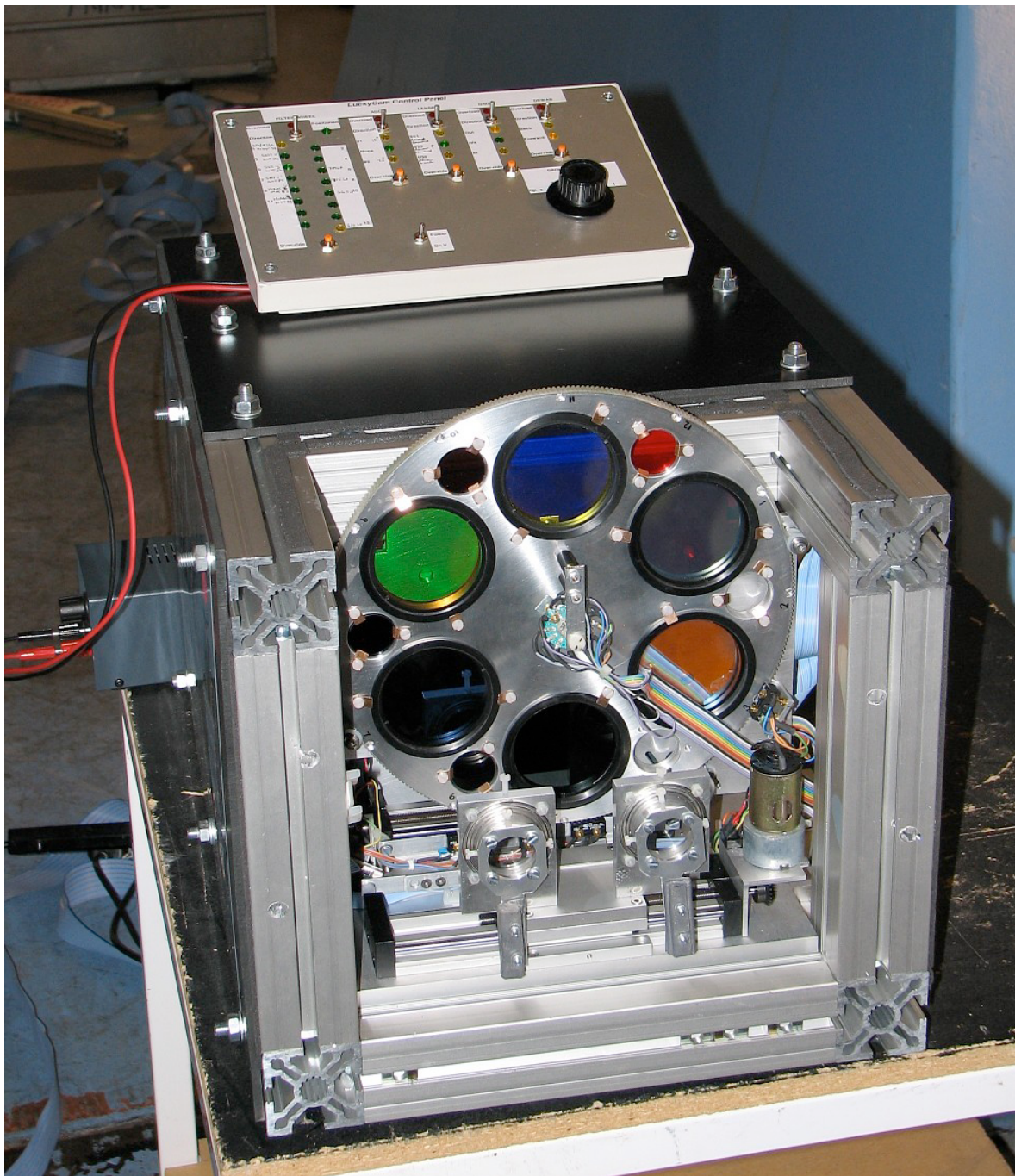


Figure 2.2: The November 2005 version of LuckyCam, in final preparation for attachment to the telescope (with filters installed).

CCD87. The optics were adjusted to give a re-imaged aperture plane, into which circular aperture masks were introduced to test the effects of changing the telescope aperture size on the Lucky Imaging quality.

2004. The optics were redesigned to give a straight-through optical path. A grism was added for low-resolution spectroscopy (see below) and the CCD was replaced by a thinned back-illuminated E2V CCD97.

2005. The 2004 optical layout was maintained, with the addition of atmospheric dispersion correctors and electronically-controlled interchangeable optical elements. The instrument is shown in figure 2.1. The L3CCD clocking and readout electronics were upgraded (and are described in Mackay et al. (2004)), improving camera performance and allowing an LVDS interface to a standard Matrox frame-grabber PCI card (see section 2.4).

2006. This version is a complete redesign (LuckyCam HighRes) for aperture masking trials as well as conventional Lucky Imaging, at the Nasmyth focus of the NTT. The optical path is much the same as the 2005 version, but the addition of a re-imaged aperture plane and the different focal length of the NTT necessitated a much longer instrument. All components of the system are controllable in software (see section 2.4.5).

Most of the observations described in chapter 4 were performed using the 2001-2004 versions of LuckyCam. Chapters 6 and 7 are based on observations using the 2005 version of LuckyCam. I describe the 2005 LuckyCam in detail in the next section; most of the below discussion is applicable to the other versions of the system.

2.2.1 LuckyCam in 2005

Taking the optical path in order from the point of light entry, the principal components of the 2005 version of LuckyCam are listed below. Figure 2.2 shows LuckyCam at the NOT in November 2005, and figure 2.3 is a sketch of the optical layout.

1. **Atmospheric Dispersion Corrector** (ADC), to correct for the chromatic effects of atmospheric refraction, which become very significant for high resolution observations at large zenith distances (e.g. Stone (1996)). At 50° from the zenith the relative dispersion between 700nm and 750nm wavelength light is $\sim 0.1\text{arcsec}$, the width of a diffraction-limited PSF, requiring correction for high-resolution imaging. The two ADCs are designed for correction at 30° and 45° degrees from the zenith for observations at the NOT, and give improvements for a large range of angles surrounding those values. The ADCs are mounted on a movable stage, and their orientation is controlled by a simple system of weights – the downward direction at the Cassegrain focus of the altitude-azimuth NOT always points in the direction of the atmospheric dispersion. The ADCs were designed by David King. Almost all observations presented in the thesis were performed without

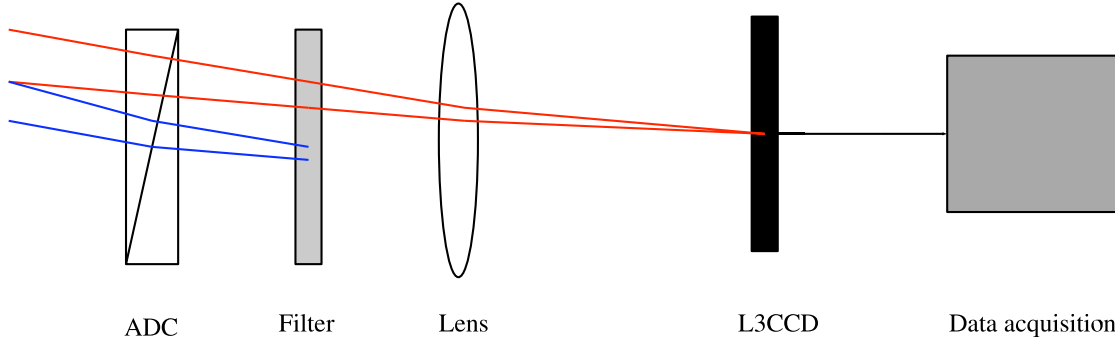


Figure 2.3: A sketch of the optical layout of the 2005 version of LuckyCam.

the ADCs but close to the zenith, where the relative dispersion is negligible.

2. **Filter wheel** 12 filter positions are available for quick changes during observation runs.
3. **Lens** Two lenses are selectable, for imaging at f/33 (0.04 arcsec per pixel) or f/22 (0.08 arcsec per pixel). A third position has no lens fitted, giving the raw f/11 NOT imaging at 0.12 arcsec per pixel. Because the focal length changes at the different magnifications, the CCD dewar is also mounted on a movable stage to give greater focus position changes than available from the telescope.
4. **Grism.** Two positions (in the beampath or out) are available, with the grism mounted on a movable stage. Approximately 90% of the light passing though the grism is dispersed into a spectrum ~ 100 pixels long. The remaining 10% of the light passes straight though, to serve as the guide star. Selecting and aligning the best frames of the guide star also selects and aligns the best spectrum frames, as they have passed though the same atmospheric turbulence. An example high-spatial-resolution spectrum produced by the grism is presented in chapter 4.
5. **L3CCD chip and Dewar.** The L3CCD chip is mounted in a liquid nitrogen dewar attached to a movable stage. The L3CCD chip is read out at a 7MHz pixel rate. When full frames (536×528 pixels) are read out, this corresponds to a frame rate of ~ 20 Hz. The vertical frame size can be reduced, to give smaller frames read out proportionally more often, at up to 100 frames per second for a 536×100 frame size.

Each optical element is mounted on a movable stage (wheel in the case of the filters), driven by motors controlled from a custom board located in the telescope control room (the board is shown at the top of figure 2.2). The LuckyCam optics are designed for the diffraction-limited resolution of the 2.5m NOT in the visible, but are otherwise fairly standard for CCD imagers. The main difference of LuckyCam from other CCD imaging systems lies in its L3CCD and custom CCD clocking and readout electronics.

2.3 L3CCDs

CCDs (Charge Coupled Devices) are very widely used in astronomy, and meet many of the properties of an ideal astronomical imager: they offer intrinsically linear performance, quantum efficiencies (the fraction of light detected) of >80 per cent over much of the visible spectrum, very low dark currents when cooled and are available in (very) large format arrays.

In a standard CCD (see Janesick (2001) for a review), light impinges on a set of pixels set up in a silicon wafer. Each absorbed photon produces a single electron, which is trapped in the nearest pixel. Once the selected integration time has been reached, the stored charge is transferred out of the chip one pixel at a time. The charge from each pixel is read out through a single amplifier; the number of detected electrons from each pixel directly gives the number of photons absorbed by that pixel.

Most astronomical CCD system are read out slowly (10s of seconds to read out full frames, 10s of KHz pixel rates), and still reach readout noises only little better than ~ 2 electrons per pixel (Jerram et al., 2001) – thus, 12 input photons are required in a single pixel for a detection of flux with a signal-to-noise ratio of 3.

Lucky Imaging systems (and other short-exposure systems) must run at MHz pixel rates to get sub-second readout times on reasonably large chips. The high-speed readout raises the readout noise to 10-100 electrons per pixel (Jerram et al., 2001), so only bright stars are detectable in each frame. If, as in Lucky Imaging, we require an estimate of the PSF of the guide star in every frame, many hundreds of photons from the guide star are thus required – limiting them to be unfeasibly bright. For example, the initial Lucky Imaging experiments performed by the Cambridge group, using a standard CCD camera, were limited to stars brighter than +6 mags (Baldwin et al., 2001).

L3CCDs Jerram et al. (2001) (Low Light Level CCDs, also known as Electron Multiplying CCDs) offer a solution to the CCD readout noise problem. The imaging area of an L3CCD has the same design as that of a standard frame-transfer CCD, but each pixel is read out through an electron multiplication register (figure 2.4).

In the multiplication register, one of the three electron transfer phases is clocked to a much higher level (20–40V) than is needed for electron transfer. This accelerates charge-carrier electrons to sufficiently high velocities to generate additional carriers by impact ionisation. Although the probability of an electron-multiplication event is low (typically 1-2%) in each transfer, the total gain can be very high after transfer through the hundreds of elements in a typical register.

Typical gains used on LuckyCam range from 1000-10000 output electrons per input electron. Each photon then presents a signal of several thousand electrons to be detected above a few hundred electron readout noise of standard CCD readout electronics – and L3CCDs give high-

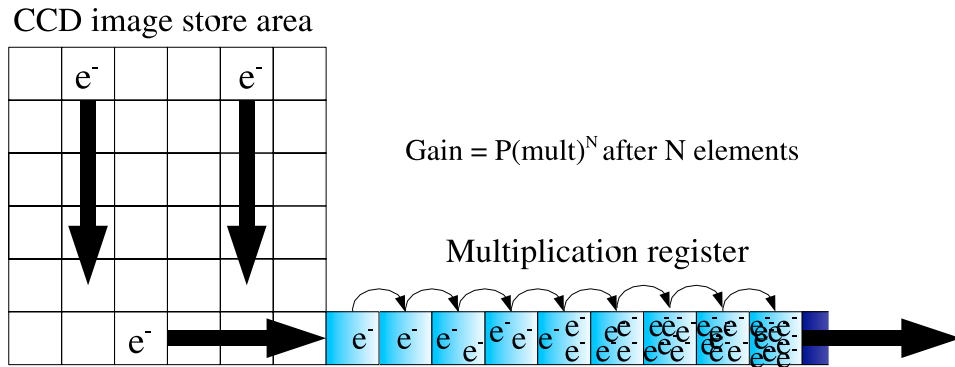


Figure 2.4: A cartoon describing an L3CCD / EMCCD. Electrons are transferred from the imaging area to the store area of the frame transfer CCD, then clocked out through the multiplication register. In each inter-pixel transfer the electrons have a probability $P(\text{mult})$ of exciting more electrons.

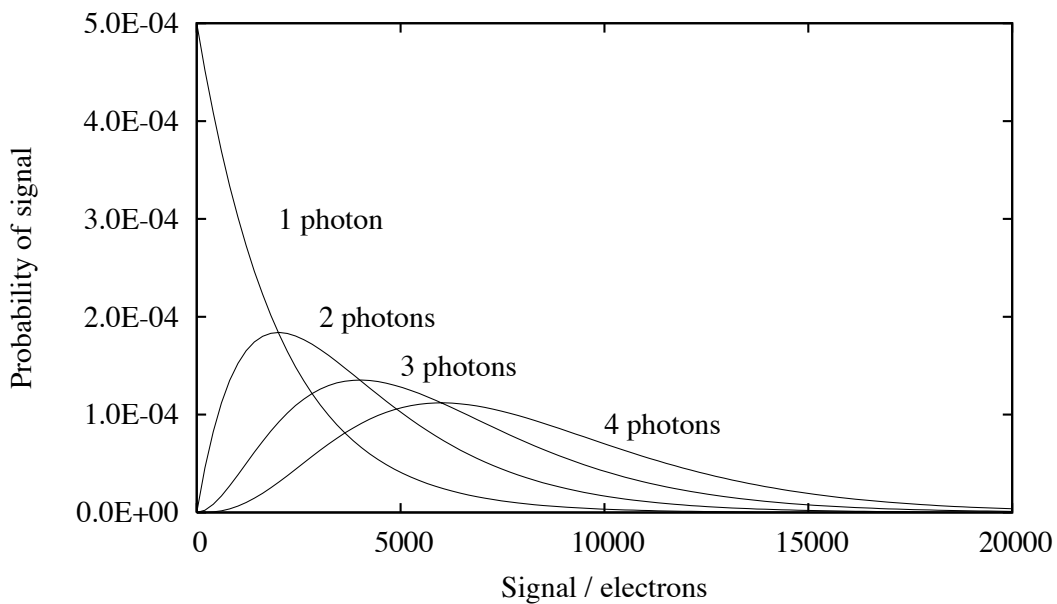


Figure 2.5: The probability distribution of output signals produced by 1–4 input photons/electrons, for an L3CCD gain of 2000. Note that the distributions overlap, leading to uncertainty in the number of input electrons for a given output signal.

frame-rate photon counting with full CCD quantum efficiencies.

L3CCDs are manufactured by E2V Technologies* and are available back or front-illuminated in a variety of image sizes. A second manufacturer, Texas Instruments, also produces CCDs with very similar electron-multiplication technology, under the trade name Impactron. In this thesis I refer to electron-multiplying chips as L3CCDs, but the discussion applies equally well to other electron multiplication register equipped CCD devices.

Because the multiplication register is run at very high voltages, care must be taken to avoid the spontaneous generation of charge carriers within the register. These appear as photon-like events in the camera data, and if present in large numbers effectively lead to an increase in the sky-background. Tests of the LuckyCam L3CCD camera show that the system produces a very small number of these events compared with other L3CCD systems currently available (Tulloch, 2004).

2.3.1 Multiplication noise

Because the generation of additional charge carriers is a stochastic process, the output signal from the multiplication register for a given input signal is spread over a wide range. For an input signal of n photons and a long multiplication register, an approximation to the probability distribution of the output signal $p(x)$ is given by (Basden et al. (2003)):

$$p(x) = \frac{x^{n-1} \exp(-x/g)}{g^n (n-1)!} \quad (2.1)$$

where x is the output signal, g is the mean gain, the photon input level is relatively small ($n < \sim 15$) and the gain is large. The distributions for 1-4 input photons are shown in figure 2.5.

The output signal distribution has a mean of $n \times g$ (so simple signal averaging produces a linear response [figure 2.6]), and a variance of $n \times g^2$ (Basden et al., 2003). The variance in the distribution introduces an extra noise into the output signal beyond the Poisson photon noise. The final signal-to-noise ratio (SNR) of the output in the absence of readout noise, but with Poisson photon noise thus becomes:

$$\text{SNR} = \frac{n \times g}{(ng^2 + (n^{1/2} \times g)^2)^{1/2}} = \frac{n^{1/2}}{2^{1/2}} \quad (2.2)$$

i.e. the L3CCD multiplication process introduces an extra factor of $\sqrt{2}$ into the noise of a photometric measurement compared to a perfect photon counting imager.

*<http://e2v.com>

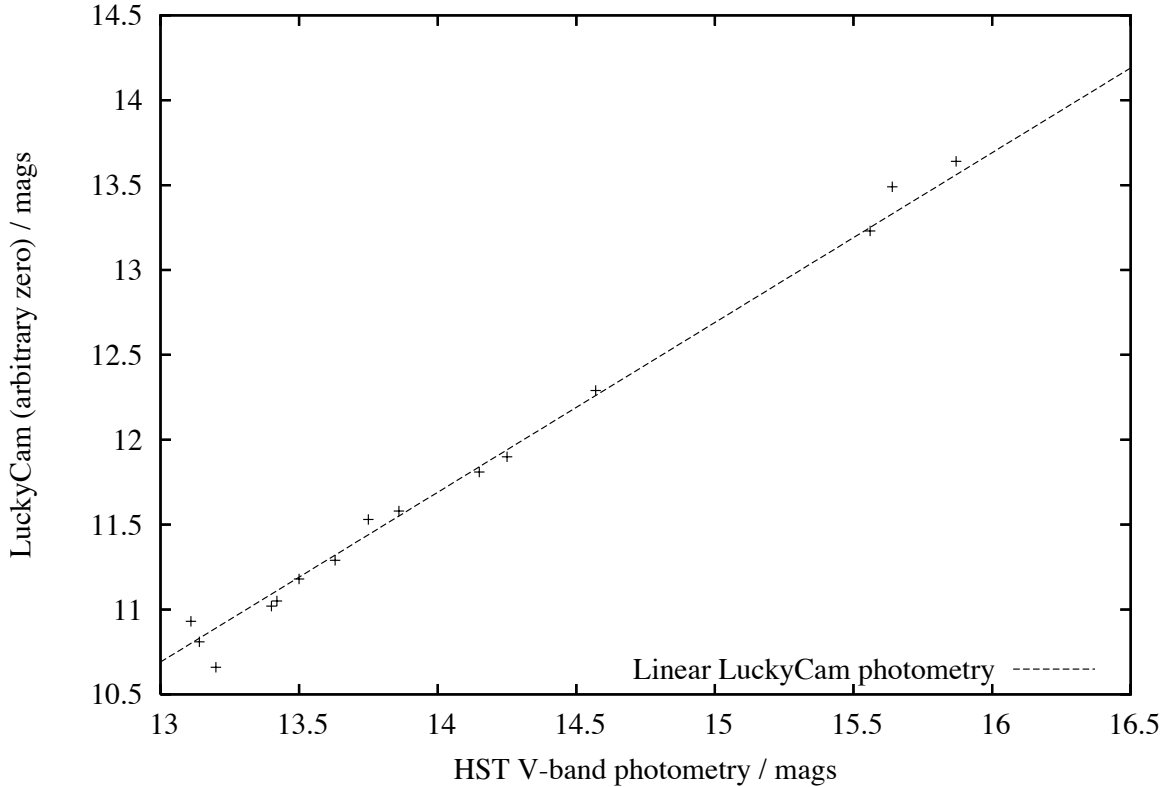


Figure 2.6: A verification of the linearity of LuckyCam. I compared V-band Hubble Space Telescope photometry of the core of M3 (Guhathakurta et al., 1994) against V-band LuckyCam photometry of the same stars. The dashed line shows the 1:1 relationship for completely linear photometry, assuming matched filters and detectors. The LuckyCam photometry matches that of the Hubble to within the approximately 10% measurement errors (limited by the difficulty of photometry in this crowded field).

2.3.2 Photon counting

L3CCDs, when run at high gains, show an easily detectable signal for each input photon, allowing photon counting with the full quantum efficiency of a standard CCD. However, the $\sqrt{2}$ S/N reduction produced by L3CCD multiplication decreases the effective quantum efficiency by a factor of two when integrating by simply summing the recorded frames. In addition, the CCD readout amplifiers introduce readout noise which, while it may be an order of magnitude lower than the average photon event level (figure 2.7), also decreases the S/N.

If the signal in one pixel is known to be very much less than one photon per frame, the L3CCD output signal can be thresholded to remove both problems (Basden et al., 2003). Each pixel is set only to contain a photon or not (figure 2.8), based on whether its data value is above or below a threshold level. The level is set such that each claimed photon is a significant detection above the readout noise. The L3CCD multiplication noise is therefore eliminated, by using the prior information that each pixel is only likely to contain at most one photon – and thus removing the overlap between photon input distributions.

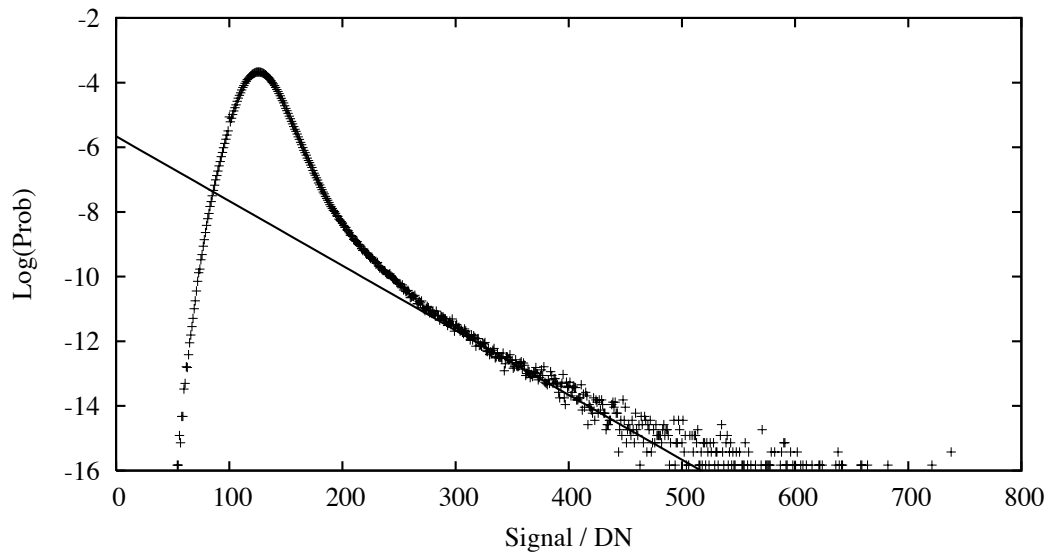
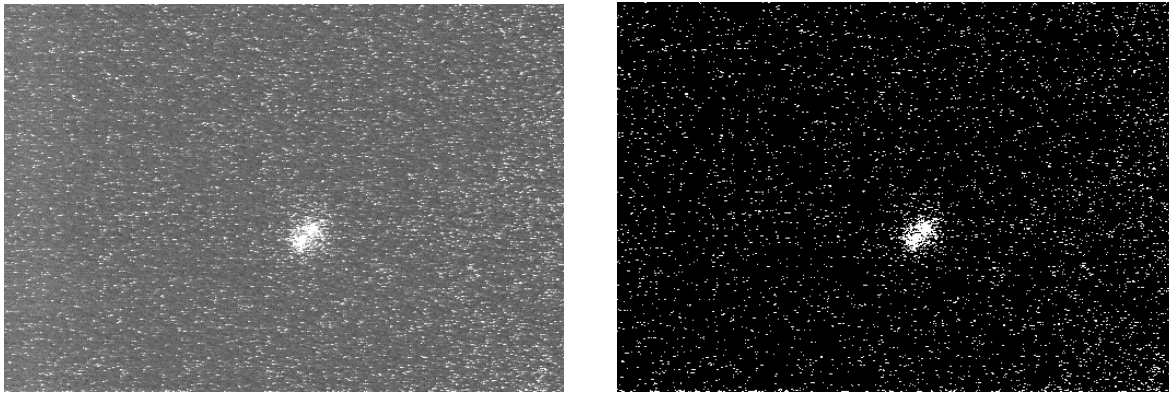


Figure 2.7: A typical histogram from a sky background region of a June 2005 LuckyCam run with a gain of 50 DN (data numbers) per photon. The distribution is the convolution of the electronics' Gaussian readout noise and the L3CCD electron multiplication probability distribution. The bias level has been set to an arbitrary value during processing. The readout noise has a standard deviation of approximately 13 DN, and an average single photon event (with 50 DN above the zero level, defined from the peak of the distribution) is a 5σ detection above the noise. The theoretical single-photon L3CCD output distribution is shown by the solid line. The high-signal events which are well above the single photon distribution are probably rare two-photon events.



(a) Raw data (cleaned using CLEANUP)

(b) Photon-counted

Figure 2.8: Photon counting. The left panel shows a frame from the June 2005 LuckyCam run, taken with a gain of 190DN/photon and a readout noise of 11DN RMS per pixel. The right panel shows the image with a threshold level set at a 7σ deviation above the background noise. This threshold level leads to approximately 30% of the photons being rejected. Some of the detected events are likely to be spurious events generated on the L3CCD.

However, photon-counting must be applied with care for two reasons:

1. **Photon losses.** Thresholding removes all those photon events which fall below the threshold level. The output signal probability distribution for a single input photon is an exponential decrease with signal level. The threshold level and/or system gain must therefore be set with care to avoid losses of possibly large numbers of photons multiplied to a level below the threshold level. In most observations we operate LuckyCam such that the mean single-photon signal is 5-10× the readout noise, a compromise value that avoids excessive dynamic range loss.
2. **Non-linearity.** If a thresholded pixel happens to actually contain more than one photon, it is still only counted as a single photon by the thresholding scheme. This leads to a large loss in signal for bright sources. The thresholding scheme can thus only be applied when the target in question is known to be faint. In practise this is not a significant limitation for most LuckyCam science observations, as sources which generate several-photon events in each of several thousand frames in a typical run are usually sufficiently bright that their S/N is dominated by other factors than multiplication noise.

More complicated thresholding schemes have been discussed, in which the signal is thresholded into a number of different photon event levels (Basden et al., 2003). However, each scheme introduces non-linearity into the output signal. While it is easy to calibrate this problem out for a input signal known to have a constant light level, it is not clear how to apply these schemes to the continually varying fluxes in LuckyCam images. For this reason, photon counting is not used by default in the Lucky imaging pipeline; the vast majority of the data presented in this thesis is not photon counted, although LuckyCam was run at gains that would enable photon counting once the reduction strategies have been further developed.

2.3.3 Bias, flats & cosmic rays

Standard CCD reduction usually proceeds by first removing a pixel-dependant bias value (measured from an image integrated with no incident light) and then dividing out pixel-to-pixel sensitivity variations using a constant-illumination flat field. Cosmic rays are usually removed by comparing multiple pointings or multiple integrations of the same field.

Cosmic rays can be detected in L3CCD images as a “splash” of saturated pixels on a single frame. Their removal is trivial with Lucky Imaging images, as the masking of large sections of a single frame around a cosmic ray event does not significantly affect the statistics of a typical Lucky image constructed from tens to hundreds of frames.

I elected to generate L3CCD bias frames from on-sky data, as in most frames only a small percentage of pixels contain photons. The CLEANUP and BIASGEN portions of the Lucky Imaging data reduction pipeline (chapter 3) perform this step for both large-scale bias variations and

the faint vertical line biases introduced by the camera electronics. Hot/stuck pixels can be detected by eye in summed images. In all the LuckyCam data none were present more than 10 pixels from the edge of the imaging area, and so were easily removed by masking.

Flat fields (flats) are made from twilight observations of the bright sky, in the same way as for standard CCD imaging. Depending on the calibration requirements, I generated flats from the sum of either a few hundred very bright frames, or a much longer integration at low enough light levels to ensure that each pixel had < 1 photon/pixel/frame.

Bright flat fields (with several photons per pixel per frame) give a high SNR flatfield measurements, but the zero level determination is particularly difficult because flux is present in each pixel. Measurement of an accurate zero level is critical for the production of flat fields, as it has a direct effect on the derived fractional amplitude of the flat field variations. LuckyCam zero levels change from frame-to-frame and row-to-row (chapter 3), complicating this determination.

The CCD87 & CCD97 chips used for the 2003+ LuckyCam observations have a set of three rows designated as dark – i.e. masked off from incoming light. I calibrated the bright flat fields such that these rows are set to zero average flux. However, because there is some light leakage (at the few per cent level) into the rows, the accuracy of calibration using bright flat fields is limited to the few percent level.

An ideal L3CCD flat field can be constructed from the sum of many frames imaged with a flat-field illumination constrained to be much less than one photon per pixel per frame. The zero level in each pixel can then be determined from those frames that do not contain photon events. However, this approach requires very long integrations to achieve a good SNR in each pixel. For example, with an average input photon rate of 0.2 photons/pixel/frame and added L3CCD multiplication noise, a 25,000 frame (1250 second) integration is required to reach a SNR of 50 in each pixel. When we attempted twilight flat observations with a sufficiently low photon event rate, faint stars in the skyflat field often became visible during the long integration.

Since these long integration flats are taken during times of relatively low background illumination compared to standard skyflats, the flatfield observing uses time that could have otherwise been used for science programmes. I would therefore recommend that future L3CCD observations take long-integration dome flats, if a sufficiently low illumination level can be achieved in the dome.

All the flat fields used for the data presented in this thesis are produced using the bright-sky method.

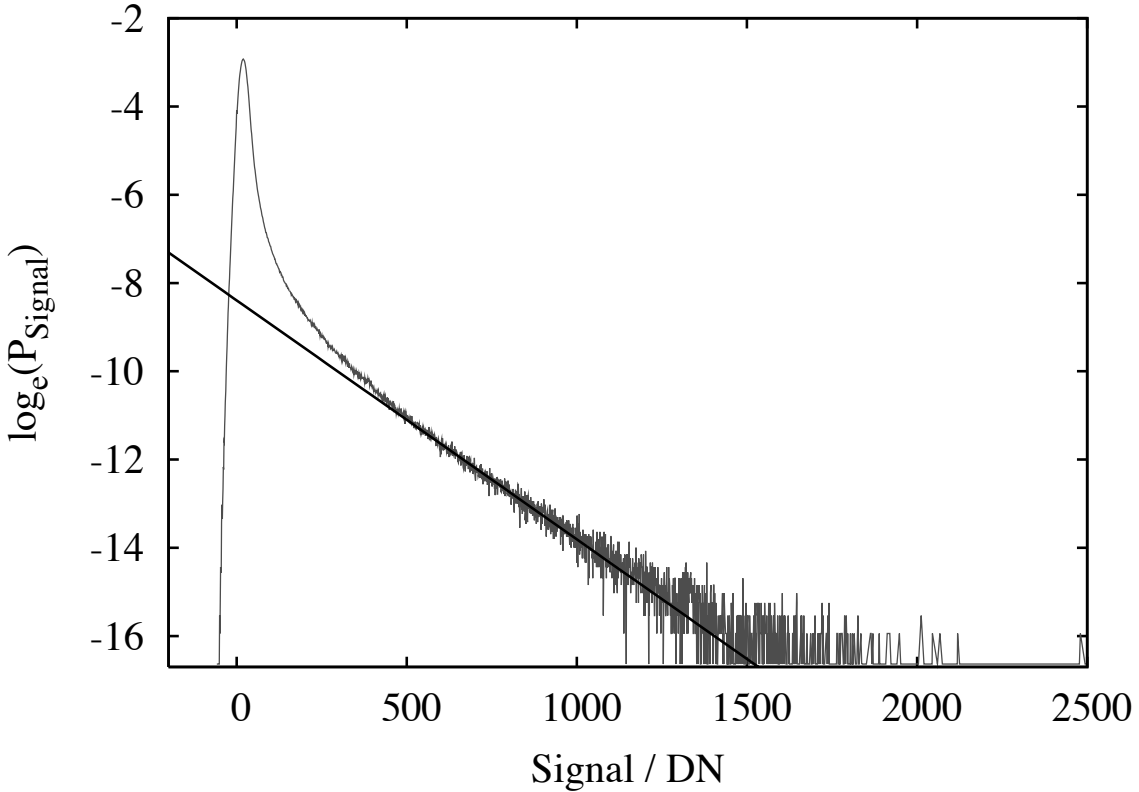


Figure 2.9: L3CCD gain measurement. A linear-log histogram of the measured probability of obtaining a signal in a single pixel in a background region of a typical LuckyCam observation, much the same as figure 2.7. The solid black line is a best-fit straight line to the best gain measurement area of the graph, chosen as described in section 2. The line has a gradient of $-0.0054 = -1/g$. The system gain for this observation is thus 185 DN/photon in the brightest pixel of each event.

2.3.4 Gain calibration

During observations at the NOT in June 2005, the LuckyCam system gain varied by as much as 10% on timescales of a few minutes and up to 25% over a night, probably due to small temperature variations in the L3CCD. Although relative photometry of targets in the same field is not affected, if photometry taken at different times is to be compared the L3CCD gain must be measured. Because of the rather rapid variations in gain, this should ideally be performed on a per-target basis.

During the 2005 runs, the gain was measured in two independent ways, which were tested and used simultaneously during data reduction:

Bright calibrator stars. In these tests we targeted a bright star which was detectable at reasonable SNR without gain. Data was then taken both with and without gain, if necessary defocusing the star to avoid saturation. The gain in DN is measured from the factor of total signal increase when gain is engaged.

Single-photon event histograms. Sky-background areas in almost all LuckyCam observations have much less than one photon per pixel per frame. The distribution of pixel values in those areas consists of an exponential from the statistics of single electrons in the multiplication register convolved with a Gaussian from the readout-noise (figure 2.9, and below). As suggested in for example Tulloch (2004), the multiplier of the exponential decrease is simply $-1/g$, where g is the gain in DN/photon. To measure the gain an exponential decrease can be fit to the histogram of pixel values, with the gain as a free parameter.

Both gain measurement techniques produced the same gain values (to within the $\sim 10\%$ measurement errors).

For the following reasons, I chose to use the event histogram method as the standard gain calibration technique:

1. Observing gain calibrator stars every few minutes would introduce an unacceptable time overhead.
2. The event histogram method is performed completely simultaneously with the observations, eliminating the need to compensate for any rapid gain drift.
3. Some variations in gain across the L3CCD chip were found. The histogram method allows the gain determination region to be customised to the location of each of multiple objects in the field, a procedure that would be very difficult using gain calibration stars.

Accurate gain determination using the event histogram method has a number of subtleties. To give more precise and accurate gain measurements than can be obtained by fitting the histogram in the simple way described above, I implemented the following procedures:

1. **Area of image for event acquisition.** To get the best signal-to-noise in the gain determination, the best strategy would be to use all the image areas which do not contain bright sources. However, tests on the June 2005 data also showed the gain can vary by as much as 10% horizontally across the LuckyCam field of view. For this reason, I restricted the acquisition areas to 100 pixel wide boxes centered directly below the sources that required photometric calibration.
2. **Choice of fit region.** In a linear-log plot the exponential decrease becomes a straight line (figure 2.9). Low data values are affected by the readout-noise Gaussian shape, while the highest data values are affected by low event numbers, rare two-photon events, and saturation at the highest gains. The best region of the histogram for gain determination is the region of the graph which best corresponds to a straight line. The gain determination region can be selected automatically (based on the goodness-of-fit to a straight line) or manually.
3. **CTE effects** Charge transfer efficiency (CTE) is typically 70-90% in LuckyCam images (see figure 2.10). That is, each photon event has 70-90% of its total flux in its brightest

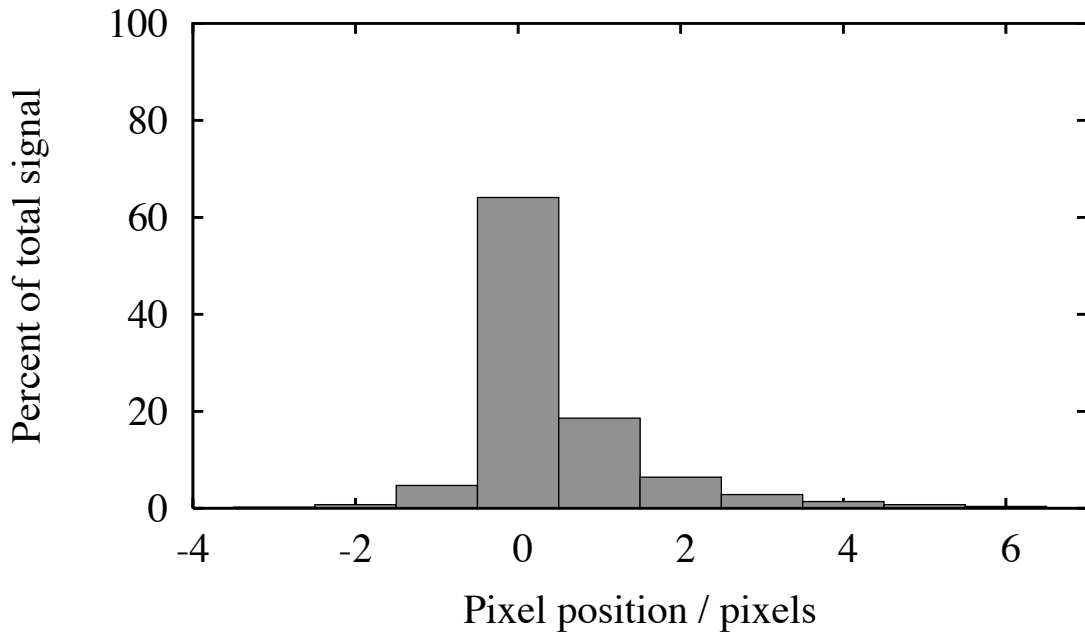


Figure 2.10: The average horizontal shape of single-photon events during a typical LuckyCam observation (the same as that analysed in figure 2.9).

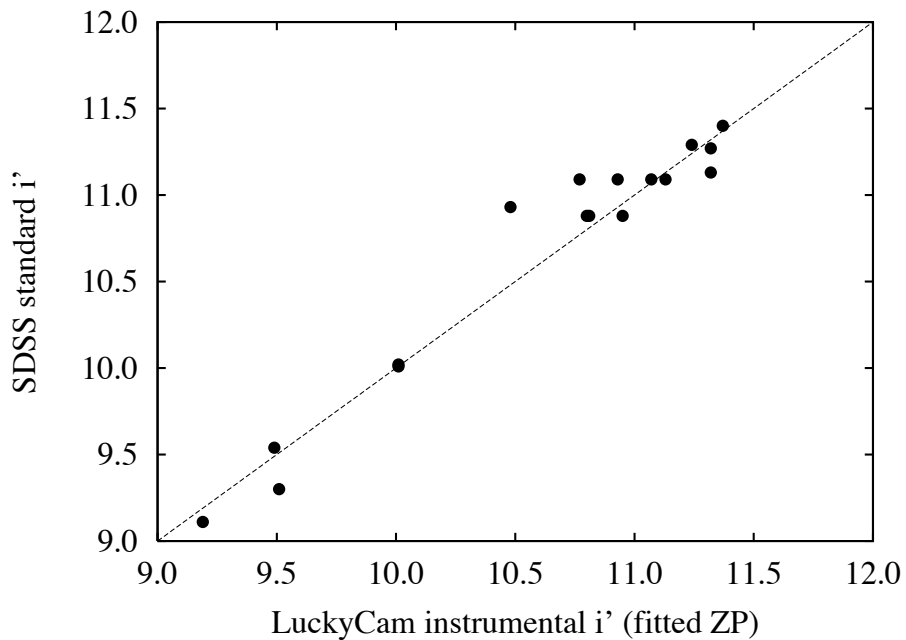


Figure 2.11: Calibration of LuckyCam photometry against SDSS standards from Smith et al. (2002). The LuckyCam gain was calibrated for each observation using the methods described in the text. The dashed line has a gradient of 1.0, and corresponds to perfect agreement with the SDSS photometry. The residual RMS error is ~ 0.1 mag.

pixel. A simple single pixel-value histogram thus underestimates the true gain by the 10–30% of flux missing from each event. Although this effect can be removed by summing 3-4 pixels in a line for each histogram event, this can lead to problems when multiple events occur in the 3-4 pixel window (such as in the high background cores of globular clusters). However, trials using the June 2005 data showed that the CTE does not vary at more than the 10 per cent level, and so single pixel gains can be used for calibration at that accuracy – with the caveat that they systematically underestimate the true gain.

4. **Spurious events** The L3CCD multiplication register can occasionally excite a spontaneous electron, which is then multiplied in the remaining portion of the register as if it were a photo-electron from the imaging area of the chip. Spurious events generated at the start of the register have gains identical to that of real photons. However, most spurious events are generated somewhere in the middle of the register. They thus pass through a smaller section of the register, and so have reduced gain. If there is a very low sky photon rate the apparent gain can thus be reduced by being weighted towards these low-gain events. Accurate gain determinations must thus be made using low-speed ($\leq\sim 30$ FPS) data, to ensure sufficient sky-photon numbers in each frame (the gain is not dependant on the frame-rate, as the pixels are read out at the same speed irregardless of the frame size). The current LuckyCam gives spurious events which would be detected as photons at about 1/2 of the dark-sky photon rate at 30 FPS. Although this level of events may affect the gain readings, the number of spurious events would have to vary widely and rapidly to affect the relative gain determinations, and that is not observed.

Figure 2.11 shows gain-calibrated LuckyCam photometry of SDSS standard stars. The photometric accuracy is about 10% RMS, even though the actual L3CCD gain values for the observations range between 25 and 81 DN/photon. Better (and more easily automated) fits may be obtained by fitting a model including the straight line component, the Gaussian read noise and other effects, and these models will be investigated in further work.

2.4 Data acquisition - PixCel LC

LuckyCam data acquisition is performed on a standard PC equipped with a frame grabber system and fast disk storage.

The LuckyCam data acquisition system has gone through two major versions.

2001-2004 This version was based on PixCel, a commercial package used to drive the AstroCam family of cooled CCDs, running on a standard PC equipped with fast RAID data storage. Camera control was via a custom ISA custom transputer card, and pixel data was received using a custom PCI card. Approximately 90 seconds of data (1000 full-frame images) could be recorded into main system memory; data recording was then halted while the system wrote

the data to disk, taking a further 90 seconds. This two-step process led to a very low observing efficiency, while the need to split entire nights of observations into 90 second runs required an unacceptable observer workload.

2005+ I designed and implemented a new data acquisition system, offering continuous recording for entire nights, realtime data compression and realtime Lucky Imaging.

The 2005+ data acquisition system is based on a 3.4GHz Pentium 4 PC running the Windows XP Professional operating system, with custom software written in Microsoft Visual C++. Data is received from the camera using a standard frame-grabbing PCI card (the Matrox^{*} Meteor Digital II). Two fast Serial ATA hard drives are run in a software RAID-0 mode, striping data in 4 kilobyte chunks alternately between the drives to give 24 MB/sec sustained writing performance. Hot-swappable 300 GB Maxtor OneTouch-II external USB 2.0 hard disk drives provide secondary disk storage for data transfer and backup, as well as direct raw data storage when the realtime compression systems are enabled.

The graphical user interface and data acquisition software of the previous LuckyCam system – PixCel[†] – was mature and well-suited to the data acquisition tasks. The LuckyCam team were given access to the source code to the system. For rapid development of a useful imaging system, I decided to replace the backend of the previous software (the hardware interface tasks) with my own code to interface to the 2005+ camera electronics. I also added many LuckyCam specific user interface sections.

The user interface (figure 2.12) includes a wide variety of tools to facilitate both data acquisition and camera development. I replaced references and calls to the previous hardware with either stub (do-nothing) functions or hooks to new code to interface to the Matrox hardware. The following section describes my upgrades to the camera software, now named PixCel LC (LuckyCam).

2.4.1 Interface upgrades

The Lucky Imaging specific PixCel interface upgrades I have implemented are labelled in figure 2.12 (next page) and discussed in order below.

1. **Realtime Lucky Imaging display.** The previous version of PixCel could not display images as they were recorded (although a live video display was available when not saving data). In PixCel LC, realtime images are displayed at up to 100 frames per second while frame recording is progressing, allowing easy monitoring of the integration's progress. The display also shows the results of the realtime Lucky Imaging & other analysis subsystems, when enabled.

^{*}<http://www.matrox.com>

[†]originally developed by AstroCam Ltd. and later by Perkin-Elmer Life Sciences.

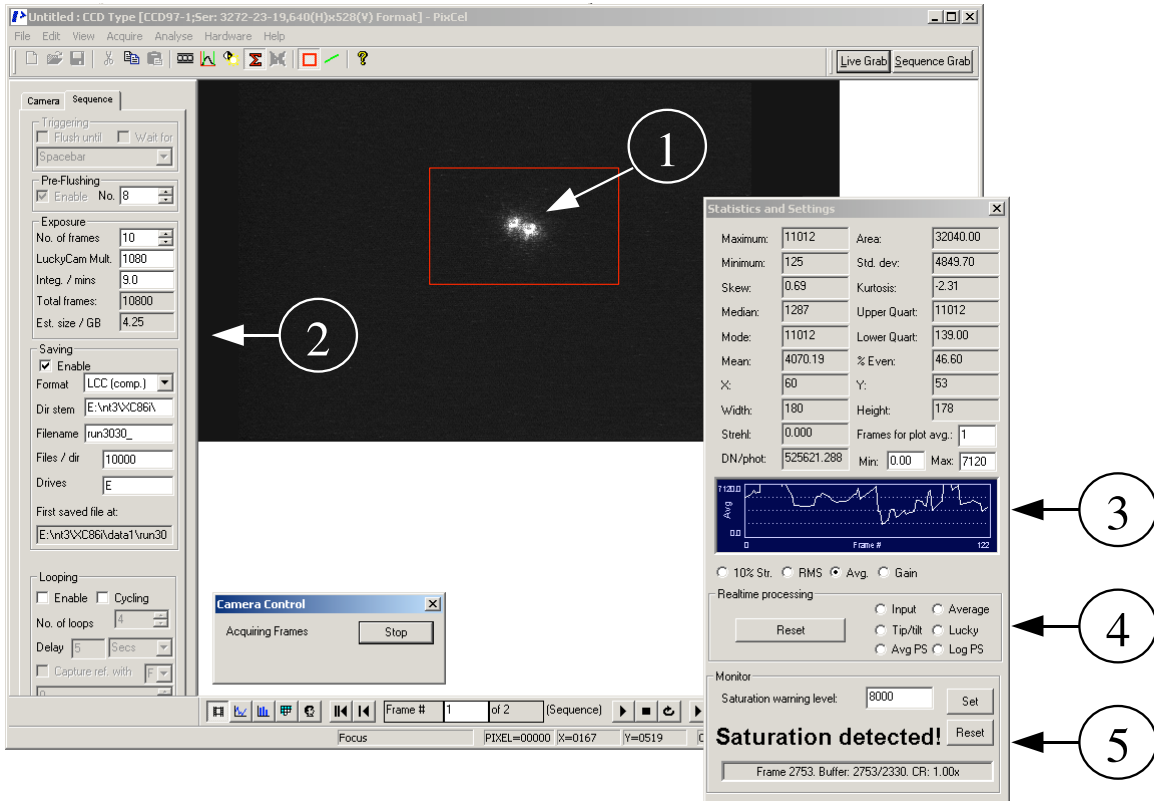


Figure 2.12: A screenshot of PixCel LC, with labelling (described in section 2.4.1) showing the upgrades to the interface for Lucky Imaging observations.

2. **File storage settings.** Various run storage settings unique to LuckyCam are set here, including the options to enable realtime compression and store frames to multiple removable hard disk drives simultaneously. Long runs can be automatically split into multiple directories containing several thousand files each.
3. **Image quality analysis graph.** This graph is continually updated during data acquisition, showing a number of statistics describing the image area within the (user-specified) red box. The standard deviation of the pixels within the box, and the total flux are particularly useful during camera calibration and testing, while the 10% Lucky-selected Strehl ratio graph assists in focusing the telescope by giving a continually updated estimate of the Lucky Imaging output image quality.
4. **Realtime Processing.** PixCel LC can calculate and display integrations, Lucky Imaging previews and summed power spectra in realtime. The implementation of this processing is described in section 2.4.3.
5. **Status display and Saturation Warning.** Some data in the 2004 run was affected by saturation of the guide stars. This is hard to see by eye, because the frame quality variations lead to the very best quality frames having more than 10x the light concentration

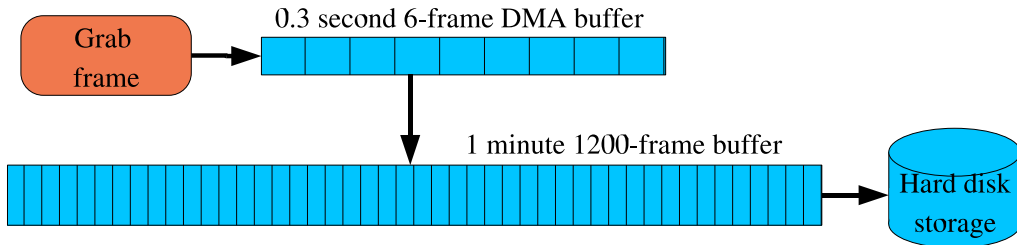


Figure 2.13: The path LuckyCam data takes though the PixCel LC backend. Each transfer (the arrows) is controlled by a separate thread (simultaneously executing sections of the program), which run on different frames as they become available to that section of the pipeline. On the diagram, priority of the threads decreases left-to-right and up-to-down.

of average frames. Those frames which offer the best resolution are therefore also more likely to be saturated, which can be a severe problem for Lucky Imaging observations. To avoid this problem I implemented a saturation watch system, which monitors the maximum pixel value within the user-selected red box and alerts the observer if saturation is detected in any frame.

2.4.2 The PIXEL LC backend

The Pixel LC data acquisition backend is completely self-contained, and could in principle be run without the GUI. The extreme data storage speed and size requirements of the LuckyCam system (14 MB/sec sustained for several hours, at frame rates of up to 100 FPS) required careful software design to ensure that all data is recorded, without skipping or losing frames.

In particular, a key capability of the new system is continuous recording sustained for several hours, requiring a robust buffering implementation to ensure that other processes on the computer cannot cause frame dropping or interruptions to data acquisition. To achieve this I designed a multi-stage pipeline (figure 2.13). Each stage runs in a separate program execution thread and so effectively runs simultaneously with the others, processing data as it becomes available from further up the pipeline. The allocation of a generous intermediate storage buffer eliminates the problems of transient hard disk recording speed reductions (due to, for example, file fragmentation or system load), which could otherwise lead to pauses in data acquisition.

The data from the camera passes though the following threads in the PixCel LC backend:

1. **Initial gapping** The Matrox API is told to schedule a grab of the next frame, and return the data from the previous grab. This call is issued immediately on completion of the previous grab but does not return until new data is available. Data is rapidly transferred directly from the grabber board to main system memory by a DMA (Direct Memory Access) transfer, which does not involve any processing by the CPU. The initial grab

thread has an ~3.0 MB circular frame buffer. Once a new frame has arrived, the next thread (number 2 below) is told to activate, while the grabbing thread waits for the next grab to complete.

2. **Move to secondary memory storage** This thread transfers frames from the small circular grabbing frame buffer to a much larger circular buffer, also stored in main memory but not accessible to DMA transfers. The grabber thread's circular buffer can only store ~ 0.3 seconds of data. The secondary buffer is 1.0GB in size, and can store over a minute of data, sufficient to avoid the effects of all likely hard disk recording slowdowns.
3. **Hard disk recording** When new data is entered into the secondary buffer the hard disk recording thread is woken; it iterates through the new frames available and writes them to disk with optional realtime compression.

The separation into threads allows prioritisation of these processes. The Windows threading model passes execution control from one thread to another based on the thread's priority. If a high priority thread signals that it is ready for activity (for instance, a grab is ready to be scheduled) while a lower priority thread is executing, system control is immediately passed to the high priority thread.

The grabbing thread is given the highest, near-realtime, priority to ensure that no chance of receiving a frame is lost. However, the grabbing instruction itself is very cheap in terms of execution time, so this thread remains paused waiting for a grab for most of its execution time. A just-grabbed frame's move to secondary storage must occur before the grabbing thread's circular buffer is full, i.e. within ~0.3 seconds, so the secondary memory storage thread is also given a high priority. Because of the large secondary buffer, the hard disk recording need only occur within approximately one minute; this lenient criterion allows this thread to be run at standard priority, so it cannot interfere with the grabbing process.

In addition, there are several further threads which run as part of the Pixel GUI, including the realtime Lucky Imaging capabilities. These are not critical to the data recording and are thus allocated very low priority. In times of high system load (for example, when running at very high frame rates) the GUI threads are often not activated for several frames, reducing the frame rate of the on-screen display but ensuring that sufficient time is allocated to the more important grabbing and data storage threads.

2.4.3 Realtime Lucky Imaging

At the telescope it is very useful have high-resolution imaging of the targets as they are being observed, allowing changes to be made in the observation programme to suit both conditions and newly revealed details of the objects under investigation. For this reason, I implemented a simple realtime Lucky Imaging system as part of the data acquisition software.

The full LuckyCam pipeline (described in chapter 3) runs at approximately 1/4-1/3 realtime on the 3.4GHz Pentium 4 used for development - i.e. a 1 minute run would be fully reduced in 3-4 minutes. However, a preview Lucky Imaging reduction can be produced in a far shorter time if lower quality is accepted. The realtime Lucky Imaging subsystem implemented in PixCel LC does not attempt to remove camera artifacts, do flat-fielding or bias removal, or employ the noise-reduction and sub-pixel shifting strategies used by the full pipeline. It does, however, run at less than 15% CPU utilisation on the data acquisition computer, and can thus run fully concurrently with the data recording system*.

In use, a box containing the guide star is drawn on the realtime video display are by the user. When engaged, the realtime system tracks the brightness of the brightest pixel within that box, finding the average and standard deviation of that value. Frames with highest pixel brightnesses greater than one standard deviation above the average are selected, then shifted to align their brightest pixels, and added to a realtime preview image displayed to the user. Because the seeing is constantly changing, this procedure does not select a particular percentage of frames, but on-telescope trials gave selection fractions of usually 10-20%. Note that the procedure works best in constant atmospheric conditions; if the seeing becomes very much worse compared to the start of the integration the average and standard deviation pixel brightnesses must be reset, or all frames may be selected (or all rejected). Future versions of the software could use a running average to avoid this problem.

The system proved very effective during the November 2005 LuckyCam run, including the rapid discovery of a 0.12 arcsec binary star system during observations in \sim 0.6 arcsec seeing.

Several other realtime processing options are available in PixCel LC, including frame shifting only (no frame selection, giving a fast shift-and-add imaging system) and direct averaging of the input frames. The power spectrum of the area within a user selected box can also be calculated and displayed in realtime, for fringe visibility checks during the 2006 LuckyCam Hires experiments.

2.4.4 Realtime compression

The LuckyCam data storage requirements are extreme. A single night of observation often produces over 250GB of data. Hard disk technology available during the design of the 2005 system offered USB external hard disk capacities of up to 300 GB for \sim £120. If all data is to be backed up onto two separate disks, a minimum of two hard disks are thus required per night, leading to significant extra costs during long observing runs. This number of (heavy) external hard disks also entails difficulty in safely shipping the data back from the telescope site. A reduction in the LuckyCam data storage requirements therefore has a direct benefit to

*A DSP (digital signal processor) based system is currently being designed to run the full Lucky Imaging pipeline in realtime.

the running costs and convenience of the system.

For those reasons I implemented a realtime lossless data compression system that reduces the storage and hard disk speed requirements by a factor of two. Because the speed requirement is greatly reduced, data acquisition can be performed directly and simultaneously to two USB external hard disks, fully backing up the data as it is acquired, instead of a much slower and more complicated two-step process with initial recording to a fast RAID array.

The compression system takes advantage of the structure of LuckyCam astronomical frames. Each pixel contains either no astronomical signal, or photon events from the sky, faint extended objects and a few bright stars. Each pixel also contains readout noise. For typical observations (excepting planetary imaging and skyflats), 90-99% of LuckyCam data consists of pixels containing only readout noise.

The LuckyCam electronics samples the images with 14-bit resolution, giving data values from 0 to 16,184, which for ease of processing are stored as 16-bit integers by the Matrox frame grabbing hardware. The previous LuckyCam software stored all pixels as 16-bit integers.

The readout noise is approximately Gaussian with a 1σ deviation of only \sim 10-14DN. Therefore, given a known average base level, pixels containing only readout noise need only be represented as 8-bit deviations from that average level (data values -128 to +127), while those containing photon events require the full 14-bit resolution.

The realtime compression system is implemented based on these observations. Each frame is first sampled to determine an approximate average base level. The system then loops through each pixel in the frame. Those that can be are stored as single signed 8-bit values (-128 to +127) compared to the zero level. One value, -128, is reserved as a flag. If a pixel value does not fit into the 8-bit range, most likely because it contains a photon event, the flag value is written, followed by the full 16-bit value of that pixel. Pixels containing photons therefore require three bytes of storage – while the other pixels, making up the vast majority of each frame (see figure 2.14), require only one byte. This compares very well with the 2 bytes per pixel required by uncompressed images.

In typical astronomical observations compression factors of 1.8-1.9 are achieved, relative to standard 16-bit storage method. The scheme is capable of losslessly encoding all images produced by LuckyCam, and does not give compression only if bright extended objects take up more than 3/4 of the field of view. The compression algorithm is also used throughout the LuckyCam pipeline; on cleaned images with reduced noise stored during analysis compression factors of 1.98 are usual.

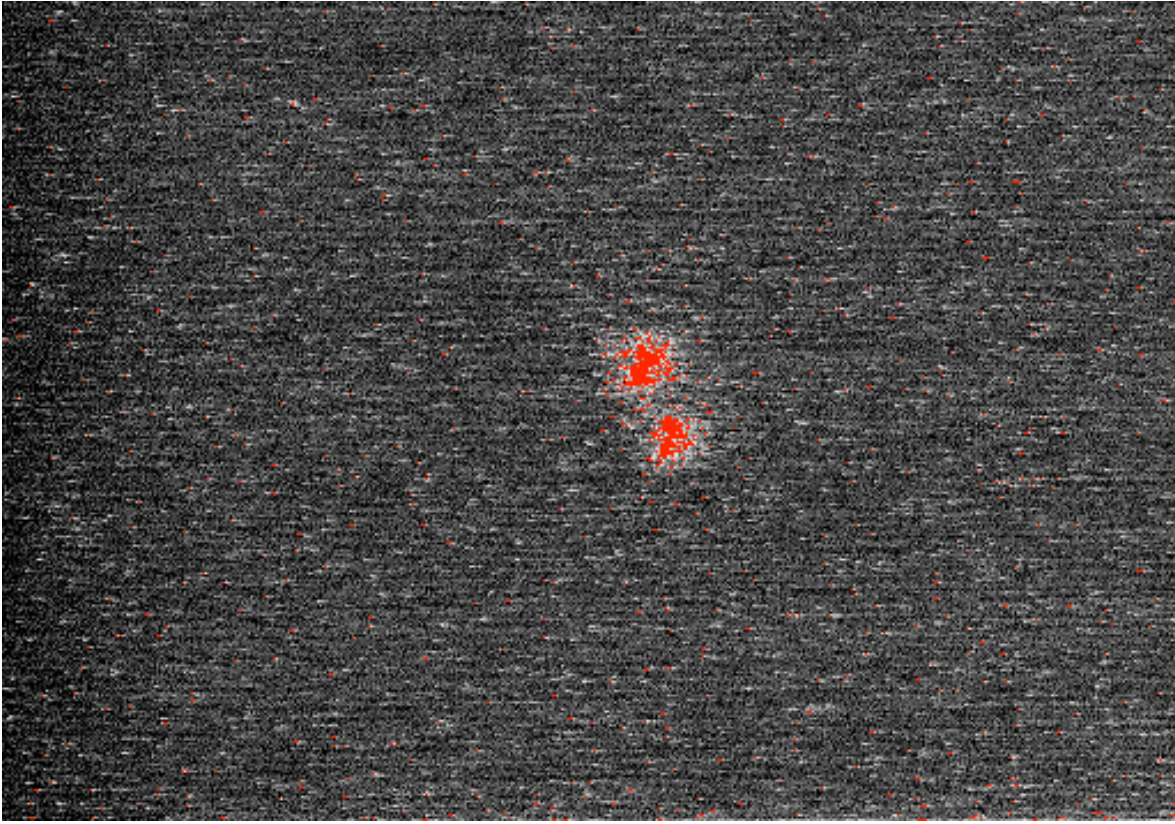


Figure 2.14: A typical LuckyCam frame, from the June 2005 run. All pixels with values which are stored as a single byte in the PixCel LC compression scheme are in greyscale; those which require three bytes are in red. There is clearly a very large storage requirement saving over the standard two bytes for each pixel.

2.4.5 LuckyCam control

The 2006 LuckyCam is designed for extensive aperture-masking trials, which requires customisable and repeatable optical alignment to greater precision than achieved by the previous LuckyCams' systems. For this reason, it has a number of movable optical elements under software control, allowing automated recording of the camera setup used during observations, and easy camera configuration repeatability. Previous LuckyCams were controlled either by hand (2001-2004) or electronically from a custom control board located in the telescope control room (2005, depicted at the top of figure 2.2).

Following design and construction of the LuckyCam hardware and electronics by Craig Mackay, I wrote custom LuckyCam control software (figure 2.15), to be used on the data acquisition computer both during optical tests at Cambridge and at the telescope during observations.

The movable elements of the 2006 LuckyCam are controlled in two different ways. The filter wheel (close to the CCD dewar) and aperture mask wheel (at a replicated pupil plane) are

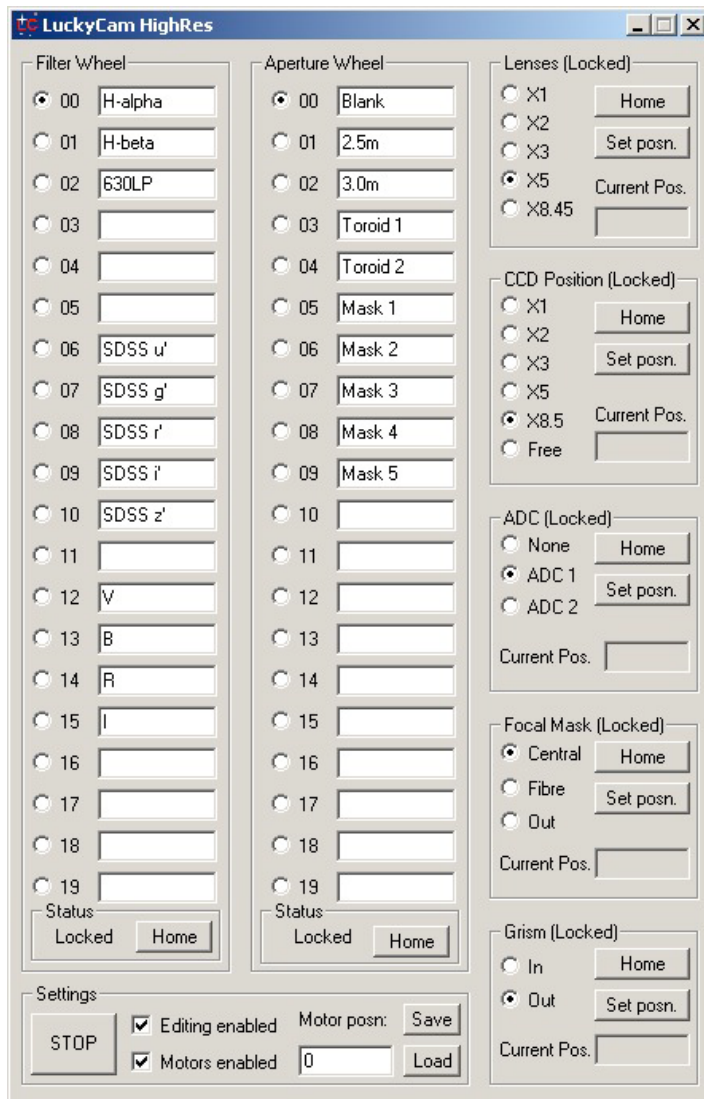


Figure 2.15: The LuckyCam control interface.

purchased from Finger Lakes Instrumentation* and controlled by a manufacturer supplied API (application programming interface). The remaining elements (the lens, grism, ADC and focal mask elements and the movable CCD dewar) are mounted on movable stages driven by stepper motors. The motors are controlled via an RS232 serial link to a programmable single axis controller board, connected to a custom multiplexer to allow the single controller to control all five motors.

The control software is written in Microsoft Visual C++. Because there is only a single motor controller, only one stepper motor can be moved at any time, although the filter and aperture wheels can be moved simultaneously. For maximum observing efficiency (and to reduce observer frustration) it is desirable to move as many elements simultaneously as possible. I therefore implemented each independent system in the software as a separate thread (figure

*<http://www.fli-cam.com/>

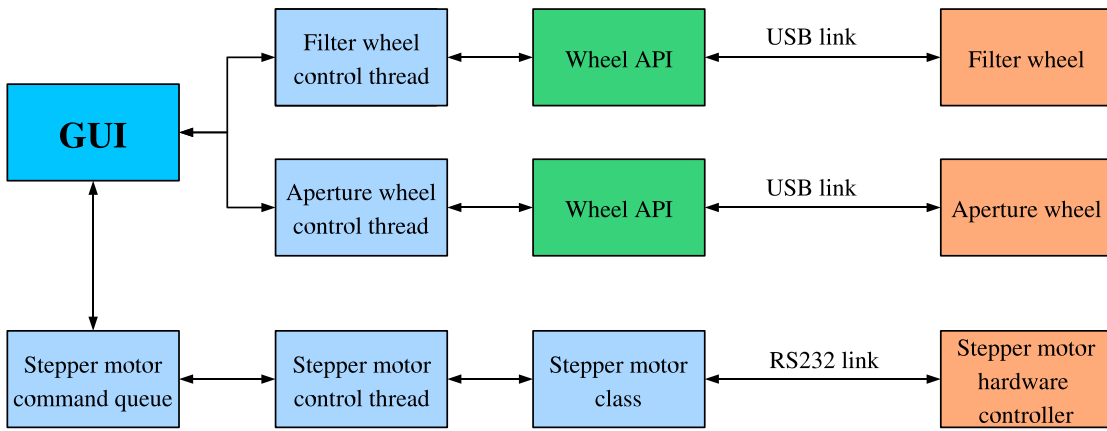


Figure 2.16: A schematic of the LuckyCam control system. The GUI takes commands from the observer and passes them to the hardware controllers, as well as receiving status updates from the hardware and queue systems. In this figure the subsystems that I have written are shown in blue.

2.16). The user can issue any number of motor commands in one action, and those that cannot be executed simultaneously are queued.

The stepper motor's positions are calibrated in the following manner. Each motor is first homed – returned to a known zero position. The motor in question is moved at a normal speed (~ 4 revs/sec) towards one of two limit microswitches, which stop the motor when triggered. The control software then drives the motor back a few revolutions (about 1cm of physical motion of the stage), and back to the switch trigger position at a very slow rate, to give a repeatable reference position.

The control software then tracks the current position of the motor, given all motion commands issued, and re-homing is only necessary if the motor is moved while not under the control of the software (for example, during manual optical realignment). All responses of the motor controller board are checked for error conditions, and each motor move is monitored to give visual feedback of the motion to the observer, who is usually located in the telescope control room, far from the instrument.

2.5 Summary

- The LuckyCam optics are passive and very simple, consisting essentially of a reimaging lens and a filter. The system is therefore very cheap.
- An L3CCD (EMCCD) gives LuckyCam the ability to perform photon counting at high frame rates with the full CCD quantum efficiency.

- I describe various calibration methods specific to the L3CCD, most importantly a way to calibrate the system gain using data taken during science exposures.
- My implementation of a new LuckyCam data acquisition system enables continuous recording of data from LuckyCam at 14MB/sec, sustained for entire observing nights.
- The data rate is reduced by a factor of two by a realtime compression system that takes advantage of the photon-detection capabilities of the L3CCD.
- The data acquisition system can also perform a realtime preview of the Lucky Imaging results during observations, as well as various tests and diagnostics.
- I also designed the software control system for the optics of the 2006 version of Lucky-Cam.

3

The Lucky Imaging Data Reduction Pipeline

The Lucky Imaging Pipeline is a fully automatic data reduction system designed for Lucky Imaging data. The input is a disk containing data produced by PixCel LC at the telescope over the course of a night or nights; the output is a set of directories containing fully reduced runs at a selection of frame selection levels and, optionally, the hundreds of thousands of input individual frames cleaned of camera artifacts.

3.1 The Lucky Imaging Process

The standard Lucky Imaging process, used to reduce almost all LuckyCam data, proceeds as follows:

1. Determine the quality for each frame on the basis of the guide star's Strehl ratio.
2. Determine the shift for each frame that aligns the brightest speckles.
3. Sort the frames according to quality.
4. Align and co-add the best frames using the Drizzle algorithm (section 3.5.4).

The algorithm which determines the quality and alignment vector of each frame can be altered according to the science programme and the prevailing conditions.

3.1.1 Frame selection

The standard Lucky Imaging pipeline described in this chapter selects frames on the basis of the degree of correlation to a diffraction-limited PSF. This produces very similar results to selecting on the basis of Strehl ratio (the ratio of the peak flux to that expected in a diffraction-limited core), but blurs the input PSFs to match the telescope's maximum resolution, increasing the SNR of the peak amplitude determination.

This procedure selects the frames with the best light concentration – that is, the frames with the largest fraction of the flux within the diffraction-limited core. It thus produces images with a maximised output on-axis Strehl ratio.

However, some science programmes benefit from different frame selection strategies. If there is a requirement for a wide field of view (i.e. a smaller drop-off in resolution with distance from the guide star), two or more guide stars can be used. Frames can then be selected on the basis of both the correlation between the two guide star PSFs and their light concentration, biasing the frame selection towards the periods with the largest isoplanatic patches.

As another example, if there is a faint close companion to a bright star, the PSFs which have less light from the bright star in the position of the companion can be selected (similar to the Dark Speckles method, Boccaletti et al. (1998)). These asymmetrical PSFs can be detected either by searching for a lack of light in the companion position or (to avoid biasing the selection towards periods where photon statistics reduce the light from the companion) an excess of light elsewhere. I performed some very preliminary experiments on this method, and found that the background within 1 arcsec from the guide star could be reduced by approximately a factor of two, although the Strehl ratio of the faint companion was also reduced because the poorer more asymmetric frames were preferentially selected.

The method of frame quality cutoff can also be varied. In the standard LuckyCam reductions only the frames which meet some quality criterion are included. This can be generalised to including all frames, but each weighted by some quality criterion. Tubbs (2004) investigated weighting frames on the basis of both Strehl ratio and the fraction of power in high frequencies, but found that the final output image was not improved in resolution from the simple cutoff method.

3.1.2 Image alignment

The standard data reduction system described below aligns frames on the basis of the peak position of the brightest speckle, ensuring that the maximum possible light is included in the center of the guide star image.

This approach can lead to problems with faint guide stars, where photon noise becomes im-

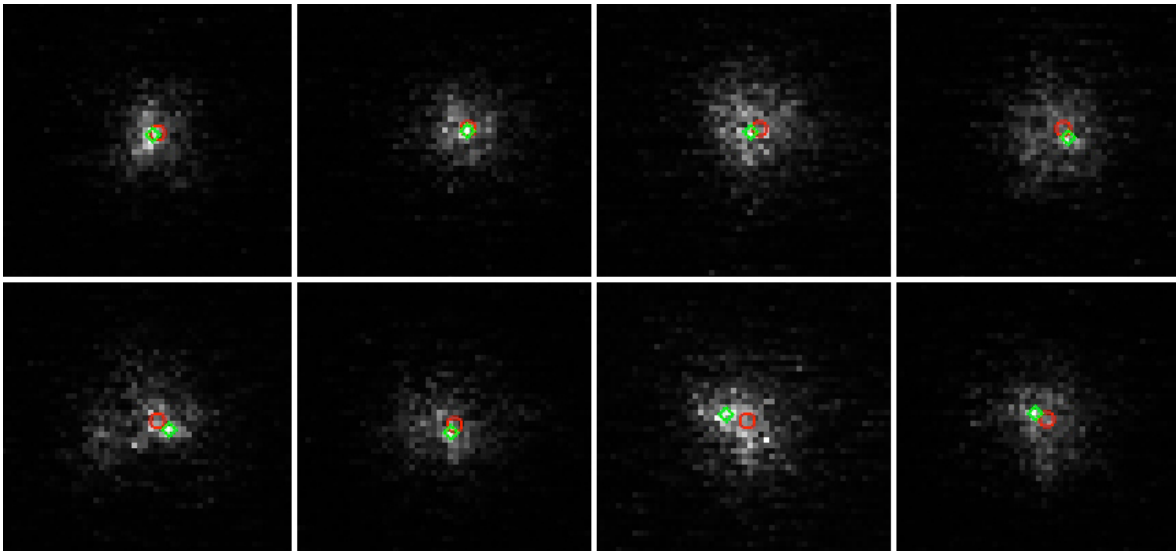


Figure 3.1: A comparison between the brightest speckle position (green diamonds) and the centroid position (red circles) for a variety of observed speckle patterns. The brightest speckle position is measured after resampling and correlation with a diffraction-limited PSF, as described in the text. The best PSFs show little difference between the two positions, but in the poorer frames the centroid position is corrupted by the faint asymmetrical halo, preventing the formation of a diffraction-limited width core in the final images.

portant and the measured peak position is actually just the position of the brightest L3CCD photon event in the star PSF (see chapter 5). The Lucky Imaging reduction system described below has the capability to add frames together to increase the SNR sufficiently to obtain the true position of the brightest speckle, at the cost of time resolution.

An alternate approach is to align using the PSF centroid position, which can be measured with high SNR on PSFs containing far fewer photons than the brightest-speckle method (which relies only on the 10-20% of the PSF photons within the diffraction-limited core).

Christou (1991) gives a comparison of the centroid-centering vs. brightest speckle centering approaches using simulated near-infrared 8m telescope data, and finds that the brightest speckle method has significantly better performance.

On LuckyCam data, the centroiding approach does indeed recover resolution in cases where the guide star is too faint for Lucky Imaging; its use is demonstrated with one of the VLM binaries in chapter 7, where the $I = \sim +12\text{m}$ target was observed through ~ 5 magnitudes of cloud cover. However, if the short exposure PSF is even slightly asymmetric (as most individual speckle patterns are; see the speckle patterns in chapter 1) the centroid position does not match that of the diffraction-limited core of the PSF (figure 3.1).

In that case, the final added image contains many separate diffraction-limited cores distributed over an area set by the differences between the centroid and peak positions. The distribution is often much larger than the diffraction-limited core size (figure 3.2). The (low-Strehl-ratio)

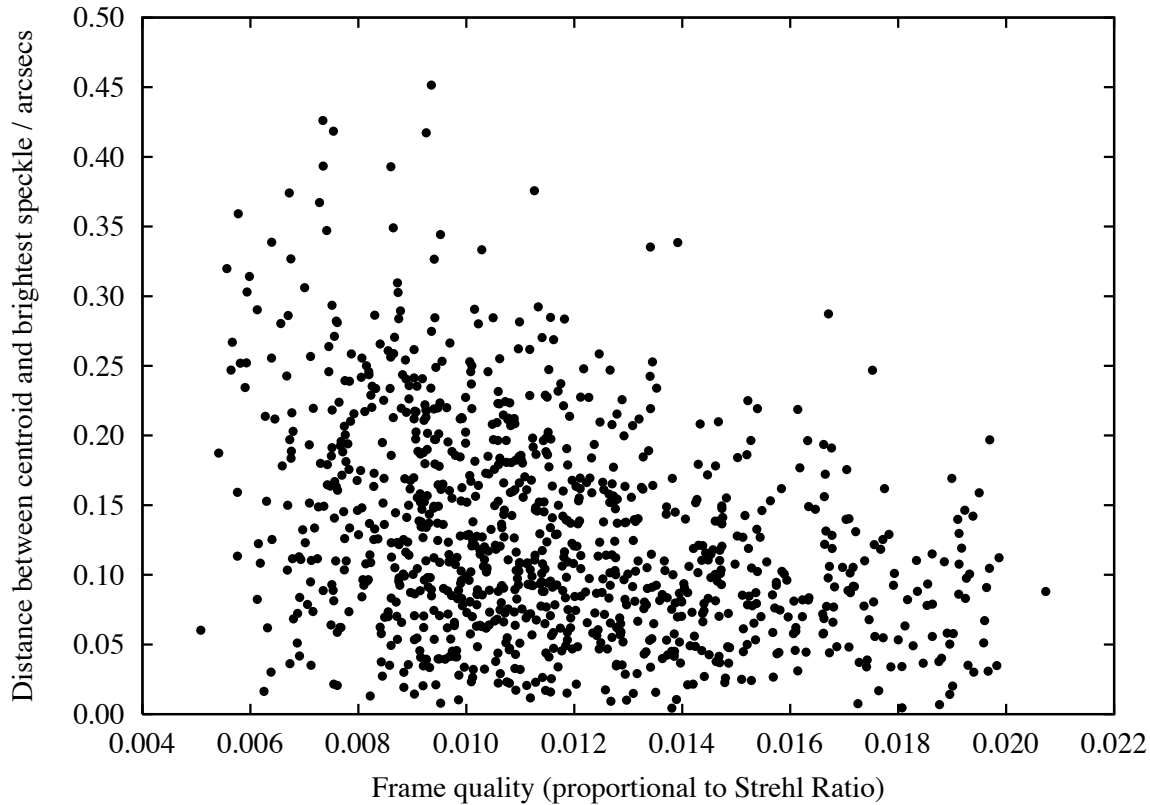


Figure 3.2: The distance between the PSF centroid and the brightest speckle, as a function of frame quality, measured from 1,000 frames of a single run (the same as that shown in figure 3.1). The star is sufficiently bright that even the poorest frames retain good SNR in the PSF core, so the differences in position determination are not the result of photon noise. At poorer frame qualities the average difference in position is 1-2× larger than the diffraction-limited core size of 0.09 arcsec FWHM.

diffraction limited core that would be recovered by the brightest-speckle method is therefore not present. For that reason, almost all LuckyCam reductions presented in this thesis are performed aligning on the brightest speckle.

3.2 Pipeline Implementation

The pipeline consists of a collection of C++ programs which are run sequentially on an observation run, and is implemented using the GCC V3.4 C++ compiler operating in Linux. I chose to implement the pipeline in C++ for two reasons:

Speed. Reduction of LuckyCam data requires high-speed data analysis. A typical observing run produces 1TB+ of data, which must be reduced in a timely fashion. In practise this involves processing the data at speeds comparable to its acquisition – i.e. megabytes per second. A relatively low-level language such as C++ gives the speed and flexibility required for this.

Flexibility and Code Reuse. C++ offers object-orientated features that significantly speed

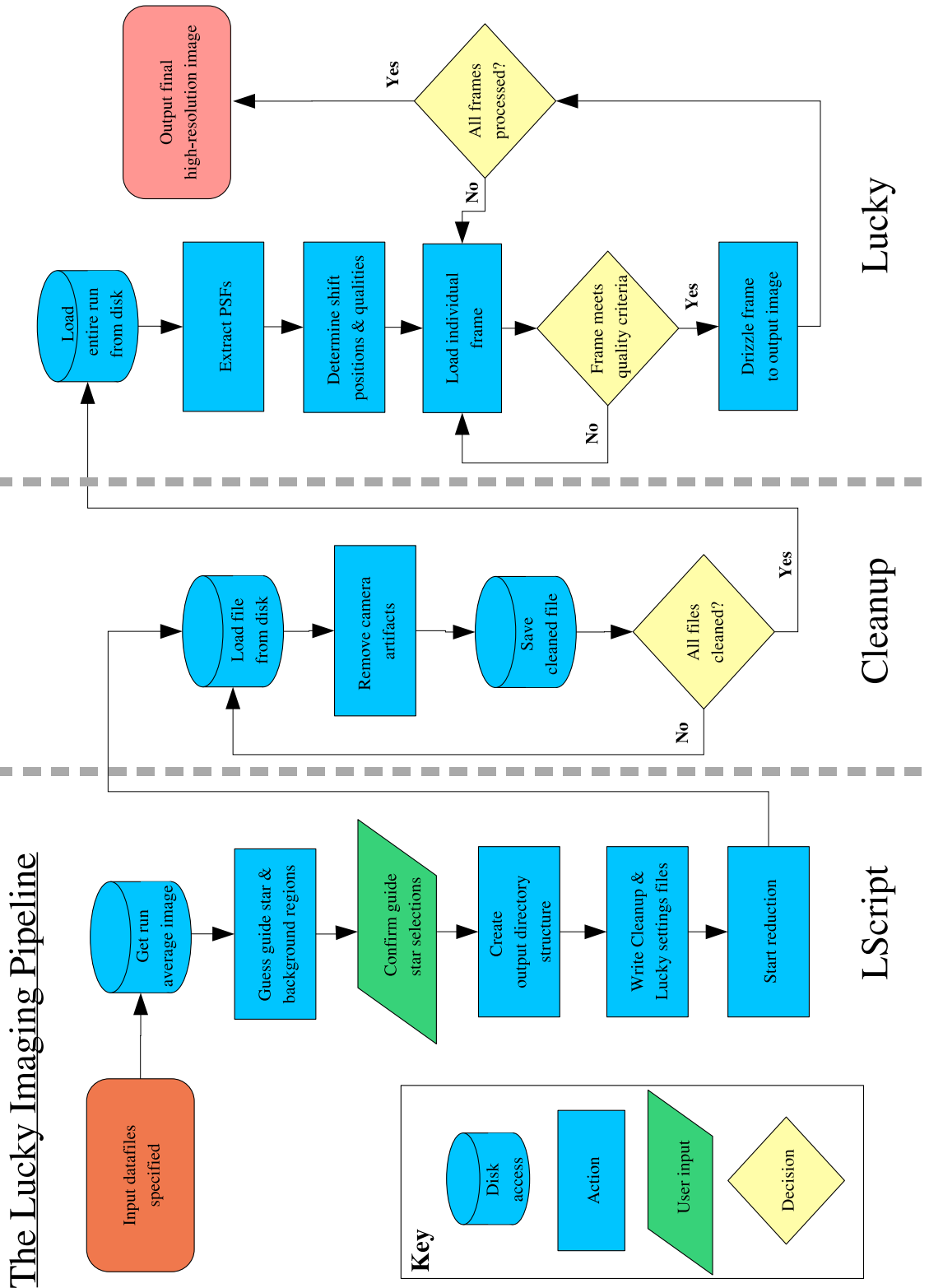


Figure 3.3: A simplified flowchart describing the LuckyCam pipeline. Only one user input is required, for confirmation of the guide star selections.

up the development process. For example, each program in the pipeline must load, save and manipulate images in a variety of formats. By implementing a C++ image class, I shared all the relevant code between the different pipeline programs. Although this could be performed in C (for example) by sharing source files, the encapsulation of all the relevant image data (memory storage, dimensions, etc.) and functions in a single object very significantly reduced the complexity of the final code.

As a second example of the use of objects, all stages of the processing within LUCKY, the final Lucky Imaging process portion of the pipeline, are implemented as classes and can thus be easily swapped for objects which offer the same interfaces. This allows very easy modification of the pipeline process, with the guarantee that (as long as the class interface specifications are followed) modifications to one part of the process will not affect the rest. In particular, the frame selection and alignment algorithms are implemented as a set of virtual classes, where *only* the interface is specified to other parts of the program. The initial processing and final image construction code can then remain completely agnostic as to the details of the frame selection processes, allowing very easy experimentation with different Lucky Imaging methods.

All the pipeline programs can be run manually, but are more usually scripted to run on a collection of observations by a pre-processing program, LSCRIPT. An overview of the pipeline reduction process is shown in figure 3.3. I discuss each component of the pipeline in detail below, in order of execution during processing.

3.3 LSCRIPT

LSCRIPT scripts the data processing sequence. In fully automatic mode it searches for LuckyCam runs on a data disk and picks suitable reference stars, background areas and bias generation areas automatically (figure 3.4). The program then creates a well-organised output directory structure including the relevant settings files for CLEANUP and LUCKY. Finally, a shell script is produced to schedule all the reductions, which the user can then run at their convenience.

3.4 CLEANUP & BIASGEN

Because the camera electronics must operate at very fast frame rates, some trade-offs between speed and image quality must be made. The CLEANUP section of the pipeline is responsible for removing artifacts introduced to the raw data by the camera electronics. In general the 2002-2004 camera suffered from greater artifact problems than the 2005 camera; the artifact removal systems are, however, applicable to both cameras.

CLEANUP detects and removes the following artifacts, listed here in rough order of importance.

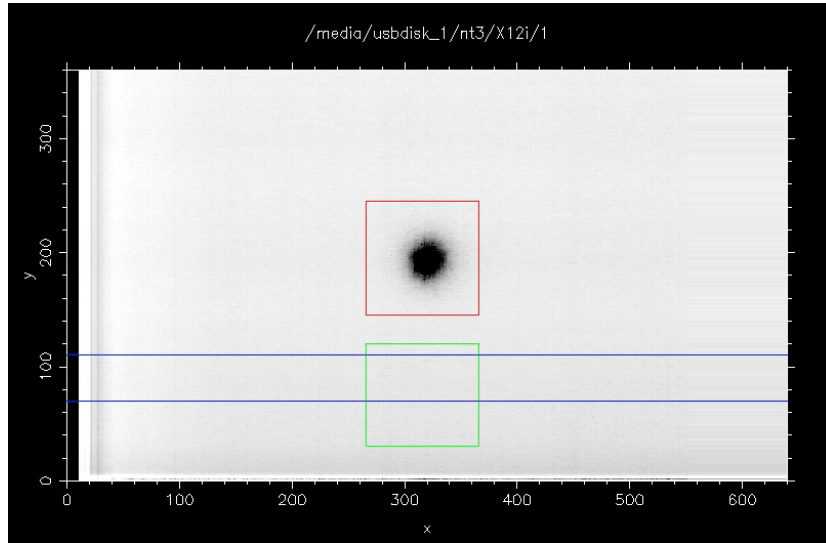
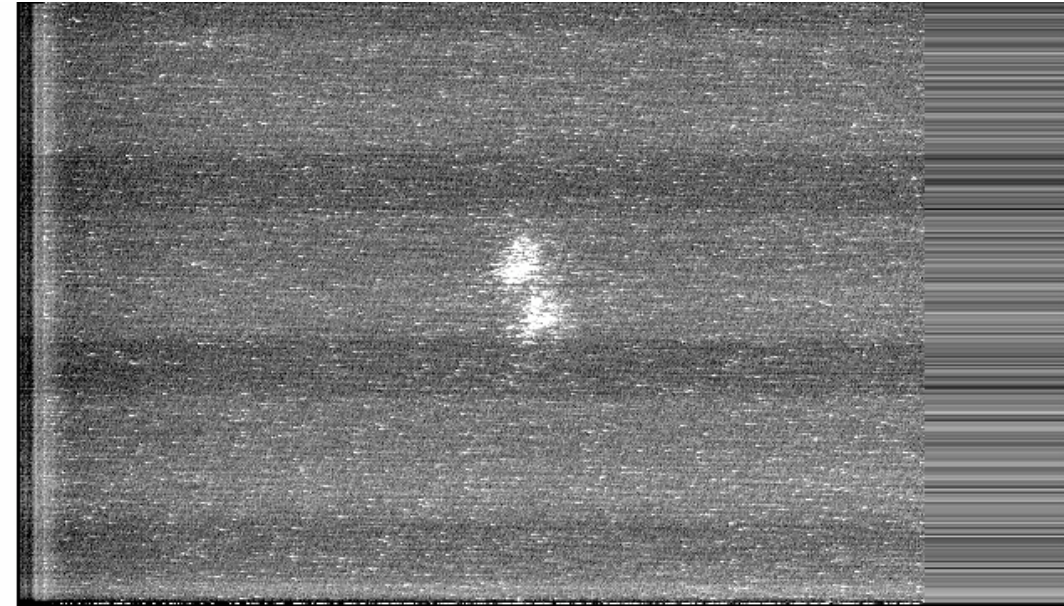


Figure 3.4: Automated selection of guide star (red), background region (green), and bias estimate region (blue). The selected regions for each run are presented to the user for verification and possible alteration.

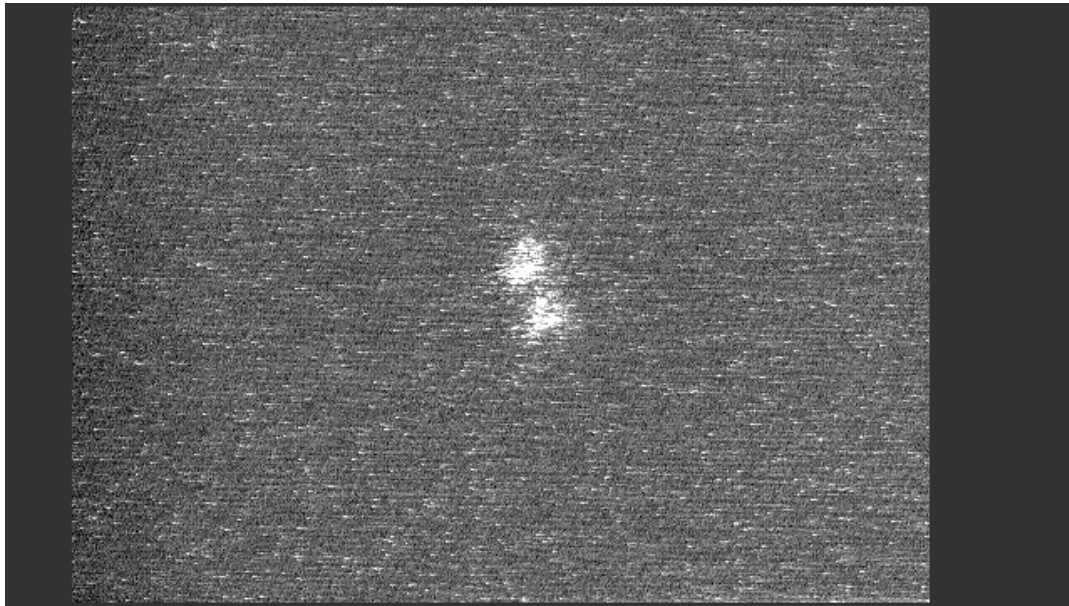
An example before-and-after comparison is shown in figure 3.5.

- **Row-to-row bias variations** The bias level of individual rows is defined by the camera electronics on the basis of the average level in the dark pixels on the left side of the row. A spurious event within that area leads to the bias level of the entire row being set incorrectly. Low frequency noise also affects the bias levels of groups of rows. I remove these problems by resetting the bias level of each row such that the lowest 5th percentile of all data values within that row is set to zero. Using the 5 per cent level rather than a simple average ensures that only pixels which do not contain photon events are used.
- **Horizontal Slope** The images often have a slowly-varying horizontal slope in bias level. I model and then subtract this slope with a cubic fit to the 5th percentile levels in each column.
- **Pattern noise** The 2002-2004 camera experienced high levels of pattern noise with a wavelength of 2 pixels. The phase of the pattern was very consistent within each row, and so the pattern noise was removed by simply clipping out the pattern noise's peak in the Fourier transform of the row. Bright objects within the row can lead to an overestimation of the noise because they contribution high-frequency signal. To avoid an incorrect noise subtraction, they are thus masked out during the pattern noise removal.

For each run, CLEANUP loops through the input frames written during data acquisition and stores cleaned frames onto a fast RAID-0 array in the data reduction computer. This second storage step allows subsequent reprocessing of the data without re-cleaning of the input frames and re-loading from the relatively slow USB external hard disk used for initial data storage. Since several later data reduction stages (determination of the run gain, for example) require



(a) Raw camera output



(b) Post-cleanup

Figure 3.5: A single LuckyCam frame from June 2005, of a binary star before and after CLEANUP processing. The speckles in the background are individual photons from the sky (and some spurious events).

reprocessing of the cleaned data this intermediate storage gives a very significant time saving over the course of the reduction process. CLEANUP by default writes compressed files, in the same format used by PixCel LC, saving significant storage space and increasing the (often hard-disk-limited) speed of the pipeline processing.

The 2005 camera introduced an extra effect, a different bias level for each column. The effect, at the 2-5DN/pixel/frame level, is too faint to be visible on individual images, but appears as strong vertical lines on summed images. Because the column bias levels can only be measured accurately on summed post-CLEANUP images, I introduced an additional step into the pipeline to measure and subtract them.

BIASGEN generates a bias image that contains the values of the vertical lines introduced by the camera hardware into the images. The user (or LSCRIPT) selects a set of rows which are relatively clear of stars. The average value in each column is then determined from a large (>1000) number of frames. The average is constructed from twice-iterated 1σ clipped values to remove any faint stars within the given areas. Because the lines have no vertical structure, the measured values can then be applied to the entire image.

The column bias estimates are subtracted from each frame in subsequent processing by LUCKY and other programs. Because the vertical line structure changes slowly, the bias estimates are regenerated every run or 10,000 frames, whichever is the shortest.

3.5 LUCKY

The LUCKY section of the pipeline performs the actual Lucky Imaging processing. Briefly, input files are calibrated, the quality of each frame is determined and the highest-quality frames are then aligned and added together into a set of high-resolution output images. The full processing performed by LUCKY is detailed in figure 3.6 and the major components described in detail below.

3.5.1 Setup

Reduction settings and the parameters of the input run are read in from a text file (for an example, see figure 3.7) written by the user or generated by LSCRIPT. The file gives details of the data (location and camera/telescope properties during acquisition), the regions to be used for the guide star and background and a large number of processing options.

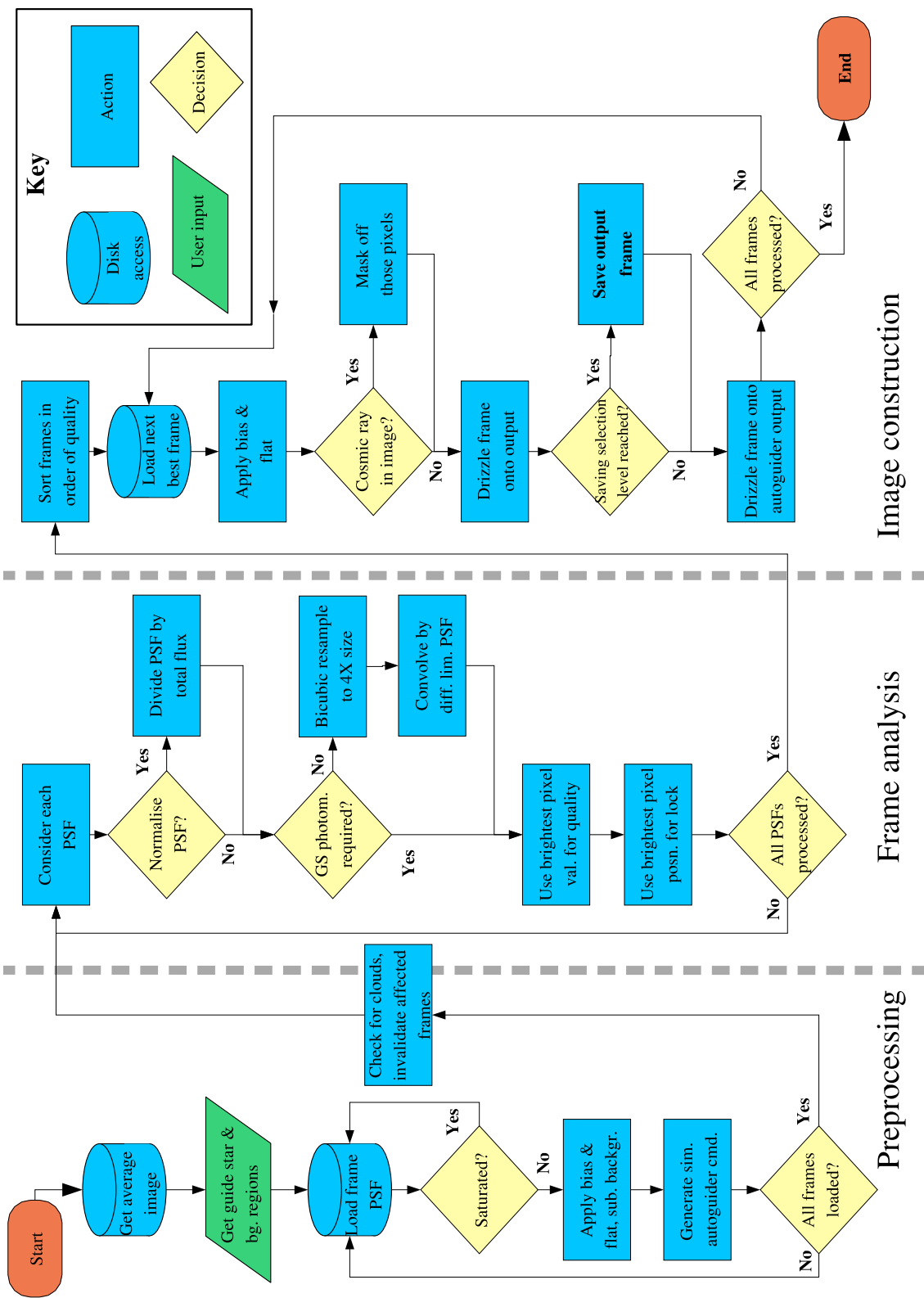


Figure 3.6: A flowchart of LUCKY processing. The major processing options are represented, including the options necessary to allow accurate photometry of the guide star (GS photom reqd., see chapter 5). Alternate frame selection strategies, such as signal-to-noise tracking Lucky, are not included and are inserted in place of the standard ‘‘Frame Analysis’’ section shown here.

```

# Input file for Lucky
# Version: 5.2
# -----
# Program mode : normal

# Input files
0      /data/nml27/images/run05/nt3/x9i/1/run3027_rn_.lcc    0-2999

Strehls
# run ID   Region num   Coords
0       1      (267,160),(367,260)

Background
# run ID   Coords
0       (267,35),(367,135)

# Processing options
Metric (strehls, snt) : strehls
Use resample in initial metric (yes/no) : yes
Use autocorrelation in initial metric : yes
Frame shift centre (pixel, centroid) : pixel
Generate simulated autoguided image : yes
Bias file (filename/none) : bias.fits
Flat (filename/none) : flat_i.fits
Normalise psfs : no
Cloud protection (aggressive) : no
Detriple : no
Interactive bground & ref star selection : no

# Output options
Output selection type : percent
Percent of images to select : 1.0 (1p.fits), 2.0 (2p.fits),
                             2.5 (2_5p.fits), 5.0 (5p.fits), 10.0 (10p.fits), 20.0 (20p.fits), 30.0 (30p.fits),
                             40.0 (40p.fits), 50.0 (50p.fits), 75.0 (75p.fits), 100.0 (100p.fits)
Position to shift to (input file scale) : default
Display results in program : yes
Output PSF summary image : psfs.fits
Pgplot device (? to ask on run) : /NULL

# Drizzle settings
Drizzle pixfrac (0..1) : 0.45
Drizzle scale factor (>= 1) : 2.0

#Telescope parameters
m" / pixel : 40.0
Typical wavelength (m) : 785.0e-09
Telescope diameter (m) : 2.56

# PSF summary image
PSFs to include : 40
Columns : 4
PSF size (pixels diameter around center) : 100

# Autoguider parameters
Autoguider output image file : autog.fits

# Saturation parameters
Saturation threshold : 10000.0
Ignore saturated frames : no

```

Figure 3.7: An example LUCKY settings file. This file will produce a range of output images with between 1% and 100% of frames selected, as well as simulating the output of a standard telescope autoguider system. The parameters are the defaults used to reduce most LuckyCam data.

3.5.2 Initial processing

Reduced images are prepared in two steps, first the determination of the quality of the frames and then the construction of the high-resolution images. The two step process is required to derive the relative quality statistics for different sections of the individual runs, before the final image reconstruction. A realtime lucky Imaging system does not have this luxury, and must decide on the quality of a frame solely on the basis of past frames. For an example of this style of processing, see chapter 2.

To save memory for the first reduction stage only the PSF of the guide star is extracted from each frame, after the frames have been debiased and flat-fielded. Each PSF is checked for saturation and calibrated to a zero background level by subtracting the average flux in the selected background regions, before the set of PSFs is passed to the next stage:

3.5.3 Frame quality and shift-lock determination

There are two standard versions of Lucky Imaging currently implemented within the LUCKY framework. The standard Lucky Imaging system (labelled “Strehls” in LUCKY), in its simplest form, selects frames on the basis of the amount of light within the brightest pixel of its input image (equivalent to selecting on the brightest speckle), and aligns the image shift onto that pixel. Frames with the greatest concentration of light have the highest quality; this selection corresponds to selecting the frames with the best Strehl ratio.

Two main options are available to increase the quality of the processing, both of which are enabled in almost all circumstances (except when accurate photometry of the guide star is required; see chapter 5).

1. **Resampling.** The PSF images are bicubically interpolated to 4 \times the original size, allowing sub-pixel determination of the best shift position from the brightest pixel in the resultant resampled image. This sub-pixel value is then used by the image reconstruction system.
2. **Convolution / Correlation.** After resampling, the PSFs are convolved with a diffraction-limited PSF matched to the observation’s telescope size, pixel scale and effective wavelength. The brightest pixel in the image then corresponds to the position that best matches a diffraction-limited PSF, and its value gives the degree of correlation. This procedure effectively blurs the images down to the maximum resolution of the telescope, increasing the signal-to-noise in each pixel without losing real spatial information, and thus improves the quality of image reconstruction for fainter guide stars.

The second Lucky Imaging technique implemented in LUCKY is Signal-to-Noise Tracking Lucky (SNT Lucky). This proceeds in exactly the same way as the standard method described above,

except that the signal-to-noise of the frame quality and shift position determination is tracked. If the guide star flux is too low for an accurate determination of those quantities, adjacent frames are added together until the signal-to-noise becomes sufficient; effectively, the frame rate is adjusted according to the prevailing seeing conditions.

This is particularly important for the faintest guide stars. There is a very sharp drop-off in the accuracy of frame shift-position determination when the number of photons in the PSF core drops to less than 1 photon per pixel. In that regime, the frame selection system is likely to lock onto the more numerous random photons in the star halo rather than those in the core. Although the SNT Lucky reduction of the effective frame rate does reduce the quality of the Lucky Imaging, very faint guide stars benefit greatly from increasing the amount of light within the core of the star to several photons per pixel. For this reason, SNT Lucky is the default approach for the reduction of images with faint guide stars.

Variable cloud cover can also cause the light in the brightest pixel to change, possibly corrupting the frame selection process. I describe methods to minimise this problem in section 3.5.5.

3.5.4 Final high-resolution image reconstruction

The above processing produces a list of frame qualities and shift positions. As a final step, the frames are sorted according to quality, then shifted and co-added using the Drizzle algorithm (figure 3.8), starting with the best quality frame. The addition continues until a user-specified selection level (such as the best 5% of frames) is reached, upon which an output image is written (unless there remain more inclusive selection levels to be made).

If the images were simply interpolated by the non-integer pixel shifts and added, each input pixel would be reduced in resolution. To see this, consider a frame to be shifted by 1/2 of a pixel horizontally and vertically. Each pixel of the image is then spread equally over 4 pixels of the output image – thus reducing the output resolution (top panels of figure 3.9). However, more complicated algorithms can avoid much of this resolution loss, essentially by reducing the size of the input pixel relative to those of the output image.

Earlier Lucky Imaging software Tubbs et al. (2002, 2003) used filtered sinc-resampling to increase the image resolution before image shifting. This worked well for the technical trials in which it was used, but introduces ringing in the output data and an unphysical “texture” in the background. I compare the output of this algorithm to several others in figure 3.9.

For all images presented in this thesis I elected to co-add the images using a custom implementation of the DRIZZLE algorithm (Fruchter & Hook, 2002), which offers the resolution achieved by the sinc-resampling methods without any associated ringing.

Drizzle proceeds by “drizzling” the input pixels onto a larger grid, generally 2 \times the size of the

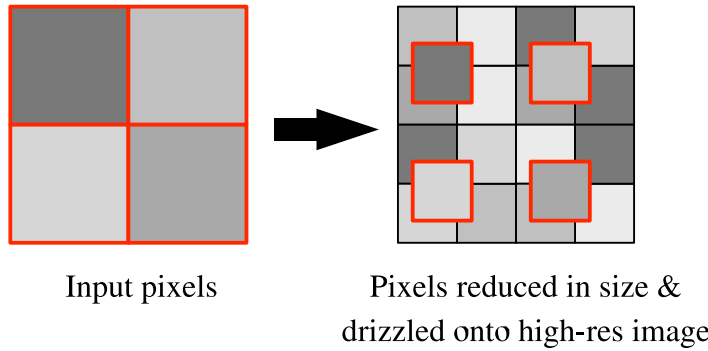


Figure 3.8: The Drizzle process. Input pixels are reduced in size, then interpolated onto a higher-resolution output grid.

input pixel grid (figure 3.8). This process can also be represented by making each input pixel decrease in size (but not separation) by a factor of two before addition. At each stage of the addition both the output image and a weight map for each pixel is updated.

Each input pixel is dropped onto an area of the output grid that usually overlaps several pixels. If the fractional area of overlap with a single output pixel is represented by F the signal $S(x, y)$ and weights $W(x, y)$ of that pixel are updated to be:

$$W(x, y) = F * W_P(x, y) + W'(x, y) \quad (3.1)$$

$$S(x, y) = \frac{F * W_P(x, y) * S_{input} + S'(x, y) * W'(x, y)}{W(x, y)} \quad (3.2)$$

where S' and W' denote the current signals and weights, S_{input} is the signal from the input pixel, and $W_P(x, y)$ are individual pixel weights for the current frame that can be used to remove (for example) cosmic ray affected areas.

This operation corresponds to making a weighted average of the input pixel values in each output pixel. After each frame addition $S(x, y)$ contains an estimate of the final high-resolution image, which is used directly as the LUCKY output image.

3.5.5 Further processing

Full data reduction of a run with LUCKY often involves several further processing steps to improve and/or calibrate the quality of the final output. The most important options are detailed in the following sections.

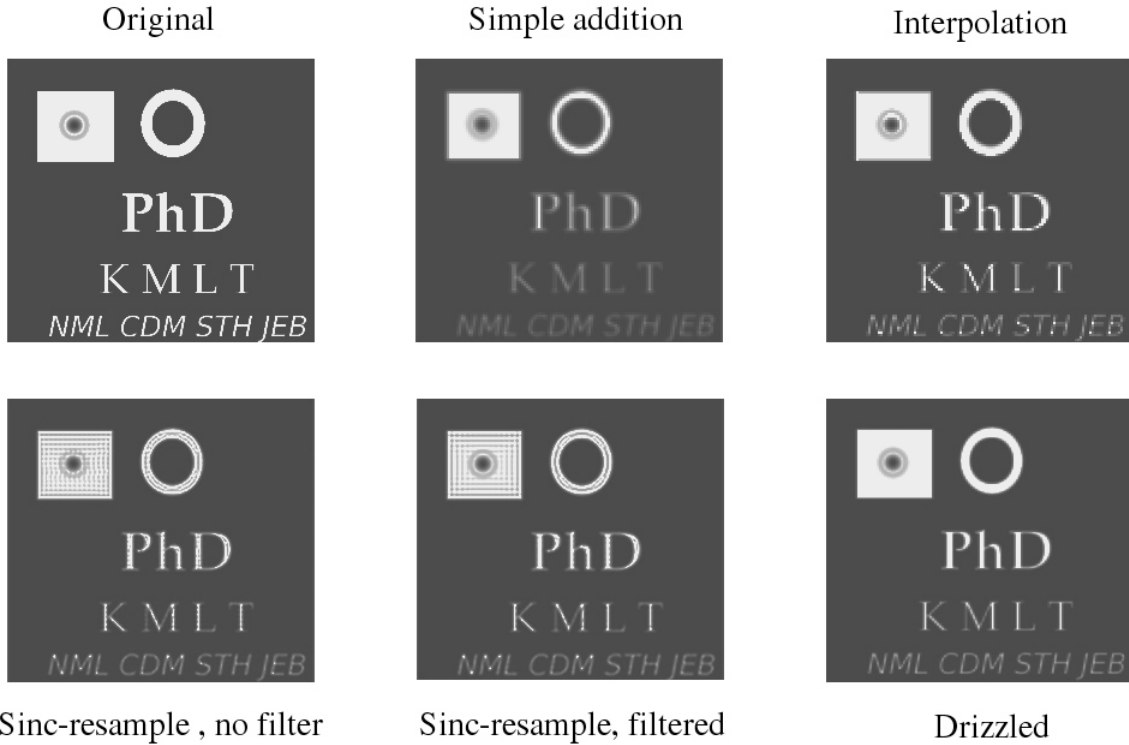


Figure 3.9: A comparison of several high-resolution image reconstruction methods which have applicability to Lucky Imaging. The images are shown on a log scale to enhance the visibility of the reconstruction errors, but all have the same greyscale. For these tests, the original image (top left, constructed to include detail on several scales as well as a diffraction-limited PSF) is undersampled by a factor of four, and placed in 30 different sub-pixel shift positions. Simple addition of the undersampled images (top middle) leads to a large resolution loss compared to the original image. Interpolation of images during addition taking into account sub-pixel shifts (top right) improves this somewhat, but resolution loss is still evident. The sinc-resampling and filtering methods described by Tubbs et al. (2002, 2003) have much improved resolution compared to the first two methods. However, both suffer from ringing (although reduced in the filtered version), which particularly affects the image of the diffraction-limited PSF, as well as altering the shapes of the text in varying ways. Drizzle (bottom right) attains the resolution of the sinc-resampling methods without any associated ringing, and offers excellent performance for Lucky Imaging.

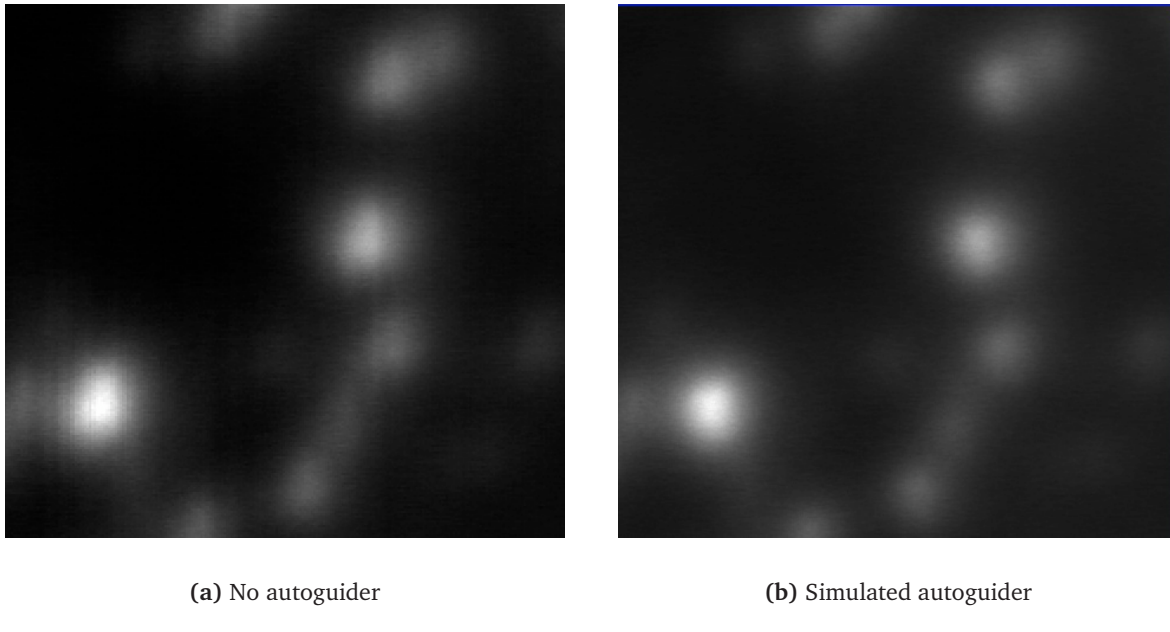


Figure 3.10: The effect of the simulated autoguider. The seeing here is ~ 1.0 arcsec FWHM, and the images have a vertical dimension of 9 arcsec. The left panel shows a simple sum of the recorded frames (targeted on a section of the core of the globular cluster M3), with the NOT autoguider turned off. The right panel shows the same data with much reduced image elongation after processing with a simulated NOT autoguider.

Autoguider simulation

In parallel with the Lucky Imaging reconstruction, the user can also elect to simulate a standard telescope autoguider system. Telescope autoguiders are designed to remove the telescope motion produced by incorrect tracking and other long-timescale (longer than 1 sec) effects. LuckyCam samples images at a high enough rate to allow full simulations of the commands an image motions that would be produced by an autoguider guiding on a bright star within the LuckyCam FOV.

During LuckyCam observations at the NOT the autoguider system is disabled (to avoid introducing extra image motion) so a simple addition of frames in a run usually produces very elongated images that do not give a true estimate of the natural seeing. A direct simulation of a standard autoguided telescope imaging system from the LuckyCam data allows a simultaneous comparison of LuckyCam performance with that of the standard imaging system. The often very rapidly changing seeing conditions necessitate a simultaneous comparison of LuckyCam with other imaging systems, to ensure the same level of turbulence is being measured for each system (see chapter 4).

LUCKY simulates the Nordic Optical Telescope autoguider system. The system samples at 12.5 frames per second, and can thus be adequately simulated by LuckyCam at all frame rates (in all observing runs, LuckyCam has run at a minimum of 12 frames per second). The autoguider

tracks the centroid motion of a bright star, starts to send correction commands when the star's offset from the current position is > 0.1 arcsec, and corrects at a maximum rate of 0.2 arcsec per sec. The commands from the autoguider system are smoothed by a low-pass filter with a 1-sec time constant (Graham Cox, private communication).

For simulation of the autoguider system in LUCKY, the PSF centroids are tracked during initial processing, and the simulation of the autoguider is performed as the final part of the initial processing. An additional output image is then constructed by Drizzle, using the simulated autoguider image shift commands instead of the Lucky-derived shift positions.

The seeing values derived from FWHM measurements of the simulated image match those derived simultaneously from on-site RoboDIMM (O'Mahony, 2003) measurements. However, a real telescope does not respond instantly to the autoguider commands, and may not be capable of tracking at 100 milli-arcsec resolution. The simulated system thus corresponds to an idealised autoguider.

Cosmic ray removal

Cosmic rays appear on LuckyCam images as isolated “splashes” of saturated pixels 3-5 pixels high and 4-7 pixels long. These are important to remove from (or at least detect in) LuckyCam images, because if a cosmic ray falls inside a guide star box it could be mistaken for a very high quality frame. The frame would then be shifted in the output image such that the cosmic ray appears at the nominal guide star position while the guide star itself appears somewhere nearby – where it could, for example, be mistaken for a faint companion star.

LUCKY detects cosmic rays by searching for very high-valued pixels in each frame. If a cosmic ray falls within a guide star box, the frame is not used for imaging. Otherwise, the drizzle weights of the cosmic ray pixels are set to zero, along with the surrounding eight pixels to eliminate the effects of charge leakage from the saturated pixel. Cosmic-ray removal can be very vigorous with LuckyCam data, because each output pixel is the weighted sum of at least tens of input frames, and cosmic rays are only likely to affect one to two of those frames.

Cloud protection

The standard Lucky Imaging methods described above assume no clouds are present. Clouds cause the total flux from the guide star to vary rapidly and unpredictably (figure 3.11). The naïve quality-from-brightest-pixel approach is then vulnerable to selecting frames with the highest transmission rather than the highest quality. I implemented two sequential cloud detection and protection measures, to be enabled when reducing suspected cloud-affected data.

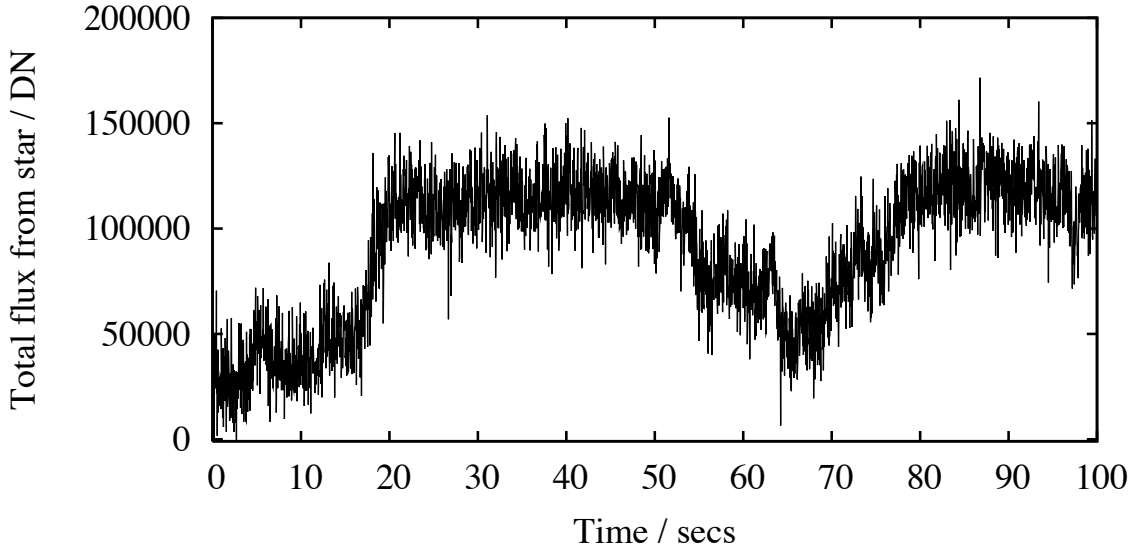


Figure 3.11: An example of rapid variations in cloud transmission, measured at 30 frames per second in the November 2005 LuckyCam run. The flux is measured in a 4 arcsec box centred on the star's average position. No drift in the apparent stellar position was observed, so all variations shown here are due to changing cloud transmission. The apparent flux from the star varies by more than a factor of five over periods of less than 20 seconds; there are also variations on much shorter timescales.

1. Each PSF is divided by its total flux, for a normalised estimate of the frame quality. This works well for thin clouds, but thicker clouds can occasionally reduce the flux from the star sufficiently to leave only a few single photon events. Under this scheme they appear to have superb light concentration, with most of the flux from the star concentrated into a single pixel, which can lead to preferential selection of the worst frames.
2. If the cloud transmission is very variable and drops to very low values, for the above reason the frames with the thickest clouds must be dropped. The total flux in each PSF is tracked, and if frame dropping is enabled those frames with less than half the maximum total flux are removed from the selection process. The remaining frame qualities are then normalised as point 1 above.

Although some frames may have to be dropped, these methods allowed full performance Lucky Imaging even under the very cloudy conditions of the November 2005 LuckyCam run, where most observations were performed through at least three magnitudes of (rapidly varying) cloud cover.

Binary de-tripling

In standard LUCKY processing guide stars are selected in boxes based on the initial seeing-limited summed data. These boxes must be sufficiently large to include all apparent image motion of the guide star. For this reason, close companions to the guide star (unresolved by

seeing-limited instruments) may also fall within the guide star region. If the close companion is of roughly equal brightness to the guide star, photon statistics will cause the “brightest speckle” to randomly shift between the two stars. In some frames that are added to the high-resolution output image, the companion will thus appear in the position of the actual guide star, and the guide star will appear as a second companion displaced in the opposite direction to the true companion (figure 3.12, left panel).

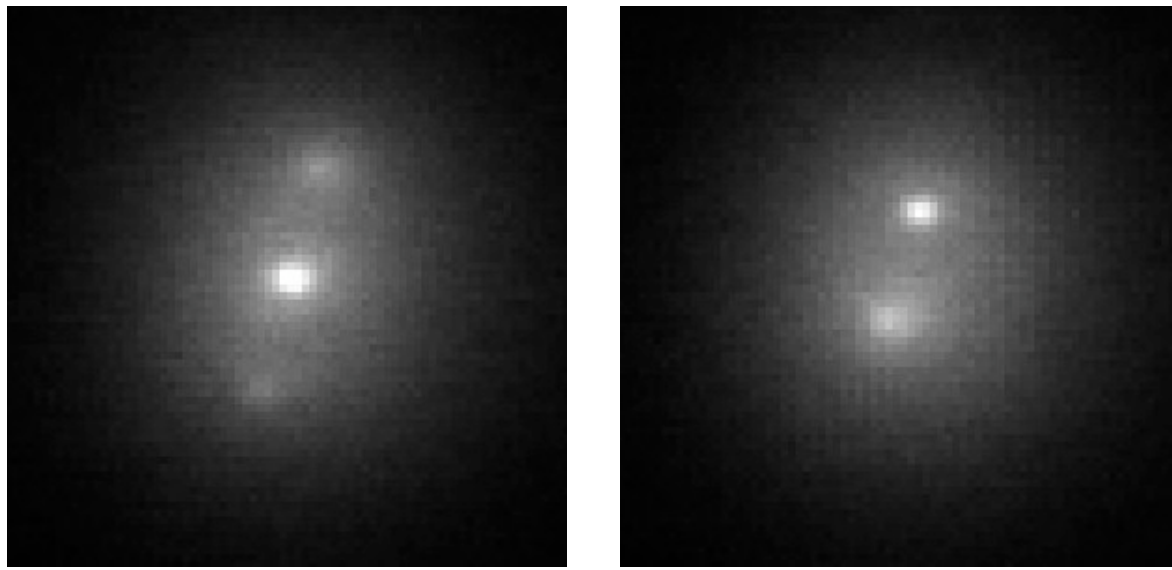
The binary system will thus appear to be a very improbable-looking triple star system arranged into an exact line. This case is easy to detect by eye, and resolved photometry for the guide star and companion can be calculated from the resolved flux from the three apparent stars (see chapter 5). However, this effect must be removed to produce convincing images of these binary systems.

The LUCKY de-triple option adds an extra stage to the guide star selection for use on guide stars with close companions. After an initial coarse (standard) guide star box has been drawn, a new intermediate-resolution image is made by aligning the brightest pixel of the guide star PSF in each frame. This produces an image that allows separation of the binary system’s components, which is presented to the user. The guide star box is then drawn around one of the components, and all frame selection and alignment proceeds in that box, which is moved relative to each frame’s initial shift position. Image motion is thus removed during the frame selection process, and only light from the selected component is used for the guide star.

Example results of this procedure are shown in figure 3.12. The algorithm works well for binary separations down to 0.2 arcsecs. Below this value, the diffraction-limited cores of the binary components merge, and further processing is required to confirm the binary system (see the speckle imaging sections of chapter 5).

3.6 Summary

- The standard Lucky Imaging process is: 1/ Determine the quality of frames on the basis of Strehl Ratio; 2/ Align frames on the position which best correlates with a diffraction-limited PSF; 3/ Select the best frames, then align and sum them using the Drizzle algorithm.
- Other Lucky Imaging algorithms are possible; the above algorithm gives very good performance in most situations but some more specialised methods are of use in particular cases.
- I have implemented a Lucky Imaging data reduction pipeline, to automatically reduce entire nights of frame data to sets of high-resolution Lucky images.
- The pipeline automatically picks guide stars, cleans the input frames of camera artifacts,



(a) Standard Lucky Imaging

(b) De-tripling enabled

Figure 3.12: Detripling the 0.33 arcsec binary LSPM J0503+2122. The left image shows the result of standard Lucky Imaging with a guide star box including both stars (the binary is unresolved in a seeing limited image). The right side shows the result of guiding on the upper component, with a small guide star box that moves with the brightest pixel in the PSF.

and processes them for Lucky Imaging.

- The Lucky Imaging section of the pipeline, as well as implementing the above methods, has many options to improve the quality of the output image under a variety of conditions.

4

Lucky Imaging Performance

In this chapter I evaluate the performance of Lucky Imaging systems in a wide variety of conditions. The evaluations are based upon 10 nights of data taken during LuckyCam runs in 2000–2004; I participated in the June 2004 observing run (as well as the two 2005 LuckyCam runs).

The performance tests detailed here demonstrate that the prototype Lucky Imaging cameras give a very valuable increase in I-band resolution over a large area, with only modest signal loss due to frame selection. In section 4.1 I describe the point spread function improvements produced by Lucky Imaging and in section 4.2 I detail the performance produced in a variety of conditions. Section 4.3 addresses the effect on limiting magnitudes of the Lucky Imaging frame selection. Finally, section 4.4 discusses the guide star and hardware requirements.

In most observations presented here the camera is run approximately 2–3× too slowly to fully sample changes in the atmospheric turbulence and so these results cannot demonstrate properly the full potential of Lucky Imaging. Later chapters present data from the 2005–2006 Lucky Imaging system, which runs approximately 2× faster, and so more routinely achieves diffraction limited resolution. However, even with slow camera used for the results the resolution gains are spectacular.

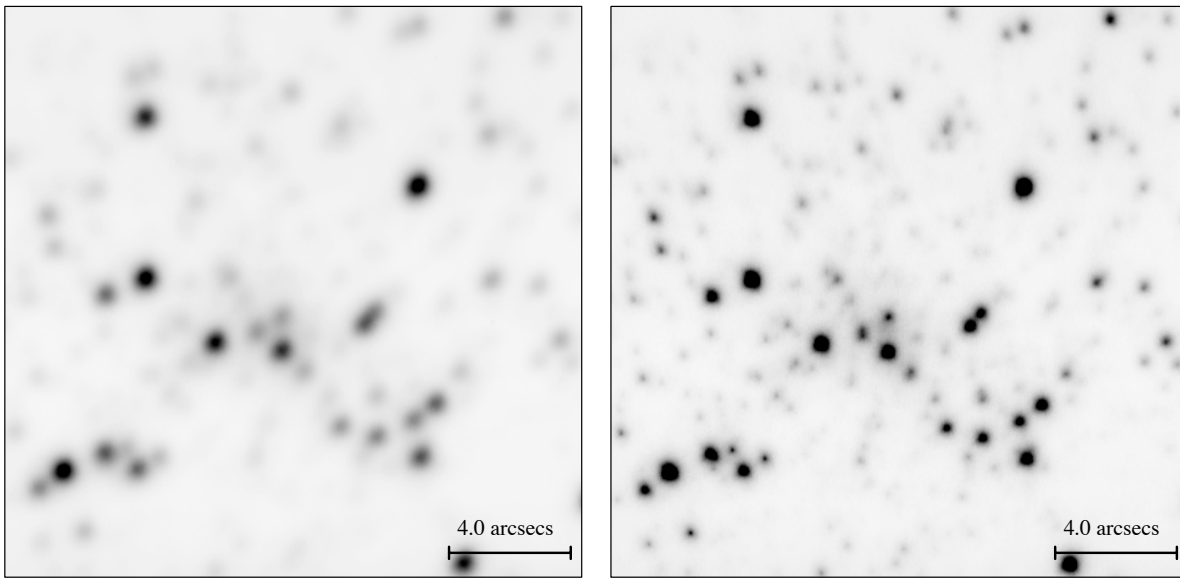


Figure 4.1: Lucky Imaging of the core of M15. The left panel is the output from an autoguider system (FWHM 0.63''); the right shows the 10% frame selection Lucky output from the same exposures (FWHM 0.26''). Both images are on the same grayscale. The increased resolution makes more faint objects visible in the Lucky image.

4.1 The PSFs produced by Lucky Imaging

Figure 4.1 gives a typical example of the wide field PSF improvements obtained with Lucky Imaging, and examples of the general form of the Lucky Imaging PSF are given in fig. 4.2.

As with adaptive optics images, the radial shape takes the expected form for an image with partially compensated Kolmogorov turbulence (e.g.. Hardy (1998) and references therein) - a wide halo and a central compact core. As the selection of frames is made more stringent the fraction of light in the compact central core progressively increases.

The Strehl ratio (commonly used as a high-resolution imaging performance measurement) is the peak value of a PSF divided by the theoretical diffraction-limited value. Figure 4.2 clearly shows that Lucky imaging offers a substantial Strehl ratio improvement over both autoguider and shift-and-add (effectively 100% selection) systems. Lucky Imaging routinely obtains I-band Strehl ratios in the range of 0.15-0.2 at high frame rates in good seeing on the 2.5m NOT.

It should be noted that the NOT is not designed to obtain diffraction limited images, with a specification to concentrate 80% of the light within 0.4 arcseconds*. Compared to a diffraction limit which concentrates approximately 80% of the light within 0.08 arcsecs, it is very likely that the performance of Lucky Imaging is limited by the telescope. Although on some occasions phase errors in the atmosphere can correct for telescope phase errors, this happens

*<http://www.not.iac.es/telescope/>

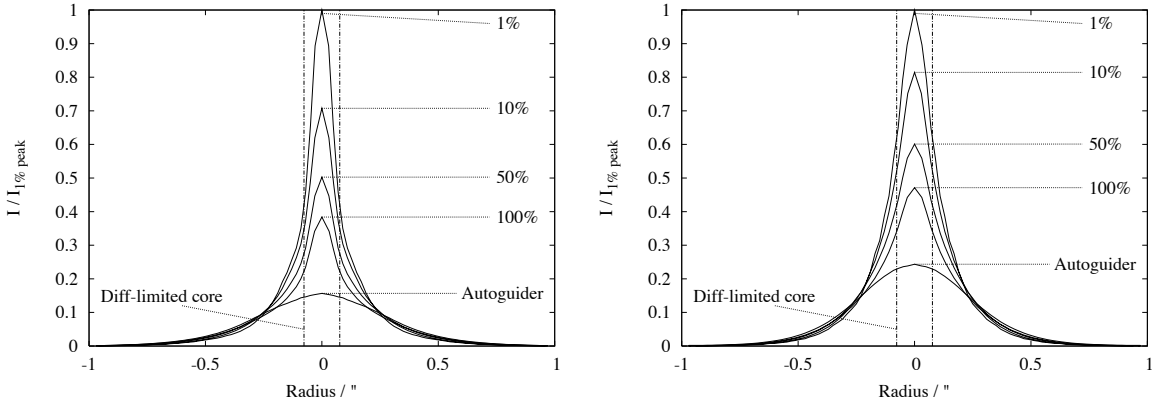


Figure 4.2: Average radial Lucky Imaging profiles. Data for the left figure was taken at 30Hz in 0.6" seeing; the right figure shows the results of 12Hz imaging in 0.55" seeing. 100% selection is simple shift-and-add. When selecting 1% of frames the Strehl ratio is more than doubled relative to the 100% selection, while the light from the star is concentrated into an area approximately four times smaller.

with reduced probability compared to a simple flat wavefront requirement. This subject has been treated in detail in Tubbs (2004); I here simply note that Lucky Imaging systems benefit from as high a telescope image quality as possible. Tests on the NTT telescope in Chile in June 2006, with a different telescope quality, are expected to quantify the effect of the telescope error budget.

It is difficult to directly compare the Lucky Imaging performance to the standard imaging system on the NOT (which uses an autoguider), since it is not possible to take images simultaneously with the two systems. For all seeing values given in this chapter I apply a detailed simulation of the NOT autoguider (both the image analysis and the pointing system) to the LuckyCam data, effectively allowing a simultaneous test of the two systems. The simulation system is described in chapter 3.

The quoted seeings are measured from the FWHM of elliptical 2D Moffat profile fits to simulated autoguider images. They are thus measured at an effective wavelength of $\sim 850\text{nm}$ and should be increased by approximately 10% to convert to a standard seeing quoted at 550nm. All other FWHMs detailed in this chapter are similarly measured from elliptical 2D Moffat profile fits.

The 1-D Moffat profile (eg. Trujillo et al. (2001) and references therein) is described by:

$$F(r) \propto \left(1 + \frac{r^2}{r_s^2}\right)^{-\beta} \quad (4.1)$$

where r is the radius from the peak, r_s is a scale radius and β can be varied between 1 and ∞ .

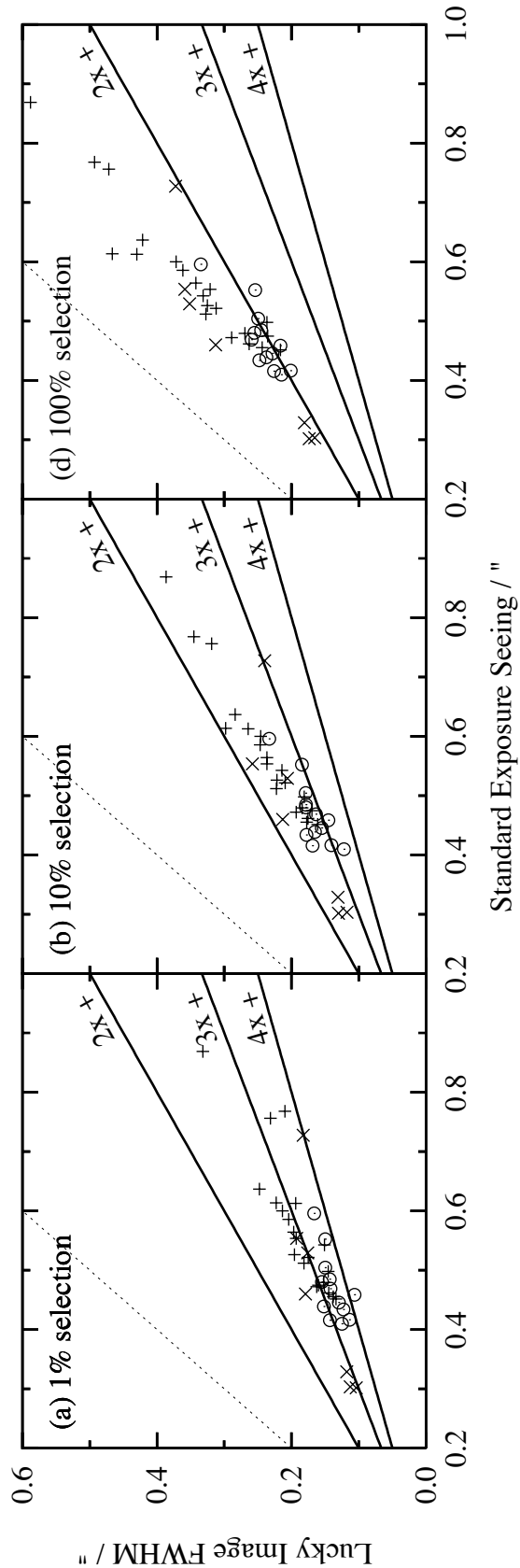


Figure 4.3: FWHM of target stars 1-3 arcsec from the reference star. Lines correspond to resolution increase factors of 1 \times , 2 \times , 3 \times & 4 \times . Most of the scatter in the FWHMs is caused by the range of target star to guide star distances. Vertical crosses are runs taken at 12Hz in 2003 & 2004; diagonal crosses are runs taken at 18Hz in 2001 & 2002 and circles are runs taken at 36Hz in 2003.

4.2 Lucky Imaging Performance

The presented results are based on observations taken during 10 nights on five observing runs in May, June & July, 2000–2004. The 2.56m Nordic Optical Telescope on La Palma in the Canary Islands was used for all observations, which were principally made in several different fields in the cores of the Globular Clusters M3, M13 and M15. The 2001-2004 dataset is split into 42 short (2-3 minute) runs, totalling ~132,000 frames. All fields were observed in I-band.

I here investigate science-target performance - i.e. that for a star near the guide star. In each of the fields I chose a target star for PSF measurement at 1-3" separation from the guide star. The particular difficulties associated with using the guide star PSF are discussed in chapter 5.

4.2.1 On-axis resolution improvement

The improvement in FWHM obtainable in different atmospheric conditions and with different percentage selections is shown in fig. 4.3. Much of the scatter in values is due to the range of distances of target stars from the reference star (section 4.2.2).

Figure 4.3 shows that under a wide range of conditions the resolution is improved by factors as large as $\times 4$ in the most stringent selections in all of the 42 observations reduced. Less stringent selections give smaller improvements. There is an approximately linear correspondence between the autoguided long exposure seeing and the resolution attainable. This suggests that, at least over the ~200 second timescale of these observations, the standard measures of seeing are a reasonable guide to the atmospheric turbulence statistics. I thus adopt the seeing as the standard measure of the atmospheric turbulence strength in a particular run.

Figure 4.4 shows the effects of selecting differing fractions of images using empirical fits to the 12FPS data. Although limited by the slow frame rate, in 0.5 arcsec seeing the most stringently selected images are within ~0.06 arcsec of the 0.08 arcsec diffraction limit and Strehl ratios are >0.1 .

The advantages of the full-frame field of view led the Lucky Imaging team to obtain most of our data in LuckyCam's relatively slow 12 or 18 FPS modes. To obtain images with light reliably concentrated into bright single speckles, unblurred by image motion, the atmospheric coherence time must be oversampled. This would typically require > 40 FPS at the NOT. However, the image quality varies on every timescale slower than the coherence time and so image selection can always be expected to improve the resolution – even if very slow frame rates are used.

To acquire a high-quality frame there is a requirement for both an excellent point spread function and a stable atmosphere for longer than the frame integration time; this occurs with increasing probability as the frame rate is increased. As expected, the faster frame rates pre-

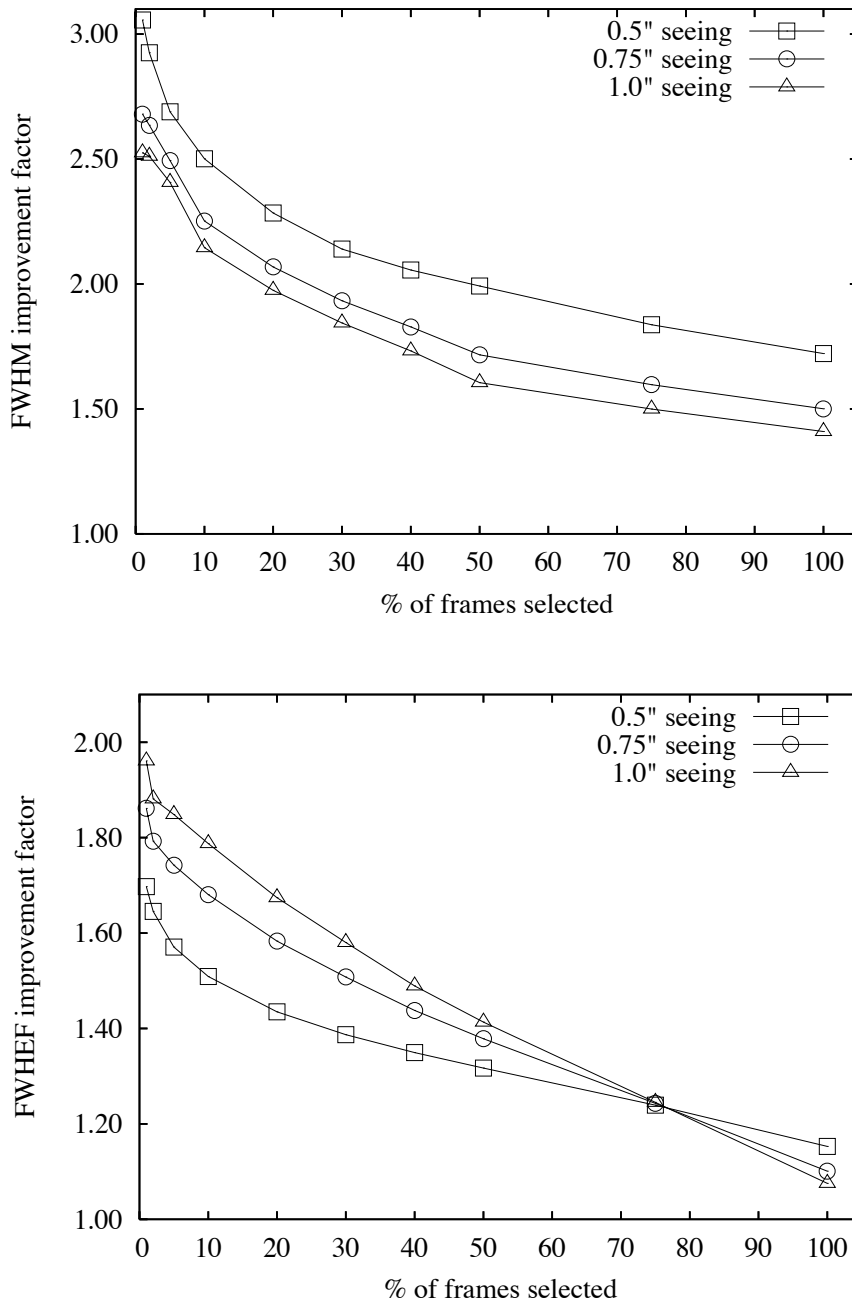


Figure 4.4: The factors by which FWHM and FWHEF (full width at half enclosed flux) are improved at slow frame rates (12FPS), at three seeings. Obtained from linear fits to figure 4.3 and similarly derived results for the FWHEF. Starting at the leftmost point of each line, datapoints correspond to selecting frames at the 1%, 2%, 5%, 10%, 20%, 30%, 40%, 50%, 75% and 100% levels respectively.

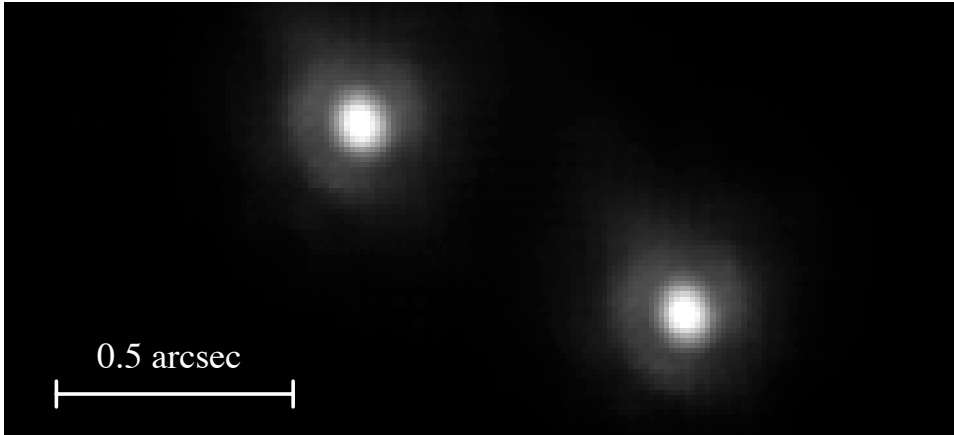


Figure 4.5: A 1% selected image of ζ Boötis with a Strehl ratio of 0.26 and a FWHM of ~ 0.1 arcsec, taken in 0.42 arcsec seeing.

sented in fig. 4.3 on average give a greater resolution improvement than the slower rates. In good seeing the output resolution at fast frame rate is within 0.03 arcsec of the diffraction limit of the telescope, limited at least in part by LuckyCam's slight PSF undersampling as well as the image quality of the telescope.

Although the resolution can be adjusted by altering the number of frames selected, in poorer seeing the probability of a superb frame is greatly reduced. Empirically this appears to limit the LuckyCam resolution increase to a factor of $\sim 3\text{-}4$ when the seeing is poor.

The FWHM gives a good estimate of the system's performance for resolution enhancement – i.e. the separation of two closely separated objects. However, for many observations (notably precision photometry) the degree of light concentration within the larger halo is also important. Figure 4.4 also details the Full Width at Half Enclosed Flux (FWHEF) performance. The FWHEF is the aperture size which contains half the light of the star and thus is a better measure for crowded observations where photometry is to be performed. The current LuckyCam improves the FWHEF by up to a factor of two, corresponding to concentrating half the light from a star into an area four times smaller than in seeing-limited images.

With a faster camera higher resolutions have been reached. Figure 4.5 shows an I-band image of the 0.8 arcsec binary ζ Boötis with a Strehl ratio of 0.26, taken in 0.42 arcsec seeing. The first Airy ring is clearly visible at a radius of ~ 0.1 arcsec, showing the point spread function is indeed diffraction-limited in width. This dataset was taken at 200Hz, approximately 5 \times faster than the coherence time of the atmosphere requires.

Chapters 6 and 7 detail the LuckyCam VLM binary survey, performed entirely at 30 FPS. Almost all of the 121 survey target were imaged with diffraction-limited cores and Strehl ratios up to 0.25.

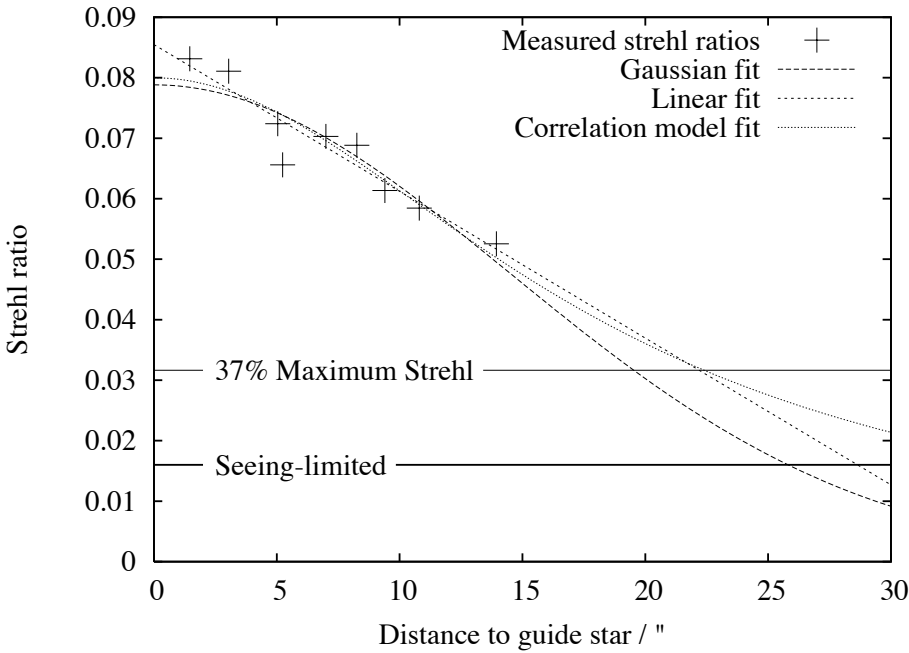


Figure 4.6: An example set of isoplanatic patch extrapolations. Measured Strehl ratios of a number of stars (from a 0.5 arcsec seeing run at 1% selection) are plotted as a function of distance from the reference star; three empirical models are fit.

4.2.2 Isoplanatic patch

Resolution enhancement systems such as LuckyCam provide useful turbulence correction only within some angular distance to the guide star. This distance is commonly quantified by the isoplanatic patch radius - the radius at which the Strehl ratio of stars is reduced by a factor of e^{-1} from those very close to the guide star. I here use this definition of the useful field size, although noting that the low frame rate wide-field data discussed here has generally smaller Strehl ratios (of order 0.1) than are usually used for this measurement.

The difference in Strehl ratio between stars close to the guide star and those up to 25 arcsec off-axis (the 2001–2004 LuckyCam field limit) can be measured for several of the globular cluster fields in the dataset. I then calculate the isoplanatic patch radius from the point at which an empirical function fitted to the Strehl ratios drops to e^{-1} of its on-axis value. The models (fig. 4.6) suggest that in five fields of M15 taken over two nights in 2003 the isoplanatic patch size ranged from 17-30 arcsec in radius. However, it should be noted that the exact isoplanatic patch radii are extrapolated, as the isoplanatic patch width is larger than LuckyCam’s field of view in these observations. Selecting a larger fraction of the frames gives an improved patch size (up to 10 arcsec wider) as the degree of turbulence correction achieved on-axis is decreased along with the output resolution.

It is clear that the atmospheric turbulence corrections produced even with a low frame rate camera have a remarkably large effective radius, in most cases larger than LuckyCam’s field

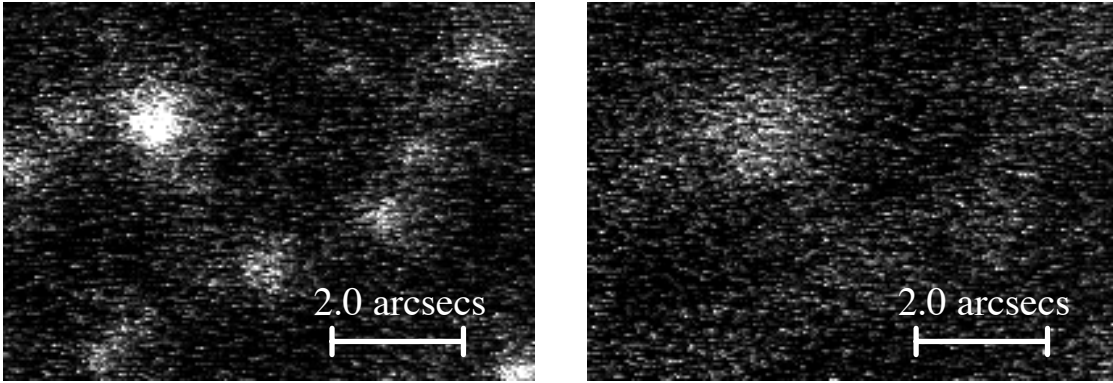


Figure 4.7: An example of fast seeing variations. These images were taken with an 83ms exposure time in the core of M3 in average 0.85 arcsec seeing – 0.33 seconds apart. This is not a result of the short timescale statistical fluctuations in image resolution expected for a constant r_0 – the 5-second averaged seeing changed by approximately a factor of two between these two images. Although extreme, these fast variations are present in most of the runs analysed here. Each bright pixel in these images is a detection of at least one photon.

of view. These results (from data taken in 2003) agree with earlier Lucky Imaging results presented in Tubbs et al. (2002), suggesting that the large patch size may be inherent to the technique over a wide range of conditions.

The isoplanatic patch for speckle imaging is expected to be proportional to r_0 , the standard atmospheric coherence length (Vernin & Munoz-Tunon (1994) and references therein). r_0 is known to vary on relatively short timescales (fig. 4.7). If LuckyCam selects periods when r_0 is larger (and not just periods when the turbulence induced phase errors randomly sum to a small value) it would be expected that those periods would have larger isoplanatic patches, as is observed.

4.2.3 Wide-field Lucky Imaging in the blue

Although most observations presented in this chapter are taken in I-band, we have also tested Lucky Imaging at shorter wavelengths, down to B-band (430nm). Although diffraction-limited images are not obtained far blueward of I-band, very useful resolution improvements are still achieved.

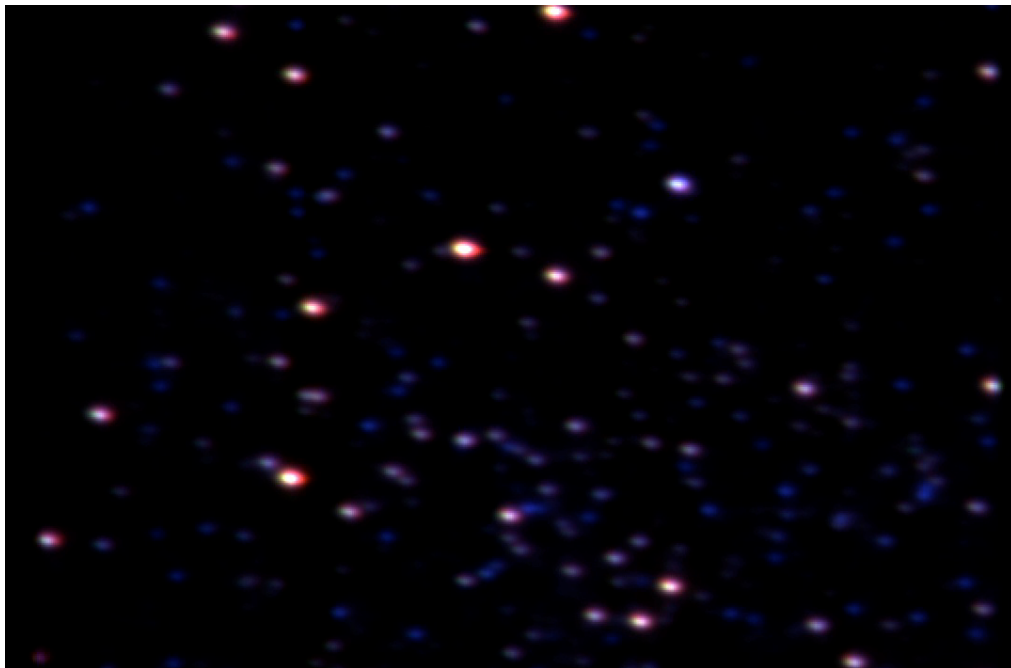
As discussed in chapter 1, the probability of obtaining a diffraction-limited frame is:

$$P \approx 5.6 \exp \left[-0.1557 (D/r_0)^2 \right] \quad (4.2)$$

for Kolmogorov atmospheric turbulence, where D is the diameter of the telescope and r_0 is the Fried seeing parameter. r_0 scales as $\lambda^{6/5}$ (Fried, 1967) and thus the probability of obtaining a



(a) 5% selection from 2000 frames at 20 frames per second



(b) Autoguider image simulated from the same data

Figure 4.8: Lucky Imaging of the core of the globular cluster M3, with a one arcminute field of view, taken in poor (~ 1.2 arcsec) seeing in June 2005. In these images blue is B-band (430nm), green is SDSS r' (625nm) and red is SDSS z' (880nm). The 2005 LuckyCam was not designed for very-high-resolution imaging in the blue over the full one arcminute FOV, and so some chromatic aberration is visible on the left of the image. The brightest stars are saturated in the z' filter, leading to red trails to the right. The guide star is the bright unsaturated star just up from the center of the images.

good frame decreases very rapidly as the wavelength becomes shorter. We would therefore not expect to acquire any diffraction limited images at B-band.

However, at short wavelengths the individual frames still show large variations in the underlying seeing (figure 4.7) and large image motion and so (as in poor seeing Lucky Imaging) much improved resolutions can be achieved even if the diffraction limit is not reached.

In figure 4.8 I present a three-colour Lucky Imaging image, where the blue corresponds to B-band, the green to SDSS r' and the red to SDSS z'. The image thus spans the visible light wavelength range (and a little into the infrared). The red light is best concentrated but the B-band FWHM resolution is also improved by approximately a factor of two (accurate measurement of this is complicated by the undersampled pixel scale). The PSFs are also very stable across the FOV, further illustrating Lucky Imaging's very large isoplanatic patch (or more probably in the case of B-band, isokinetic patch).

Although we have not yet acquired a large enough B-band dataset for detailed investigation of Lucky Imaging performance in the blue, these results are very encouraging for further investigations.

Figure 4.8 also shows the wide-field imaging capabilities of the June 2005 LuckyCam. By changing the pixel scale to 0.12 arcsec/pixel (such that even at I-band the diffraction limited PSF is severely undersampled) the LuckyCam FOV is increased to 1 arcminute, at the expense of some resolution. In poor seeing or at short wavelengths, such as figure 4.8, when a diffraction limited PSF is unlikely, this mode takes advantage of the expectation of lower resolution.

4.2.4 Narrow-Band imaging

LuckyCam is also capable of narrow-band imaging, achieved simply by using a narrow-band filter. Narrow filters require accordingly brighter guide stars, but otherwise narrow-band imaging proceeds in exactly the same manner as broad-band observation.

4.2.5 Spectroscopy

Insertion of the grism allows low-resolution spectroscopy with the spatial resolution offered by Lucky Imaging (see chapter 2). Some trial observations have been performed in this mode (eg. figure 4.9), which show both spectral features and spatially resolved spectra of binaries as close as 0.24 arcsecs.



Figure 4.9: Lucky Imaging low-resolution spectroscopy of the 1.56 arcsec very low mass X-ray emitting binary GJ 3928. An absorption feature is visible towards the left side of each spectrum. The spectra are tilted because of atmospheric dispersion.

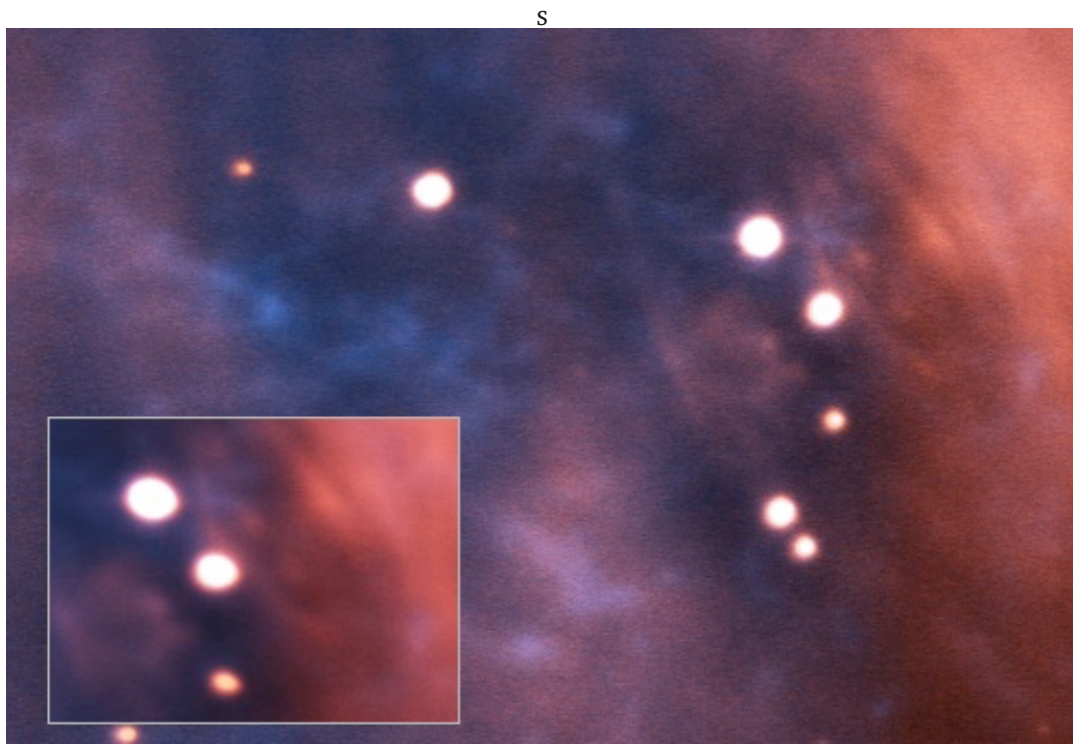


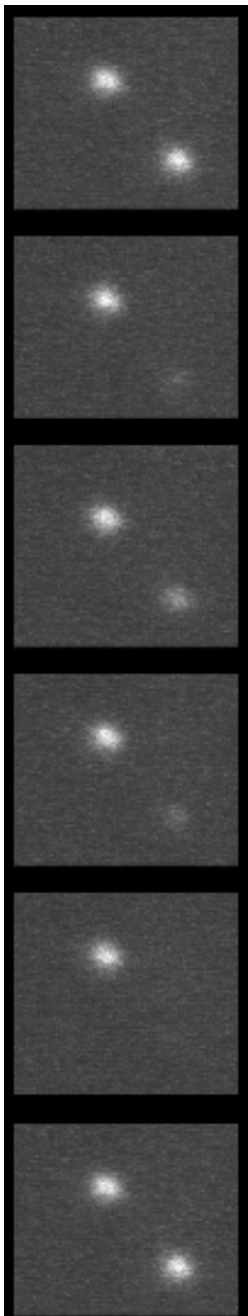
Figure 4.10: Lucky Imaging of the Crab Nebula, with a 20% frame selection. Blue is R-band, red is I-band and the green channel is equally from both. The seeing was approximately 1.2 arcsecs. A simulated autoguider image of the region around the pulsar is shown in the inset. Because of the very poor seeing and a pixel scale undersampled by a factor of three, LuckyCam only improves on the seeing-limited resolution by a factor of two.

4.2.6 Nebulosity

Since Lucky Imaging improves the PSF resolution, the detail visible in nebulosity is improved. However, it could be thought that the wide halo of Lucky Imaging PSFs would “wash-out” the improved detail when observing extended objects.

To test this, we preformed Lucky Imaging of the high-surface-brightness nebulosity around the Crab Pulsar (figure 4.10), in R-band and I-band. Comparison to the seeing-limited inset shows that the detail displayed in the nebulosity in both colours is indeed much improved by Lucky Imaging.

4.2.7 High time resolution imaging with LuckyCam



Every observation performed with LuckyCam comes with high-time-resolution data for free. In addition to use for atmospheric turbulence correction, the high-time-resolution capability offers a very interesting facility for observations of rapidly varying astrophysical objects, a capability that has only previously been available from specialised instruments (for example, ULTRACAM (Dhillon et al., 2002)).

The Crab pulsar has a period of $\sim 1/30$ sec with a double-peaked light curve. It is thus an ideal target with which to demonstrate LuckyCam’s high time resolution capabilities.

We observed the Crab pulsar in November 2005, during a short period with only small cloud extinction. We operated LuckyCam in its fastest frame mode, 10 ms/frame with a 536×100 pixels frame size.

The pulses are clearly visible in individual LuckyCam frames. The LuckyCam pulsar light curve is shown in figure 4.11, compared to a simple model used to accurately determine the period and phase of the pulsar. Using this model, each frame can be assigned a phase on the period-folded pulsar light curve. The frames can then be summed into phase-resolved bins. The resultant sequence of high signal-to-noise images is shown running down the left hand side of this page. Both pulses detailed in Percival et al. (1993) are clearly resolved with the expected flux ratios, and the times of no light output from the pulsar are also resolved.

Although the images to the left are each a simple sum of ~ 100 frames, with a larger set of frames Lucky Imaging can be performed on each phase-resolved bin. This would attain phase-resolved diffraction-limited imaging of faint objects in I-band at 10ms time resolution, a unprecedeted ground-based capa-

bility for studies of transient phenomena.

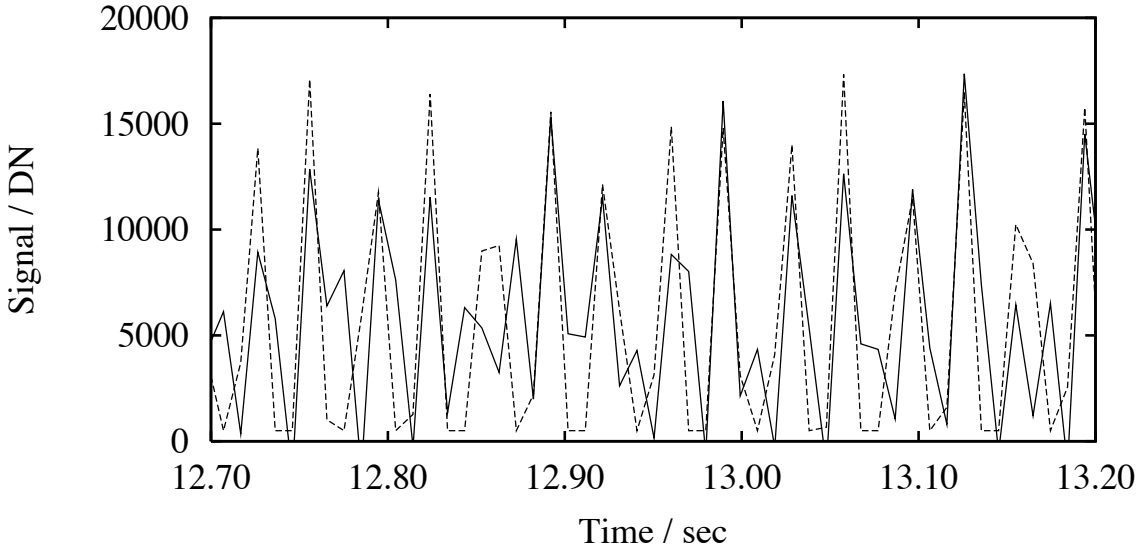


Figure 4.11: A small portion of the Crab Pulsar light curve. The solid line is the measured light curve – each data point is the total light in a 1.2 arcsec diameter box around the pulsar in a single 10 ms frame. The dashed line shows a simple two-pulse model fitted to the data. Each pulse is assumed to have a 15% duty cycle and to be separated by 1/2 of the pulsar period. The second pulse is assumed to have 30% of the amplitude of the first pulse. To fit the pulsar light curve, the phase, total amplitude and model frequency are allowed to vary. Despite its over-simplifications, the model reproduces the observed light curve fairly well, including the large variations in pulse amplitude due to pulses straddling frame-time boundaries.

4.2.8 A comparison with HST

The 2.5m Hubble Space Telescope (HST) has the same diffraction-limited resolution as the 2.5m Nordic Optical Telescope. The Advanced Camera for Surveys (ACS) Wide Field Camera (Ford et al., 1998) has a plate scale of 0.05 arcsec per pixel, and is designed to achieve an 82% Strehl ratio. An HST ACS WFC image is therefore a good estimate of an ideal diffraction-limited image, and affords an excellent baseline with which to test the LuckyCam system.

In figure 4.12 I show an ACS WFC camera field of the core of M3, compared to a 5% LuckyCam selected image of the same field. The two images are taken using very similar I-band filters (and the chip responses are much the same), although they unfortunately have very different exposure times – after image selection, the LuckyCam image has a 40× shorter exposure time (8 seconds).

Because of the much shorter exposure, the fainter objects visible in the HST exposure are not visible in the LuckyCam image. However, the FWHM resolution of the LuckyCam image is very similar to that of the HST image for all objects within a few arcseconds of the guide star. The fall-off in resolution due to the isoplanatic patch becomes visible compared to the HST image towards the upper right, at approximately 10 arcseconds radius from the guide star.

The most significant PSF difference between the LuckyCam and the HST images is the wide

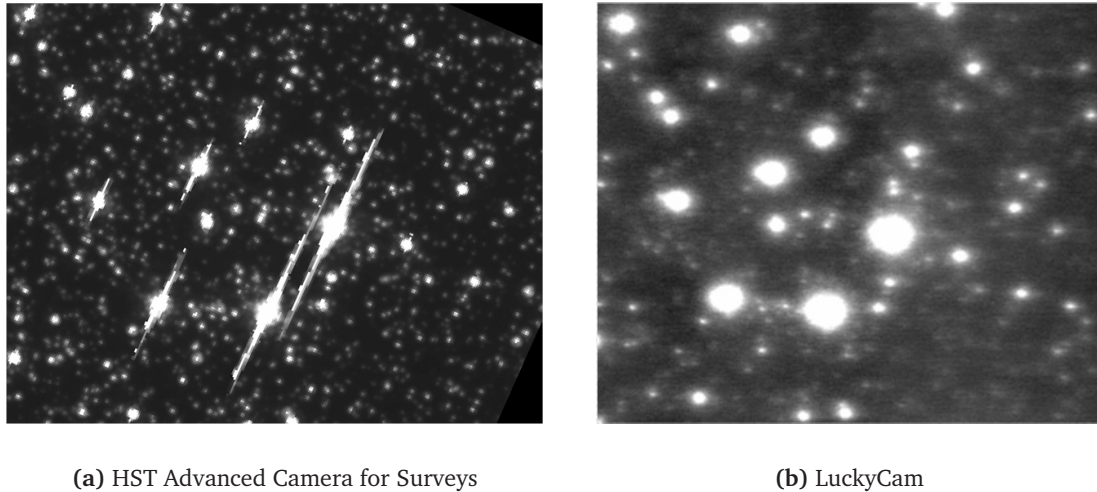


Figure 4.12: A comparison of HST and LuckyCam I-band imaging. The HST image has 40× the exposure time of the LuckyCam image. The HST image has been rotated to match the LuckyCam North-South orientation. The images have a vertical dimension of approximately 14 arcsecs, and the guide star is the leftmost of the three brightest stars.

halo around the LuckyCam diffraction-limited cores. The halos limit the maximum small-radius contrast ratios that can be reached with LuckyCam compared to HST. However, as discussed in chapter 6, LuckyCam does reach very useful contrast ratios, for example enabling the detection of substellar companions around late M-dwarfs in only 100 seconds of observation.

Although not achieving the superb atmosphere-free imaging quality of the HST, LuckyCam reproduces the FWHM I-band resolution of HST in a very much cheaper and easier-to-construct system, even on a telescope not designed to give diffraction-limited images.

4.3 Signal-to-noise Ratio (SNR) Considerations

An improvement in resolution allows smaller photometric apertures to be used. A smaller aperture contains fewer pixels and so less sky noise and (here negligible) detector noise, giving an increased SNR.

In figure 4.13 I compare modelled LuckyCam SNR performance with optimised apertures to measured results for an $I=+19\text{m}$ star in the core of M15. The model assumes that the only sources of noise are photon shot noise from the sky and star (and L3CCD multiplication noise); the imaging resolution is modelled from the performance detailed in section 4.2.1. As for this star the noise in these images is background dominated, the SNR is measured by comparing the signal contained inside an aperture to the RMS noise in a nearby empty (background) aperture.

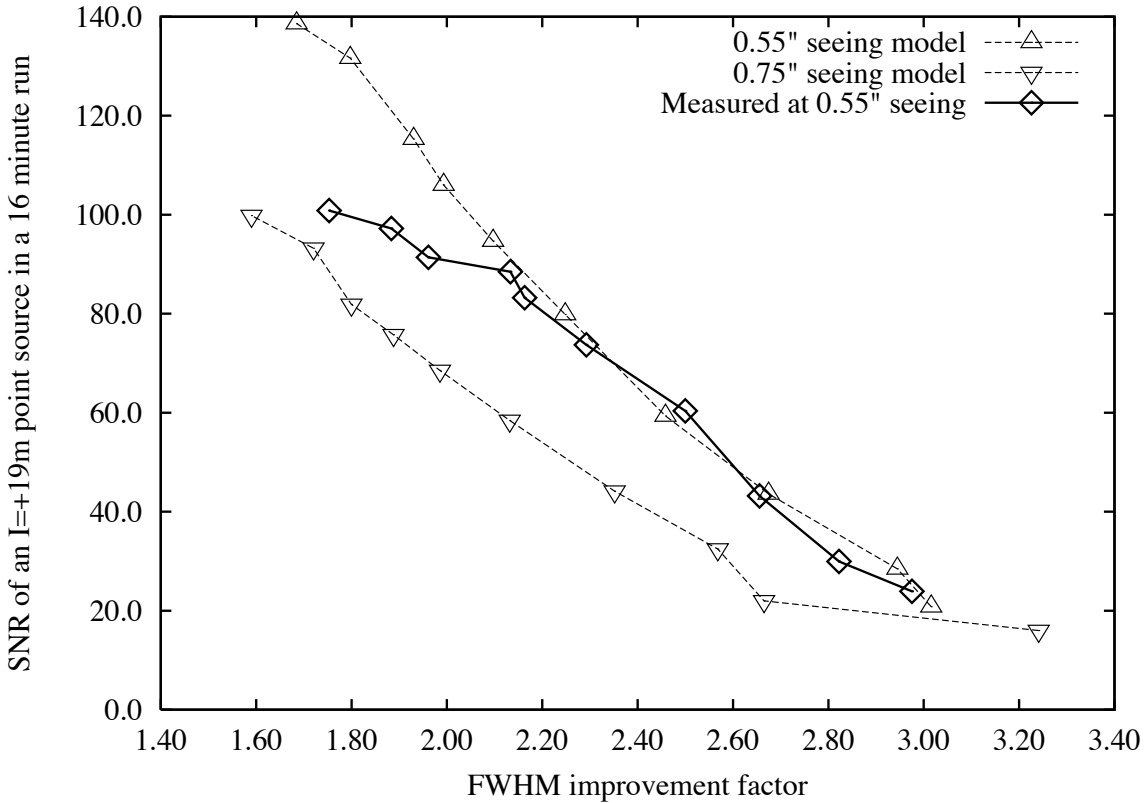


Figure 4.13: The SNR (both measured and modelled) of an $I=+19m$ point source in a 16 minute exposure, as a function of the Lucky Imaging improvement in FWHM. The aperture size is set to the PSF diameter at half enclosed flux. Starting at 100% at the upper end of each line the data points represent frame selection fractions of 100%, 75%, 50%, 40%, 30%, 20%, 10%, 5%, 2% and 1%. Note that these observations were made in the central core of M15 and have $\sim 4\times$ higher background than an empty field – i.e. the SNRs are reduced by a factor of two.

The 0.55 arcsec seeing model agrees well with the measured SNR in high-resolution observations but diverges by $\sim 25\%$ at lower resolutions. This is due to increased crowding (the fields are in the cores of globular clusters) leading to an increased background. This aside, the standard CCD photometric noise estimates model LuckyCam’s performance well, once the applicable aperture size changes are taken into account.

Although a 1% selection of frames would be expected to decrease the SNR by a factor of $\sqrt{100} = 10$ for a star in an empty field, the smaller aperture sizes that can be used reduce the decrease to $\sim 6.5\times$ in both seeings in fig. 4.13 . At the 50-75% selection level the SNR matches that available in a standard autoguided image, with resolution increased by a factor of ~ 2 .

It is worth emphasising that Lucky Imaging’s ability to increase resolution by large factors even in poor seeing effectively increases the usable observation time at the telescope. For example, if a particular observation requires 0.5 arcsec seeing selecting a few percent of frames in 1.5 arcsec seeing will produce usable data in telescope time that would otherwise have been lost.

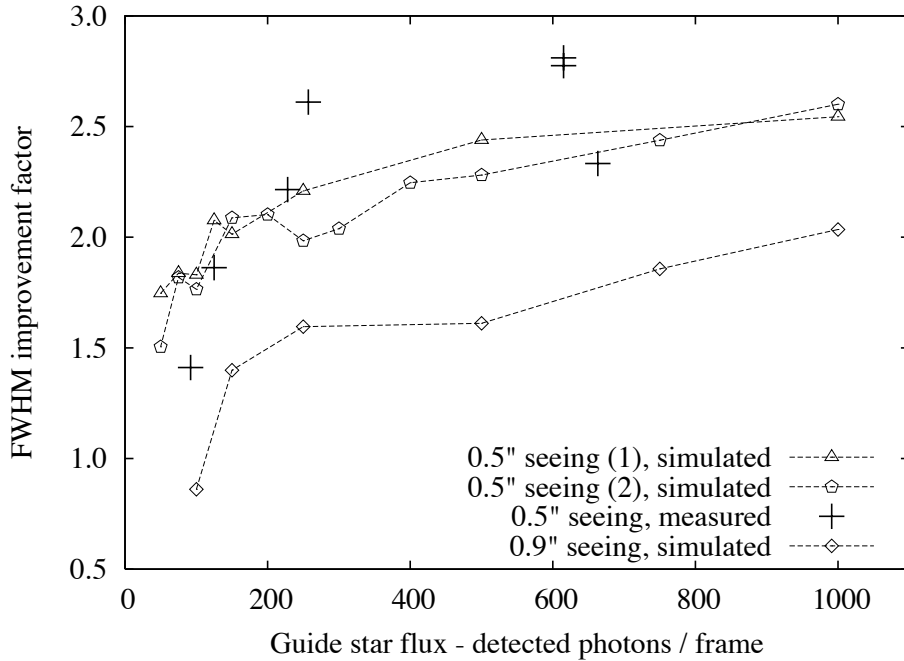


Figure 4.14: The factor by which the target star FWHM is improved as a function of the guide star flux at a 10% selection. The dashed lines show results based on simulating a faint star by adding photon & L3CCD multiplication noise to a bright star's PSF; also shown (with crosses) are measurements using actual stars.

4.4 Lucky Imaging Requirements

In this section I detail the two main requirements for a successful Lucky Imaging observation - a sufficiently bright guide star and a sufficiently fast camera.

4.4.1 Guide star flux

I simulated the effect of using a faint guide star by rescaling a bright (> 2000 photons / frame) star PSF to a specified flux, taking Poisson and L3CCD multiplication noise into account. As a check of the simulations' accuracy I also performed the same measurements with some non-simulated faint guide stars.

Figure 4.14 shows, at a 10% selection, the reference star flux requirements at two seeings. The requirements are similar at all percentage selections.

At a guide star flux of 150 photons/frame ($I \sim +16m$) the resolution is reduced by 22% from that achieved with a very bright star. Because there appears to be a rapid falloff in resolution below that flux level I adopt 150 photons/frame as the minimum flux required for high resolution imaging.

The more spread out PSFs in poorer seeing require more photons to give an acceptable SNR

in the PSF core. The real (non flux rescaled) guide stars give matching results, although with higher noise induced by anisoplanatism.

The ~ 150 photons/frame requirement can be understood in the following way. Even in poor seeing the best frames consist of a single speckle surrounded by a halo. If the speckle contains only a few tens of photons, Poisson shot-noise becomes a limiting factor for frame selection on the basis of Strehl ratios, thus degrading the output resolution.

If a field contains several stars which are individually fainter than the guide star limit, John Baldwin has found that it is possible to add the stars' PSFs together to provide a useful estimate of a bright guide star PSF which can then be used in the standard way for Lucky Imaging.

4.4.2 Sky coverage

The isoplanatic patch and reference star flux requirements directly give LuckyCam's achievable sky coverage. If the system is to achieve its most useful resolution gains an $I \sim 16$ reference star within $25''$ of our target is required.

At a galactic latitude of $60 - 70^\circ$ approximately 7% of the sky can be used with chance-placed guide stars, based on averaged star counts from the USNO-B1.0 catalogue (Monet et al., 2003). 30% of the sky is accessible at a latitude of $20 - 30^\circ$ while at lower galactic latitudes sky coverage is virtually complete.

4.4.3 Frame rates

Freezing the effects of atmospheric turbulence requires exposures that are shorter than the atmospheric coherence time. One sufficiently fast (60Hz) trial dataset is presented in fig. 4.15, temporally rebinned to produce a range of effective effective frame rates. Although this is a single observation the performance at 12FPS and 30FPS is consistent with that found in the more numerous trials in previous sections of this chapter, and is thus probably not atypical.

Selection of frames (as opposed to simple shift-and-add) gives an improvement at all measured frame rates. At even 0.3 FPS the frame selection gives gains in FWHM of over $1.6\times$, with an estimated limiting reference star magnitude of $I = +19m$ in dark time.

At ~ 30 FPS the atmospheric coherence time is well sampled in the best 10% of frames; there is no improvement with faster frame rates. The frames with poorer quality do, however, benefit from still faster rates. The periods of poor seeing have a relatively smaller atmospheric coherence time because there are more isophase patches per unit area to be swept over the telescope aperture by the wind. The more inclusive frame selections include these periods and so require a faster frame rate than when selecting only the very best frames.

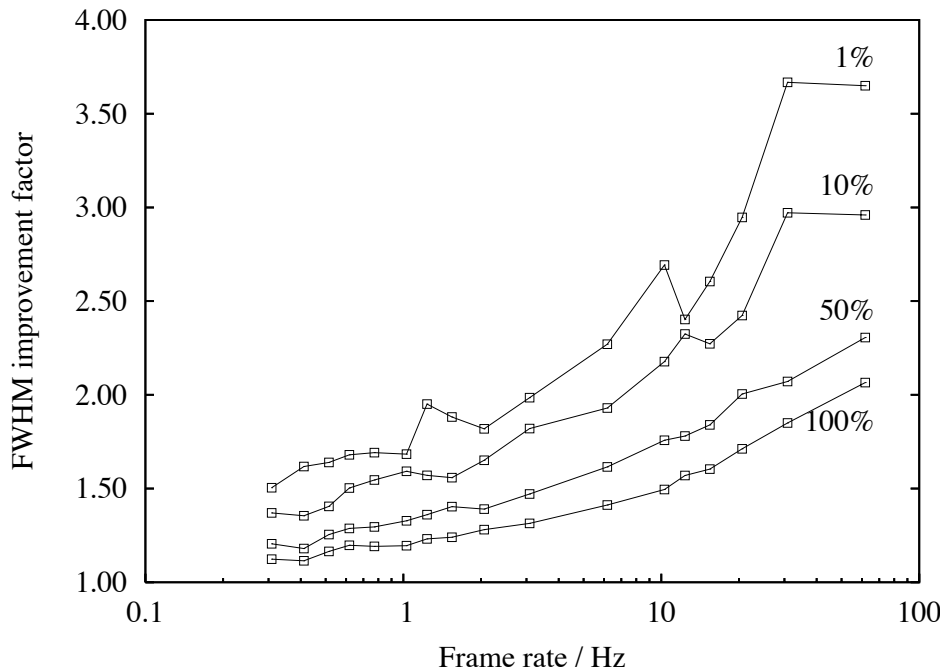


Figure 4.15: Imaging performance as a function of frame rate for in 0.42" seeing. Shift-and-add (100% selection) FWHM performance is always a significant improvement over the autoguider performance because the autoguider uses the image centroid rather than the PSF peak as a position reference.

4.5 Summary

- Lucky Imaging offers reliable and very valuable resolution enhancement in all encountered conditions, even with the slow non-ideal camera used for most of the observations in this chapter.
- In poor seeing FWHMs are improved by up to a factor of four; in good seeing near diffraction limited images are achieved in I-band.
- LuckyCam greatly improves the resolution of images taken even in B-band.
- The angular radius over which the system can usefully operate in I-band is as large or larger than the 22" x 20.5" field of view in all measured fields.
- The system can work with guide stars as faint as $I = 16$ with full performance, giving near 100% sky coverage at galactic latitudes $< 20^\circ$ and >7% sky coverage at $< 70^\circ$.
- Signal-to-noise ratio losses from frame selection are compensated by the greatly improved resolution.
- The system increases the range of conditions that are usable for particular observations – and can thus use otherwise lost telescope time

5

Measuring Close Binary Parameters with LuckyCam

5.1 Introduction

In this chapter I describe a number of methods that I have developed for the measurement of the parameters of the close binaries discovered by LuckyCam in chapters 6 and 7. Many of these techniques are specific to the use of data from L3CCDs and/or Lucky Imaging. As the high-speed high-QE photon counting capabilities of L3CCDs are extremely useful for astronomy, and Lucky Imaging shows excellent promise for very extensive astronomical use, these methods are likely to be useful for a range of instruments in the future.

5.2 Close Binary Photometry

Performing accurate and precise photometry of very close binary systems is particularly challenging, because the PSFs of the binary components are often blended. An extra complication is introduced in Lucky Imaging images – faint guide stars have different PSFs from all other stars in the field. In this section I first describe the faint guide star problem, followed by the development and tests of a general photometry system for LuckyCam images of close binaries.

5.2.1 The faint guide star PSF

If the Lucky Imaging guide star is faint, so that photon shot noise in the PSF core becomes significant, the frame selection and alignment can be biased away from the true brightest speckle of the PSF by high excursions of the photon noise. In the final high-resolution images the guide star then has a photon-event-shaped core overlayed on the real PSF. The PSF is also degraded in resolution by mis-alignments.

The guide star shares its underlying PSF with the other stars in the field (within the limits of anisoplanatism), because each star is corrected with the same field motions and frame selections. However, only the guide star suffers from the photon-event-shaped core, as all other stars have photon noise uncorrelated with that of the guide star. Because of the (often very) different guide star PSF, standard PSF fitting photometry cannot include a faint guide star. Since many LuckyCam targets serve as their own guide stars, this would be a serious limitation without corrective measures.

The problem is made worse by the standard Lucky Imaging image construction. Because the convolution section of the frame alignment process effectively blurs the registration on individual photon events, the photon-event-shape overlay on the guide star acquires the shape of a diffraction-limited PSF core. Although the photon events themselves are not convolved by the diffraction-limited PSF during the Drizzle reconstruction, the blurred alignment leads to the final shape of the many summed events to replicate that of the convolution kernel. This is very hard to remove, because the real PSF itself includes a diffraction-limited core component (figure 5.1, top left).

Although in principle a calibrator star could be used to determine the level of this effect, the star would have to be matched to the target's brightness, because the strength of the effect is photon-noise and seeing dependent. A second calibrator would also have to be found nearby to estimate the non-guide star PSF.

The effect can, however, be limited if PSF convolution and resampling is disable during the Lucky Imaging process. Alignment and selection then proceeds purely on the brightest pixel in the input image. This mode limits Lucky Imaging performance, but constrains any high excursions of photon noise to a single pixel – as each pixel contains photon noise uncorrelated with that of its neighbours. That pixel may then be ignored or re-estimated in subsequent PSF fitting procedures (top two images of figure 5.1). In practise, CTE effects lead to the two pixels to the right of the peak also being affected, and those pixels must also be masked.

5.2.2 Tripling

As discussed in chapter 3, very close binaries often appear as triple systems because the Lucky Imaging system occasionally shifts lock from one component of the binary to the other. This

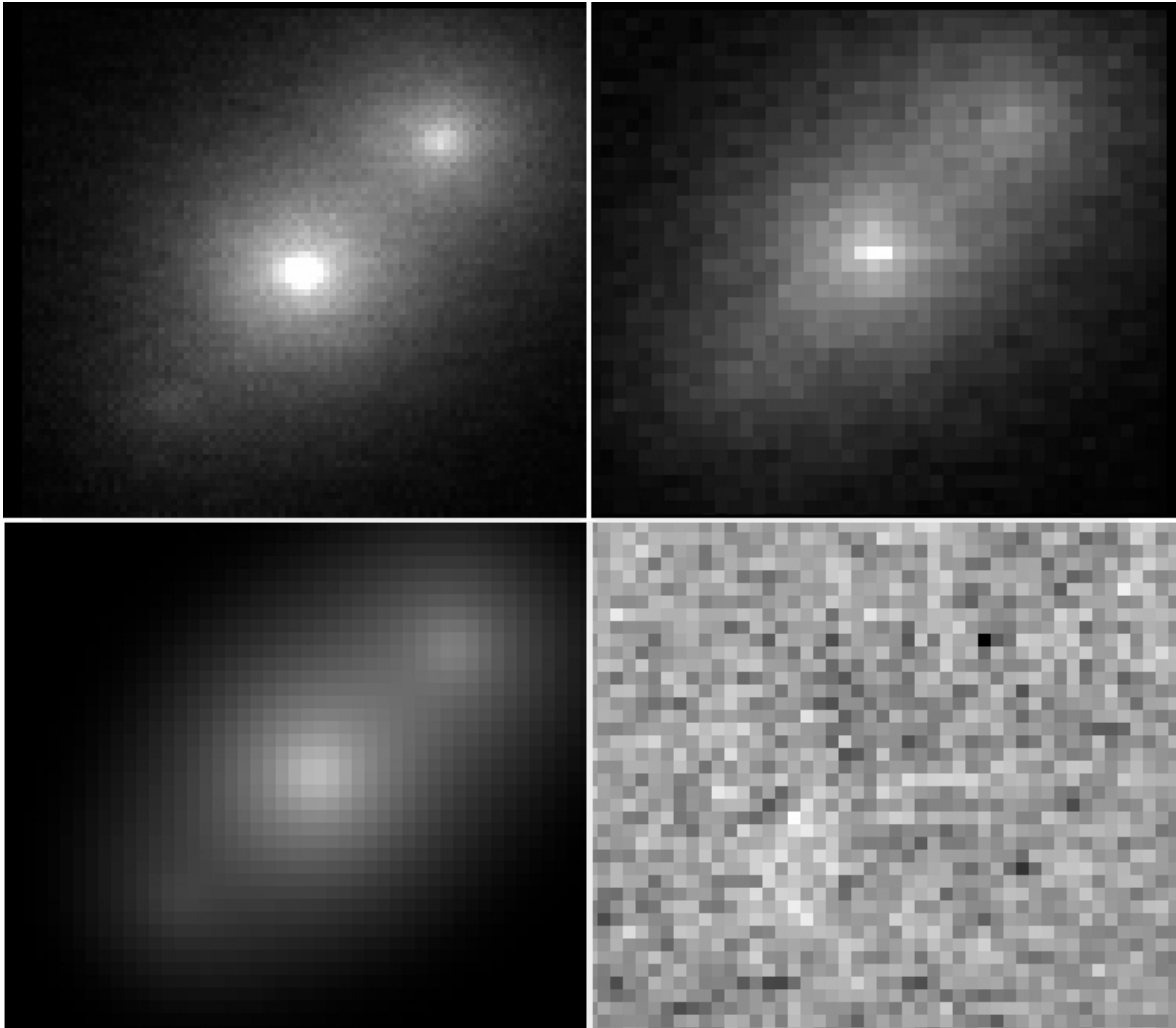


Figure 5.1: An example of the automated PSF fitting performed by PSFFIT. Top left: A 20% selected standard Lucky image of the binary GJ 3554. The excess light concentration of the primary is visible as the saturated region of the center of the PSF; a faint tertiary image is also visible. Top right: the reduced resolution image used by PSFFIT. Note that the light concentration now only affects the central three pixels of the primary's PSF. Bottom left: The model of the image. Bottom right: the residuals after the model has been subtracted from the real image (with central pixel brightnesses re-estimated).

leads to the secondary appearing in the position of the primary in some fraction of the images. The primary then forms a tertiary image separated from the guide star by the binary separation, but in the opposite direction (clearly visible in figure 5.1).

The three components of the triple image have the following fluxes, with F_1 being the flux of the image in the position of the true primary, F_2 that in the position of the true secondary, and F_3 the flux in the position of the tertiary image:

$$F_1 = (1 - P)F_P + PF_S \quad (5.1)$$

$$F_2 = (1 - P)F_S \quad (5.2)$$

$$F_3 = PF_P \quad (5.3)$$

F_P and F_S are the true primary and secondary components' fluxes respectively, and P is the probability of mistakenly using the secondary component as a guide star instead of the primary.

P varies with the flux ratio between the two components and the SNR of the brightest speckles. Equal-flux binaries will swap lock between the two components with $P=50\%$. Bright binaries with high contrast ratios and high SNRs will have a very small P ; for an example of this, see the observations of the $i=+11$ mags Ross 530 (chapter 6), which is a 0.15 arcsec binary but does not suffer from tripling. If the SNR is low, however, even high contrast ratio binaries have high P – see the observations of the possible substellar companion to LSPM J1735+2634 in chapter 6.

For useful photometry, we wish to recover the original primary and secondary fluxes from the above three measurements. The de-tripling procedure described in chapter 3 operates only down to separations of ~ 0.25 arcsec, requires significant manual experimentation to find the best guide star box positions, and may fail in poor seeing conditions. For these reasons, in the LuckyCam VLM binary survey I chose to measure the fluxes of the three images visible in standard Lucky Imaging images, and solve the above equations simultaneously for the true binary flux ratio.

If we define I_{12} as F_1/F_2 and I_{13} as F_1/F_3 then F_R (the true binary flux ratio), is:

$$F_R = \frac{2I_{13}}{I_{12}I_{13} + \sqrt{I_{12}^2I_{13}^2 - 4I_{12}I_{13}}} \quad (5.4)$$

This equation is undefined when the tertiary image has no flux (although it has the correct asymptotic behaviour); in that case the binary flux ratio is just the simple flux ratio of the two components. The PSF fitting tests described in the next section include simulated tripling, and the true binary flux was recovered using the above equation.

5.2.3 PSF fitting

Because the LuckyCam VLM survey requires resolved photometry for a large number of close binaries, I developed an automated PSF fitting program. PSFFIT fits identical PSFs to the components of a LuckyCam image of a binary with the aim of retrieving the binary contrast ratio. Because the LuckyCam VLM binary survey did not include PSF reference stars taken very close in time and space to the targets, I fit the PSF using a parameterised model.

Each PSF is parameterised at a radius r as follows:

$$F(r) = F_S \left[F_H \left(1 + \frac{r^2}{r_s^2} \right)^{-\beta} + e^{-\frac{r^2}{r_a^2}} \right] \quad (5.5)$$

The first term is a Moffat point spread function describing the halo of the PSF, where r_s is the Moffat scale factor, β varies between 1 and ∞ , and F_H denotes the proportion of the star's light contained within the PSF halo. The second term is a 2D Gaussian that models the diffraction-limited core of the PSF. r_a is the width of the core and is generally 1-2 pixels. F_S is proportional to the total flux from the star. For simplicity, the normalisation of the two PSF terms not included, because identical PSFs are fitted and the system need only produce the flux ratio between the binary components.

Before fitting, the pixels affected by the faint guide star problem described above are rescaled to the average flux of the pixels just above and below them*. All the above PSF parameters are allowed to vary on a per-image basis, as well as the binary position, separation and the two flux ratios (of the primary to the secondary and tertiary images). I use a simulated annealing (Press et al., 1988) algorithm to minimise χ^2 summed over all the pixels in the input image. The noise value in each pixel is estimated from the number of photon events within that pixel. An example of the quality of fit is shown in figure 5.1.

To improve the quality of the derived parameters, multiple fits are performed using images of the binary with different PSFs. The wealth of Lucky Imaging frames allows these multiple tests to be performed very easily. By default Psffit uses 5 per cent non-cumulative selections from a LuckyCam run – that is, the best 5 per cent of frames shifted-and-added into a high-resolution image, followed by the next-best 5 per cent, and so on. Each selection level provides an independent image of the binary, with a unique PSF. 5 separate images ranging from the best 5 per cent of frames to the 20-25 percentiles are used, greatly improving the reliability of the derived binary flux ratios.

I tested the performance of the PSF fitting against simulated binaries of known flux ratio. Real LuckyCam images of single stars from the VLM binary surveys were replicated to form binaries at three flux ratios, in the 5 separate PSFs available for each of the 6 stars tested. For each PSF a large variety of binary separations and position angles were tested. 540 trials were performed in total, with 30 different PSFs covering a wide variety of atmospheric conditions and guide star brightnesses. The trials give two separate results: both the fitting accuracy and precision. The accuracy is found from comparing the measured flux ratio to the simulated input flux ratio; since real PSFs are used the fitting is not perfect. The fitting precision is found from the range of flux ratios derived from different simulated images with different input PSFs.

*Although this procedure does not conserve the total flux from the system, the error introduced is less than 5%, well below other fitting errors and the 20-40% error present in an uncorrected PSF.

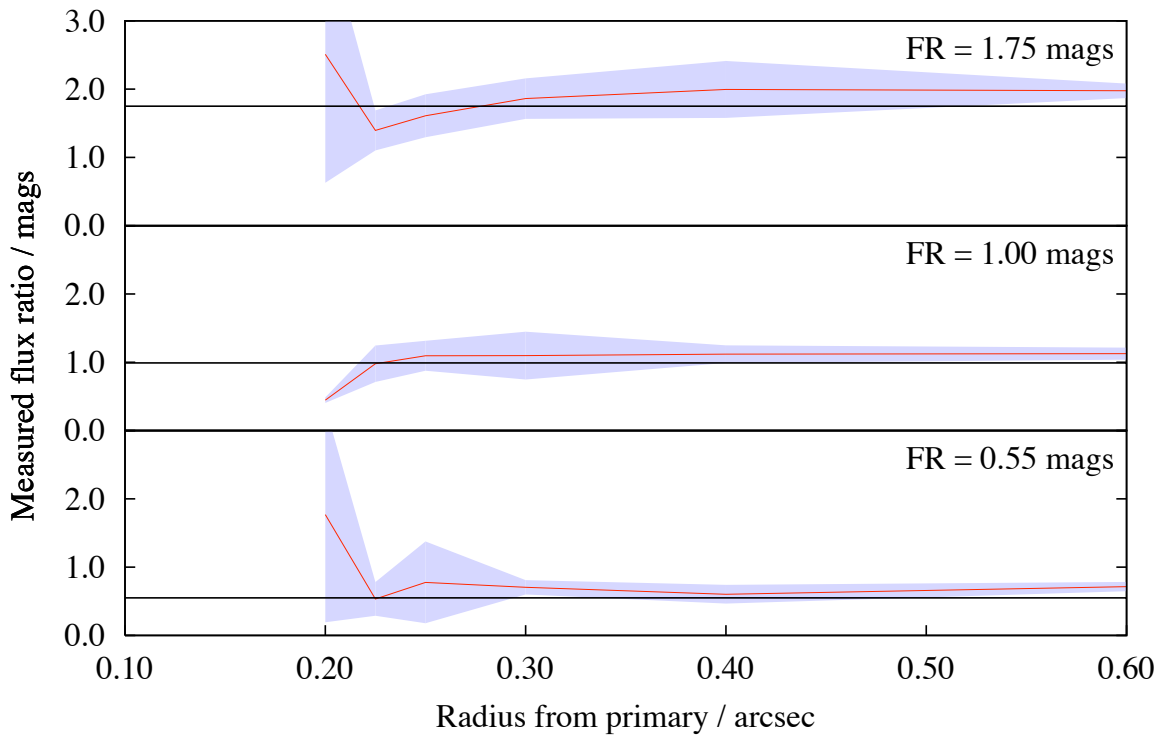
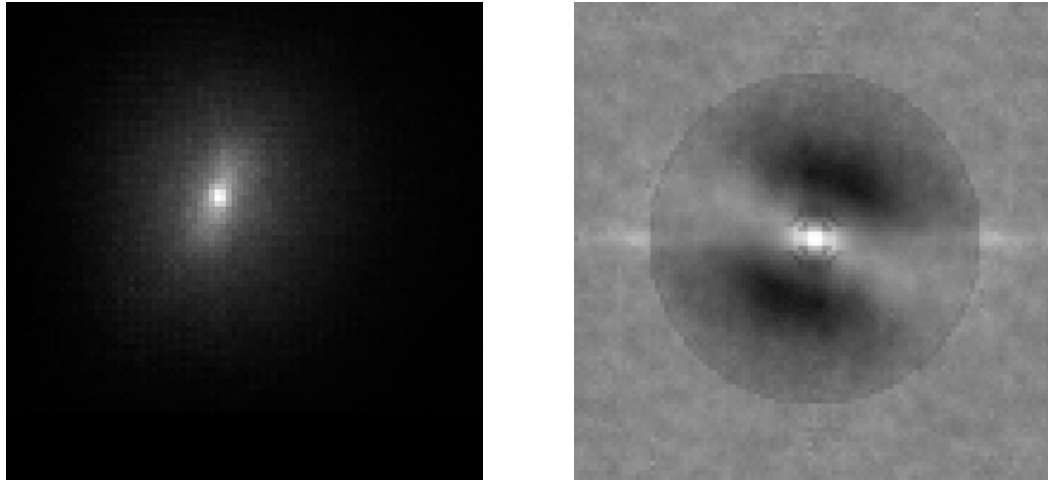


Figure 5.2: The accuracy of Psffit, based on 540 separate trials at three different flux ratios (0.5, 1.0, 1.75 mags). The black horizontal lines in each panel are the true flux ratios; the shaded regions are the 1σ uncertainties in the derived flux ratios. Fitting performance falls off at closer radii as the PSFs become more blended. At larger radii (> 0.5 arcsec) the fitting slightly overestimates the flux ratio; this is likely due to anisoplanatism slightly decreasing the light concentration of the secondary.

The test results are shown in figure 5.2. Down to 0.3 arcsec separation, at a variety of flux ratios, fitting performance is roughly constant at an error of 0.2-0.3 mags. The performance is much poorer at 0.2 arcsec separation, because at this radius the 0.08 arcsec FWHM diffraction limited cores of the two stars become close enough to blend.

Under good conditions speckle imaging and AO measurements achieve precisions of 0.1-0.2 mags down to about 0.2 arcsec separation (see eg. Horch et al. (2004) and references therein). These techniques make use of an unresolved PSF reference star, selected to be very close to the target binary, both in sky position and time of observation. LuckyCam photometry would similarly benefit from the availability of reference PSFs.

The LuckyCam VLM binary survey, which the PSF fitting technique was designed for, is based on a quick look at 50-60 targets per night and did not include nearby PSF reference stars because of time constraints. However, in subsequent reobserving of the detected binaries (to follow the orbital motion of the companion) nearby PSF reference stars will be targeted, and this is likely to very significantly improve the quality of the binary contrast ratio measurements.



(a) 5% Lucky Imaging z' image

(b) Summed & calibrated power spectrum of 1000 frames

Figure 5.3: The very close (0.14 arcsec) binary G 256-25 (discovered with LuckyCam). The diffraction-limited cores (~ 0.09 arcsec FWHM in this z' image) are blended, and so the system is resolved into a blended line by Lucky Imaging. The summed calibrated power spectrum (right) of the frames shows a clear minimum, from the position of which the binary separation can be calculated.

5.3 Speckle Interferometry with L3CCDs

Astrometric measurements of very close binaries (<0.2 arcsec) on LuckyCam images is challenging because the crowding of the PSFs, which may be separated by less than a diffraction-limited core width (figure 5.3).

LuckyCam produces a very large data cube of images in each observation, consisting of many thousands of individual frames, each with a different PSF. Although direct Lucky Imaging gives very high resolution images, further processing of the raw data can achieve higher precision determination of the parameters of some targets. In this section I present an example of such processing: speckle imaging to retrieve the separation and position angle of very close binary systems.

5.3.1 The speckle imaging method

Speckle imaging is briefly described in chapter 1. Essentially, the method relies on the fact that each frame $I(x, y)$ is the result of a convolution of some object brightness distribution $O(x, y)$ with a PSF $P(x, y)$:

$$I(x, y) = O(x, y) * P(x, y) \quad (5.6)$$

If, for example, the object is a binary star (two point sources) the resultant image will have two copies of the PSF slightly displaced. Short exposure PSFs, consisting of speckles with diffraction-limited sizes, retain information at the diffraction limit after convolution with the object brightness distribution. Speckle interferometry searches for correlations in the image that suggest the observed PSF could be represented as a number of superimposed and displaced PSFs, and in that way recovers the object brightness distribution.

The simplest speckle technique, first suggested in Labeyrie (1970), is to sum the power spectra of many short exposure speckle frames. In the power spectrum, binary stars appears as set of fringes (figure 5.3). The fringes are preserved under addition, unlike the high-resolution components in a simple addition of short-exposure frames. The binary parameters can then be retrieved from fits to the fringes.

The short exposure high SNR frames obtained by LuckyCam meet the requirements of a speckle imager as well as a Lucky imager, and both techniques can operate on the same data.

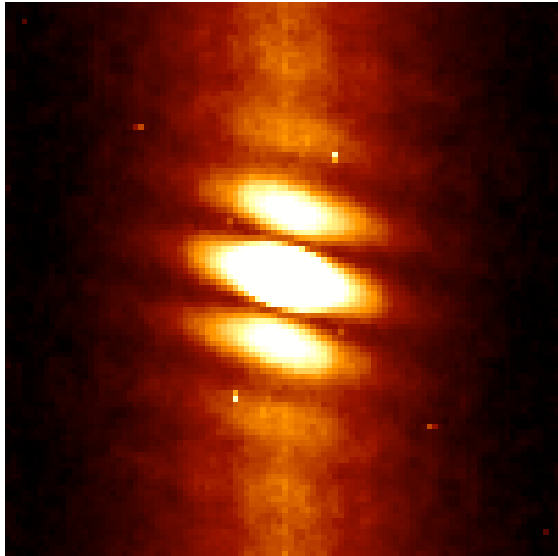
To obtain the separations and position angles of very close binary stars to high precision I implemented a Fourier Transform speckle imaging system for use on LuckyCam data. The program automatically fits the expected speckle pattern of a close binary to several independent data sets of ~ 1000 frames targeted at the same star. The independent binary parameter estimates are combined to single values with improved accuracy, and estimates of the random errors are found from the range in parameter fits.

As can be readily seen from the images of the fringes, the position angle of the binary has a 180° uncertainty. This is because phase information is lost during image reconstruction. This information can be recovered via more complicated processing techniques (notably the bispectrum speckle masking techniques described in Weigelt (1977); Weigelt & Wirnitzer (1983); Lohmann et al. (1983)). However, when conditions allow Lucky Imaging resolved images of the binary (as for all observations presented here), it is simpler to use those images to resolve the uncertainty (using the detripling procedures if necessary).

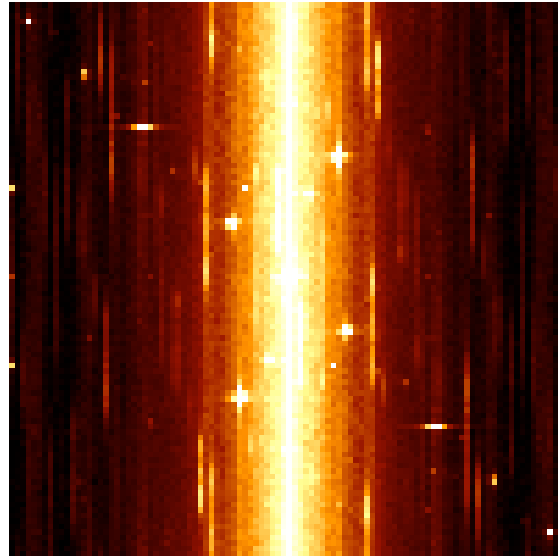
5.3.2 L3CCD specifics

On any instrument, speckle data requires extensive calibration before it can be used for parameter estimation. In particular, the shape of photon events leads to a spatially varying background in Fourier space that can be complicated to remove. In the following, I detail the effects that must be calibrated out from L3CCD speckle images. Figure 5.4 shows the stages in the calibration.

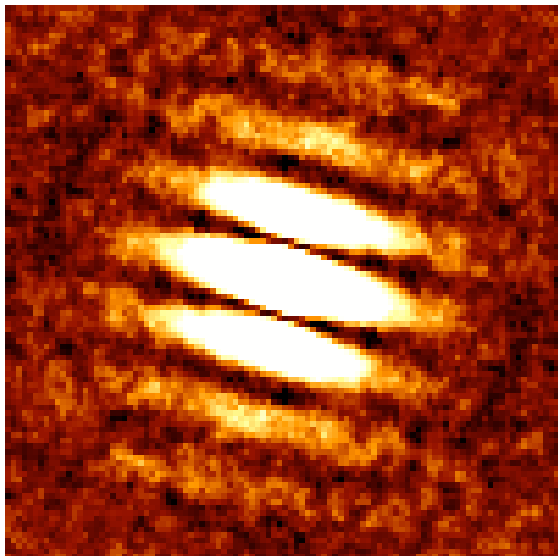
The raw power spectrum, figure 5.4(a), shows clear fringes, as expected for a close binary. In this case, chosen for clarity, the binary separation is 0.31 arcsec, and so several fringe peaks are visible. In most cases where speckle interferometry is necessary to get accurate separation



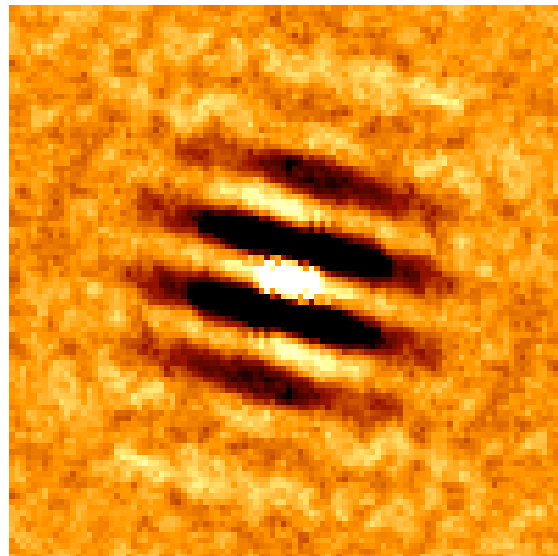
(a) Raw summed power spectrum



(b) Summed background power spectrum



(c) Power spectrum, background removed



(d) Power spectrum, calibrated

Figure 5.4: The stages in the reduction and calibration of the summed power spectrum of the 0.31 arcsec binary NLTT 14406.

values only one fringe peak (or even only one minimum) is visible.

As for all detectors, noise terms must be added to the imaging equation (eg. Pluzhnik (2005) and references therein):

$$I(x, y) = O(x, y) * P(x, y) * S(x, y) + N(x, y) \quad (5.7)$$

where the convolving $S(x,y)$ is the photon event shape for the detector (which convolves the shape of all objects in the frame) and $N(x,y)$ is a noise bias floor, which includes pattern noise in the detector. These noise terms are obvious in the power spectrum (figure 5.4). Firstly, and most obviously, there is a vertical bar extending down the center of the power spectrum. This shape corresponds to structures in image space that are single-pixels high but several pixels long – CTE-shaped photon events.

The noise term $N(x,y)$ is introduced by LuckyCam’s electronics, and takes the form of lines and points in the power spectrum (figure 5.4(b)). I remove it by subtracting the power spectrum of a background region of the frames from that of the foreground region. The speckle imaging code also detects those rare cases where the background noise does not subtract well, and masks off those areas as bad pixels.

The remaining two multiplicative terms in the power spectrum are divided out, thus deconvolving the binary power spectrum from their effects. Perhaps the most obvious way to remove the photon-event-shape bar is to divide by a suitably scaled event shape taken from a background region of the same image (figure 5.4(b)). However, as can be seen from the power spectra, the photon event shape is different in the stellar and background regions, because the CTE effects are (weakly) dependent on the amount of charge (light) within the pixels. For this reason, I estimate the shape of the photon events from the topmost and bottommost rows of the PSF power spectrum. These high frequency regions are beyond the frequency limit of the telescope, and so should be dominated by the photon event shape. I then divide the power spectrum by the estimated photon-event power spectrum (corresponding to deconvolving the input image by the photon event shape).

The results of these two background removal procedures are shown in figure 5.4(c). However, the power spectrum does not take the ideal form of a set of cosine fringes, being instead heavily peaked towards the center. This is because the fringe pattern from the binary is multiplied by an envelope function – the power spectra of the two unresolved point source PSFs making up the binary.

Left uncalibrated, the point source power spectrum can “push” a minimum away from the center of the fringe pattern, artificially decreasing the measured binary separation. I remove this effect by dividing the entire power spectrum by a 1-D power spectrum taken through the center of the fringe pattern. The 1-D power spectrum is measured along the central fringe,

corresponding to the power spectrum of a single unresolved point source. This deconvolution proceeds under the assumption of circular symmetry of the atmosphere-corrupted power spectrum of the single point source, an assumption that appeared to be reasonable from tests of the speckle patterns from single stars. The final calibrated fringe pattern after the division is shown in figure 5.4(d).

In summary, the procedure developed to make a calibrated speckle power spectrum using data from a LuckyCam-like L3CCD imaging system is:

1. Find summed power spectra for PSF and background regions from 100s-1000s of frames.
2. Normalise both power spectra.
3. Subtract the background power spectrum from the PSF power spectrum.
4. Mask off any remaining bad pixels (frequencies).
5. Estimate a photon event shape from the highest vertical frequency regions of the PSF power spectrum, and divide it out.
6. Divide the resultant fringe pattern by the power spectrum of an unresolved point source, estimated from the profile perpendicular to the fringe pattern.

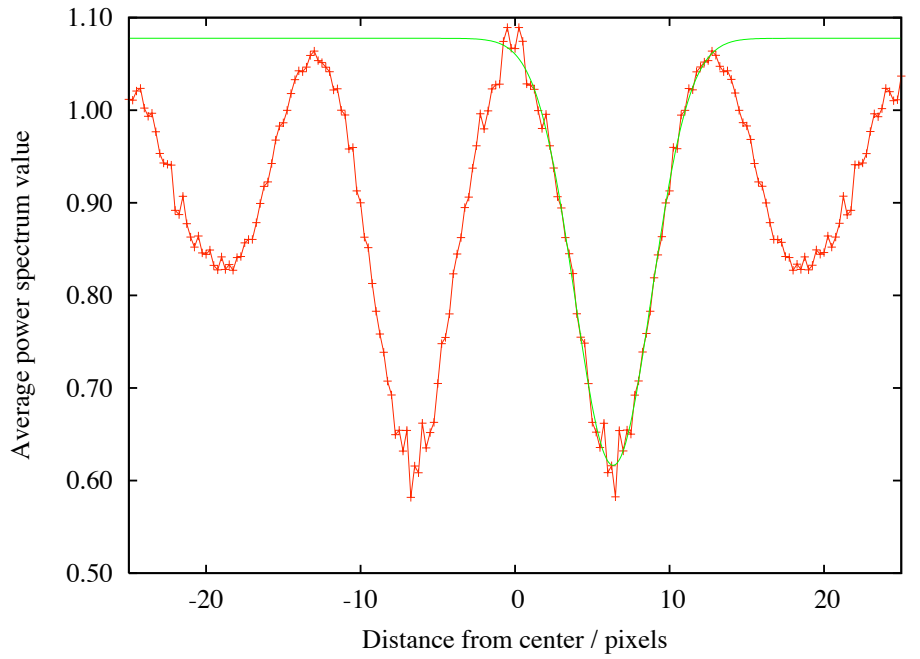
5.3.3 Measuring binary parameters from speckle data

I developed an iterative procedure that, given a very rough estimate of the binary separation, converges on the true values of the binary separation and position angle. It proceeds as follows:

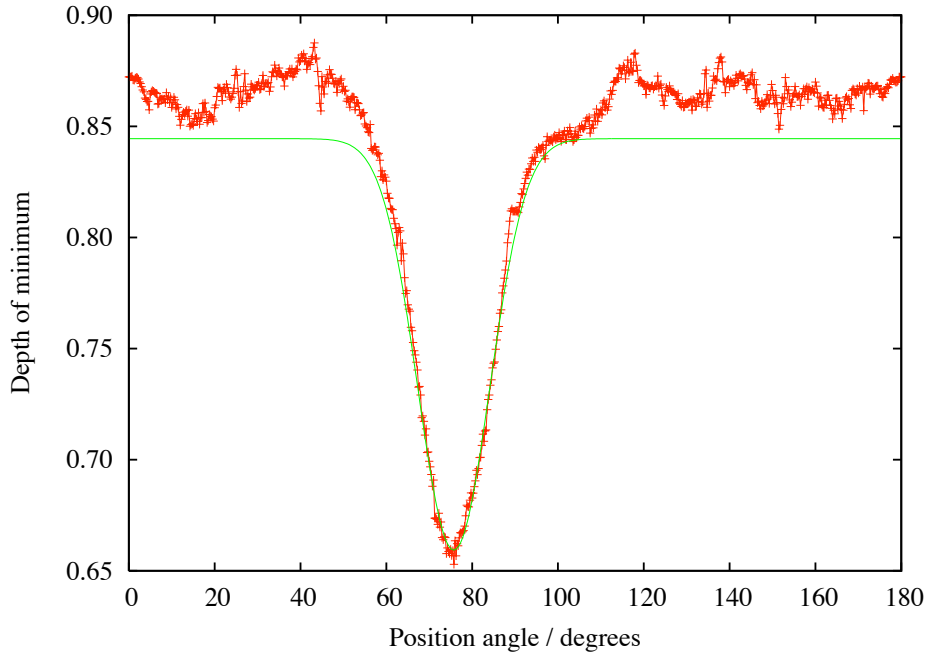
1. For each probable position angle, take a summed profile perpendicular to the expected fringe pattern – eg. figure 5.5(a). Find the minimum value around the expected minimum for the initial guess for the binary separation.
2. Fit a Gaussian curve to the depth increase in the minimum around the correct position angle (figure 5.5(b)) – the minimum depth corresponds to correct alignment with the fringe pattern.
3. To determine a best-fit value for the binary separation, fit a Gaussian to the fringe pattern around the first minimum for the best-fit position angle
4. Repeat steps 1-3 using the new separation value; repeat until convergence (almost always only one repeat is required).

The procedure could be easily extended to fit more peaks and troughs than just the first minimum, but this is not necessary for the LuckyCam VLM binary survey data – the close binaries that require speckle imaging for parameter determination rather than simple centroid-fitting possess only one minimum within the telescope resolution boundaries.

I found this procedure to be more robust than direct fitting of the fringe pattern in binaries with marginal SNR or very close separations. For 0.1-0.2 arcsec binaries, typical variations in the measured binary parameters with a range of different PSFs are less than 0.01 arcsec in separation and 1-3° in position angle. The derived values agree well with (higher-uncertainty) parameters measured from Lucky Imaging data.



(a) Gaussian fitting (green) of the speckle imaging separation. Only the first minimum is fit, although in this case the binary is sufficiently wide to show a further power spectrum minimum.



(b) Fitting of the speckle imaging position angle. A Gaussian fit to the region around the minimum depth is shown in green.

Figure 5.5: Fitting the binary parameters to quantities derived from the summed power spectra of the 0.31 arcsec binary NLTT 14406.

5.4 Summary

- In this chapter I present several data reduction methods which I have developed to better measure the parameters of close binary systems using LuckyCam data.
- Close binary resolved photometry is made difficult in many cases by the Lucky Imaging faint guide PSF being different from that of all other stars in the field, including any close companions to the guide star.
- An alteration to the Lucky Imaging process constrains the PSF error to only 1-3 pixels, which can then be re-estimated from the rest of the PSF or ignored as constraints during PSF fitting.
- Close binaries are resolved by LuckyCam into three images because of the frame alignment lock randomly shifting between the components of the binary (unless correction measures are employed). For photometric measurements, the flux ratio of the binary is most easily calculated from the fluxes of the three images.
- I present methods to obtain resolved binary photometry using Lucky images by simultaneous fits of parameterised PSFs.
- LuckyCam is an excellent speckle camera as well as Lucky Imager, although it required the development of specialised reduction techniques to calibrate and remove the effects of the L3CCD.

6

The LuckyCam Survey for VLM Binaries I. M5.5-M8 dwarfs within 40pc

In this chapter I describe the first part of the LuckyCam VLM binary survey, a survey of M5.5-M8 M-dwarfs within 40pc.

6.1 Introduction – VLM Binaries

There are compelling reasons to search for companions to nearby stars. In particular, the properties of binary systems provide important clues to their formation processes. Any successful model of star formation must be able to account for both the frequency of multiple star systems and their properties (separation, eccentricity and so forth) – as well as variations in those properties as a function of system mass. In addition, the orbits of binary systems provide us with the means to directly measure the mass of each component in the system. This is fundamental to the calibration of the mass-luminosity relation (MLR: Henry & McCarthy 1993; Henry et al. 1999; Ségransan et al. 2000).

The stellar multiplicity fraction appears to decrease with decreasing primary mass (eg. Siegler et al. 2005). Around 57% of solar-type stars (F7–G9) have known stellar companions (Abt & Levy, 1976; Duquennoy & Mayor, 1991), while imaging and radial velocity surveys of early M dwarfs suggest that between 25% & 42% have companions (Henry & McCarthy, 1990;

Fischer & Marcy, 1992; Leinert et al., 1997; Reid & Gizis, 1997). Later spectral types have been studied primarily with high resolution adaptive optics imaging: Close et al. 2003 and Siegler et al. 2005 find binary fractions of around 10–20% for primary spectral types in the range M6–L1. Bouy et al. 2003 and Gizis et al. 2003 find that 10–15% of L dwarfs have companions, and Burgasser et al. 2003 find that 10% of T dwarfs have binaries. These very low mass (VLM) M, L and T systems appear to have a tighter and closer distribution of orbital separations, peaking at around 4 AU compared to 30 AU for G dwarfs (Close et al., 2003).

However, each of these surveys have inevitably different (and hard to quantify) sensitivities, the effect of which is especially evident in the large spread in the derived multiplicity of early M-dwarfs. In particular, high-resolution imaging surveys are sensitive only to companions wider than $\sim 0.1''$ while radial velocity surveys are much more sensitive to closer (shorter period) companions. Maxted & Jeffries (2005), by examining a small sample of radial velocity measurements, estimate that accounting for systems with orbital radius < 3 AU could increase the overall observed VLM star/BD binary frequency to 32–45%. Basri & Reiners (2006) also find that taking into account spectroscopic binaries doubles the binary fraction (in a more heterogeneous sample of VLM stars and brown dwarfs).

The orbital radius distribution of VLM binary systems is also quite uncertain (figure 6.1). A well-constrained peak is found at around 4 AU, but several systems have been found at much wider radii. It is important to enlarge the sample of VLM binaries to ascertain how common these wide systems are, and whether they form a separate population of large-radius systems or are simply the tail of the distribution which peaks at 4 AU.

For these reasons, we decided to use LuckyCam to target several well-understood samples of low-mass and very low mass stars. The surveys have the aim of both increasing the known number of VLM binary systems (and finding more exotic systems such as triples and substellar companions), and constraining the binary statistics in a number of different samples.

In this thesis, I define VLM stars to have a V-K colour of > 6 (M5 and later, Leggett (1992)) and therefore a mass of $< 0.11 M_{\odot}$, following the stellar models described in Baraffe et al. (1998) for ages > 2 Gyr. The distinction between VLM and low mass stars is somewhat arbitrary, and some authors (eg. Burgasser et al. (2006)) would place the cut-off at the slightly lower primary mass of $0.10 M_{\odot}$.

6.1.1 Why high-resolution imaging?

VLM binary stars are an excellent example of a science programme which cannot be performed with seeing-limited instruments. Figure 6.1 shows the distribution of the orbital radii of known VLM binaries as of 2005 (prior to the LuckyCam survey). Only 45 VLM binaries were known (the figure at the time of writing is only on the order of 80, spanning a wide range of system total mass, mass ratios and separations). Almost all are at smaller orbital radii than 10AU.

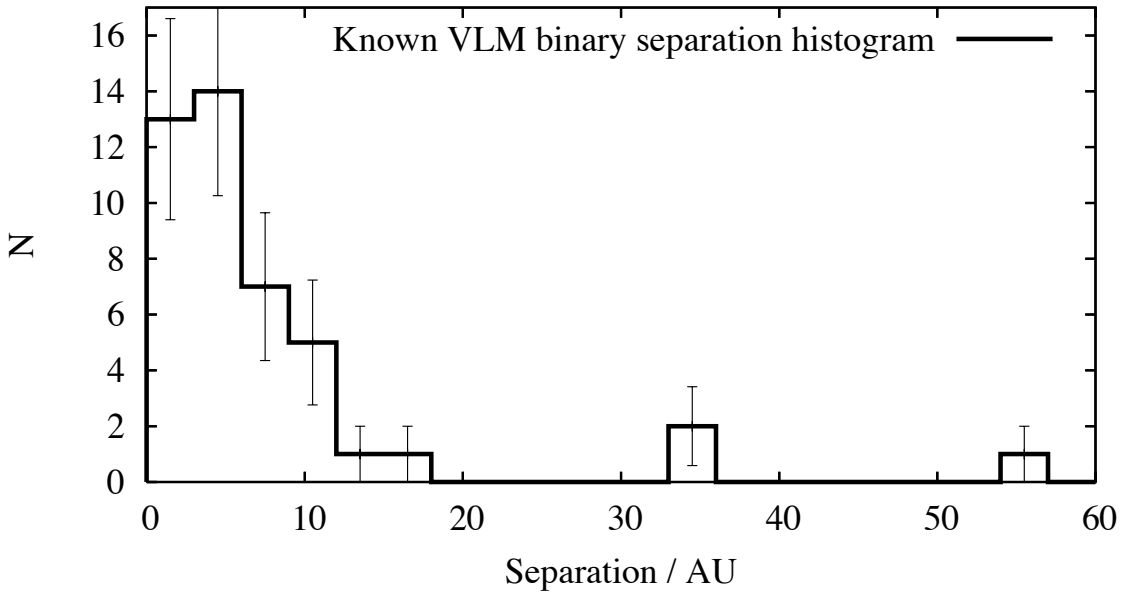


Figure 6.1: The histogram of known VLM binaries, from data collated in Siegler et al. (2005). Poisson error bars are shown on the histogram bins; note the uncertainty in the large-radius orbital distribution.

Generating a larger sample of VLM binaries for statistical studies of the nature of these systems, the aim of the LuckyCam survey and others like it, requires including target stars up to a sufficiently large distance from the Sun that a large number of M-dwarfs are within the survey volume. As figure 6.1 shows, at 10pc distance almost all VLM binaries have separations smaller than 1.0 arcsec, and 60% are at separations smaller than 0.5 arcsec. Essentially all the stars within 10pc have been surveyed for close companions; significantly extending the VLM binary sample thus requires observations with consistently better than 0.5 arcsec resolution if any large number of new systems are to be resolved. Detailed studies of the nature of the systems and the measurement of accurate astrometry requires still higher resolution. A high-resolution imaging system, capable of around 0.1 arcsec resolution, is thus required.

6.1.2 Why LuckyCam?

VLM binary surveys have been pursued using HST (eg. Bouy et al. (2003); Gizis et al. (2003)) and AO (eg. Close et al. (2003); Siegler et al. (2005)) systems. Obtaining time for an extensive survey using HST is difficult, given the popularity of the telescope. Adaptive optics surveys can be very time intensive, as each of the tens-to-hundreds of targets requires a separate re-lock of the AO systems. For example, the NAOS-CONICA AO system on the VLT requires 5-10 minutes for AO acquisition per target before data can be taken (VLT NAOS-CONICA User Manual*, 2006). Furthermore, the M-dwarfs in question are very red objects, and are thus faint in the

*http://www.eso.org/instruments/naco/doc/VLT-MAN-ESO-14200-2761_v78.pdf

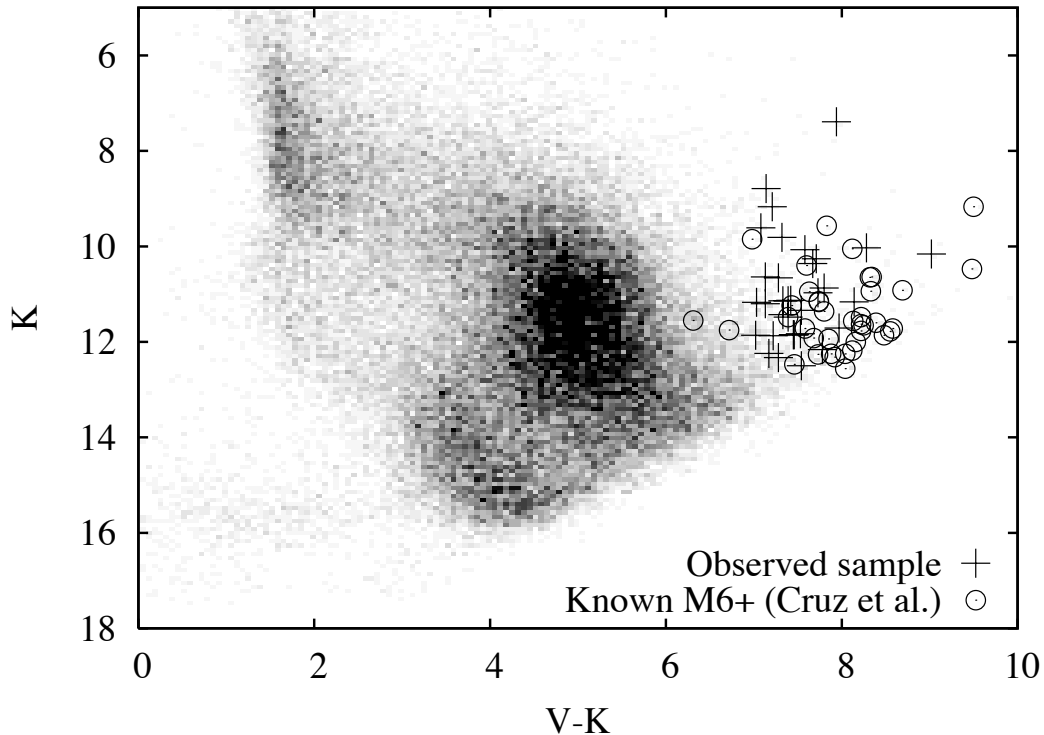


Figure 6.2: The observed sample (crosses), plotted in a V/V-K colour-magnitude diagram. The background distribution shows all stars in the LSPM-North catalogue. Circles show 38 spectroscopically confirmed M6 and later dwarfs from Cruz et al. 2003, which also appear in the LSPM-North; all but two (both M6) are recovered by the selection criteria.

visible wavelengths used by most AO systems for wavefront sensing (NAOS-CONICA has both visible and infrared WFSs).

LuckyCam offers capabilities that make it an excellent instrument for VLM binary surveys. It is a completely passive system, so data is taken as soon as the telescope is pointed. A complete observation of a candidate VLM binary target usually takes 6-7 minutes, including telescope pointing, target finding and 100 second integrations in two filters. The faint guide star capabilities of LuckyCam also allow observations of M-dwarfs that are fainter than most AO systems can use (apart from those with infrared wavefront sensors, as these objects are very red). For example, the binaries newly discovered with LuckyCam in chapter 7 are all fainter than the previously known ones in the same sample of targets.

In this chapter I present results from a 32-star VLM binary sample, completed in only 5 hours of on-sky time. I present five new VLM binaries and evaluate the utility of LuckyCam for programmes of this type, including the use of calibrated high-spatial resolution photometry.

Table 6.1: The observed sample. The quoted V & K magnitudes are taken from the LSPM catalogue. K magnitudes are based on 2MASS photometry; the LSPM-North V-band photometry is estimated from photographic B_J and R_F magnitudes and is thus approximate only, but is sufficient for spectral type estimation (figure 6.2). Spectral types and distances are estimated from the V & K photometry and the young-disk photometric parallax relations described in Leggett (1992). Spectral types are accurate to approximately 0.5 spectral classes and distances to $\sim 30\%$.

LSPM ID	2MASS ID	V	V-K	PM / arcsec/yr	Estimated spectral type	Photom. dist./pc	Newly detected companion?
LSPM J1235+1318	12351726+131805	18.0	7.7	0.219	M6.5	14	*
LSPM J1235+1709	12351850+170937	19.3	7.5	0.570	M6.5	29	
LSPM J1246+0706	12460939+070624	17.7	7.1	0.549	M6.0	19	
LSPM J1303+2414	13034100+241402	19.6	7.9	0.370	M7.0	24	
LSPM J1305+1934	13053667+193456	18.4	7.3	0.554	M6.5	22	
LSPM J1314+1320	13142039+132001	15.9	7.2	0.307	M6.0	7.7	
LSPM J1336+1022	13365393+102251	18.7	7.3	0.381	M6.5	26	
LSPM J1341+0805	13413291+080504	18.5	7.4	0.269	M6.5	22	
LSPM J1354+0846	13540876+084608	19.3	8.2	0.219	M7.0	17	
LSPM J1423+1318	14231683+131809	17.9	7.3	0.174	M6.5	18	
LSPM J1423+1426	14234378+142651	17.9	7.7	0.638	M6.5	13	
LSPM J1428+1356	14280419+135613	18.3	8.3	0.605	M8.0	10	
LSPM J1432+0811	14320849+081131	16.3	7.2	0.455	M6.0	9.2	
LSPM J1440+1339	14402293+133923	19.0	7.7	0.337	M6.5	22	
LSPM J1454+2852	14542356+285159	18.6	7.0	0.212	M6.0	32	
LSPM J1516+3910	15164073+391048	17.1	7.3	0.224	M6.5	12	
LSPM J1554+1639	15540031+163950	19.9	7.8	0.529	M7.0	30	
LSPM J1605+6912	16050677+691232	19.3	7.5	0.224	M6.5	29	
LSPM J1606+4054	16063390+405421	17.6	7.6	0.735	M6.5	12	
LSPM J1622+4934	16225554+493457	19.4	7.2	0.316	M6.0	39	
LSPM J1626+2512	16263531+251235	19.3	7.5	0.271	M6.5	29	
LSPM J1646+3434	16463154+343455	16.6	7.0	0.550	M6.0	13	
LSPM J1647+4117	16470576+411706	18.5	7.4	0.289	M6.5	22	
LSPM J1653+0000	16531534+000014	18.6	7.8	0.287	M7.0	17	
LSPM J1657+2448	16572919+244850	18.8	7.5	0.391	M7.5	23	
LSPM J1703+5910	17031418+591048	18.8	7.0	0.572	M6.0	35	
LSPM J1735+2634	17351296+263447	19.1	9.0	0.349	M9.0	9.2	
LSPM J1741+0940	17415439+094053	18.7	7.8	0.435	M7.0	17	
LSPM J1758+3157	17580020+315726	18.2	7.1	0.158	M6.0	24	
LSPM J1809+2128	18095137+212806	18.3	7.1	0.193	M6.0	32	
LSPM J1816+2118	18161901+211816	19.0	7.2	0.171	M6.0	32	
LSPM J1845+3853	18451889+385324	19.4	8.4	0.408	M8.0	16	

6.2 The Sample

We selected a distance, flux and colour limited sample of stars from the LSPM-North Catalogue (Lépine & Shara, 2005), which is the result of a systematic search for stars with declination > 0 and proper motion $> 0.15''/\text{year}$ in the Digitized Sky Surveys. Most stars in the catalogue have 2MASS IR photometry as well as V-band magnitudes estimated from the photographic B_J and R_F bands.

6.2.1 Proper motion biases

The selection of high-proper-motion stars ensures that the stars are nearby. Historically, the vast majority of stars now known to be in the solar neighbourhood were first identified as high-proper-motion stars (Lépine, 2005). However, stars with motion vectors pointing towards or away from the sun are not detected, and some distant stars can have large proper motions if their relative velocity is also large, such as stars on Galactic halo orbits (Lépine, 2005). For this reason, to construct a well-defined sample, I use colour, magnitude and photometric distance cuts to narrow down the parameter space of the targets. Giant stars are excluded by the proper motion and magnitude cut, because even halo stars, with velocities typically 2-5 \times larger than disk objects, are only likely to be 2-5 \times more distant than the rest of the candidates (Lépine & Shara, 2005).

Lépine (2005) finds that the census of nuclear-burning stars within 33pc is $\sim 68\%$ complete in the LSPM (and 82% complete within 25pc), where the main source of incompleteness is the lower proper motion limit. High-velocity stars (halo, old disk) tend to be selected from a larger distance, and may thus bias the sample (Lépine & Shara, 2005). However, in both the survey presented in this chapter and that in chapter 7 we select stars which are significantly brighter than the $V = +19.0\text{m}$ 90% completeness limit of the LSPM North survey (figure 6.2), excluding the more distant population of high-velocity stars.

6.2.2 Target List

The properties of the selected stars are detailed below:

1. $V - K > 7$; thus selecting approximately M6 and later stars (Leggett, 1992).
2. Distance $< 40\text{pc}$. Absolute magnitudes are estimated from the $V-K$ colours quoted in the LSPM and the $V-K$ vs. M_K relations described in Leggett (1992). Distances are then estimated by comparing the estimated absolute magnitude to the observed K magnitude.
3. $m_i < +15.5$; Lucky Imaging requires a $m_i = 15.5$ guide star for full performance. All targets serve as their own guide star.

4. We removed all stars from the remaining sample that had been to our knowledge previously observed at high angular resolution.

The remaining sample consists of 91 stars in the R.A. and declination range that was accessible during the survey period (June 2005). 32 were selected for these observations (picking the brightest targets first, as well as those close to the zenith during the observations), and are detailed in table 6.1. The region of colour-magnitude space in which they are found is shown in figure 6.2; the distributions of magnitudes and colours are detailed in figure 6.3.

The V-band LSPM photometry has been estimated from observations in the photographic B_J and R_F bands (as detailed in Lépine & Shara 2005), and its use therefore requires some caution. To test its utility for late M-dwarf target selection I have confirmed that a sample of spectroscopically confirmed late M-dwarfs (Cruz et al., 2003) is fully recovered by the V-K selection (figure 6.2). In addition, LuckyCam resolved SDSS i' and z' photometry gives confirmation of estimated spectral type for the objects in the full survey. In all checked cases the spectral type and distance estimated from LSPM-North V-K photometry matches that derived from LuckyCam SDSS i' and z' photometry. The LSPM V & K photometry is used extensively in the survey described in chapter 7, where more detailed checks on its accuracy are made.

6.3 Observations

We performed observations with the Cambridge Lucky Imaging system, LuckyCam, on the 2.56m Nordic Optical Telescope in June 2005, during 5 hours of on-sky time spread over 4 night observing run. Each target was observed for 100 seconds in each of the SDSS i' and z' filters. SDSS standard stars (Smith et al. 2002) were observed for photometric calibration; globular clusters and similar fields were imaged for astrometric calibration. The seeing measured by the Isaac Newton Group RoboDIMM at the observatory site varied between 0.5" and 1.0" during the observations, with a median of ~0.8".

Each target observation was completed in an average of 10 minutes including telescope pointing, 100 seconds of integration in each filter, the observation of one standard star for every three targets, and all other overheads.

For this survey we operated LuckyCam at 30 frames per second, with each frame being 552x360 pixels. The image scale was 0.04"/pixel, giving a field of view of 22×14.4 arcseconds². The observations totalled approximately 100GB. The dataset was reduced with the standard Lucky Imaging pipeline (chapter 3).

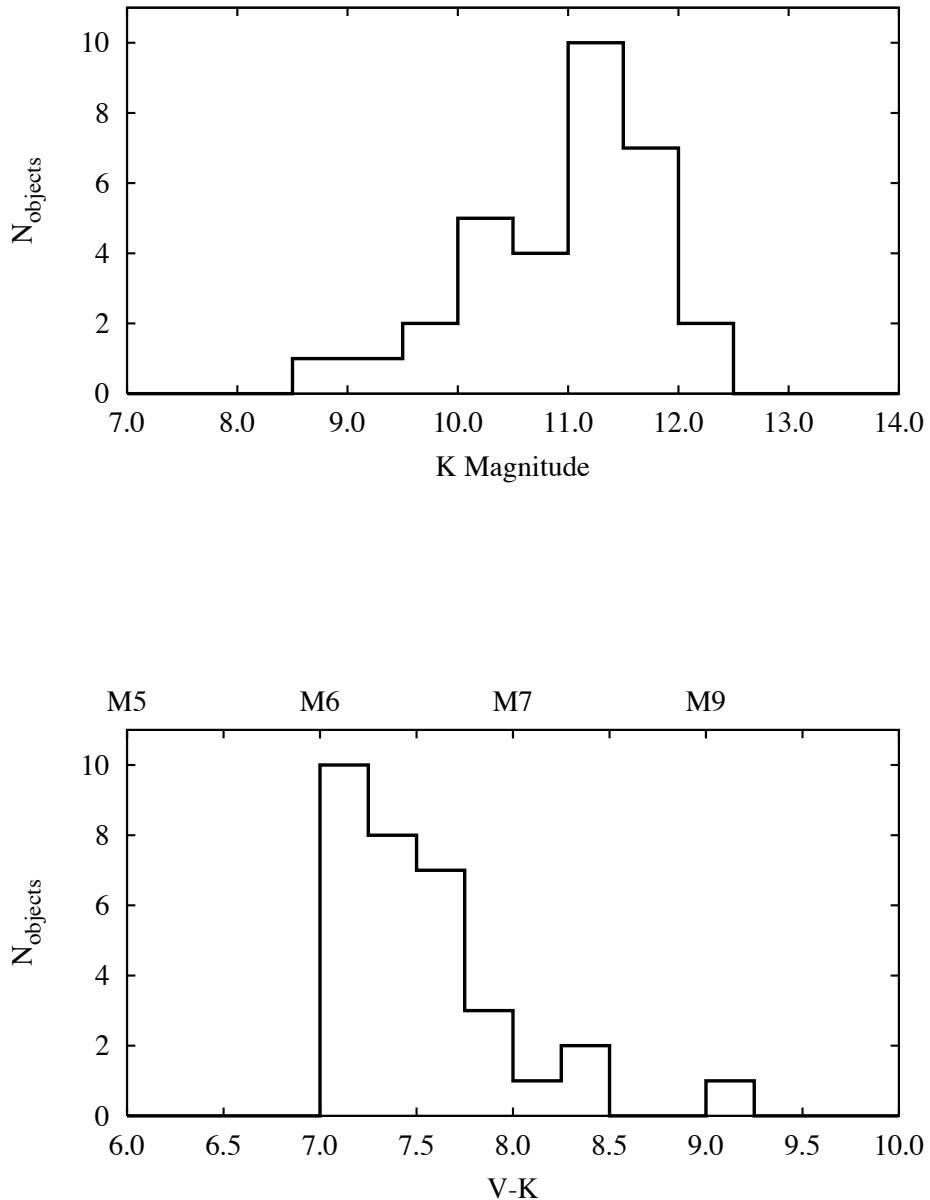


Figure 6.3: The distribution of the target sample in K magnitude and V-K colour, both from LSPM-North photometry.

6.3.1 Binary detection and photometry

Obvious binaries with a low contrast ratio and/or $> 0.5''$ separation were detected by eye in reduced images including $\leq 10\%$ of frames. I limited the companion detection radius to $1.5''$, allowing use of the remainder of the $20'' \times 14''$ fields as control areas. Because the chance probability of an object falling within the small detection radius is very low, any detections are likely to be physically associated with the target star.

In order to detect fainter companions I fit and subtract a model Moffat profile point spread function (see chapters 4 and 5) to each target, using 50% of the recorded frames to increase the SNR of faint companions at the expense of some resolution. Candidate companions were detected using a sliding-box method, with custom software implementing the detection criteria.

We stipulated the detection of a faint companion to require a 10σ deviation above the background noise, which is due to both photon and speckle noise and varies with distance from the primary star. The background noise at each radius was specified to be the upper 1σ excursion from the average RMS noise at several azimuthal positions.

In addition, I implemented the following criteria to confirm the detection of faint companions:

1. the candidate must maintain a constant flux per frame as more frames are included in the reduced images - most persistent speckles appear in only a fraction of frames and so fail this test.
2. detection must be repeated in the same position in each filter.
3. the candidate must appear point-like (extended objects are thus not detected).
4. the candidate must not be visible in the PSFs of other stars observed within a few minutes of the target, thus any removing persistent speckles and ghost images.

I measured resolved flux measurements and errors for binaries wider than $0.4''$ with simple aperture photometry. However, at closer radii more sophisticated strategies were required, especially since four of the five detected binaries had primaries fainter than $i'=15m$. As detailed in chapter 5, if a Lucky Imaging guide star is faint, its PSF is altered by frame selection proceeding partially on the basis of high excursions of photon-shot-noise. Since the companion and primary now have different PSFs, point spread function subtraction is difficult (although possible with sufficiently similar calibrator binary observations). The closest binary detected in these observations was sufficiently bright to avoid these problems, however.

Extensive experimentation confirmed that simple aperture photometry also provides accurate flux measurements at close radii for Lucky Imaging PSFs, provided that care is taken in the choice of foreground and background aperture sizes. The contrast ratios of the two close binaries with relatively faint primaries were reduced in this manner. The accuracy and precision of

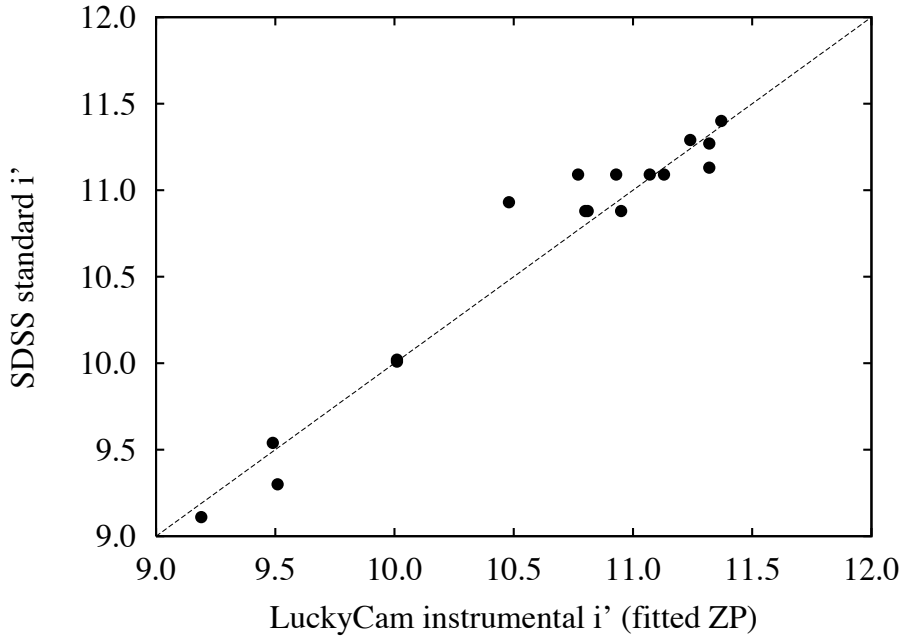


Figure 6.4: Calibration of the LuckyCam photometry against SDSS standards from Smith et al. (2002). The dashed line has a gradient of 1.0. As all the targets are very red the standards with the highest i' - z' available were used; there is no i' - z' colour term detectable within the photometric errors. As shown in chapter 2, the photometric accuracy of the LuckyCam system has also been verified with much fainter targets.

the derived contrast ratios was measured by repetition over several different frame selection fractions (and thus several different PSFs). The accuracy of the algorithms was also checked against simulated binary images. Note that these reductions were performed before the development of the more sophisticated PSF fitting routines described in chapter 5 and used in chapter 7.

For this survey, I measured photometry in the SDSS system from the total integrated flux in a 3" radius aperture, calibrated against SDSS standards (Smith et al. 2002, figure 6.4). I then used the measured contrast ratios to derive resolved photometry. In each observation the L3CCD gain is calibrated as described in chapter 2. The calibrated magnitudes are then calculated as:

$$\text{mag} = \text{ZP} - 2.5\log_{10}(\text{gain} \times \text{DN/sec}) \quad (6.1)$$

where the raw photometry is given in data numbers (DN) per second, gain is measured in photons per DN, and ZP is the photometric zero point of the system. Airmass corrections are not calculated because all observations were performed within 30° of the zenith; the approximately 10% uncertainty in the L3CCD gain calibration dominated the remaining errors.

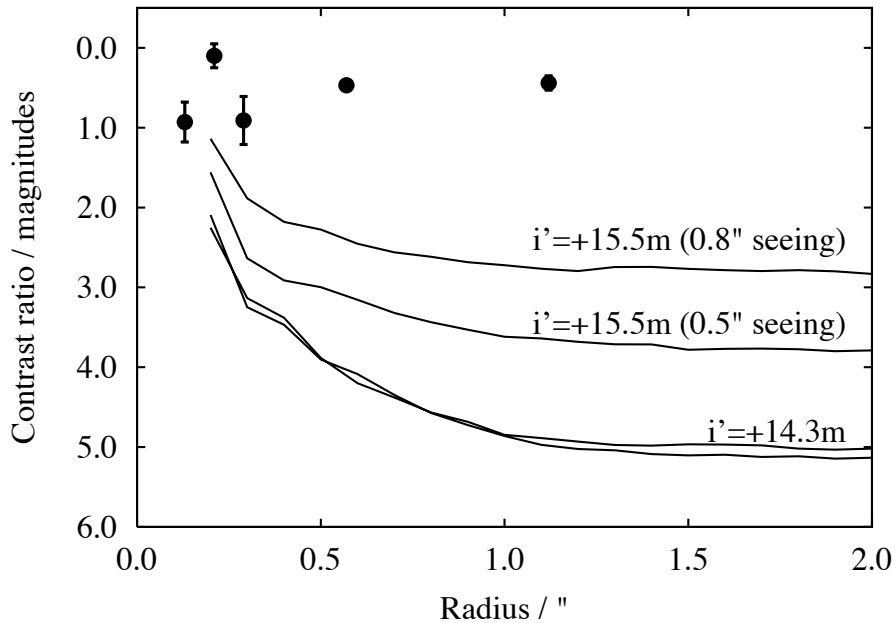


Figure 6.5: The 10σ contrast ratios achieved in a variety of conditions. The $i'=+14.3m$ star is shown in both $0.5''$ and $0.8''$ seeing; the imaging performance is not dependent on this small difference in seeing for bright stars. However, poorer seeing reduces the average light per pixel sufficiently to affect the faint guide star imaging performance (similar to the rapid falloff in image quality with guide star brightness described in chapter 4). The detected binaries are also shown; the measured contrast ratio uncertainties are often smaller than the plotted points. At radii $< 0.2''$ the cell-size of the faint companion detection algorithm does not adequately sample the shape of the PSF; detectable contrast ratios in this area are approximately 2 magnitudes, as demonstrated by the clear detection of the faint 0.15 arcsec companion to Ross 530 (section 6.4.5).

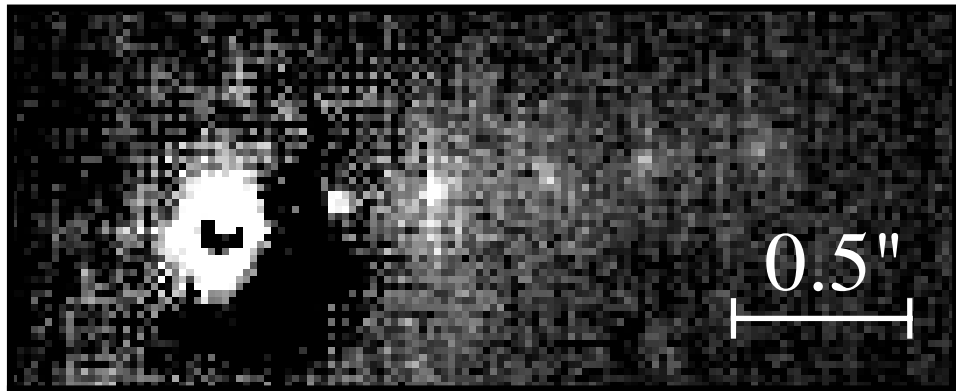


Figure 6.6: Simulated faint companion PSFs around an $i'=14m$ star. At each radius in each of the 2800 frames in this observation I added to the background a version of the primary PSF, rescaled to the 10σ detection flux shown in figure 6.5 and with appropriate Poisson and L3CCD multiplication noise added. For clarity the primary's PSF has been subtracted. The simulated companions become brighter at lower radii to allow detection above both photon and speckle noise from the primary's PSF. The residual ring around the central star is largely due to the Airy ring expected in near diffraction limited images, which is not included in the model PSF.

6.3.2 Sensitivity

Beyond $1.0''$ radius from the primary detection sensitivity is primarily limited by the sky background; at smaller radii both azimuthal variations in the target star's PSF and its photon shot noise limit the detection sensitivity. The SDSS i' detection contrast ratios for two typical stars are shown in figure 6.5 and example faint companion simulated PSFs are shown in figure 6.6.

The survey is sensitive to the detection of brown dwarf companions around all the surveyed stars. For example, around a star with $m_i \leq 14$, the survey is sensitive to $\Delta m_i = 5$ at radii $> 1.0''$ and $\Delta m_i = 4$ at $> 0.5''$. At an age of 5.0Gyr an object at the hydrogen-burning limit has $M_i \approx 16$. Typical stars in this sample have $M_i \approx 13 - 15$. Figure 6.5 thus implies the survey is sensitive to brown dwarf companions at $> 1.0''$ around all surveyed stars – and much closer (or, equivalently, much fainter) brown dwarf companions around many of the stars.

6.4 Results & Analysis

I detected five previously unknown binaries in the sample, with separations ranging from $0.13''$ to $1.12''$. Resolved i' and z' images of each binary are given in figure 6.7; their directly observed properties are summarised in table 6.2.

6.4.1 Confirmation of the binaries

In the entire June 2005 VLM binary survey observation set (including those targets from the chapter 7 sample that were observed in June 2005), covering $(22'' \times 14.4'') \times 48$ fields, there is only one field object. The object would be characterised as a companion if it had fallen close to a target star (the object is in the sample not presented in this chapter). Limiting our detection radius to $1.5''$, and thus reducing the likelihood of chance associations, the probability of one or more false associations in our dataset (i.e. the probability of any number of the new binaries not being physically associated) is therefore only 1.5%.

I also find below that the estimated photometric parallaxes of each binary's components are equal (within the stated errors), and they are therefore at equal distances, further decreasing the likelihood of contamination. Thus, I conclude that all of these candidate binaries are physically associated systems. As all of these systems have high proper motion, confirmation of common proper motion can be easily determined from repeat measurements on year timescales.

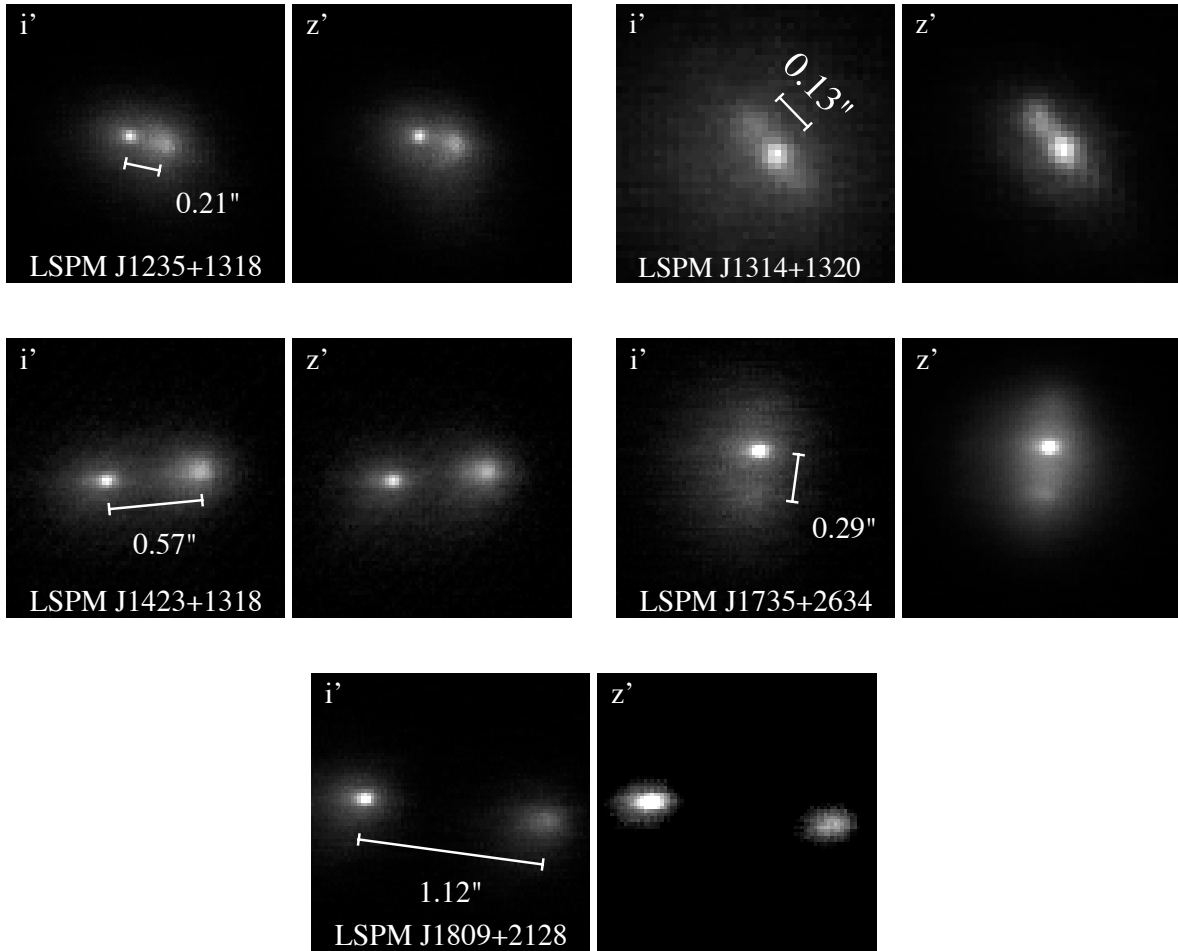


Figure 6.7: Lucky imaging of the five new binaries. All images are a 10% selection from 3000 frames taken at 30FPS, with the exception of the 0.13" binary LSPM J1314+1320 which required a more stringent selection. The very close binary's i' image is the result of a 2.5% selection from 3000 frames and its z' image is a 1.0% selection from 10,000 frames taken at the higher frame rate of 50FPS. In each case the image greyscale covers the full dynamic range of the images. All images are orientated with North up and East left. In many cases the guide star has a very compact core, due to the Lucky Imaging system aligning images partially on the basis of high photon-shot-noise excursions.

6.4.2 Distances, ages and masses

I show derived properties of the individual binary components in table 6.3. Masses of each component are estimated by comparing the component absolute magnitudes with the models presented in Baraffe et al. (1998), custom-integrated over the SDSS i' passband (I. Baraffe, private communication). In the absence of published age estimates for these targets the full range of ages found in the solar neighbourhood (0.5-10.0 Gyr (Gizis et al., 2002), with 5 Gyr as our adopted best-estimate value) is assumed (figure 6.8).

None of the 5 systems have trigonometric parallaxes, so in table 6.3 I estimate distances using the $i'-z'$ vs. M_i relations given in Hawley et al. (2002). In all cases the binary components were found to be at equal distances, within the stated errors, and I combine their values for a single more precise system distance.

6.4.3 Sensitivity to white dwarf companions

Kilic et al. (2006) describes typical cool white dwarfs in the SDSS survey, which are expected to have $i-z$ colours in the range -0.5 to +0.5 magnitudes and i' absolute magnitudes of ~ 13 -16 mags. A typical white dwarf companion would thus be detectable around all stars in this survey, and would have $i-z$ colour differing by at least .5 magnitudes from a late M-dwarf companion (although cooler white dwarfs can have similar colours to late M-dwarfs). However, it should be noted that a white dwarf companion with higher temperature than the M-dwarf primary would bias the V-K colour of the system bluewards, and so the survey V-K colour selection introduces a bias against such systems.

The four newly detected companions in this chapter which have measured $i-z$ colours are all consistent with being late M-dwarfs. Farihi et al. (2005) find that $\sim 3\%$ of white dwarfs have companions that are M5 or later; futher LuckyCam observations of many late-M-dwarfs as part of the VLM binary survey will further constrain the frequency of such systems.

6.4.4 Notes on the new systems

None of these stars have been previously investigated in detail in published work; no previous high resolution imaging or spectroscopy (resolved or unresolved) is available.

LSPM J1235+1318 A close to equal-mass 0.21" binary with an estimated distance of 24.4 ± 2.5 pc and an estimated orbital radius of 5.1 ± 0.9 AU.

LSPM J1314+1320 Resolved at a separation of only 0.13", and the system is one of the two nearest binaries presented here (9.8 ± 2.0 pc), with an orbital radius of only 1.3 ± 0.3 AU. SDSS i' photometry could not be calculated because (in this observation only) the camera gain was

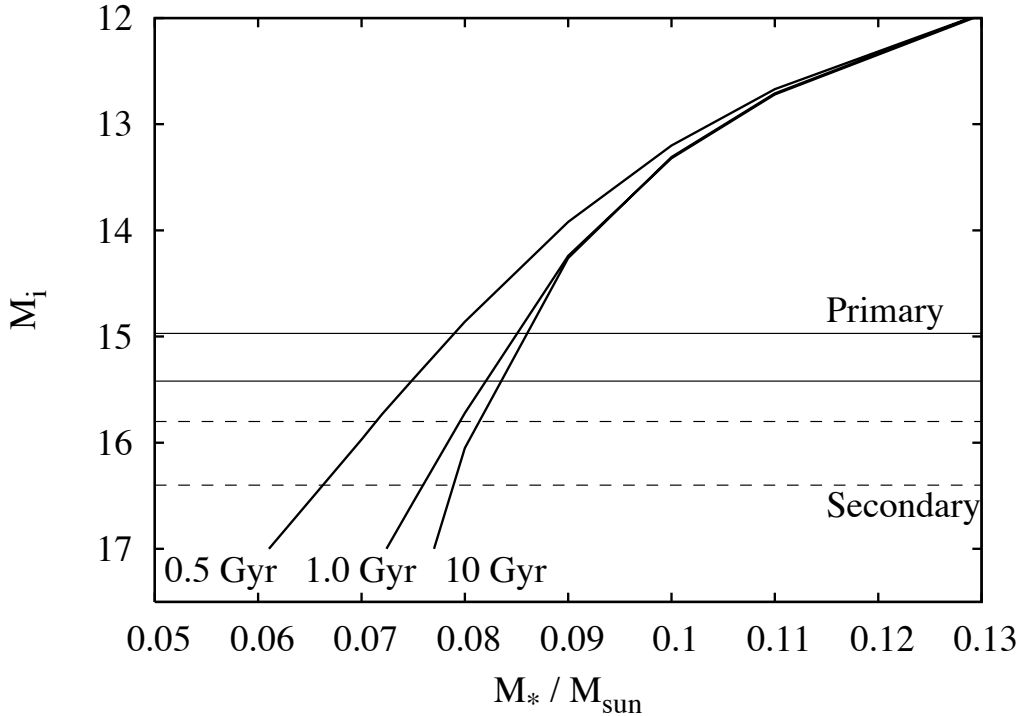


Figure 6.8: The allowed mass ranges for the components of LSPM J1735+2634. The solid horizontal lines delimit the allowed mass range for the system’s primary, given its calculated absolute magnitude; the dashed lines show the mass range of the secondary. The isochrones are from Baraffe et al. (1998); I here assume an age range covering the distribution in the solar neighbourhood, 0.5-10.0 Gyr (Gizis et al., 2002).

set too low to accurately calibrate. This system’s distance has been estimated from the V & K magnitudes listed in the LSPM North and the young disk photometric distance relations from Leggett (1992), assuming that the two components have equal V-K colours.

LSPM J1423+1318 A 0.57” binary estimated to be M5.5/M5.5 with an estimated distance 33.1 ± 3.4 pc and an orbital radius of 18.9 ± 2.0 AU.

LSPM J1735+2634 This system contains a possible brown dwarf companion, and is located at only 10-12pc. The faintness of the companion leads to difficulties in estimating resolved photometry of this system, so only upper and lower limits are noted for many of this system’s properties.

The companion has a lower mass limit of $0.066M_{\odot}$ and thus may be a brown dwarf; the allowed mass ranges are detailed in figure 6.8. Changing seeing conditions and the very red colour of the system gave a more clearly resolved image in the z’ filter; in this image the secondary appears very elongated approximately (not exactly) East-West. This elongation suggests that it is possible that the secondary is an unresolved (~ 0.04 arcsec) brown dwarf binary. This very close pair would have a very short period and can thus be rapidly confirmed with followup observations of the elongation direction.

Table 6.2: Observations of the new binary systems. Errors are 1-sigma and derived from the variation in fit values with different frame selection fractions (and thus PSFs). The position angle (PA.) error includes a 1.0° uncertainty in the orientation calibration. The companion to LSPM J1735+2634 is very faint and so only upper and lower limits to the i' and z' contrast ratios are given.

LSPM ID	2MASS ID	$\Delta i'$	$\Delta z'$	Separation (arcsec)	PA. (deg)
LSPM J1235+1318	12351726+131805	0.10 ± 0.15	0.07 ± 0.15	0.21 ± 0.03	257.0 ± 2.5
LSPM J1314+1320	13142039+132001	0.93 ± 0.25	0.97 ± 0.25	0.13 ± 0.02	46.0 ± 2.0
LSPM J1423+1318	14231683+131809	0.47 ± 0.03	0.48 ± 0.05	0.57 ± 0.01	275.6 ± 2.0
LSPM J1735+2634	17351296+263447	$0.61 - 1.21$	$0.62 - 1.11$	0.29 ± 0.01	171.2 ± 2.1
LSPM J1809+2128	18095137+212806	0.44 ± 0.09	0.40 ± 0.10	1.12 ± 0.01	262.7 ± 2.0

Table 6.3: The new binary systems' component properties. Spectral types and distances have been derived from the i' - z' relations in Hawley et al. (2002). The spectral type relations have a plateau in i' - z' at L0-L3, limiting precision for the later spectral classes. I further constrained the earliest spectral types (M5-M6) by comparing the derived i' and z' absolute magnitudes to those expected for those spectral types (Hawley et al., 2002). Orbital radius uncertainties are 1σ and are estimated in quadrature from the system distance and separation uncertainties. Masses are estimated from the allowed ranges given by the models of Baraffe et al. 1998 (figure 6.8), between the 1σ photometric errors and the range of ages in the solar neighbourhood. Values of $q > 1.0$ imply that the true primary of the system may have been identified as the secondary. LSPM J1735+2634B is very faint, leading to difficulties in estimating resolved photometry, and so I only note upper and lower limits to the system's observed and derived properties. The L3CCD gain for the i' observation of LSPM J1314+1320 was set too low to accurately calibrate, so I do not give i' photometry for this system.

LSPM ID	SDSS i' mag	SDSS z' mag	i' - z'	Spectral type	Mass / M_{\odot}	q (M_s/M_p)	Dist. / pc	orbital rad. / AU
LSPM J1235+1318A	15.1 ± 0.20	13.8 ± 0.20	1.25 ± 0.23	M5 - M7	0.097 - 0.107	0.89 - 1.08	24.4 ± 2.7	5.1 ± 0.9
LSPM J1235+1318B	15.2 ± 0.13	13.9 ± 0.13	1.30 ± 0.18	M6 - M7	0.097 - 0.106			
LSPM J1314+1320A	...	11.9 ± 0.32	9.8 ± 2.0	1.3 ± 0.3
LSPM J1314+1320B	...	12.8 ± 0.21		
LSPM J1423+1318A	15.1 ± 0.11	13.9 ± 0.12	1.21 ± 0.16	M5 - M6.5	0.108 - 0.122	0.82 - 0.99	33.1 ± 3.4	18.9 ± 2.0
LSPM J1423+1318B	15.6 ± 0.10	14.4 ± 0.11	1.20 ± 0.15	M5 - M6.5	0.099 - 0.109			
LSPM J1735+2634A	15.3 - 15.5	13.6 - 13.8	1.52 - 1.85	M7 - L3	0.077 - 0.086	0.85 - 0.96	10 - 12	2.8 - 3.6
LSPM J1735+2634B	16.1 - 16.5	14.4 - 14.7	1.69 - 2.11	M8 - L4	0.066 - 0.082			
LSPM J1809+2128A	15.6 ± 0.14	14.4 ± 0.15	1.17 ± 0.21	M5 - M6	0.124 - 0.109	0.82 - 1.03	41.8 ± 4.4	46.8 ± 5.0
LSPM J1809+2128B	16.0 ± 0.11	14.8 ± 0.12	1.21 ± 0.16	M5 - M6	0.101 - 0.112			

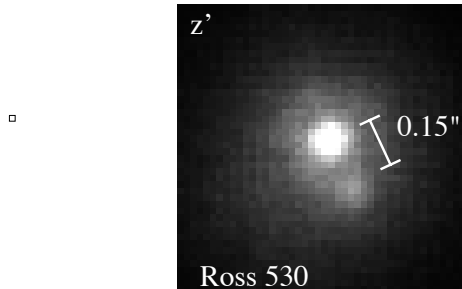


Figure 6.9: The companion to Ross 530. 5% selection from 900 frames in SDSS z'. The 0.15" binary is very clearly resolved; the diffraction limit of the telescope in z' is 0.09".

This system is an excellent target for resolved infrared photometry or spectroscopy to confirm the nature of the secondary. With an expected orbital period of approximately 15-30 years it is also well suited for astrometric followups to measure a dynamical mass.

LSPM J1809+2128 A 1.12" binary; proper motion $0.19''/\text{year}$, estimated distance $41.8 \pm 4.4\text{pc}$. With an orbital radius of $46.8 \pm 5.0\text{AU}$ this estimated M5/M5.5 system is one of the very few known VLM binaries wider than 30AU (Siegler et al., 2005; Phan-Bao et al., 2005).

6.4.5 A companion to Ross 530

During the observations I also detected a companion to Ross 530, one of the SDSS standard stars (figure 6.9). The system is very clearly resolved at only 0.15" separation.

Ross 530 is known to be a metal-poor spectroscopic binary (Latham et al., 2002), but to our knowledge this is the first resolved image of this system. From this single observation it is unclear if the single-lined spectroscopic binary has been resolved or if a new companion has been detected.

6.5 Discussion

6.5.1 The binary frequency of M5.5-M8.0 stars in this survey

5 new binaries were detected in a 32 star sample, giving a raw binary fraction of $16^{+8}_{-4}\%$. However, this survey is based on a magnitude-based distance limit that assumes all the targets are single stars. Unresolved binaries in the LSPM survey appear to be brighter and thus closer than single stars for a specific colour, as there are two luminous bodies. The observed binary fraction is thus biased as a result of leakage of binaries into the sample from further distances.

I compensate for the distance bias by comparing the volume containing the single stars in the

sample to the larger space which would contain any binaries. Lacking a useful constraint on the contrast ratios of low mass binaries I again assume a range of possible distributions - from all binaries being equal magnitude systems to a flat distribution of contrast ratios (Burgasser et al., 2003). Including the probability distribution of the raw binary fraction and the range of contrast ratio distributions yields a distance bias corrected binary fraction of $7^{+7}_{-3}\%$.

The derived binary statistics are very similar to the sample of 36 M6.0-M7.5 M-dwarfs described in Siegler et al. (2005), who obtain a distance-corrected binary fraction of $7^{+4}_{-2}\%$.

6.5.2 Contrast Ratios

I did not detect any companions at SDSS i' contrast ratios >1 magnitude, although the survey is sensitive to up to 5 magnitude differences (figure 6.5), well into the brown dwarf regime.

The new binaries are all close to equal mass (figure 6.10), in common with other VLM binary surveys which are sensitive to faint companions (eg. Close et al. 2003; Siegler et al. 2005).

6.5.3 The distribution of orbital radii

The new binaries' orbital radii are shown in figure 6.11, compared to the distribution of known VLM binary systems with primaries later than M6 (as of 2005, from Siegler et al. 2005). Three of the five new systems fall within 1-5AU, the most common radius for known VLM binaries (the surveys are incomplete at very small radii). However, one binary (LSPM J1809+2128) is one of only very few (Siegler et al., 2005; Phan-Bao et al., 2005) known VLM binaries wider than 25AU. It is important to enlarge the sample of VLM binaries to ascertain how common these wide systems are, as well as to constrain the fraction of higher order multiple systems.

6.6 Summary

- LuckyCam's very low time overheads allowed a 32 VLM star sample to be imaged at high angular resolution in only 5 hours on a 2.5m telescope.
- Lucky Imaging shows great promise for surveys of this type, offering a unique ground-based faint-guide-star visible-light imaging capability.
- I found five new VLM binaries in a 32 star sample, giving a raw binary fraction of $16^{+8}_{-4}\%$ and a distance-bias corrected fraction of $7^{+7}_{-3}\%$.
- Primaries were M5.5 to M8; most secondaries were only slightly redder than the primaries. However, one newly found system is a possible M-dwarf brown-dwarf binary.

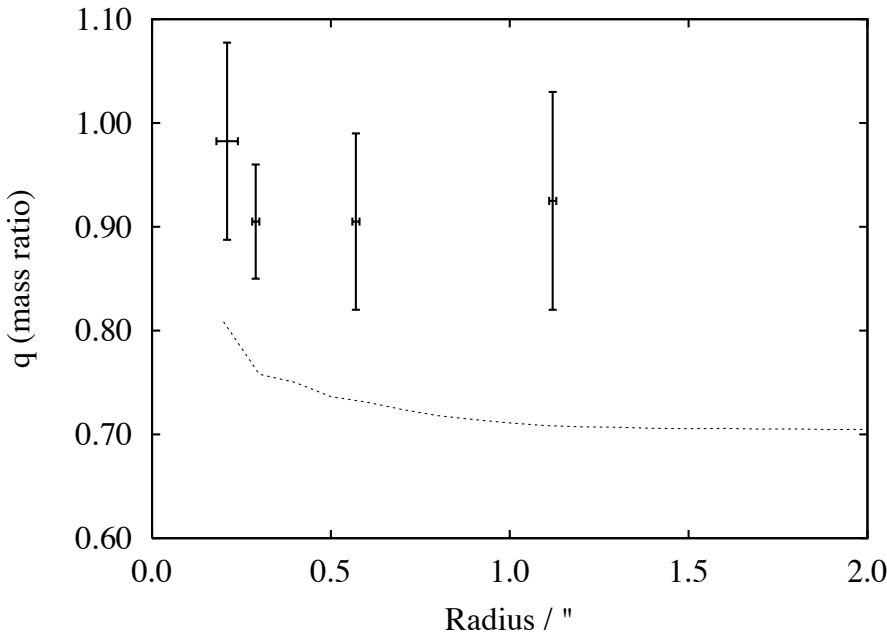


Figure 6.10: The binaries' mass ratios; an example curve shows the minimum detectable binary mass ratio for a typical star in our survey, an M6.5 primary at approximately 20pc. To generate the curve, the contrast ratios shown in figure 6.5 were used to calculate a minimum detectable companion mass from the 5.0 Gyr models given in figure 6.8.

- The distribution of orbital radii is in broad agreement with previous results, with a peak at 1-5AU, but one newly detected binary is very wide, at 46.8 ± 5.0 AU.
- No systems with a high contrast ratio were detected, even though the survey is sensitive well into the brown dwarf regime.

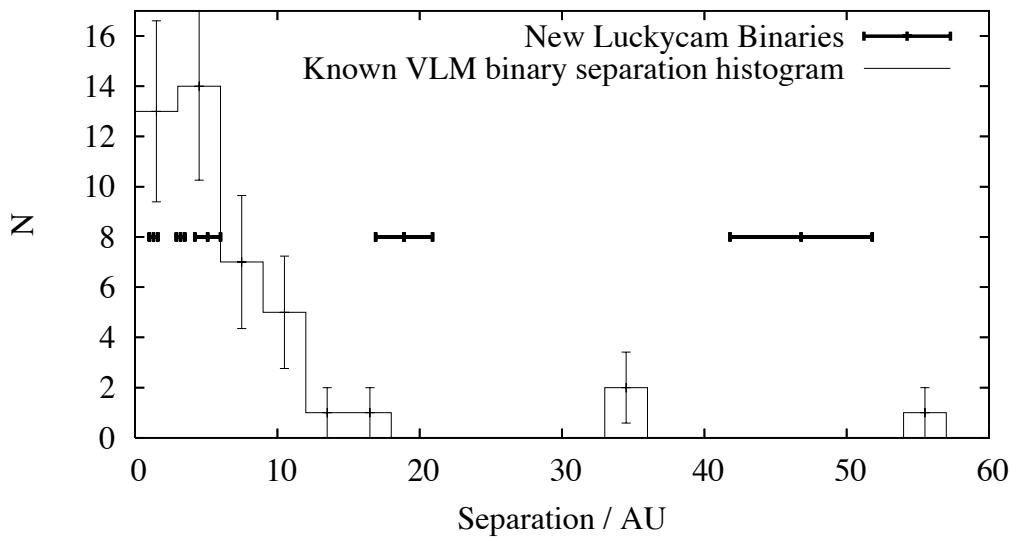


Figure 6.11: The 1σ range of orbital radii for each detected binary, compared with a histogram of the previously known sample collated in Siegler et al. (2005) (and the 33 AU VLM binary described in Phan-Bao et al. 2005). Poisson 1σ error bars are shown for the histogram - and illustrate the necessity for increased sample sizes. For reasons of clarity, the 200AU system described in Luhman (2004) is not displayed.

7

The LuckyCam Survey for VLM Binaries II. M4.5-M6.0 Targets

This chapter discusses the second of two LuckyCam VLM Binary surveys, carried out in June and November 2005. The survey is designed to further increase the number of known VLM binaries by observing targets that were not accessible to the June 2005 survey. The target sample is also more constrained and has slightly more massive targets than that of chapter 6, being a magnitude-limited survey of M-dwarfs between $V-K = 6$ ($\sim M4.5$) and $V-K = 7$ ($\sim M6$). As an additional investigation, the sample is further divided into X-ray emitting and non-emitting stars.

In this survey, a further 14 new VLM binaries were discovered using LuckyCam, in 78 targets imaged in only 11 hours on-sky.

7.1 The Sample

As in chapter 6, I selected a magnitude and colour limited sample of nearby late M-dwarfs from the LSPM-North High Proper motion catalogue (Lépine & Shara, 2005). The LSPM-North catalogue is a survey of the Northern sky for stars with annual proper motions larger than $0.15''/\text{year}$. Most stars in the catalogue are listed with both 2MASS IR photometry and V-band magnitudes estimated from the photographic B_J and R_F bands.

The LSPM-North high proper motion cut ensures that all stars are relatively nearby, and thus removes contaminating distant giant stars from the sample. I cut the LSPM catalogue to include only stars with V-K colour ≥ 6 , and K-magnitude brighter than 10. The colour cut selects approximately M5 and later stars; its effectiveness is confirmed in section 7.3.2, and also discussed in chapter 6.

7.1.1 X-ray selection

After the colour and magnitude cuts, the sample contains 231 late M-dwarfs. I then divide the late M-dwarfs into two target lists on the basis of X-ray activity. Since this is a large sample of VLM stars, we decided that interesting extra investigations would be enabled by ensuring that the observed sample contained a statistically-significant number of X-ray bright targets.

It has been demonstrated that increased magnetic activity indicators (including X-ray fluxes) correlate with increased stellar rotation rate (eg. Simon (1990); Soderblom et al. (1993)) – the so-called rotation-activity paradigm. The stellar rotation rate and therefore X-ray activity evolves with age (eg. Scholz & Eislöffel (2004)), depending on the stellar environment (for a review on the evolution of angular momentum, see Herbst & Mundt (2005)). Any correlations found between X-ray emission and the number and properties of discovered companions may then give insight into the formation environments of multiple stars.

Makarov (2002) found that field stars (mostly F & G spectral types) detected in the ROSAT Bright Source Catalogue are 2.4 times more likely to be members of wide (> 0.3 arcsec) multiple systems than those not detected in X-Rays. They suggest two hypotheses to explain the bias: 1/ The X-ray sample selects younger stars which may have higher binarity and 2/ the wide binaries have a different angular momentum evolution from single stars.

A goal of the X-ray sample selection in this chapter is to test for a correlation between X-ray emission and binarity among our sample of much later-type stars. Such a bias, if present, would be both useful and interesting. Firstly, the search for VLM binaries (and presumably higher-order systems) could be sped up by the addition of X-ray selection into target samples. Secondly, constraints on the dynamical evolution of 1AU+ radius VLM binary systems could be set by appealing to the rotation-activity paradigm.

In this chapter, I mark a star as X-ray active if the target star has a ROSAT All-Sky Survey detection from the Faint Source Catalogue (Voges et al., 2000) or the Bright Source catalogue (Voges et al., 1999) within $1.5 \times$ the 1σ uncertainty in the X-ray position. Known or high-probability non-stellar X-Ray associations noted in the QORG catalogue of radio/X-ray sources (Flesch & Hardcastle, 2004) are removed. Finally, I manually checked the Digitized Sky Survey (DSS) field around each star, and removed those stars which did not show an unambiguous association with the position of the X-ray detection. The completeness and biases of the X-Ray selection are discussed in section 7.4.2.

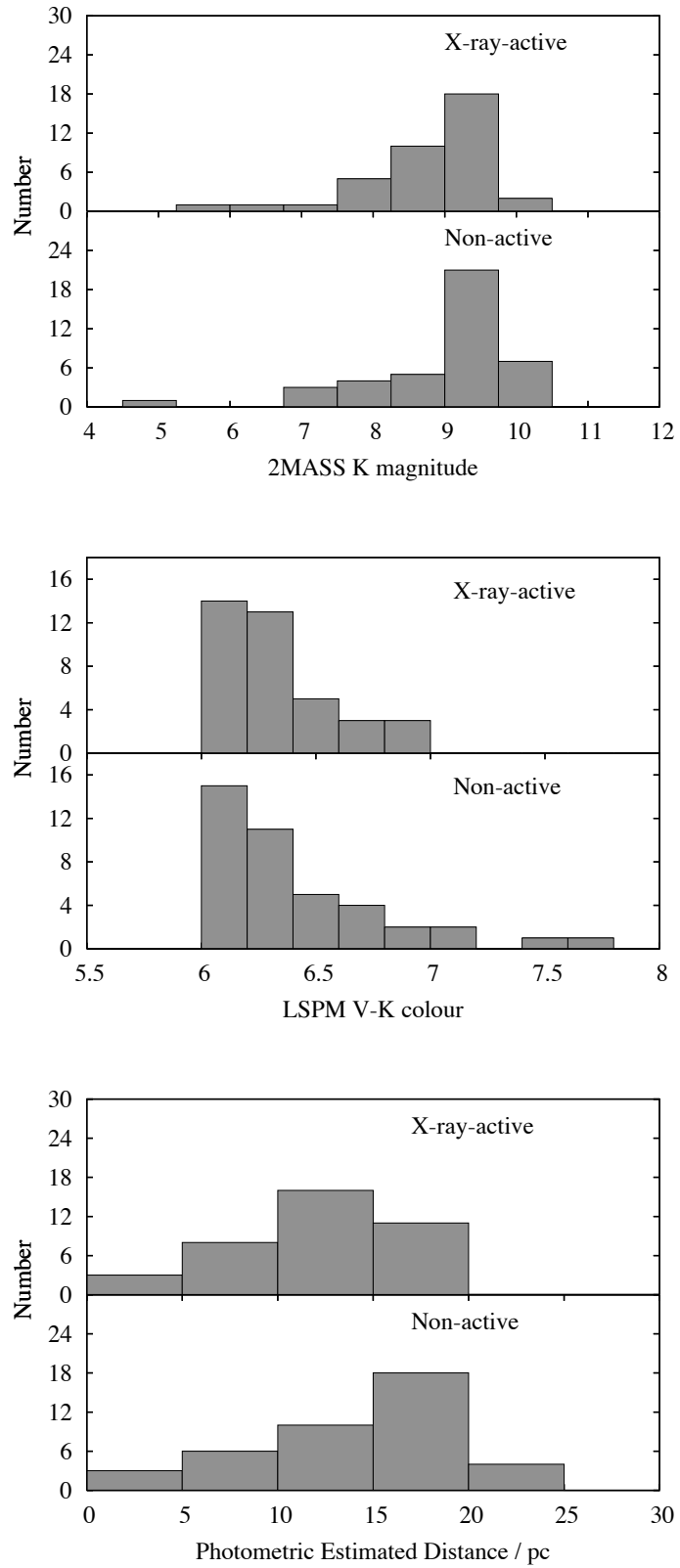


Figure 7.1: The 2MASS K-magnitude, V-K colour and distance distributions of the X-ray-active and non-X-ray-active samples. Distances are estimated from the LSMP V-K colours of the samples and the V-K photometric absolute magnitude relations detailed in Leggett (1992). The distances are accurate to approximately 30%, and assume that all targets are single stars.

LSPM ID	Other Name	K	V-K	Est. spectral type	PM/arcsec/yr
LSPM J0023+7711	LHS 1066	9.11	6.06	M4.5	0.839
LSPM J0035+0233		9.54	6.82	M5.0	0.299
LSPM J0259+3855	G 134-63	9.52	6.21	M4.5	0.252
LSPM J0330+5413		9.28	6.92	M5.0	0.151
LSPM J0406+7916	G 248-12	9.19	6.43	M4.5	0.485
LSPM J0408+6910	G 247-12	9.40	6.08	M4.5	0.290
LSPM J0409+0546		9.74	6.34	M4.5	0.255
LSPM J0412+3529		9.79	6.25	M4.5	0.184
LSPM J0414+8215	G 222-2	9.36	6.13	M4.5	0.633
LSPM J0417+0849		8.18	6.36	M4.5	0.405
LSPM J0420+8454		9.46	6.10	M4.5	0.279
LSPM J0422+3900		9.67	6.10	M4.5	0.840
LSPM J0439+1615		9.19	7.05	M5.5	0.797
LSPM J0501+2237		9.23	6.21	M4.5	0.248
LSPM J0503+2122	NLTT 14406	8.89	6.28	M4.5	0.177
LSPM J0546+0025	EM* RJHA 15	9.63	6.50	M4.5	0.309
LSPM J0602+4951	LHS 1809	8.44	6.20	M4.5	0.863
LSPM J0604+0741		9.78	6.15	M4.5	0.211
LSPM J0657+6219	GJ 3417	7.69	6.05	M4.5	0.611
LSPM J0706+2624		9.95	6.26	M4.5	0.161
LSPM J0711+4329	LHS 1901	9.13	6.74	M5.0	0.676
LSPM J0722+7305		9.44	6.20	M4.5	0.178
LSPM J0736+0704	G 89-32	7.28	6.01	M4.5	0.383
LSPM J0738+4925	LHS 5126	9.70	6.34	M4.5	0.497
LSPM J0738+1829		9.81	6.58	M5.0	0.186
LSPM J0810+0109		9.74	6.10	M4.5	0.194
LSPM J0824+2555		9.70	6.10	M4.5	0.233
LSPM J0825+6902	LHS 246	9.16	6.47	M4.5	1.425
LSPM J0829+2646	V* DX Cnc	7.26	7.48	M5.5	1.272
LSPM J0841+5929	LHS 252	8.67	6.51	M5.0	1.311
LSPM J0849+3936		9.64	6.25	M4.5	0.513
LSPM J0858+1945	V* EI Cnc	6.89	7.04	M5.5	0.864
LSPM J0859+2918	LP 312-51	9.84	6.26	M4.5	0.434
LSPM J0900+2150		8.44	7.76	M6.5	0.782
LSPM J0929+2558	LHS 269	9.96	6.67	M5.0	1.084
LSPM J0932+2659	GJ 354.1 B	9.47	6.33	M4.5	0.277
LSPM J0956+2239		8.72	6.06	M4.5	0.533
LSPM J1848+0741		7.91	6.72	M5.0	0.447
LSPM J2215+6613		7.89	6.02	M4.5	0.208
LSPM J2227+5741	NSV 14168	4.78	6.62	M5.0	0.899
LSPM J2308+0335		9.86	6.18	M4.5	0.281

Table 7.1: The observed non-X-ray-emitting sample. The quoted V & K magnitudes are taken from the LSPM catalogue. K magnitudes are based on 2MASS photometry; the LSPM-North V-band photometry is estimated from photographic B_J and R_F magnitudes and is thus approximate only, but is sufficient for spectral type estimation – see section 7.3.2. Spectral types and distances are estimated from the V & K photometry (compared to SIMBAD spectral types) and the young-disk photometric parallax relations described in Leggett (1992). Spectral types are accurate to approximately 0.5 spectral classes and distances to $\sim 30\%$.

LSPM ID	Other Name	K	V-K	ST	PM/as/yr	ROSAT BSC/FSC ID	ROSAT CPS
LSPM J0045+3347		9.31	6.50	M4.5	0.263	1RXS J004556.3+334718	2.522E-02
LSPM J0115+4702S		9.31	6.04	M4.5	0.186	1RXS J011549.5+470159	4.323E-02
LSPM J0200+1303		6.65	6.06	M4.5	2.088	1RXS J020012.5+130317	1.674E-01
LSPM J0207+6417		8.99	6.25	M4.5	0.283	1RXS J020711.8+641711	8.783E-02
LSPM J0227+5432		9.33	6.05	M4.5	0.167	1RXS J022716.4+543258	2.059E-02
LSPM J0432+0006		9.43	6.37	M4.5	0.183	1RXS J043256.1+000650	1.557E-02
LSPM J0433+2044		8.96	6.47	M4.5	0.589	1RXS J043334.8+204437	9.016E-02
LSPM J0610+2234		9.75	6.68	M5.0	0.166	1RXS J061022.8+223403	8.490E-02
LSPM J0631+4129		8.81	6.34	M4.5	0.212	1RXS J063150.6+412948	4.275E-02
LSPM J0813+7918	LHS 1993	9.13	6.07	M4.5	0.539	1RXS J081346.5+791822	1.404E-02
LSPM J0921+4330	GJ 3554	8.49	6.21	M4.5	0.319	1RXS J092149.3+433019	3.240E-02
LSPM J0953+2056	GJ 3571	8.33	6.15	M4.5	0.535	1RXS J095354.6+205636	2.356E-02
LSPM J0958+0558		9.04	6.17	M4.5	0.197	1RXS J095856.7+055802	2.484E-02
LSPM J1000+3155	GJ 376B	9.27	6.86	M5.0	0.523	1RXS J100050.9+315555	2.383E-01
LSPM J1001+8109		9.41	6.20	M4.5	0.363	1RXS J100121.0+810931	3.321E-02
LSPM J1002+4827		9.01	6.57	M5.0	0.426	1RXS J100249.7+482739	6.655E-02
LSPM J1125+4319		9.47	6.16	M4.5	0.579	1RXS J112502.7+431941	5.058E-02
LSPM J1214+0037		7.54	6.33	M4.5	0.994	1RXS J121417.5+003730	9.834E-02
LSPM J1240+1955		9.69	6.08	M4.5	0.307	1RXS J124041.4+195509	2.895E-02
LSPM J1300+0541		7.66	6.02	M4.5	0.959	1RXS J130034.2+054111	1.400E-01
LSPM J1417+3142	LP 325-15	7.61	6.19	M4.5	0.606	1RXS J141703.1+314249	1.145E-01
LSPM J1419+0254		9.07	6.29	M4.5	0.233	1RXS J141930.4+025430	2.689E-02
LSPM J1422+2352	LP 381-49	9.65	6.38	M4.5	0.248	1RXS J142220.3+235241	2.999E-02
LSPM J1549+7939	G 256-25	8.86	6.11	M4.5	0.251	1RXS J154954.7+793949	2.033E-02
LSPM J1555+3512		8.04	6.02	M4.5	0.277	1RXS J155532.2+351207	1.555E-01
LSPM J1640+6736	GJ 3971	8.95	6.91	M5.0	0.446	1RXS J164020.0+673612	7.059E-02
LSPM J1650+2227		8.31	6.38	M4.5	0.396	1RXS J165057.5+222653	6.277E-02
LSPM J1832+2030		9.76	6.28	M4.5	0.212	1RXS J183203.0+203050	1.634E-01
LSPM J1842+1354		7.55	6.28	M4.5	0.347	1RXS J184244.9+135407	1.315E-01
LSPM J1926+2426		8.73	6.37	M4.5	0.197	1RXS J192601.4+242618	1.938E-02
LSPM J1953+4424		6.85	6.63	M5.0	0.624	1RXS J195354.7+442454	1.982E-01
LSPM J2023+6710		9.17	6.60	M5.0	0.296	1RXS J202318.5+671012	2.561E-02
LSPM J2059+5303	GSC 03952-01062	9.12	6.34	M4.5	0.170	1RXS J205921.6+530330	4.892E-02
LSPM J2117+6402		9.18	6.62	M5.0	0.348	1RXS J211721.8+640241	3.628E-02
LSPM J2322+7847		9.52	6.97	M5.0	0.227	1RXS J232250.1+784749	2.631E-02
LSPM J2327+2710		9.42	6.07	M4.5	0.149	1RXS J232702.1+271039	4.356E-02
LSPM J2341+4410		5.93	6.48	M4.5	1.588	1RXS J234155.0+441047	1.772E-01

Table 7.2: The observed X-ray emitting sample. The star properties are estimated as described in the caption to table 7.1. ST is the estimated spectral type; the ROSAT flux is given in units of counts per second.

It should be noted that the fraction of stars which show magnetic activity (as measured in H α) reaches nearly 100% at a spectral type of M7, and the X-ray selection here only picks especially active stars (Gizis et al., 2000; Schmitt & Liefke, 2004). For convenience, in the remainder of the chapter the sample of stars without evidence for X-Ray activity are called non-X-ray active.

One star in the remaining sample, LSPM J0336+3118, is listed as a T-Tauri in the SIMBAD database, and was therefore removed. I note that in the case of the newly detected binary LSPM J0610+2234, which is $\sim 0.7\sigma$ away from the ROSAT X-Ray source I associate with it, there is another bright star at 1.5σ distance which may be the source of the X-Ray emission.

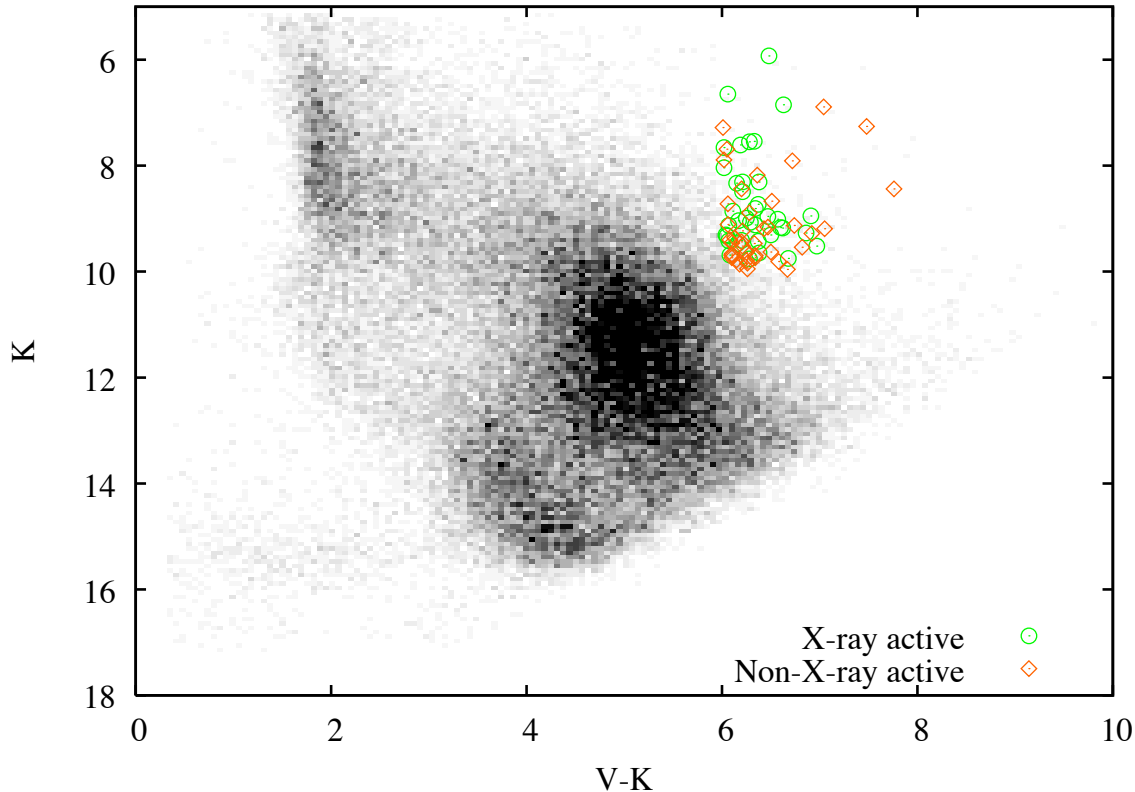


Figure 7.2: The observed samples, plotted in a V/V-K colour-magnitude diagram. The background distribution shows all stars in the LSPM-North catalogue.

Name	Ref.
GJ 3417	Henry et al. (1999)
G 89-32B	Henry et al. (1997)
V* EI Cnc	Gliese & Jahreiß (1991)
LP 595-21	Luyten (1997)
GJ 1245	McCarthy et al. (1988)
GJ 3928	McCarthy et al. (2001)
GJ 3839	Delfosse et al. (1999)

Table 7.3: The previously known binaries in this survey which are re-detected by LuckyCam.

7.1.2 Target distributions

These cuts left 51 X-ray active stars and 179 stars without evidence for X-Ray activity. I drew roughly equal numbers of stars at random from these both these lists to form the final observing target set of 37 X-Ray active stars and 41 non-X-ray active stars described in tables 7.1 and 7.2. 4 of the X-Ray active stars and 3 of the non-X-ray stars are previously known to be binary systems (detailed in table 7.3), but we reimaged them with LuckyCam to ensure a uniform survey sensitivity in both angular resolution and detectable contrast ratio.

Figure 7.1 shows the survey targets' distributions in K magnitude, V-K colour and photometrically estimated distance. Figure 7.2 compares the targets to the rest of the stars in the LSPM catalogue. The X-ray and non-X-ray samples are very similar, although the non-X-ray sample has a slightly higher median distance, at 15.4pc rather than 12.2pc (the errors on the distance determination are about 30%).

7.2 Observations

All 78 targets were imaged in approximately 11 hours of on-sky time in November 2005, using LuckyCam on the 2.56m Nordic Optical Telescope. Each target was observed for 100 seconds in both the SDSS i' and the z' filters.

The observations were performed through varying cloud cover with a median extinction on the order of three magnitudes. This did not significantly affect the imaging performance, as all these stars are 3-4 magnitudes brighter than the LuckyCam guide star requirements, but the sensitivity to faint objects was reduced. No calibrated photometry was attempted because of the rapid variations in cloud transmission, although I did perform relative photometry of the components of the detected binaries. As discussed in later sections, good constraints can be set on the orbital radii and spectral types of the systems solely on the basis of their measured separations and catalogued unresolved V-K colours.

7.2.1 Binary detection and photometry

Companions were detected according to the criteria described in detail in chapter 6. We required 10σ detections above both photon and speckle noise; the detections must appear in both SDSS i' and z' images. Detection is confirmed by comparison with point spread function (PSF) reference stars imaged before and after each target; in this case, because the observed binary fraction is only $\sim 30\%$, other survey sample stars serve as PSF references.

I measured resolved photometry of each binary system by the fitting and subtraction of two identical PSFs to each image, modelled as Moffat functions with an additional diffraction-limited core (see chapter 5). In some cases, where the target binary is faint and its components are of nearly equal brightness, photon noise can cause the Lucky Imaging software to occasionally align the images on the basis of the wrong star. This leads to an image showing three equally spaced stars in a line; in those cases, as described in chapter 5, I fit three identical PSFs and use the two flux ratios to solve for the true binary flux ratio.

7.2.2 Sensitivity

The sensitivity of the survey was limited by the cloud cover. Because of the difficulty of flux calibration under very variable extinction conditions I do not give an overall survey sensitivity. However, a minimum sensitivity can be estimated. LuckyCam requires an $i' = +15.5$ m guide star to provide good correction; all stars in this survey must be at least that bright*. The sensitivity of the survey around a $i = +15.5$ m star is calculated in chapter 6 and the sensitivity as a function of companion separation is discussed in section 7.4.4.

As noted in chapter 6, the survey is also sensitive to white dwarf companions around all stars in the sample. However, until calibrated resolved photometry is obtained for the systems it is not possible to distinguish between the M-dwarf and white-dwarf companions. Since a large sample of very close M-dwarf companions to white dwarf primaries have been found spectroscopically (for example, Delfosse et al. (1999); Raymond et al. (2003)), but few have been resolved, it will be of interest to further constrain the incidence of these systems.

7.3 Results & Analysis

14 new low mass and very low mass binaries were found, as well as two possible detections. The binaries are shown in figure 7.3 and the observed properties of the systems are detailed in table 7.4. In addition to the new discoveries, we confirmed seven previously known binaries, also detailed in table 7.4.

GJ 376B is known to be a common-proper-motion companion to the G star GJ 376, located at a distance of 134 arcsec (Gizis et al., 2000). Since the separation is very much greater than can be detected in the LuckyCam survey, I treat it as a single star in the following analysis.

G 256-25 and GJ3971 both show PSF elongation indicative of binarity but are not fully resolved; the elongation is not present in stars taken before or after those targets. Both targets were taken at high zenith angle without an ADC, and so their elongation may be the result of atmospheric dispersion. For that reason, I do not include the two stars as confirmed binary detections, and followup observations of the targets are required.

7.3.1 Confirmation of the binaries

In the entire LuckyCam VLM binary survey, covering a total area of $(22'' \times 14.4'') \times 122$ fields, there are 10 objects which would have been detected as companions if they had happened to be close to the target star. One of the detected objects is a known wide common proper motion

*LSPM J2023+6710 was observed through ~ 5 magnitudes of cloud, and was too faint for Lucky Imaging. However, it is a 0.9 arcsec binary with roughly equal brightness components, and so could be detected in centroid-centred images

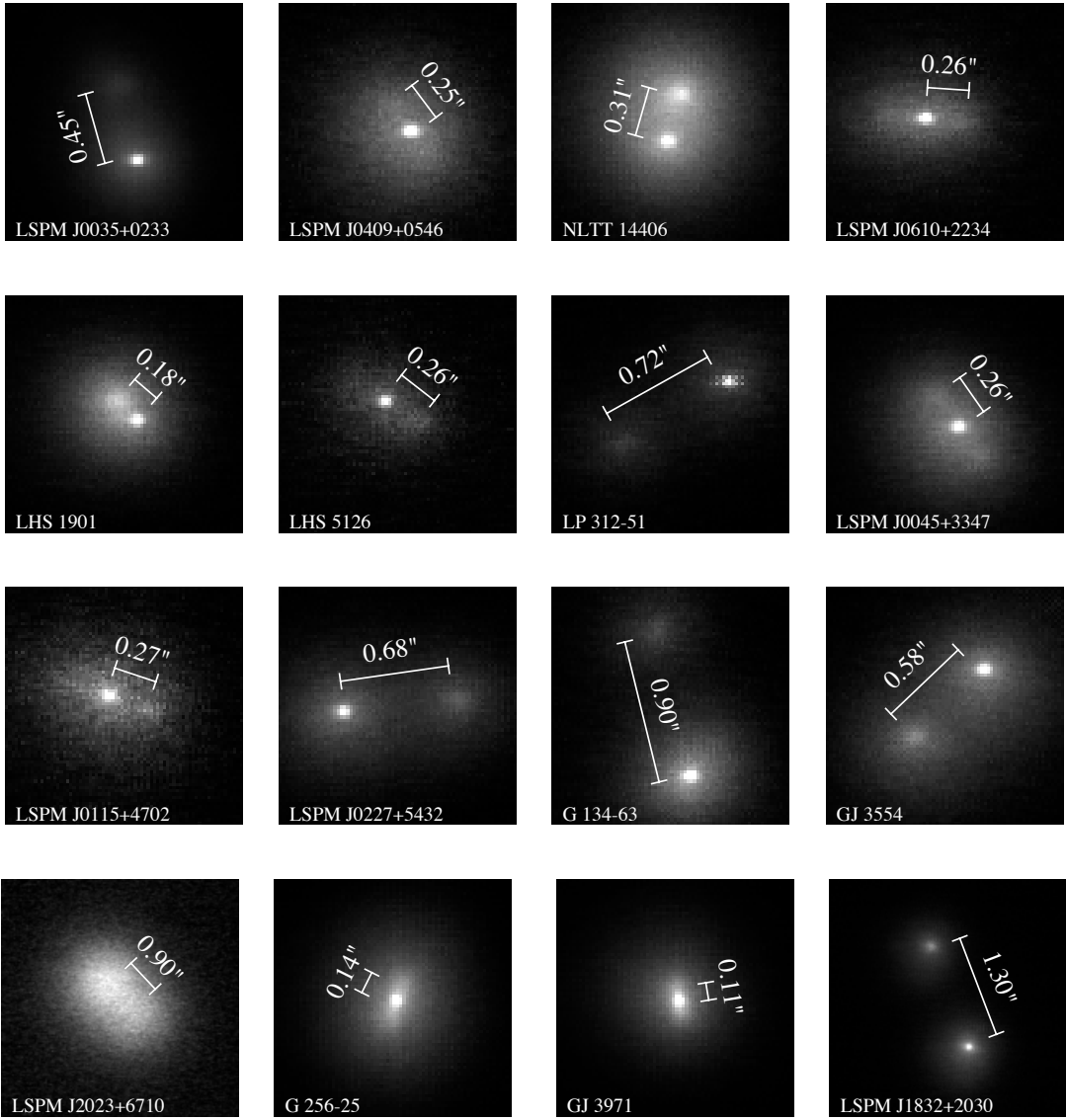


Figure 7.3: The newly discovered binaries. All images are orientated with North up and East to the left. The images are the results of a Lucky Imaging selection of the best 10% of the frames taken in SDSS i' , with the following exceptions: LSPM J0409+0546, LSPM J0610+2234 and LSPM J0859+2918 are presented in the z' band, as the cloud extinction was very large during their i' observations. The image of LSPM J0738+4925 uses the best 2% of the frames taken and LSPM J0115+4702S uses the best 1%, to improve the light concentration of the secondary. LSPM J2023+6710 was observed through more than 5 magnitudes of cloud extinction, and was thus too faint for Lucky Imaging; a summed image with each frame centroid-centred is presented here, showing clear binarity.

Name	$\Delta i'$	$\Delta z'$	Sep. (arcsec)	PA. (deg)	Epoch	X-ray emitter?
LSPM J0035+0233	1.30 ± 0.30	...	0.446 ± 0.01	14.3 ± 1.4	2005.9	
LSPM J0409+0546	< 1.5	< 1.5	0.247 ± 0.01	40.0 ± 3.2	2005.9	
NLTT 14406	1.30 ± 0.30	0.77 ± 0.30	0.310 ± 0.01	351.6 ± 1.1	2005.9	
LSPM J0610+2234	< 1.0	< 1.0	0.255 ± 0.01	268.4 ± 2.7	2005.9	*
IHS 1901	1.30 ± 0.70	1.30 ± 0.70	0.177 ± 0.01	51.4 ± 1.6	2005.9	
IHS 5126	0.50 ± 0.20	0.50 ± 0.30	0.256 ± 0.02	235.1 ± 3.4	2005.9	
LP 312-51	0.74 ± 0.10	0.51 ± 0.10	0.716 ± 0.01	120.5 ± 1.1	2005.9	
LSPM J0045+3347	0.80 ± 0.35	0.77 ± 0.35	0.262 ± 0.01	37.6 ± 1.9	2005.9	*
LSPM J0115+4702S	0.55 ± 0.25	0.73 ± 0.25	0.272 ± 0.01	249.8 ± 1.3	2005.9	*
LSPM J0227+5432	0.60 ± 0.10	0.59 ± 0.10	0.677 ± 0.01	275.8 ± 1.1	2005.9	*
G 134-63	1.55 ± 0.10	1.35 ± 0.10	0.897 ± 0.01	13.6 ± 1.1	2005.9	
GJ 3554	0.51 ± 0.20	0.57 ± 0.20	0.579 ± 0.01	44.0 ± 1.1	2005.9	*
LSPM J2023+6710	0.55 ± 0.20	...	0.900 ± 0.15	232.5 ± 3.2	2005.9	*
LSPM J1832+2030	0.48 ± 0.10	0.45 ± 0.10	1.303 ± 0.01	20.6 ± 1.1	2005.4	*
GJ 3417	1.66 ± 0.10	1.42 ± 0.10	1.526 ± 0.01	-39.8 ± 1.0	2005.9	
G 89-32	0.43 ± 0.10	0.38 ± 0.10	0.898 ± 0.01	61.3 ± 1.0	2005.9	
V* EI Cnc	0.62 ± 0.10	0.49 ± 0.10	1.391 ± 0.01	76.6 ± 1.0	2005.9	
LP 595-21	0.74 ± 0.10	0.60 ± 0.10	4.664 ± 0.01	80.9 ± 1.0	2005.9	*
GJ 1245AC	2.95 ± 0.20	2.16 ± 0.20	1.010 ± 0.01	-11.3 ± 1.0	2005.4	*
GJ 3928	2.32 ± 0.20	2.21 ± 0.20	1.556 ± 0.01	-10.7 ± 1.0	2005.4	*
LP 325-15	0.36 ± 0.10	0.33 ± 0.10	0.694 ± 0.01	-21.5 ± 1.0	2005.4	*

Table 7.4: The observed properties of the detected binaries. The top group are stars with newly detected companions; the bottom group are the previously known systems. LSPM J0409+0546 and LSPM J0610+2234 were observed through thick cloud and in poor seeing, and so only upper limits on the contrast ratio are given. LSPM J2023+6710 was not observed in z' , and cloud prevented useful z' observations of LSPM J0035+0233.

LSPM ID	Years since DSS obs.	Motion since DSS obs.
1RXS J004556.3+334718	16.2	4.3"
G 134-63	16.2	4.1"
NLTT 14406	19.1	3.4"
LHS 1901	16.0	10.8"
LHS 5126	6.8	3.4"
LP 312-51	7.6	3.3"
GJ 3554	15.8	5.0"
LSPM J2023+6710	14.2	4.2"

Table 7.5: The newly discovered binaries which have moved far enough since DSS observations to allow confirmation of the common proper motion of their companions.

companion; others are due to random alignments. For the purposes of this section, I assume that all detected widely separated objects are not physically associated with the target stars.

Limiting the detection radius to 2 arcsec around the target star (I confirm wider binaries by testing for common proper motion against DSS images) 0.026 random alignments would be expected in our dataset. This corresponds to a probability of only 2.5 per cent that one or more of the apparent binaries detected here is a chance alignment of the stars. I thus conclude that all the detected binaries are physically associated systems.

8 of the newly discovered binaries have moved more than one DSS PSF-radius between the acquisition of DSS images and these observations (table 7.5). With a limiting magnitude of $i_N \sim +20.3m$ (Gal et al., 2004), the DSS images are deep enough for clear detection of all the companions found here, should they actually be stationary background objects. None of the DSS images show an object at the present position of the detected proposed companion, confirming the common proper motions of these companions with their primaries.

7.3.2 The nature of the target stars

Because of the cloudy conditions during most of the observations, calibrated resolved photometry is not available for the components of 12 of the 14 new systems, and thus individual estimates of the spectral types and masses of the components are difficult to obtain. However, unresolved V & K-band photometry listed in the LSPM survey allows useful constraints on the nature of these targets. Because the LSPM V-band magnitudes are only approximate estimates from photographic magnitudes, it is necessary to check their accuracy and precision for spectral type determination.

The MK spectral type of approximately one third of the stars in our sample is listed in the SIMBAD database, based on spatially unresolved spectroscopy from Jaschek (1978). Plotting the LSPM V-K colour against the spectroscopic spectral type (figure 7.4) we find that all survey

targets are M3 and later. Stars with $6.0 < V-K < 6.5$ have an average spectral type of M4.5, with a 1σ range of 0.5 spectral types, while those with redder V-K colours are all later than M5.

The estimated spectral type of the unresolved system is dominated by the primary's spectral type, as shown in table 7.6. Unresolved V & K-band photometry thus allows a reasonably precise determination of the primary component's spectral type. The secondary's spectral type can then be constrained on the basis of the contrast ratio of the binary.

To ensure that all binaries are measured on the same spectral type system, I list spectral types derived in the above way for all systems, notwithstanding if a spectroscopic spectral type is available in the literature.

7.3.3 Distances

The measurement of the distances to the stars is a vital step in the determination of the orbital radii of the systems. None of the newly discovered binaries presented here has a measured parallax (although four* of the previously known systems do) and calibrated resolved SDSS i' and z' photometry is not available for almost all the systems. I therefore calculate distances to the newly discovered systems using the V-K colour-absolute magnitude relations described in Leggett (1992). Calculation of the distances in this manner requires care, as the V and K-band photometry is unresolved, and so two luminous bodies contribute to the observed colours and magnitudes.

The estimated distances to the systems, and the resulting orbital separations, are given in table 7.7. The stated 1σ distance ranges include the following contributions:

- A 0.6 magnitude Gaussian-distributed uncertainty in the V-K colour of the system (a combination of the colour uncertainty noted in the LSPM catalogue and the maximum change in the V-K colour of the primary induced by a close companion, as discussed in section 7.3.2).
- A 0.3 magnitude Gaussian-distributed uncertainty in the absolute K-band magnitude of the system, from the uncertainty in the colour-absolute magnitude relations
- A 0.75 magnitude flat-distributed uncertainty in the absolute K-band magnitude of the system, to account for the unknown K-band contrast ratio of the binary system (which can be between equal magnitude and almost all the light coming from the primary).

*G 132-25 (NLTT 2511) is listed in Reid & Cruz (2002) and the SIMBAD database as having a trigonometric parallax of 14.7 ± 4.0 mas, based on the Yale General Catalogue of Trigonometric Stellar Parallaxes (van Altena et al., 2001). However, this appears to be a misidentification, as the star is not listed in the Yale catalogue. The closest star listed, which does have the parallax stated for G 132-25 in Reid & Cruz (2002), is LP 294-2 (NLTT 2532). This star has a very different proper motion speed and direction to G 132-25 (0.886 arcsec/yr vs. 0.258 arcsec/yr in the LSPM catalogue & SIMBAD). In addition, the G 132-25 LSPM V and K photometry is inconsistent with an M-dwarf at a distance of 68pc. I thus do not use the stated parallax for G 132-25.

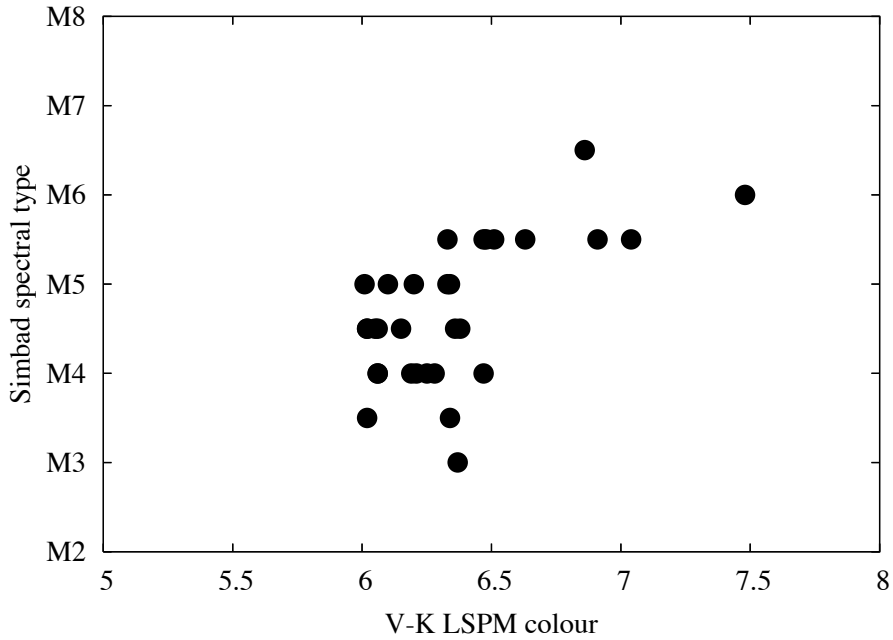


Figure 7.4: The stars in the sample which have a spectral type listed in the SIMBAD database. Stars with $V-K > 6.5$ are well-constrained to have spectral types later than M5. Stars with $6.0 < V-K < 6.5$ have an average spectral type of M4.5, with a 1σ range of 0.5 spectral types.

	Primary							
Secondary	M2	M3	M4	M5	M6	M7	M8	M9
M2	4.20 [M2]							
M3	4.34 [M2]	4.75 [M3]						
M4	4.34 [M2]	4.90 [M3]	5.25 [M4]					
M5	4.28 [M2]	4.90 [M3]	5.43 [M4]	6.00 [M5]				
M6	4.23 [M2]	4.82 [M3]	5.37 [M4]	6.20 [M5]	7.25 [M6]			
M7	4.22 [M2]	4.80 [M3]	5.33 [M4]	6.17 [M5]	7.48 [M6]	8.00 [M7]		
M8	4.22 [M2]	4.78 [M3]	5.31 [M4]	6.14 [M5]	7.53 [M6]	8.25 [M7]	8.75 [M8]	
M9	4.22 [M2]	4.78 [M3]	5.31 [M4]	6.13 [M5]	7.54 [M6]	8.28 [M7]	8.82 [M8]	8.90 [M9]

Table 7.6: The apparent V-K colour of an unresolved binary system, calculated from the V-K vs. spectral type and absolute magnitude relations detailed in Leggett (1992). Each cell of the table corresponds to a different combination of stellar spectral types; the V-K based spectral type that would be estimated for the system is given in brackets. In all cases, because of the rapid falloff in luminosity with later spectral types, the estimated spectral type from unresolved V & K-band photometry is the same as that of the most massive (earliest type) component of the binary. The uncertainties in each V-K colour are approximately 0.35 mags.

The resulting distances have 1σ errors of approximately 35%, with a tail towards larger distances due to the K-band contrast ratio uncertainties. The photometrically-estimated distances to three of the four systems with astrometric parallaxes match to within one sigma. The fourth (LP 325-15) differs by $\sim 1.5\sigma$. Although parallax-based measurements of the distance to these systems would be ideal, distances based on resolved i and z photometry for each component of the multiple systems produces only 10-15% distance uncertainties (chapter 6). We are planning photometric followup of these systems to improve the distance estimates.

7.3.4 Notes on some individual systems

Two of the detected systems benefit from detailed discussion.

NLTT 14406 – A Triple System

NLTT 14406 is identified with LP 359-186 in the NLTT catalogue (Luyten, 1995), although it is not listed in the revised NLTT catalogue (Salim & Gould, 2003). LP 359-186 is a component of the common-proper-motion (CPM) binary LDS 6160 (the Luyten Double Star catalogue; Luyten (1997)), with the primary being LP 359-216 (NLTT 14412), 167 arcsec distant and listed in the SIMBAD database as a M2.5 dwarf.

The identification of these high proper motion stars can be occasionally problematic when working over long time baselines. As a confirmatory check, the LSPM-listed proper motion speeds and directions of these candidate CPM stars agree to within 1σ (using the stated LSPM proper motion errors). In the LSPM catalogue, the two stars are separated by 166.3 arcsec at the J2000.0 epoch. I thus identify the newly discovered M6, 4.4AU companion to NLTT 14406 as a member of a triple system with an M2.5 primary located at 2280^{+1080}_{-420} AU.

The Orbit of GJ 1245AC

The astrometric binary GJ 1245AC was first resolved by McCarthy et al. (1988), using one-dimensional speckle interferometry. Schroeder et al. (2000) used HST to obtain the first direct resolved image of the system. Figure 7.5 shows a comparison of the LuckyCam imaging and the HST Wide Field Planetary Camera 2 (WFPC2) observations.

Harrington (1990) quotes an astrometrically derived orbit for GJ 1245AC. As a test of the capability of the LuckyCam VLM binary survey to calculate orbits for close binaries, I compared the predicted position of the companion star to the calculated position from the stated orbit (figure 7.6(a)). To increase the number of data points available, I supplemented the LuckyCam positions with the two positions listed in Schroeder et al. (2000). I also retrieved two

Name	Parallax / mas	Distance / pc	Orbital rad. / AU	Prim. spec. type	Sec. spec. type
LSPM J0035+0233	...	14.5 ^{+6.3} _{-2.4}	6.8 ^{+3.1} _{-1.0}	M5.0	M6.0
LSPM J0409+0546	...	19.9 ^{+9.1} _{-3.8}	4.9 ^{+2.7} _{-0.7}	M4.5	\leq M6.0
NLTT 14406	...	13.7 ^{+6.5} _{-2.5}	4.4 ^{+2.3} _{-0.7}	M4.5	M5.5
LSPM J0610+2234	...	17.0 ^{+7.5} _{-2.9}	4.6 ^{+2.1} _{-0.8}	M5.0	\leq M6.0
LHS 1901	...	12.3 ^{+5.6} _{-4.0}	2.3 ^{+1.1} _{-0.4}	M4.5	M6.0
LHS 5126	...	19.5 ^{+8.9} _{-3.7}	4.9 ^{+2.9} _{-0.6}	M4.5	M5.0
LP 312-51	...	21.5 ^{+10.1} _{-4.0}	16.1 ^{+8.2} _{-2.7}	M4.5	M5.0
LSPM J0045+3347	...	14.9 ^{+7.0} _{-2.6}	4.0 ^{+2.1} _{-0.6}	M4.5	M5.5
LSPM J0115+4702S	...	18.7 ^{+9.3} _{-3.6}	5.2 ^{+2.9} _{-0.9}	M4.5	M5.0
LSPM J0227+5432	...	18.6 ^{+9.5} _{-3.4}	13.2 ^{+7.2} _{-2.2}	M4.5	M5.0
G 134-63	...	18.8 ^{+9.3} _{-3.4}	17.6 ^{+9.4} _{-2.8}	M4.5	M5.5
GJ 3554	...	11.8 ^{+5.6} _{-2.2}	7.1 ^{+3.7} _{-1.2}	M4.5	M4.5
LSPM J2023+6710	...	13.6 ^{+5.9} _{-2.5}	12.8 ^{+6.5} _{-2.6}	M5.0	M5.0
LSPM J1832+2030	...	20.6 ^{+9.6} _{-3.9}	27.0 ^{+14.6} _{-4.0}	M4.5	M5.0
GJ 3417	87.4 \pm 2.3	11.4 ^{+0.3} _{-0.3}	17.5 ^{+0.5} _{-0.5}	M4.5	M6.5
G 89-32	...	7.3 ^{+3.9} _{-1.3}	6.5 ^{+3.5} _{-1.1}	M4.5	M5.0
V* EI Cnc	191.2 \pm 2.5	5.23 ^{+0.07} _{-0.07}	7.27 ^{+0.11} _{-0.11}	M5.5	M6.0
LP 595-21	...	16.5 ^{+8.2} _{-2.7}	76.2 ^{+38.7} _{-11.8}	M4.5	M5.5
GJ 1245AC	220.2 \pm 1.0	4.54 ^{+0.02} _{-0.02}	4.6 ^{+0.05} _{-0.05}	M5.0	M8.5
GJ 3928	...	10.2 ^{+5.6} _{-1.7}	15.7 ^{+8.8} _{-2.5}	M4.5	M6.5
LP 325-15	62.2 \pm 13.0	16.1 ^{+3.4} _{-3.4}	11.2 ^{+2.4} _{-2.4}	M4.5	M4.5

Table 7.7: The derived properties of the binary systems. The top group are stars with newly detected companions; the bottom group are the previously known binaries. All parallaxes are from the Yale General Catalogue of Trigonometric Stellar Parallaxes (van Altena et al., 2001). Distances and orbital radii are estimated as noted in the text; the stated errors are $1-\sigma$. The binary contrast ratio is the magnitude of the companion minus the magnitude of the primary. Spectral types of the primaries are derived from the V-K colour of the unresolved system and the relations in Leggett (1992). The secondaries' spectral types are derived by: 1/ assuming the estimated primary spectral type to be the true value and 2/ using the spectral type vs. i' and z' absolute magnitude relations in Hawley et al. (2002) to estimate the difference in spectral types between the primary and secondary. The primaries' spectral types have a 1σ uncertainty of ~ 0.5 subtypes (section 7.3.2); the difference in spectral types is accurate to ~ 0.5 spectral subtypes.

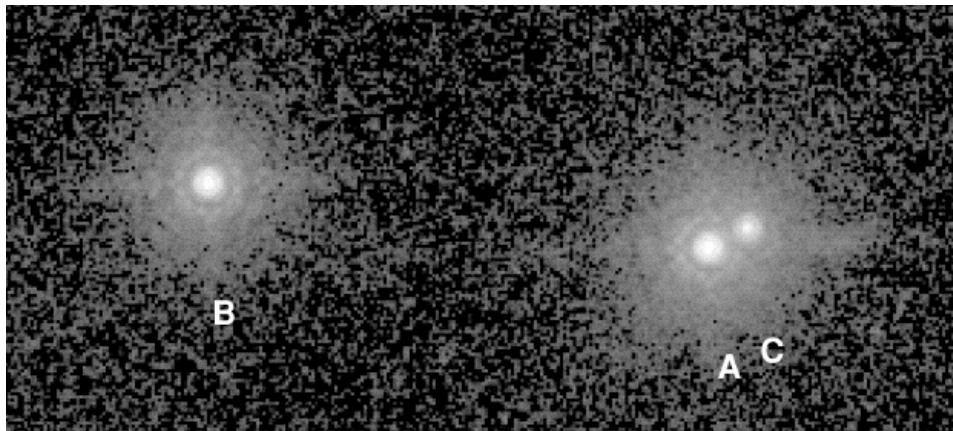
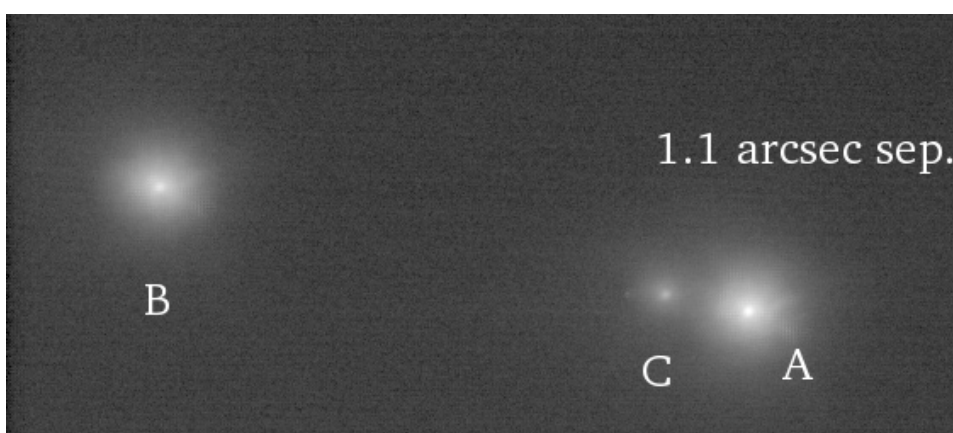
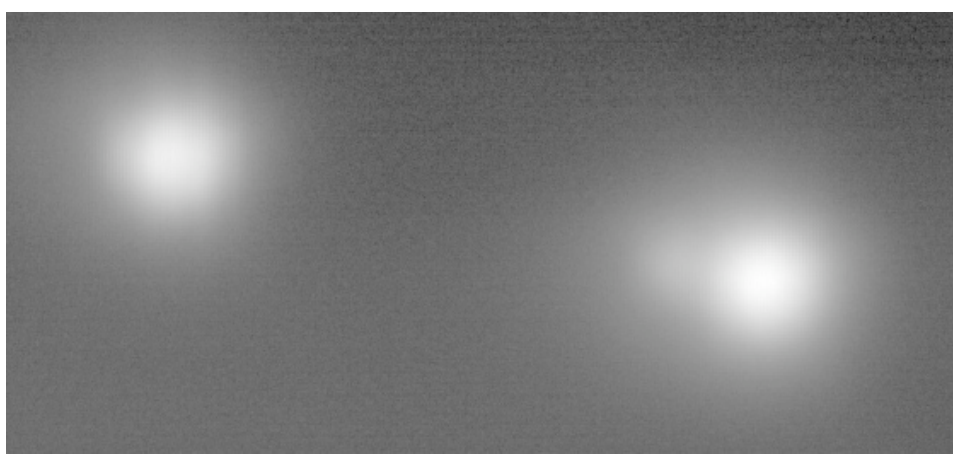
(a) HST WFPC2, $1.02\mu\text{m}$, Oct. 1997(b) LuckyCam, $0.77\mu\text{m}$, June 2005(c) Seeing-limited, $0.77\mu\text{m}$, June 2005

Figure 7.5: Imaging of the triple system GJ1245AC. The HST WFPC2 image is reproduced from Schroeder et al. (2000), and the seeing-limited image is simulated from the LuckyCam data. All the images are on a logarithmic scale, and are orientated with North up and East to the left. The orbital motion of both the C and B components is clearly evident.

epochs of archival HST observations of the system and measured the centred position of the companion for those dates.

As also found by Schroeder et al. (2000) from two measured positions, the measured orbit falls behind the calculated positions, by 18 months for the Schroeder et al. (2000) epoch and about two years for the LuckyCam measurement. The strong agreement in the direction and timing of the orbit discrepancy between the several HST measurements and the LuckyCam measurements indicates that the Harrington (1990) orbit is in error in at least one of its parameters.

In figure 7.6(b) I show a re-fit to the orbit of GJ 1245AC using the LuckyCam and HST data points. The orbit calculation follows that described in Argyle (2004); I used a simulated-annealing minimisation routine (Press et al., 1988) to fit the orbital parameters to the data. The resulting parameters are listed in figure 7.6(b); the main alteration from the Harrington (1990) orbit is an increase in orbital period, from 15.22 years to 17.65 years, and a 4% increase in the orbital radius.

Kepler's Third Law relates the orbital period and radius to the total system mass:

$$P^2 = \frac{4\pi^2 a^3}{G(M+m)} \quad (7.1)$$

where P is the orbital period, a is the orbital radius, M is the primary mass and m is the secondary mass. The total system mass was estimated to be $0.205M_\odot$ in Harrington (1990); with the new orbit the total system mass is decreased by 20% to $0.17M_\odot$. On the basis of the previous orbit, Henry et al. (1999) find that the companion straddles the stellar-brown dwarf border with a mass of $0.074M_\odot$; the lowering of the total system mass pushes the companion well into the brown dwarf regime. This test illustrates that LuckyCam can perform these orbit-tracking programmes very easily.

7.4 Discussion

7.4.1 The binary frequency of stars in this survey

14 new binaries are present in a sample of 78 VLM stars, as well as a further 7 previously known binaries. This corresponds to a binary fraction of $26.9^{+5.5}_{-4.4}\%$, assuming Poisson errors. However, as in chapter 6, this value does not take into account the larger volume of space occupied by the binary stars in our sample, compared to the single stars. Binaries appear to be brighter for a given colour because there are two luminous bodies, and so for a given distance appear closer than the single stars in our sample. Correcting for this, assuming a range of contrast ratio distributions between all binaries being equal magnitude and all contrast ratios being equally likely (Burgasser et al., 2003), I find a distance-corrected binary fraction of

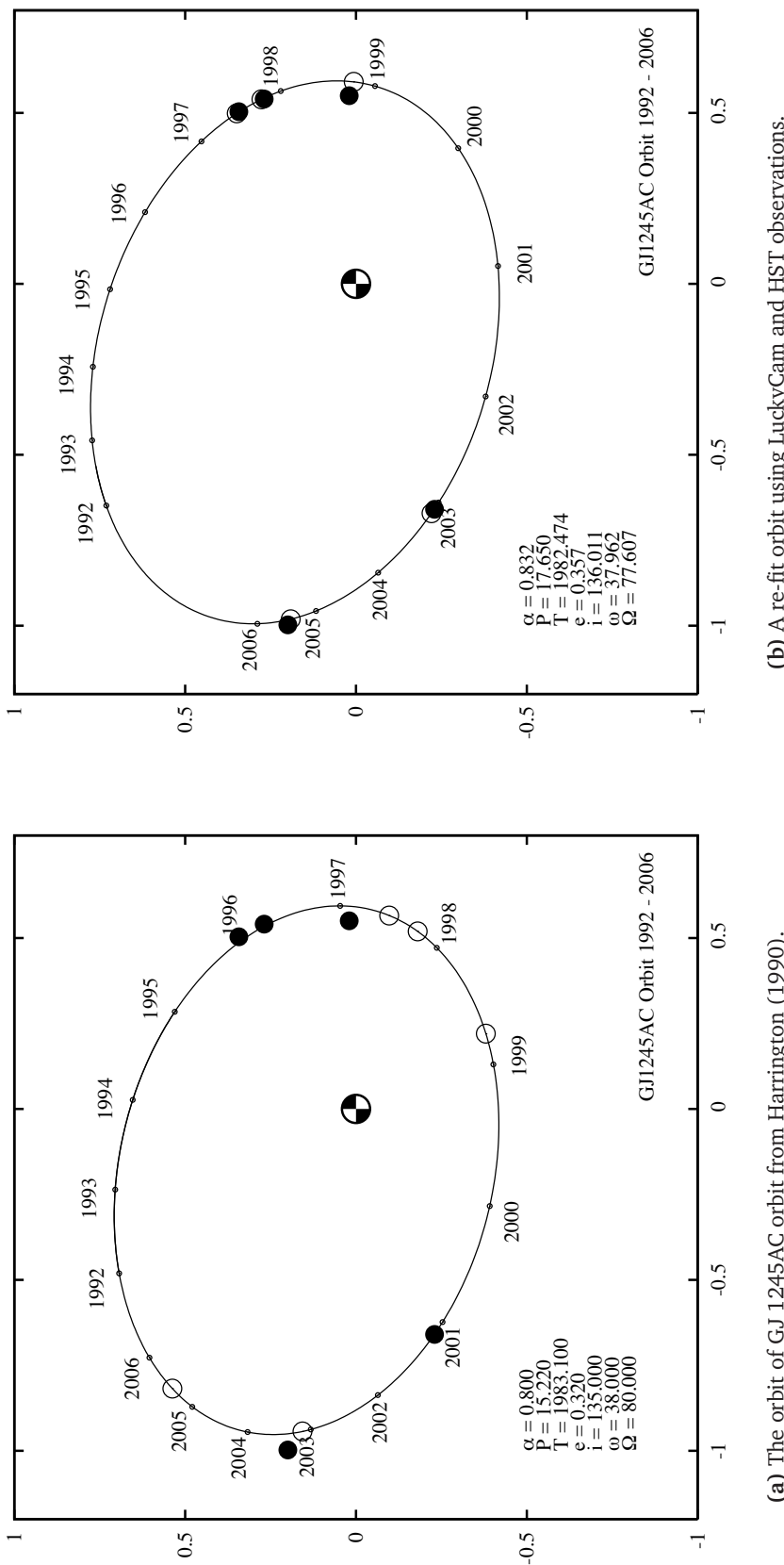


Figure 7.6: The orbit of GJ 1245AC. The year markers around the orbit show the *predicted* position of the the secondary. The filled circles are measured positions (the leftmost is from LuckyCam; all others are from HST archival data or Schroeder et al. (2000)). The open circles mark the predicted position of the secondary at the epoch of each of the measured positions. The parameters of the two orbits are noted on the figures; α is the orbital semi-major axis in arcsecs, P is the period in years, T is the periastron time, e is the eccentricity, i is the inclination in degrees, ω is the periastron argument in degrees and Ω is the position angle of the node in degrees.

$13.5^{+6.5}_{-4}\%$.

Because the binaries are more distant on average than the single stars in this survey, they also have a lower average proper motion. This implies that the LSPM proper motion cut will preferentially remove binaries from a sample which is purely selected on magnitude and colour. The above correction factor for the increase magnitude of binary systems does not include this effect, and so will overestimate the number of binaries selected in the survey.

A detailed examination of these and other biases (for sensitivity to faint companions, for example) would require a Monte-Carlo simulation of the survey. The simulation would generate a sample of several hundred thousand M-dwarfs, with velocities and masses following the ranges found in the solar neighbourhood. Companions would then be randomly assigned to the stars, and a simulation of the sensitivity of the LuckyCam imaging system applied. Comparison with the observed results would then allow the confidence ranges of the population parameters (binarity, companion mass, etc) to be determined. This procedure may be undertaken in future work.

7.4.2 Biases in the X-ray sample

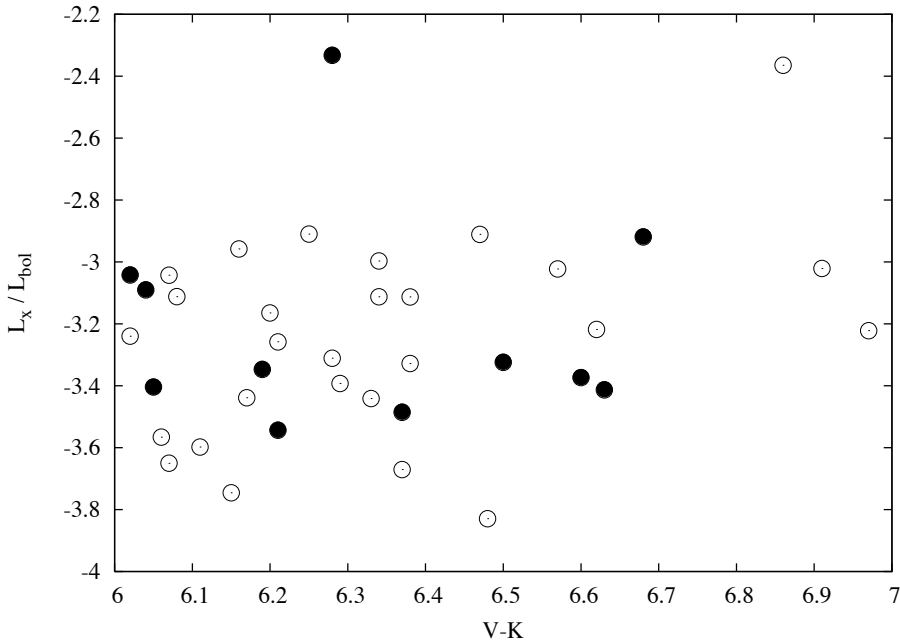
Before testing for correlations between X-ray emission and binary parameters, it is important to assess the biases introduced in the selection of the X-ray sample.

The X-ray flux assignment criteria described in section 7.1.1 are conservative. To reduce false associations, the X-ray source must appear within 1.5σ of the candidate star, which implies that $\sim 13\%$ of true associations are rejected. The requirement for an unambiguous association will also reject some fraction of actual X-ray emitters ($\sim 10\%$ of the candidate emitting systems were rejected on this basis). The non-X-ray emitting sample will thus contain some systems that do actually meet the X-ray flux-emitting limit.

The X-ray source detection itself, which cuts only on the detection limit in the ROSAT Faint Source catalogue, is biased both towards some sky regions (the ROSAT All-Sky Survey does not have uniform exposure time (Voges et al., 1999) and towards closer stars. However, these biases have only a small effect: all but three of the target stars fall within the relatively constant-exposure area of the ROSAT survey, where the brightness-cutoff is constant to within about 50%. The samples also do not show a large bias in distance – the X-ray stars' median distance is only about 10% smaller than that of the non-X-ray sample (figure 7.1).

The X-Ray active stars also represent a different stellar population from the non-active sample. In particular, the X-ray active stars are more likely to be young (eg. Jeffries (1999) and references therein). It may thus be difficult to disentangle the biases introduced by selecting young stars from those intrinsic to the population of X-ray emitting older stars.

The latter bias is very important, as it introduces uncertainty into the nature of the target



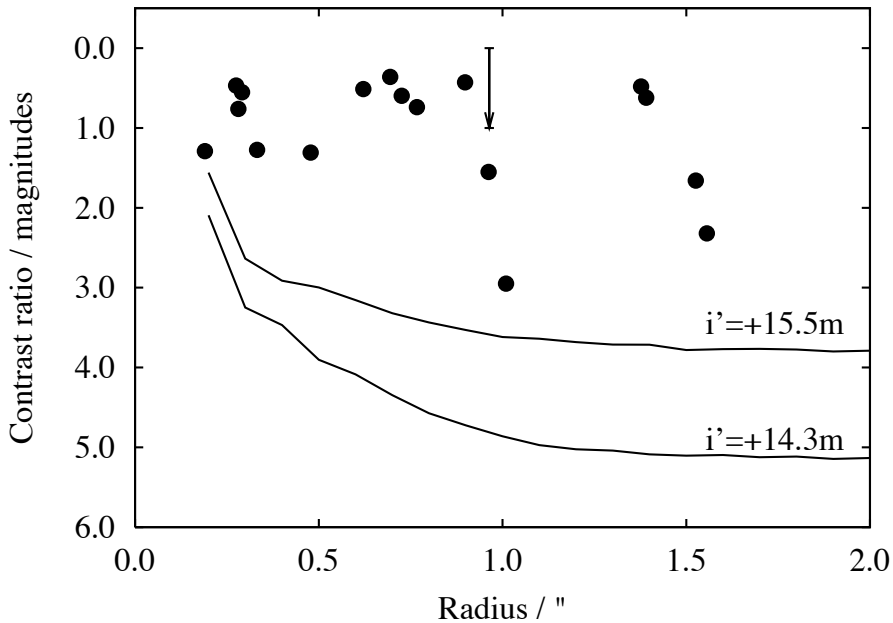


Figure 7.8: The i -band contrast ratios of the detected binaries. The sensitivity curves for two primary component magnitudes are also shown (from the tests detailed in chapter 6).

very large L_x/F_{bol} (GJ 376B and LSPM J1832+2030) are listed as flaring sources in Fuhrmeister & Schmitt (2003) (a survey of variability in the ROSAT all-sky survey) and thus were probably observed during flare events (although Gizis et al. (2000) argues that GJ 376B is simply very active).

This contrasts with the 2.4 times higher binarity among the similarly-selected sample of F & G type X-ray active stars in Makarov (2002). However, the binary fractions themselves are very similar, with a 31% binary fraction among X-ray active F & G stars, compared with 13% for X-ray mute F & G stars. Since the fraction of stars showing X-Ray activity increases towards later types, it is possible that the Makarov sample preferentially selects systems containing an X-ray emitting late M-dwarf. However, most of the stellar components detected in Makarov (2002) are F & G types, so it is unclear if the discrepancy can be explained in that way.

7.4.4 Contrast ratios

Figure 7.8 compares the contrast ratios of the detected systems to the instrumental sensitivity, derived from the tests presented in chapter 6. In common with previous surveys, all but two of the detected systems have contrast ratios lying between 0 and 1.7 magnitudes. This is well above the survey sensitivity limits, as illustrated by the two binaries detected at much larger contrast ratios. Although those two systems are at larger radii, they would have been detected around most targets in the survey at as close as 0.2–0.3 arcsec (for example, see the faint companion to Ross 530 detected at 0.15 arcsec in chapter 6).

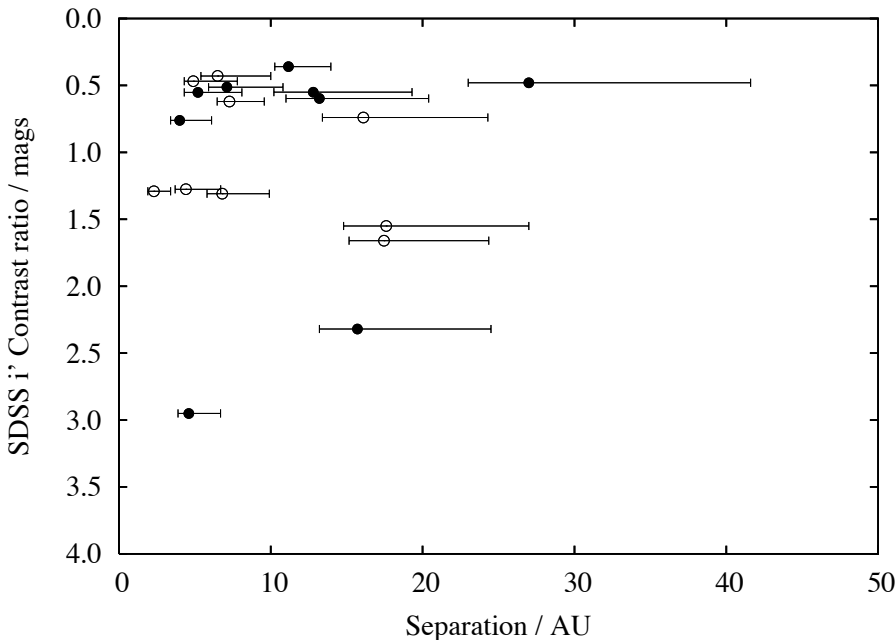


Figure 7.9: The i-band contrast ratios of the detected binaries, plotted as a function of binary separation in AU. For reasons of clarity, the 76AU binary and the contrast ratio errorbars (table 7.4) have been omitted. Filled circles are X-ray emitters.

It is difficult to obtain good constraints on the mass contrast ratio for these systems because of the lack of calibrated photometry, and so I leave the determination of the individual component masses for future work (although some progress could be made with the contrast ratios in the current data). However, an interesting feature of the sample is that no binaries with contrast ratios consistent with equal mass stars are detected (one such binary was detected in chapter 6).

There is no obvious correlation between the orbital radius and the i-band contrast ratios, nor between X-ray emission and the contrast ratios (figure 7.9).

7.4.5 The distribution of orbital radii

Previous VLM surveys have found a peak in the VLM binary orbital radius distribution at around 4AU. The orbital radius distribution derived in this survey (figure 7.10) replicates this peak, but 9 of the 21 systems are at a nominal radius of more than 10 AU (this chapter's surveyed primary stellar masses range from $0.089M_{\odot}$ to $0.11M_{\odot}$ using the models in Baraffe et al. (1998)). In the 36 M6-M7.5 M-dwarf sample of Siegler et al. (2005), 5 binaries are detected but none are found to be wider than 10AU. Note in most of these systems (as for the LuckyCam surveys) the projected separation at a particular epoch is measured, rather than the system's semi-major axis.

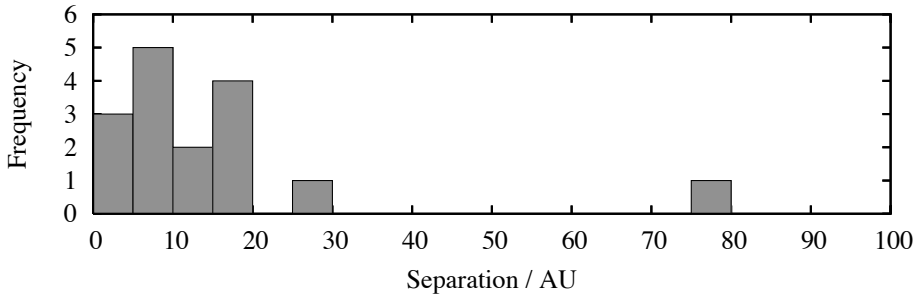


Figure 7.10: The histogram distribution of orbital radii of the detected binaries in the sample.

Looking at all known VLM systems*, only 13 out of 77 known binaries are wider than 10AU.

Early M-dwarfs and G-dwarfs binaries have a broad orbital radius peak of around 30AU (Fischer & Marcy, 1992; Duquennoy & Mayor, 1991). Is it possible that the wider orbital radius binaries detected here are drawn from a population that has the same orbital radius distribution as higher mass stars? If so, a colour bias would be expected in the orbital radius distribution, with the redder objects having smaller orbital radii. Plotting system separation against V-K colour (figure 7.11), all but one of the systems with orbital radii larger than 10AU have V-K < 6.5 , while the systems with < 10 AU orbital radius are evenly distributed between V-K = 6 and V-K = 7. However, a Kolmogorov-Smirnov (K-S) test does not find a significant difference between the two distributions, with a 29% probability that the orbital radius distributions are consistent.

To decrease the uncertainty in the comparison of distributions, I supplemented the V-K > 6.5 systems from the LuckyCam sample with the known VLM binaries from the Siegler collection (which, due to a different mass cut, all have a lower system mass than the LuckyCam sample). To reduce selection effects from the instrumental resolution cut-offs, I only considered VLM binaries with orbital radius > 3.0 AU. The resulting cumulative probability distributions are shown in figure 7.12. There is a clear deficit in wider systems in the V-K > 6.5 sample compared to the earlier type systems. A K-S test between the two orbital radius distributions gives an 8% probability that they are derived from the same underlying distribution. Although the test

*Collated by Nick Siegler at http://paperclip.as.arizona.edu/~nsiegler/VLM_binaries/; VLM there is defined at the slightly lower value of total system mass of $< 0.2M_{\odot}$

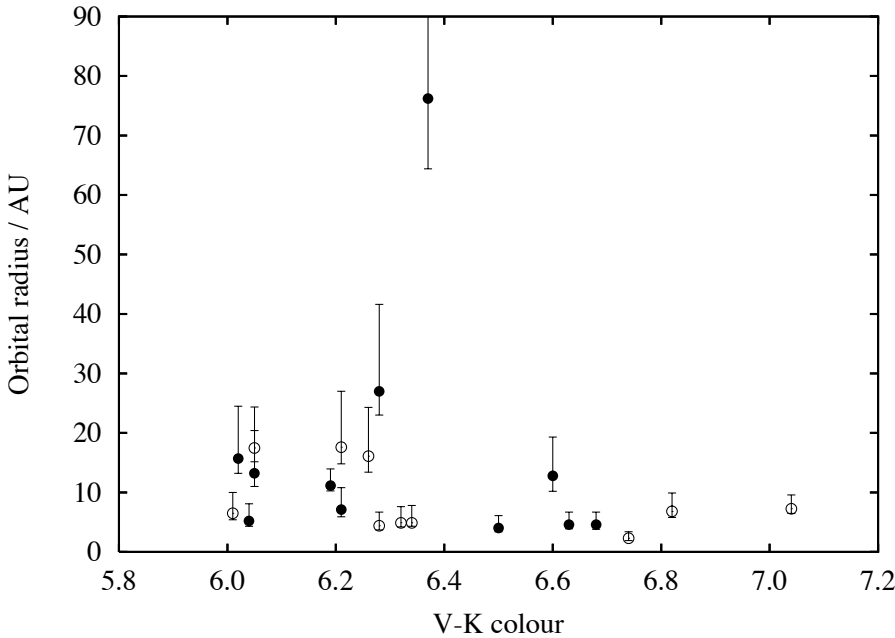


Figure 7.11: Orbital radius in the detected binaries as a function of colour. V-K=6 corresponds approximately to M4.5, and V-K=7 to M5.5. Filled circles are X-ray emitters. For clarity, the ~0.3 mags horizontal error bars have been omitted. There is no obvious correlation between X-ray emission and orbital radius.

would benefit from the more massive systems having a larger sample, there may be a sharp cut-off in the incidence of systems with orbital radii $> 10\text{AU}$, at around the M5-M5.5 spectral type. Note that the K-S test is here used to find the significance of an anomaly already noticed by eye in the data; the cutoff at V-K=6.5 is arbitrary for example. A more rigorous test would be to re-observe a similar sample of targets and find if the same cutoff is also significant for that sample.

7.5 Conclusions from the LuckyCam Surveys

What can we conclude about the nature of the VLM star formation processes from the LuckyCam surveys? The current picture of VLM star formation is usually modelled as fragmentation of the initial molecular cloud core followed by ejection of the low mass stellar embryos before mass accretion has completed - the ejection hypothesis (Reipurth & Clarke, 2001).

Multiple systems formed by fragmentation are limited to be no smaller than 10AU by the opacity limit (eg. Boss (1988)), although closer binaries can be formed by dynamical interactions and orbital decay (Bate et al., 2002).

The ejection hypothesis predicted binary frequency is about 8% (Bate & Bonnell, 2005); few very close ($< 3\text{AU}$) binaries are expected (Umbreit et al., 2005) without appealing to orbital

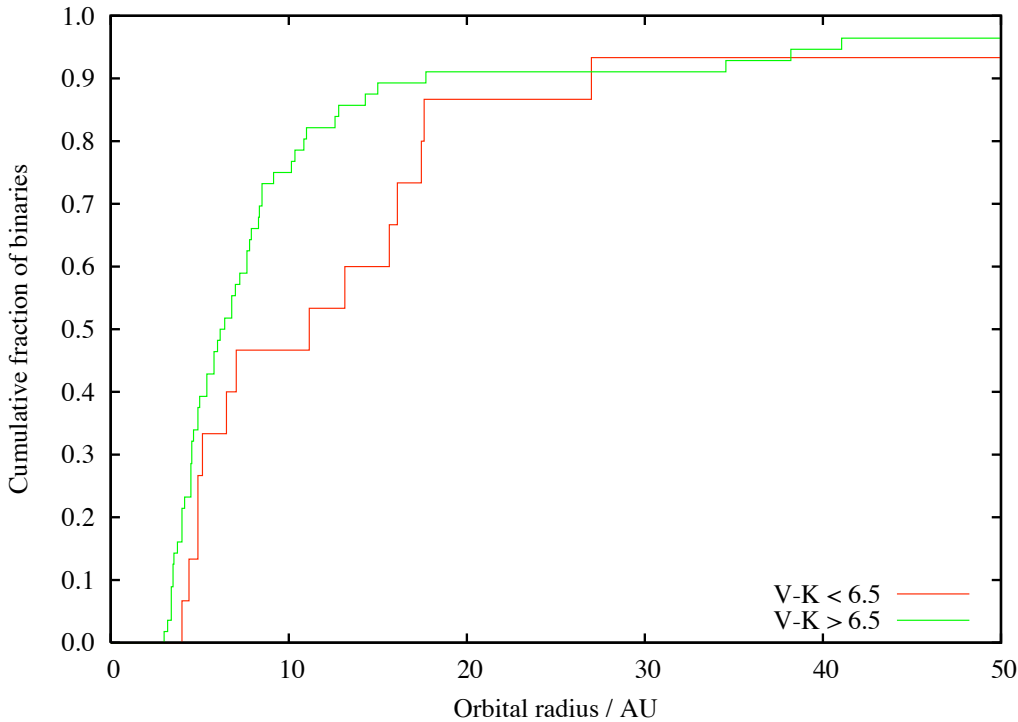


Figure 7.12: The cumulative distribution of orbital radii of the detected binaries in the sample with $V-K < 6.5$ (thick red line). The green line shows those with $V-K > 6.5$ (thin green line), with the addition of the full sample of known VLM binaries with total system masses $< 0.2M_{\odot}$, collated by Siegler. Neither distribution reaches a fraction of 1.0 because of a small number of binaries wider than 50 AU.

decay. Few wide binaries with low binding energies are expected to survive the ejection, although recent models produce some systems wider than 20AU when two stars are ejected simultaneously in the same direction (Bate & Bonnell, 2005). The standard ejection hypothesis orbital radius distribution is thus rather tight and centered at about 3-5 AU, although its width can be enlarged by appealing to the above additional effects.

The LuckyCam surveys found several wide binary systems, with 11 of the 24 detected systems at more than 10 AU orbital radius and 3 at more than 20 AU. With the latest models, the ejection hypothesis cannot be ruled out by these observations, and indeed (as suggested in Bate & Bonnell (2005)) the frequency of wider systems will be very useful for constraining later models capable of predicting the frequency in detail. The observed distance-bias-corrected binary frequency in the LuckyCam survey is consistent with the ejection hypothesis models, but may be inconsistent when the number of very close binaries undetected in the surveys is taken into account (Maxted & Jeffries, 2005; Jeffries & Maxted, 2005).

For fragmentation to reproduce the observed orbital radius distribution, including the likely number of very close systems, dynamical interactions and orbital decay must be very important processes. However, SPH models also predict very low numbers of close binaries. An alternate mechanism for the production of the closest binaries is thus required (Jeffries & Maxted,

2005), as well as modelling constraints to test against the observed numbers of wider binaries. Combining the LuckyCam surveys with radial velocity tests for much closer systems would offer a very useful insight into the full orbital radius distribution that must be reproduced by the models.

7.5.1 Extensions to the LuckyCam VLM Binary Surveys

The LuckyCam VLM binary surveys offer a wealth of targets suitable for followup.

Firstly, the binaries discovered in this chapter require follow-up LuckyCam observations, to obtain calibrated resolved photometry for the components. As in chapter 6, this will allow modelling of the component masses of the systems as well as improved constraints on their spectral types.

Secondly, the binaries which are barely resolved require higher-resolution imaging – this includes the < 0.15 arcsec binaries presented in this chapter, and the possible substellar triple system in chapter 6. Some of these systems will be observed using LuckyCam on the 3.6m New Technology Telescope in June 2006; the increased mirror size increases the diffraction-limited resolution but at the cost of a lower probability of obtaining a good frame. Since these targets are known to be binaries, however, longer integration times can be assigned, allowing smaller numbers of frames to be selected to obtain the highest resolutions.

The new binaries (especially the more exotic systems) will also be studied intensively with other instruments. Resolved near-infrared imaging of the systems will be especially useful to determine the properties of the later-type companions. Such imaging would require (in many cases) laser guide star adaptive optics systems, as the targets are faint. If possible, resolved spectroscopy of the systems would be the best method for the accurate determination of the temperatures and spectral types of the stars.

Radial velocity observations of the samples presented here would determine the number of very close binaries. These systems probably make up a substantial fraction of VLM binaries (Jeffries & Maxted, 2005), and so searches for very close companions are required for a complete census of the binarity in the samples.

In the longer term, I would like to follow the orbits of these binaries astrometrically (and with radial velocity measurements). Many of the systems presented here have short enough orbital periods to allow a full orbital solution in a relatively short time: for example, with a total system mass of $0.2M_{\odot}$ (typical for the binaries presented in this chapter) and an orbital radius of 2.3AU (the closest new binary in this chapter), the full orbital period is only 16 years (from equation 7.1). The orbital period of the possible substellar companion presented in chapter 6 is estimated to be 15-30 years. Since the orbit may be fit before the completion of a full orbital period, many of these systems will allow an accurate mass calibration of these object types

over a reasonably short timescale.

I also plan to extend the LuckyCam VLM binary survey to cover many more targets. The June 2006 run on the NTT is planned to extend the survey by several hundred Southern targets (weather permitting). This will both very significantly increase the known number of VLM binaries (by up to 100% in total) and offer the possibility of the discovery of more exotic systems, such as substellar companions or higher-order multiple systems.

7.6 Summary

- I found 21 very low mass binary systems in a 78 star sample, including one binary which is a companion in a 2300 AU wide triple system. 14 of the binary systems are new discoveries.
- All of the new systems are significantly fainter than the previously known close systems in the sample, demonstrating LuckyCam's faint-guide-star capability.
- I demonstrated the use of LuckyCam for binary orbit determination, and found that the previously known mass for the GJ1245AC system is in error by ~20%.
- The distance-corrected binary fraction is $13.5^{+6.5}_{-4}\%$, in agreement with previous results, and there is no detectable correlation between X-Ray emission and binarity.
- The orbital radius distribution of the binaries appears to show characteristics of both the late and early M-dwarf distributions, with 9 systems having an orbital radius of more than 10 AU.
- The orbital radius distribution of the binaries with $V-K < 6.5$ in this survey is not consistent with that of lower-mass objects, suggesting a possible sharp cutoff in the number of binaries wider than 10 AU at about the M5 spectral type.

8

Conclusions

In this chapter I summarise the results in my thesis, and suggest future paths for Lucky Imaging. Future plans for the VLM binary surveys are detailed at the end of chapter 7.

8.1 Lucky Imaging Performance

LuckyCam gives diffraction-limited images in the visible on a 2.5m telescope, easily and cheaply. It is clear that the system gives excellent results in a wide variety of conditions – in addition to the wide range of seeings investigated in chapter 4, all but one of the 24 VLM binaries detailed in chapters 6 and 7 were resolved with diffraction-limited resolution.

Lucky Imaging also offers a very large i-band isoplanatic patch, 15-30 arcsec at the NOT. This, along with LuckyCam’s very faint guide star capability, gives excellent sky coverage with natural guide stars. The calibrations, performance measurements and science results presented in this thesis demonstrate Lucky Imaging’s utility for a wide variety of science programmes.

Lucky Imaging degrades gracefully under difficult conditions. Images with diffraction-limited cores were obtained over a very wide variety of conditions, but when it was not possible to obtain them the output image resolution was still very much improved. For example, when operated in B-band , in very poor seeing, or at slow frame rates (chapter 4), LuckyCam still attains a very significant resolution increase even when no diffraction-limited frames at all would be expected.

This ability ensures that LuckyCam-like instruments can be used for a very wide variety of astronomical programmes. Because they offer essentially zero readout noise, and behave otherwise like standard CCD cameras (with the exception of multiplication noise), the frame-selection and recentering methods will *always* improve the output images compared to a standard system – especially as the image improvement methods can be tailored to both the science being performed and the conditions (chapter 3).

LuckyCam-like instruments are a simple, and thus very cheap method of obtaining diffraction-limited resolutions. A “standard” LuckyCam consists simply of a filter, a reimaging lens, and an L3CCD detector, and yet obtains resolutions in the visible that complicated and expensive adaptive optics systems manage only in the near infra-red on 8-10m class telescopes. Although Lucky Imaging in the form presented here operates most effectively on smaller 2.5-3m telescopes, it increases their capabilities enormously for a very small cost.

It is worth emphasising that it would have been far more complex and time-intensive to perform the VLM binary surveys without LuckyCam. At an average of 8.7 minutes per target (including all overheads), LuckyCam’s zero lock-on time for high-resolution imaging allowed the survey of 110 target stars to be completed in only 16 hours of on-sky time – despite many of the observations being performed though 3 magnitudes of cloud-cover. LuckyCam’s ability to guide on faint stars proved invaluable for the investigation of targets which are not accessible to standard AO systems. It is telling that, in the sample presented in chapter 7, the 14 new close binaries discovered with LuckyCam are all significantly fainter than the previously known systems.

8.2 Future Prospects for Lucky Imaging

The Cambridge Lucky Imaging group is currently working to further extend the utility of Lucky Imaging, by building a full realtime Lucky Imaging system (rather than the preview system described in chapter 2). This will implement the pipeline described in chapter 3 on DSP (digital signal processor) hardware, and will allow non-specialists to use the system at the telescope without having to post-process hundreds of gigabytes of data.

In the further future, the development of relatively low-noise detectors in the near-infrared will allow Lucky Imaging for diffraction-limited images on large (5-8m) telescopes in the near-infrared. This method would be much cheaper and less complex than an equivalent adaptive optics system, especially as the high sky brightness in the near-infrared necessitates the use of a short-exposure detector for any imaging.

The Lucky Imaging concept, that one can select and only use the very best data obtained by an imaging system, is also applicable to other high-resolution imaging systems. For example, a LuckyCam-like camera placed behind an Adaptive Optics system would allow the selection

of those times when the atmospheric turbulence is low, and the AO system is thus producing the very best images. It is possible that such hybrid systems would allow visible-light near-diffraction-limited imaging on 5m class telescopes, and I hope to experiment with such systems in the near future.

We also hope to test a new Lucky Imaging concept in June 2006. Developed by Craig Mackay, CLASI (the Cambridge Lucky Aperture Synthesis Instrument) combines elements of Lucky Imaging and multiple aperture interferometry (Mackay, 2005). The aperture of a large telescope is divided into several sub-apertures. Light from groups of four sub-apertures is combined at a focal plane, to give PSFs crossed with fringes. High-resolution information about the objects in the field can be recovered from the fringes, at scales corresponding to the baselines between the apertures.

Conventional aperture-masking systems require very bright targets, as the detection of fringes usually requires an aperture size of less than r_0 . However, the use of an L3CCD detector for short exposure imaging allows Lucky Imaging of the PSFs, ensuring that the images are diffraction-limited with large (1m-scale) apertures, and thus observations of faint targets. Multiple detectors observing multiple groups of apertures allow the total aperture to approach that of the fully-filled telescope.

The tests we plan to undertake in June will (hopefully) verify the concept; proposals for the development of the system to give diffraction-limited imaging at 800nm on the 8m Very Large Telescope are currently under review.

The Lucky Imaging concept enables high-angular-resolution imaging using a simple and cheap instrument. With many planned developments of the system, and a bit of Luck, the future of high-resolution imaging in the visible from the ground looks secure.

Bibliography

- ABT, H. A. AND LEVY, S. G. 1976, Multiplicity among solar-type stars, *ApJS*, 30, 273
- ARGYLE, B. 2004, in "Observing and Measuring Visual Double Stars"
- ARISTIDI, E. AND AGABI, A. AND FOSSAT, E. AND AZOUIT, M. AND MARTIN, F. AND SADIBEKOVA, T. AND TRAVOUILLO, T. AND VERNIN, J. AND ZIAD, A. 2005, Site testing in summer at Dome C, Antarctica, *A&A*, 444, 651
- BALDWIN, J. E. AND BOYSEN, R. C. AND COX, G. C. AND HANIFF, C. A. AND ROGERS, J. AND WARNER, P. J. AND WILSON, D. M. AND MACKAY, C. D. 1994, in Proc. SPIE Vol. 2200, p. 118-128, Amplitude and Intensity Spatial Interferometry II, James B. Breckinridge; Ed., ed. J. B. Breckinridge, 118–128
- BALDWIN, J. E. AND HANIFF, C. A. AND MACKAY, C. D. AND WARNER, P. J. 1986, Closure phase in high-resolution optical imaging, *Nature*, 320, 595
- BALDWIN, J. E. AND TUBBS, R. N. AND COX, G. C. AND MACKAY, C. D. AND WILSON, R. W. AND ANDERSEN, M. I. 2001, Diffraction-limited 800 nm imaging with the 2.56 m Nordic Optical Telescope, *A&A*, 368, L1
- BARAFFE, I. AND CHABRIER, G. AND ALLARD, F. AND HAUSCHILD, P. H. 1998, Evolutionary models for solar metallicity low-mass stars: mass-magnitude relationships and color-magnitude diagrams, *A&A*, 337, 403
- BASDEN, A. G. AND HANIFF, C. A. AND MACKAY, C. D. 2003, Photon counting strategies with low-light-level CCDs, *MNRAS*, 345, 985
- BASRI, G. AND REINERS, A. 2006, A Survey for Spectroscopic Binaries Among Very Low-Mass Stars, ArXiv Astrophysics e-prints
- BATE, M. R. AND BONNELL, I. A. 2005, The origin of the initial mass function and its dependence on the mean Jeans mass in molecular clouds, *MNRAS*, 356, 1201
- BATE, M. R. AND BONNELL, I. A. AND BROMM, V. 2002, The formation of close binary systems by dynamical interactions and orbital decay, *MNRAS*, 336, 705

- BOCCALETTI, A. AND LABEYRIE, A. AND RAGAZZONI, R. 1998, Preliminary results of dark-speckle stellar coronography, *A&A*, 338, 106
- BOSS, A. P. 1988, Protostellar formation in rotating interstellar clouds. VII - Opacity and fragmentation, *ApJ*, 331, 370
- BOUY, H. AND BRANDNER, W. AND MARTÍN, E. L. AND DELFOSSE, X. AND ALLARD, F. AND BASRI, G. 2003, Multiplicity of Nearby Free-Floating Ultracool Dwarfs: A Hubble Space Telescope WFPC2 Search for Companions, *AJ*, 126, 1526
- BRANDNER, W. AND ROUSSET, G. AND LENZEN, R. AND HUBIN, N. AND LACOMBE, F. AND HOFMANN, R. AND MOORWOOD, A. AND LAGRANGE, A.-M. AND GENDRON, E. AND HARTUNG, M. AND PUGET, P. AND AGEORGES, N. AND BIEREICHEL, P. AND BOUY, H. AND CHARTON, J. AND DUMONT, G. AND FUSCO, T. AND JUNG, Y. AND LEHNERT, M. AND LIZON, J.-L. AND MONNET, G. AND MOUILLET, D. AND MOUTOU, C. AND RABAUD, D. AND RÖHRLE, C. AND SKOLE, S. AND SPYROMILIO, J. AND STORZ, C. AND TACCONI-GARMAN, L. AND ZINS, G. 2002, NAOS+CONICA at YEPUN: first VLT adaptive optics system sees first light, *The Messenger*, 107, 1
- BROWN, M. E. AND BOUCHEZ, A. H. AND RABINOWITZ, D. AND SARI, R. AND TRUJILLO, C. A. AND VAN DAM, M. AND CAMPBELL, R. AND CHIN, J. AND HARTMAN, S. AND JOHANSSON, E. AND LAFON, R. AND LE MIGNANT, D. AND STOMSKI, P. AND SUMMERS, D. AND WIZINOWICH, P. 2005, Keck Observatory Laser Guide Star Adaptive Optics Discovery and Characterization of a Satellite to the Large Kuiper Belt Object 2003 EL61, *ApJ*, 632, L45
- BURGASSER, A. J. AND KIRKPATRICK, J. D. AND REID, I. N. AND BROWN, M. E. AND MISKEY, C. L. AND GIZIS, J. E. 2003, Binarity in Brown Dwarfs: T Dwarf Binaries Discovered with the Hubble Space Telescope Wide Field Planetary Camera 2, *ApJ*, 586, 512
- BURGASSER, A. J. AND REID, I. N. AND SIEGLER, N. AND CLOSE, L. AND ALLEN, P. AND LOWRANCE, P. AND GIZIS, J. 2006, in Planets and Protostars V meeting (October 2005)
- BUSCHER, D. F. 1993, Statistics of the seeing coherence time on MT Wilson, *Bulletin of the American Astronomical Society*, 25, 1306
- BUSCHER, D. F. 1994, in Proc. SPIE Vol. 2200, p. 260-271, Amplitude and Intensity Spatial Interferometry II, James B. Breckinridge; Ed., ed. J. B. Breckinridge, 260–271
- BUSCHER, D. F. AND ARMSTRONG, J. T. AND HUMMEL, C. A. AND QUIRRENBACH, A. AND MOZURKEWICH, D. AND JOHNSTON, K. J. AND DENISON, C. S. AND COLAVITA, M. M. AND SHAO, M. 1995, Interferometric seeing measurements on Mt. Wilson: power spectra and outer scales, *Appl. Opt.*, 34, 1081
- BUTLER, R. F. AND SHEARER, J. A. L. AND REDFERN, R. M. 1996, Crowded Field Photometry of M15 Using the TIRIFFID Camera, *Irish Astronomical Journal*, 23, 37

- CHESNEAU, O. AND WATERS, L. B. F. M. AND LEINERT, C. AND STEE, P. AND MEILLAND, A. AND VAN BOEKEL, R. AND MIN, M. 2005, in ASP Conf. Ser. 337: The Nature and Evolution of Disks Around Hot Stars, ed. R. Ignace & K. G. Gayley, 225–+
- CHRISTOU, J. C. 1991, Image quality, tip-tilt correction, and shift-and-add infrared imaging, *PASP*, 103, 1040
- CLOSE, L. M. AND SIEGLER, N. AND FREED, M. AND BILLER, B. 2003, Detection of Nine M8.0-L0.5 Binaries: The Very Low Mass Binary Population and Its Implications for Brown Dwarf and Very Low Mass Star Formation, *ApJ*, 587, 407
- COLAVITA, M. M. AND SHAO, M. AND STAELIN, D. H. 1987, Atmospheric phase measurements with the Mark III stellar interferometer, *Appl. Opt.*, 26, 4106
- CRAMPTON, D. AND MCCLURE, R. D. AND FLETCHER, J. M. 1992, HRCam survey for closely spaced gravitational lenses, *ApJ*, 392, 23
- CRUZ, K. L. AND REID, I. N. AND LIEBERT, J. AND KIRKPATRICK, J. D. AND LOWRANCE, P. J. 2003, Meeting the Cool Neighbors. V. A 2MASS-Selected Sample of Ultracool Dwarfs, *AJ*, 126, 2421
- DAINTY, J. C. AND HENNINGS, D. R. AND ODONNELL, K. A. 1981, Space-time correlation of stellar speckle patterns, *Optical Society of America Journal A*, 71, 490
- DANTOWITZ, R. F. AND TEARE, S. W. AND KOZUBAL, M. J. 2000, Ground-based High-Resolution Imaging of Mercury, *AJ*, 119, 2455
- DAVIS, J. AND NORTH, J. R. 2001, Binary Star Observations in Selected Instants of Good Seeing, *Publications of the Astronomical Society of Australia*, 18, 281
- DELFOSSÉ, X. AND FORVEILLE, T. AND BEUZIT, J.-L. AND UDRY, S. AND MAYOR, M. AND PERIER, C. 1999, New neighbours. I. 13 new companions to nearby M dwarfs, *A&A*, 344, 897
- DHILLON, V. AND MARSH, T. R. AND KELLY, J. AND PASHLEY, R. AND STEVENSON, M. AND ATKINSON, D. AND BEARD, S. AND IVES, D. AND PEACOCKE, T. AND TIERNEY, C. AND VICK, A. 2002, in ASP Conf. Ser. 261: The Physics of Cataclysmic Variables and Related Objects, ed. B. T. Gänsicke, K. Beuermann, & K. Reinsch, 672–+
- DI FOLCO, E. AND KOEHLER, B. AND KERVELLA, P. AND SARAZIN, M. S. AND COUDE DU FORESTO, V. AND SCHOELLER, M. AND WITTKOWSKI, M. 2003, in Interferometry for Optical Astronomy II. Edited by Wesley A. Traub . Proceedings of the SPIE, Volume 4838, pp. 1115-1126 (2003)., ed. W. A. Traub, 1115–1126
- DI SEREGO ALIGHIERI, S. AND PERRYMAN, M. A. C. 1986, in Instrumentation in astronomy VI; Proceedings of the Meeting, Tucson, AZ, Mar. 4-8, 1986. Part 1 (A87-36376 15-35).

- Bellingham, WA, Society of Photo-Optical Instrumentation Engineers, 1986, p. 201-205., ed. D. L. Crawford, 201–205
- DUQUENNOY, A. AND MAYOR, M. 1991, Multiplicity among solar-type stars in the solar neighbourhood. II - Distribution of the orbital elements in an unbiased sample, *A&A*, 248, 485
- FARIHI, J. AND BECKLIN, E. E. AND ZUCKERMAN, B. 2005, Low-Luminosity Companions to White Dwarfs, *ApJS*, 161, 394
- FISCHER, D. A. AND MARCY, G. W. 1992, Multiplicity among M dwarfs, *ApJ*, 396, 178
- FLESCH, E. AND HARDCASTLE, M. J. 2004, An all-sky optical catalogue of radio/X-ray sources, *A&A*, 427, 387
- FORD, H. C. AND BARTKO, F. AND BELY, P. Y. AND BROADHURST, T. AND BURROWS, C. J. AND CHENG, E. S. AND CLAMPIN, M. AND CROCKER, J. H. AND FELDMAN, P. D. AND GOLIMOWSKI, D. A. AND HARTIG, G. F. AND ILLINGWORTH, G. AND KIMBLE, R. A. AND LESSER, M. P. AND MILEY, G. AND NEFF, S. G. AND POSTMAN, M. AND SPARKS, W. B. AND TSVETANOV, Z. AND WHITE, R. L. AND SULLIVAN, P. AND KREBS, C. A. AND LEVITON, D. B. AND LA JEUNESSE, T. AND BURMESTER, W. AND FIKE, S. AND JOHNSON, R. AND SLUSHER, R. B. AND VOLMER, P. AND WOODRUFF, R. A. 1998, in Proc. SPIE Vol. 3356, p. 234-248, Space Telescopes and Instruments V, Pierre Y. Bely; James B. Breckinridge; Eds., ed. P. Y. Bely & J. B. Breckinridge, 234–248
- FRIED, D. L. 1966, Optical Resolution Through a Randomly Inhomogeneous Medium for Very Long and Very Short Exposures, *Optical Society of America Journal A*, 56, 1372
- FRIED, D. L. 1967, in Proc. IEEE, Volume 55, p. 57-67, 57–67
- FRIED, D. L. 1978, Probability of getting a lucky short-exposure image through turbulence, *Optical Society of America Journal A*, 68, 1651
- FRUCHTER, A. S. AND HOOK, R. N. 2002, Drizzle: A Method for the Linear Reconstruction of Undersampled Images, *PASP*, 114, 144
- FUHRMEISTER, B. AND SCHMITT, J. H. M. M. 2003, A systematic study of X-ray variability in the ROSAT all-sky survey, *A&A*, 403, 247
- GAL, R. R. AND DE CARVALHO, R. R. AND ODEWAHN, S. C. AND DJORGOVSKI, S. G. AND MAHABAL, A. AND BRUNNER, R. J. AND LOPES, P. A. A. 2004, The Digitized Second Palomar Observatory Sky Survey (DPOSS). II. Photometric Calibration, *AJ*, 128, 3082
- GALILEO. 1610, *Sidereus Nuncius*
- GIZIS, J. E. AND MONET, D. G. AND REID, I. N. AND KIRKPATRICK, J. D. AND BURGASSER, A. J. 2000, Two nearby M dwarf binaries from the Two Micron All Sky Survey, *MNRAS*, 311, 385

- GIZIS, J. E. AND REID, I. N. AND HAWLEY, S. L. 2002, The Palomar/MSU Nearby Star Spectroscopic Survey. III. Chromospheric Activity, M Dwarf Ages, and the Local Star Formation History, AJ, 123, 3356
- GIZIS, J. E. AND REID, I. N. AND KNAPP, G. R. AND LIEBERT, J. AND KIRKPATRICK, J. D. AND KOERNER, D. W. AND BURGASSER, A. J. 2003, Hubble Space Telescope Observations of Binary Very Low Mass Stars and Brown Dwarfs, AJ, 125, 3302
- GLIESE, W. AND JAHREISS, H. 1991, Preliminary Version of the Third Catalogue of Nearby Stars, Tech. rep.
- GORHAM, P. W. AND GHEZ, A. M. AND KULKARNI, S. R. AND NAKAJIMA, T. AND NEUGEBAUER, G. AND OKE, J. B. AND PRINCE, T. A. 1989, Diffraction-limited imaging. III - 30 MAS closure phase imaging of six binary stars with the Hale 5 M telescope, AJ, 98, 1783
- GUHATHAKURTA, P. AND YANNI, B. AND BAHCALL, J. N. AND SCHNEIDER, D. P. 1994, Globular cluster photometry with the Hubble Space Telescope. 3: Blue stragglers and variable stars in the core of M3, AJ, 108, 1786
- HANIFF, C. A. AND MACKAY, C. D. AND TITTERINGTON, D. J. AND SIVIA, D. AND BALDWIN, J. E. 1987, The first images from optical aperture synthesis, Nature, 328, 694
- Hardy J. W., , ed. 1998, Adaptive optics for astronomical telescopes, Adaptive optics for astronomical telescopes
- HARRINGTON, R. S. 1990, The triple system G208-44AB/45, AJ, 100, 559
- HAWLEY, S. L. AND COVEY, K. R. AND KNAPP, G. R. AND GOLIMOWSKI, D. A. AND FAN, X. AND ANDERSON, S. F. AND GUNN, J. E. AND HARRIS, H. C. AND IVEZIĆ, Ž. AND LONG, G. M. AND LUPTON, R. H. AND ET. AL. 2002, Characterization of M, L, and T Dwarfs in the Sloan Digital Sky Survey, AJ, 123, 3409
- HENRY, T. J. AND FRANZ, O. G. AND WASSERMAN, L. H. AND BENEDICT, G. F. AND SHELUS, P. J. AND IANNA, P. A. AND KIRKPATRICK, J. D. AND McCARTHY, D. W. 1999, The Optical Mass-Luminosity Relation at the End of the Main Sequence (0.08-0.20 M_{solar}), ApJ, 512, 864
- HENRY, T. J. AND IANNA, P. A. AND KIRKPATRICK, J. D. AND JAHREISS, H. 1997, The solar neighborhood IV: discovery of the twentieth nearest star, AJ, 114, 388
- HENRY, T. J. AND McCARTHY, D. W. 1990, A systematic search for brown dwarfs orbiting nearby stars, ApJ, 350, 334
- HENRY, T. J. AND McCARTHY, D. W. 1993, The mass-luminosity relation for stars of mass 1.0 to 0.08 solar mass, AJ, 106, 773

- HERBST, W. AND MUNDT, R. 2005, Rotational Evolution of Solar-like Stars in Clusters from Pre-Main Sequence to Main Sequence: Empirical Results, *ApJ*, 633, 967
- HORCH, E. P. AND MEYER, R. D. AND VAN ALTENA, W. F. 2004, Speckle Observations of Binary Stars with the WIYN Telescope. IV. Differential Photometry, *AJ*, 127, 1727
- HORCH, E. P. AND ROBINSON, S. E. AND MEYER, R. D. AND VAN ALTENA, W. F. AND NINKOV, Z. AND PITERMAN, A. 2002, Speckle Observations of Binary Stars with the WIYN Telescope. II. Relative Astrometry Measures during 1998-2000, *AJ*, 123, 3442
- JANESICK, J. R. 2001, in Scientific Charge-Coupled Devices, ed. SPIE, ""
- JASCHEK, M. 1978, Catalogue of selected spectral types in the MK system., *Bulletin d'Information du Centre de Donnees Stellaires*, 15, 121
- JEFFRIES, R. D. 1999, in ASP Conf. Ser. 158: Solar and Stellar Activity: Similarities and Differences, ed. C. J. Butler & J. G. Doyle, 75-+
- JEFFRIES, R. D. AND MAXTED, P. F. L. 2005, Close binary systems among very low-mass stars and brown dwarfs, *Astronomische Nachrichten*, 326, 944
- JERRAM, P. AND POOL, P. J. AND BELL, R. AND BURT, D. J. AND BOWRING, S. AND SPENCER, S. AND HAZELWOOD, M. AND MOODY, I. AND CATLETT, N. AND HEYES, P. S. 2001, in Proc. SPIE Vol. 4306, p. 178-186, Sensors and Camera Systems for Scientific, Industrial, and Digital Photography Applications II, Morley M. Blouke; John Canosa; Nitin Sampat; Eds., ed. M. M. Blouke, J. Canosa, & N. Sampat, 178-186
- JIM, K. T. C. AND PICKLES, A. J. AND YAMADA, H. T. AND GRAVES, J. E. AND STOCKTON, A. AND NORTHCOTT, M. J. AND YOUNG, T. AND COWIE, L. L. AND LUCCINO, G. A. AND THORNTON, R. J. AND KUPKE, R. AND SOUSA, E. AND CAVEDONI, C. P. AND KELLER, T. J. AND NAKAMURA, W. AND METZGER, M. R. 2000, The University of Hawaii 2.2 Meter Fast Tip-Tilt Secondary System, *PASP*, 112, 716
- KILIC, M. AND MUNN, J. A. AND HARRIS, H. C. AND LIEBERT, J. AND VON HIPPEL, T. AND WILLIAMS, K. A. AND METCALFE, T. S. AND WINGET, D. E. AND LEVINE, S. E. 2006, Cool White Dwarfs in the Sloan Digital Sky Survey, *AJ*, 131, 582
- LÉPINE, S. AND SHARA, M. M. 2005, A Catalog of Northern Stars with Annual Proper Motions Larger than 0.15" (LSPM-NORTH Catalog), *AJ*, 129, 1483
- LABEYRIE, A. 1970, Attainment of Diffraction Limited Resolution in Large Telescopes by Fourier Analysing Speckle Patterns in Star Images, *A&A*, 6, 85
- LATHAM, D. W. AND STEFANIK, R. P. AND TORRES, G. AND DAVIS, R. J. AND MAZEH, T. AND CARNEY, B. W. AND LAIRD, J. B. AND MORSE, J. A. 2002, A Survey of Proper-Motion Stars. XVI. Orbital Solutions for 171 Single-lined Spectroscopic Binaries, *AJ*, 124, 1144

- LAW, N. M. AND HODGKIN, S. T. AND MACKAY, C. D. 2006a, Discovery of five very low mass close binaries, resolved in the visible with lucky imaging, *MNRAS*, 398
- LAW, N. M. AND HODGKIN, S. T. AND MACKAY, C. D. AND BALDWIN, J. E. 2005, Ten new very low-mass close binaries resolved in the visible, *Astronomische Nachrichten*, 326, 1024
- LAW, N. M. AND MACKAY, C. D. AND BALDWIN, J. E. 2006b, Lucky imaging: high angular resolution imaging in the visible from the ground, *A&A*, 446, 739
- LEGGETT, S. K. 1992, Infrared colors of low-mass stars, *ApJS*, 82, 351
- LEINERT, C. AND HENRY, T. AND GLINDEMANN, A. AND MCCARTHY, D. W. 1997, A search for companions to nearby southern M dwarfs with near-infrared speckle interferometry, *A&A*, 325, 159
- LÉPINE, S. 2005, Nearby Stars from the LSPM-North Proper-Motion Catalog. I. Main-Sequence Dwarfs and Giants within 33 Parsecs of the Sun, *AJ*, 130, 1680
- Livio M., Noll K., Stiavelli M., , eds. 2003, *A Decade of Hubble Space Telescope Science, A Decade of Hubble Space Telescope Science*
- LOHMANN, A. W. AND WEIGELT, G. AND WIRNITZER, B. 1983, Speckle masking in astronomy - Triple correlation theory and applications, *Appl. Opt.*, 22, 4028
- LUHMAN, K. L. 2004, The First Discovery of a Wide Binary Brown Dwarf, *ApJ*, 614, 398
- LUYTEN, W. J. 1995, NLTT Catalogue (Luyten, 1979), *VizieR Online Data Catalog*, 1098, 0
- LUYTEN, W. J. 1997, LDS Catalogue: Doubles with Common Proper Motion (Luyten 1940-87), *VizieR Online Data Catalog*, 1130, 0
- MACKAY, C. AND BASDEN, A. AND BRIDGELAND, M. 2004, in *Optical and Infrared Detectors for Astronomy*. Edited by James D. Garnett and James W. Beletic. *Proceedings of the SPIE*, Volume 5499, pp. 203-209 (2004)., ed. J. D. Garnett & J. W. Beletic, 203–209
- MACKAY, C. D. 2005, in *Proceedings of Conference on Instrumentation for ELTs*, Ringberg
- MAKAROV, V. V. 2002, The Rate of Visual Binaries among the Brightest X-Ray Stars, *ApJ*, 576, L61
- MASON, B. D. AND HARTKOPF, W. I. AND WYCOFF, G. L. AND RAFFERTY, T. J. 2006, Speckle Interferometry at the US Naval Observatory. XI., *AJ*, 131, 2687
- MAXTED, P. F. L. AND JEFFRIES, R. D. 2005, On the frequency of close binary systems among very low-mass stars and brown dwarfs, *MNRAS*, 362, L45
- MCCARTHY, C. AND ZUCKERMAN, B. AND BECKLIN, E. E. 2001, Discovery of 14 Nearby Double Stars, *AJ*, 121, 3259

MCCARTHY, D. W. AND HENRY, T. J. AND FLEMING, T. A. AND SAFFER, R. A. AND LIEBERT, J. AND CHRISTOU, J. C. 1988, The very low mass triple system - G208-44AB and G208-45, *ApJ*, 333, 943

MCCLURE, R. D. AND GRUNDMANN, W. A. AND RAMBOLD, W. N. AND FLETCHER, J. M. AND RICHARDSON, E. H. AND STILLBURN, J. R. AND RACINE, R. AND CHRISTIAN, C. A. AND WADDELL, P. 1989, An Image Stabilization High-Resolution Camera for the Canada-France-Hawaii Telescope, *PASP*, 101, 1156

MENNESSON, B. AND KORESKO, C. AND CREECH-EAKMAN, M. J. AND SERABYN, E. AND COLAVITA, M. M. AND AKESON, R. AND APPLEBY, E. AND BELL, J. AND BOOTH, A. AND CRAWFORD, S. AND DAHL, W. AND FANSON, J. AND FELIZARDO, C. AND GARCIA, J. AND GATHRIGHT, J. AND HERSTEIN, J. AND HOVLAND, E. AND HRYNEVYCH, M. AND JOHANSSON, E. AND LE MIGNANT, D. AND LIGON, R. AND MILLAN-GABET, R. AND MOORE, J. AND NEYMAN, C. AND PALMER, D. AND PANTELEEEVA, T. AND PAINE, C. AND RAGLAND, S. AND REDER, L. AND RUDEEN, A. AND SALOGA, T. AND SHAO, M. AND SMYTHE, R. AND SUMMERS, K. AND SWAIN, M. AND TSUBOTA, K. AND TYAU, C. AND VASISHT, G. AND WIZINOWICH, P. AND WOILLEZ, J. 2005, The Dusty AGB Star RS CrB: First Mid-Infrared Interferometric Observations with the Keck Telescopes, *ApJ*, 634, L169

MEYER, R. D. AND HORCH, E. P. AND NINKOV, Z. AND VAN ALTEA, W. F. AND ROTHKOPF, C. A. 2006, RYTSI: The Rochester Institute of Technology-Yale Tip-Tilt Speckle Imager, *PASP*, 118, 162

MICHELSON, A. A. 1920, On the Application of Interference Methods to Astronomical Measurements, *ApJ*, 51, 257

MONET, D. G. AND LEVINE, S. E. AND CANZIAN, B. AND ABLES, H. D. AND BIRD, A. R. AND DAHN, C. C. AND GUETTER, H. H. AND HARRIS, H. C. AND HENDEN, A. A. AND LEGGETT, S. K. AND LEVISON, H. F. AND LUGINBUHL, C. B. AND MARTINI, J. AND MONET, A. K. B. AND MUNN, J. A. AND PIER, J. R. AND RHODES, A. R. AND RIEPE, B. AND SELL, S. AND STONE, R. C. AND VRBA, F. J. AND WALKER, R. L. AND WESTERHOUT, G. AND BRUCATO, R. J. AND REID, I. N. AND SCHOENING, W. AND HARTLEY, M. AND READ, M. A. AND TRITTON, S. B. 2003, The USNO-B Catalog, *AJ*, 125, 984

NIETO, J.-L. AND LLEBARIA, A. AND DI SEREGO ALIGHIERI, S. 1987, Photon-counting detectors in time-resolved imaging mode - Image recentring and selection algorithms, *A&A*, 178, 301

NIETO, J.-L. AND ROQUES, S. AND LLEBARIA, A. AND VANDERRIEST, C. AND LELIEVRE, G. AND DI SEREGO ALIGHIERI, S. AND MACCHETTO, F. D. AND PERRYMAN, M. A. C. 1988, High-resolution imaging of the double QSO 2345 + 007 - Evidence for subcomponents, *ApJ*, 325, 644

- NIETO, J.-L. AND THOUVENOT, E. 1991, Recentring and selection of short-exposure images with photon-counting detectors. I - Reliability tests, *A&A*, 241, 663
- NIGHTINGALE, N. S. AND BUSCHER, D. F. 1991, Interferometric seeing measurements at the La Palma Observatory, *MNRAS*, 251, 155
- O'MAHONY, N. 2003, RoboDIMM - The ING's New Seeing Monitor, The Newsletter of the Isaac Newton Group of Telescopes (ING News.), issue no. 7, p. 22-24., 7, 22
- O'SULLIVAN, C. AND SHEARER, A. AND COLHOUN, M. AND GOLDEN, A. AND REDFERN, M. AND BUTLER, R. AND BESKIN, G. M. AND NEIZVESTNY, S. I. AND NEUSTROEV, V. V. AND PLOKHOTNICHENKO, V. L. AND DANKS, A. 1998, A search for the optical counterpart of PSR B1951+32 in the supernova remnant CTB 80, *A&A*, 335, 991
- PERCIVAL, J. W. AND BIGGS, J. D. AND DOLAN, J. F. AND ROBINSON, E. L. AND TAYLOR, M. J. AND BLESS, R. C. AND ELLIOT, J. L. AND NELSON, M. J. AND RAMSEYER, T. F. AND VAN CITTERS, G. W. AND ZHANG, E. 1993, The Crab pulsar in the visible and ultraviolet with 20 microsecond effective time resolution, *ApJ*, 407, 276
- PHAN-BAO, N. AND MARTÍN, E. L. AND REYLÉ, C. AND FORVEILLE, T. AND LIM, J. 2005, Discovery of a widely separated binary system of very low mass stars, *A&A*, 439, L19
- PLUZHNIK, E. A. 2005, Differential photometry of speckle-interferometric binary and multiple stars, *A&A*, 431, 587
- PRESS, W. H. AND TEUKOLSKY, S. A. AND VETTERLING, W. T. AND FLANNERY, B. P. 1988, Numerical Recipies in C
- RACINE, R. 1996, Temporal Fluctuations of Atmospheric Seeing, *PASP*, 108, 372
- RAYMOND, S. N. AND SZKODY, P. AND HAWLEY, S. L. AND ANDERSON, S. F. AND BRINKMANN, J. AND COVEY, K. R. AND MCGEHEE, P. M. AND SCHNEIDER, D. P. AND WEST, A. A. AND YORK, D. G. 2003, A First Look at White Dwarf-M Dwarf Pairs in the Sloan Digital Sky Survey, *AJ*, 125, 2621
- REID, I. N. AND CRUZ, K. L. 2002, Meeting the Cool Neighbors. I. Nearby Stars in the NLTT Catalogue: Defining the Sample, *AJ*, 123, 2806
- REID, I. N. AND GIZIS, J. E. 1997, Low-Mass Binaries and the Stellar Luminosity Function, *AJ*, 113, 2246
- REIPURTH, B. AND CLARKE, C. 2001, The Formation of Brown Dwarfs as Ejected Stellar Embryos, *AJ*, 122, 432
- RODDIER, F. AND COWIE, L. AND GRAVES, J. E. AND SONGAILA, A. AND MCKENNA, D. 1990, in Advanced technology optical telescopes IV; Proceedings of the Meeting, Tucson, AZ, Feb.

- 12-16, 1990. Part 1 (A91-23201 08-89). Bellingham, WA, Society of Photo-Optical Instrumentation Engineers, 1990, p. 485-491., ed. L. D. Barr, 485–491
- RODDIER, F. AND GILLI, J. M. AND VERNIN, J. 1982, On the isoplanatic patch size in stellar speckle interferometry , *Journal of Optics*, 13, 63
- RODDIER, F. AND NORTHCOTT, M. AND GRAVES, J. E. 1991, A simple low-order adaptive optics system for near-infrared applications, *PASP*, 103, 131
- SALIM, S. AND GOULD, A. 2003, Improved Astrometry and Photometry for the Luyten Catalog. II. Faint Stars and the Revised Catalog, *ApJ*, 582, 1011
- SCADDAN, R. J. AND WALKER, J. G. 1978, Statistics of stellar speckle patterns, *Appl. Opt.*, 17, 3779
- SCHMITT, J. H. M. M. AND LIEFKE, C. 2004, NEXXUS: A comprehensive ROSAT survey of coronal X-ray emission among nearby solar-like stars, *A&A*, 417, 651
- SCHOLZ, A. AND EISLÖFFEL, J. 2004, Rotation periods for very low mass stars in the Pleiades, *A&A*, 421, 259
- SCHROEDER, D. J. AND GOLIMOWSKI, D. A. AND BRUKARDT, R. A. AND BURROWS, C. J. AND CALDWELL, J. J. AND FASTIE, W. G. AND FORD, H. C. AND HESMAN, B. AND KLETSKIN, I. AND KRIST, J. E. AND ROYLE, P. AND ZUBROWSKI, R. A. 2000, A Search for Faint Companions to Nearby Stars Using the Wide Field Planetary Camera 2, *AJ*, 119, 906
- SÉGRANSAN, D. AND DELFOSSE, X. AND FORVEILLE, T. AND BEUZIT, J.-L. AND UDRY, S. AND PERRIER, C. AND MAYOR, M. 2000, Accurate masses of very low mass stars. III. 16 new or improved masses, *A&A*, 364, 665
- SIEGLER, N. AND CLOSE, L. M. AND CRUZ, K. L. AND MARTÍN, E. L. AND REID, I. N. 2005, Discovery of Two Very Low Mass Binaries: Final Results of an Adaptive Optics Survey of Nearby M6.0-M7.5 Stars, *ApJ*, 621, 1023
- SIMON, T. 1990, IUE observations of rapidly rotating low-mass stars in young clusters - The relation between chromospheric activity and rotation, *ApJ*, 359, L51
- SMITH, J. A. AND TUCKER, D. L. AND KENT, S. AND RICHMOND, M. W. AND ET AL. 2002, The u'g'r'i'z' Standard-Star System, *AJ*, 123, 2121
- SODERBLOM, D. R. AND STAUFFER, J. R. AND HUDON, J. D. AND JONES, B. F. 1993, Rotation and chromospheric emission among F, G, and K dwarfs of the Pleiades, *ApJS*, 85, 315
- STONE, R. C. 1996, An Accurate Method for Computing Atmospheric Refraction, *PASP*, 108, 1051

- TAKAMI, H. AND TAKATO, N. AND HAYANO, Y. AND IYE, M. AND KAMATA, Y. AND MINOWA, Y. AND KANZAWA, T. AND GAESSLER, W. 2003, in Adaptive Optical System Technologies II. Edited by Wizinowich, Peter L.; Bonaccini, Domenico. Proceedings of the SPIE, Volume 4839, pp. 21-31 (2003)., ed. P. L. Wizinowich & D. Bonaccini, 21–31
- TATARSKI, V. 1961, Wave Propagation in a Turbulent Medium., McGraw-Hill
- TOKOVININ, A. AND BAUMONT, S. AND VASQUEZ, J. 2003, Statistics of turbulence profile at Cerro Tololo, MNRAS, 340, 52
- TONRY, J. AND BURKE, B. E. AND SCHECHTER, P. L. 1997, The Orthogonal Transfer CCD, PASP, 109, 1154
- TONRY, J. L. AND LUCCINO, G. A. AND KAISER, N. AND BURKE, B. E. AND JACOBY, G. H. 2002, in Survey and Other Telescope Technologies and Discoveries. Edited by Tyson, J. Anthony; Wolff, Sidney. Proceedings of the SPIE, Volume 4836, pp. 206-216 (2002)., ed. J. A. Tyson & S. Wolff, 206–216
- TRUJILLO, I. AND AGUERRI, J. A. L. AND CEPÀ, J. AND GUTIÉRREZ, C. M. 2001, The effects of seeing on Sérsic profiles - II. The Moffat PSF, MNRAS, 328, 977
- TUBBS, R. N. 2004, Lucky exposures: diffraction-limited astronomical imaging through the atmosphere, The Observatory, 124, 159
- TUBBS, R. N. AND BALDWIN, J. E. AND MACKAY, C. D. 2003, in Adaptive Optical System Technologies II. Edited by Wizinowich, Peter L.; Bonaccini, Domenico. Proceedings of the SPIE, Volume 4839, pp. 1093-1102 (2003)., 1093–1102
- TUBBS, R. N. AND BALDWIN, J. E. AND MACKAY, C. D. AND COX, G. C. 2002, Diffraction-limited CCD imaging with faint reference stars, A&A, 387, L21
- TULLOCH, S. M. 2004, in Ground-based Instrumentation for Astronomy. Edited by Alan F. M. Moorwood and Iye Masanori. Proceedings of the SPIE, Volume 5492, pp. 604-614 (2004)., ed. A. F. M. Moorwood & M. Iye, 604–614
- UMBREIT, S. AND BURKERT, A. AND HENNING, T. AND MIKKOLA, S. AND SPURZEM, R. 2005, The Decay of Accreting Triple Systems as Brown Dwarf Formation Scenario, ApJ, 623, 940
- VAN ALTEA, W. F. AND LEE, J. T. AND HOFFLEIT, E. D. 2001, Yale Trigonometric Parallaxes, Fourth Edition (van Altena+ 1995), VizieR Online Data Catalog, 1238, 0
- VAN DAM, M. A. AND BOUCHEZ, A. H. AND LE MIGNANT, D. AND JOHANSSON, E. M. AND WIZINOWICH, P. L. AND CAMPBELL, R. D. AND CHIN, J. C. Y. AND HARTMAN, S. K. AND LAFON, R. E. AND STOMSKI, P. J. AND SUMMERS, D. M. 2006, The W. M. Keck Observatory Laser Guide Star Adaptive Optics System: Performance Characterization, PASP, 118, 310

VERNIN, J. AND MUÑOZ-TUÑÓN, C. 1998, The temporal behaviour of seeing, *New Astronomy Review*, 42, 451

VERNIN, J. AND MUÑOZ-TUNON, C. 1994, Optical seeing at La Palma Observatory. 2: Intensive site testing campaign at the Nordic Optical Telescope, *A&A*, 284, 311

VOGES, W. AND ASCHENBACH, B. AND BOLLER, T. AND BRAEUNINGER, H. AND BRIEL, U. AND BURKERT, W. AND DENNERL, K. AND ENGLHAUSER, J. AND GRUBER, R. AND HABERL, F. AND HARTNER, G. AND HASINGER, G. AND KUERSTER, M. AND PFEFFERMANN, E. AND PIETSCH, W. AND PREDEHL, P. AND ROSSO, C. AND SCHMITT, J. H. M. M. AND TRUEMPER, J. AND ZIMMERMANN, H. U. 1999, ROSAT All-Sky Bright Source Catalogue (1RXS) (Voges+ 1999), VizieR Online Data Catalog, 9010, 0

VOGES, W. AND ASCHENBACH, B. AND BOLLER, T. AND BRAUNINGER, H. AND BRIEL, U. AND BURKERT, W. AND DENNERL, K. AND ENGLHAUSER, J. AND GRUBER, R. AND HABERL, F. AND HARTNER, G. AND HASINGER, G. AND PFEFFERMANN, E. AND PIETSCH, W. AND PREDEHL, P. AND SCHMITT, J. AND TRUMPER, J. AND ZIMMERMANN, U. 2000, ROSAT All-Sky Survey Faint Source Catalog (Voges+ 2000), VizieR Online Data Catalog, 9029, 0

WEIGELT, G. AND WIRNITZER, B. 1983, Image reconstruction by the speckle-masking method, *Optics Letters*, 8, 389

WEIGELT, G. P. 1977, Modified astronomical speckle interferometry 'speckle masking', *Optics Communications*, 21, 55

WILDI, F. P. AND BRUSA, G. AND LLOYD-HART, M. AND CLOSE, L. M. AND RICCARDI, A. 2003, in Astronomical Adaptive Optics Systems and Applications. Edited by Tyson, Robert K.; Lloyd-Hart, Michael. Proceedings of the SPIE, Volume 5169, pp. 17-25 (2003)., ed. R. K. Tyson & M. Lloyd-Hart, 17–25

WIZINOWICH, P. AND ACTON, D. S. AND SHELTON, C. AND STOMSKI, P. AND GATHRIGHT, J. AND HO, K. AND LUPTON, W. AND TSUBOTA, K. AND LAI, O. AND MAX, C. AND BRASE, J. AND AN, J. AND AVICOLA, K. AND OLIVIER, S. AND GAVEL, D. AND MACINTOSH, B. AND GHEZ, A. AND LARKIN, J. 2000, First Light Adaptive Optics Images from the Keck II Telescope: A New Era of High Angular Resolution Imagery, *PASP*, 112, 315

WIZINOWICH, P. L. AND LE MIGNANT, D. AND BOUCHEZ, A. H. AND CAMPBELL, R. D. AND CHIN, J. C. Y. AND CONTOS, A. R. AND VAN DAM, M. A. AND HARTMAN, S. K. AND JOHANSSON, E. M. AND LAFON, R. E. AND LEWIS, H. AND STOMSKI, P. J. AND SUMMERS, D. M. AND BROWN, C. G. AND DANFORTH, P. M. AND MAX, C. E. AND PENNINGTON, D. M. 2006, The W. M. Keck Observatory Laser Guide Star Adaptive Optics System: Overview, *PASP*, 118, 297